

**SCANNING TRANSMISSION ELECTRON
MICROSCOPY OF ATOMIC STRUCTURE OF
NANOPARTICLE**

by

NAN JIAN

A thesis submitted to the University of Birmingham for the degree of
DOCTOR OF PHILOSOPHY



Nanoscale Physics Research Laboratory

School of Physics & Astronomy

University of Birmingham

September 2016

UNIVERSITY OF
BIRMINGHAM

University of Birmingham Research Archive

e-theses repository

This unpublished thesis/dissertation is copyright of the author and/or third parties. The intellectual property rights of the author or third parties in respect of this work are as defined by The Copyright Designs and Patents Act 1988 or as modified by any successor legislation.

Any use made of information contained in this thesis/dissertation must be in accordance with that legislation and must be properly acknowledged. Further distribution or reproduction in any format is prohibited without the permission of the copyright holder.

Abstract

This thesis presents the researches on the size and atomic structure of the nanoclusters including ligand protected monometallic clusters, ligand protected bimetallic clusters and biological metallic clusters, by using aberration corrected HAADF-STEM. The atomic structures of Au₅₅ Schmid clusters were investigated. The atom counting method with size selected clusters as mass balance was utilized to “fractionate” the relative broad distributed sample and make the structure study focus on the “true Au₅₅” clusters. Nearly half of these clusters were found to have a hybrid structure. A combination of geometric size analysis and atom counting method was performed to determine both the size and composition of the bimetallic AuAg alloy clusters. Base on these, the core atomic structures of the (Au_xAg_{1-x})_{312±55} clusters as a function of AuAg composition were obtained. The Ag-rich clusters tend to have an icosahedral structure while the Au-rich clusters prefer the fcc structure. For the biological nanoparticles, the ferritins’ iron loadings were obtained by the atom counting method with HAADF STEM. Different morphologies of the ferritin iron cores were observed as a function of iron loading, suggesting the iron core growth process in the protein shell. The HAADF-STEM was also successfully employed to characterize the ultra-small Au and Pd catalysts supported on the TiO₂, which are helpful to understand the catalytic performance of these catalysts. A multilayer deposition method was developed to accommodate and process the large abundance of clusters from the new high-flux cluster source by producing the stack of support layer-cluster-release layer sandwiches. A through focal STEM analysis was performed on the multilayer sample, confirming the multilayer structures of the stack and the thickness of each layer. With the similar experimental setup, size-selected colloidal clusters were produced by dissolving the multilayer cluster-PVP stacks. The colloidal clusters were observed by the STEM and their sizes were found to be conserved during the dissolving process, proves the success of production of size-selected colloidal clusters.

Acknowledgements

I would like to thank my supervisor Prof. Richard E. Palmer, for giving me the opportunity to work in the NPRL. His wisdom and enthusiasm for the research always inspire me to achieve a better performance.

I would like to thank Dr. Ziyou Li for her intelligent guidance and advice on the research. Her careful and responsible attitude to the research has always been an inspiration to me.

I would like to thank Dr. Kuo-Juei Hu for his training, guidance and help. Without his great help, I will not be able to become an eligible electron microscopist.

I would like to thank Dr. Quanmin Guo, Dr. Wolfgang Theis, Dr. Fengyin, Dr. Kenton Arkill, Dr. Simon Plant, Dr. Lu Cao, Dr. Karl Bauer, Dr. Dongsheng He, Dr. Ruth Chantry and Dr. Miriam Dowle for their advices and assistance on experiment and research.

I would like to thank Dr. Quanmin Guo, Dr. Wolfgang Theis and Dr. Andrey Kaplan for their advices and helps. I would like to thank Dr. Shane Murphy, Dawn Wells, and Alex Pattison for reading and correcting my thesis. I would also like to thank all my colleagues, past and present, for the invaluable friendship and support.

Finally, I would like to thank my parents and my babe Cheng for all of their supports throughout the whole PhD.

Author's publications

Jian, N., Stapelfeldt, C., Hu, K.-J., Fröba, M. & Palmer, R. E. Hybrid atomic structure of the Schmid cluster Au₅₅(PPh₃)₁₂Cl₆ resolved by aberration-corrected STEM. *Nanoscale* **7**, 885–888 (2015).

Jian, N. & Palmer, R. E. Variation of the Core Atomic Structure of Thiolated (Au_xAg_{1-x})_{312±55} Nanoclusters with Composition from Aberration-Corrected HAADF STEM. *J. Phys. Chem. C* **119**, 11114–11119 (2015).

Rogers, S. M. , Catlow, C. R., Chan-Thaw, C. E., Gianolio, D., Gibson, E. K., Gould, A. L., Jian, N., Logsdail, A. J., Palmer, R. E., Prati, L., Dimitratos, N., Villa, A., Wells, P.. Tailoring Gold Nanoparticle Characteristics and the Impact on Aqueous-Phase Oxidation of Glycerol. *ACS Catal.* **5**, 4377–4384 (2015).

Jian, N., Dowle, M., Horniblow, R. D., Tselepis, C. & Richard, E. Morphology of the ferritin iron core by aberration corrected scanning transmission electron microscopy. *Nanotechnology* **27**, 46 (2016).

Table of Contents

LIST OF FIGURES	VIII
LIST OF TABLES.....	XV
ABBREVIATIONS	XVI
CHAPTER 1 INTRODUCTION AND BACKGROUND	1
1.1 NANOCLOUDS.....	1
1.1.1 Introduction.....	1
1.1.2 Magic number clusters: electronic shell structure	7
1.1.3 Magic number clusters: geometric shell structure	13
1.1.4 Atomic structures of metallic clusters and their transformation	16
1.1.5 Ligand-protected clusters.....	23
1.2 ELECTRON MICROSCOPY STUDIES OF NANOCLOUDS.....	27
1.2.1 Introduction.....	27
1.2.2 EM studies of the size of clusters: diameter and mass.....	29
1.2.3 EM studies of the atomic structure of clusters.....	36
1.2.4 Dynamical studies of cluster structure transformation with EM	44
1.3 Aims and objectives	47
REFERENCE:	49
CHAPTER 2 EXPERIMENTAL METHODS	62
2.1 SCANNING TRANSMISSION ELECTRON MICROSCOPY.....	62
2.1.1 A brief history of electron microscopy.....	62
2.1.2 Overview of the STEM.....	67
2.1.3 Electron source	69
2.1.4 Magnetic electron lenses	71
2.1.5 Aberration and aberration correction.....	73
2.1.6 Detectors and image formation	78

2.2 CLUSTER FORMATION BY MAGNETRON SPUTTERING AND GAS CONDENSATION	82
2.2.1 Cluster formation	83
2.2.2 Cluster beam optics	85
2.2.3 Time-of-flight mass selection.....	85
2.3 MULTISLICE STEM IMAGE SIMULATION OF CLUSTERS.....	88
REFERENCE:	93
 CHAPTER 3 HAADF STEM STUDY ON THE ATOMIC STRUCTURE OF AU₅₅(PPh₃)₁₂Cl₆ SCHMID CLUSTERS.....	 99
3.1 OVERVIEW	99
3.2 INTRODUCTION	100
3.3 EXPERIMENTAL DETAILS	102
3.4 RESULTS AND DISCUSSION	103
3.4.1 “Weighing” Clusters	103
3.4.2 Atomic structure of Au ₅₅ (PPh ₃) ₁₂ Cl ₆	107
3.4.2.1 Multislice simulation atlas.....	107
3.4.2.2 Atomic structure analysis	109
3.4.2.3 Electron beam damage	111
3.4.4.4 Discussion of the new assignment.....	113
3.5 CONCLUSION	114
REFERENCE:	116
 CHAPTER 4 HAADF STEM STUDY OF THE VARIATION OF THE CORE ATOMIC STRUCTURE OF THIOLATED (AU_XAG_{1-X})_{312±55} NANOCCLUSERS WITH COMPOSITION.....	 120
4.1 OVERVIEW	120
4.2 INTRODUCTION	121
4.3 EXPERIMENTAL DETAILS	122
4.4 RESULTS AND DISCUSSION	126
4.4.1 Metal core size of thiolated (Au _x Ag _{1-x}) _{312±55} nanoclusters	126

4.4.2 Composition of thiolated (Au _x Ag _{1-x}) _{312±55} nanocluster core.....	128
4.4.3 Atomic structure of thiolated (Au _x Ag _{1-x}) _{312±55} nanocluster cores	131
4.4.4 Variation of Au-Ag metal core structure with composition	133
4.4.5 Discussion of the atomic structure variation with composition.....	134
4.5 CONCLUSIONS.....	135
REFERENCE:	136
CHAPTER 5 INVESTIGATIONS OF THE IRON CORE OF FERRITIN BY ABERRATION-CORRECTED HAADF STEM	142
5.1 OVERVIEW	142
5.2 INTRODUCTION	143
5.3 EXPERIMENTAL DETAILS	146
5.4 RESULTS AND DISCUSSION	147
5.4.1 Integrity of the ferritin protein shell.....	147
5.4.2 Iron loading of ferritin	150
5.4.3 Morphology of the ferritin iron core.....	154
5.4.4 Relationship between morphology and iron loading of the ferritin core ...	155
5.4.5 Discussion of electron beam damage.....	157
5.5 CONCLUSIONS.....	158
REFERENCE:	160
CHAPTER 6 CHARACTERIZATION OF SMALL SUPPORTED CATALYST PARTICLES BY HAADF STEM	165
6.1 OVERVIEW	165
6.2 Au/TiO ₂ CHARACTERIZATION BY HAADF-STEM	166
6.2.1 Introduction.....	166
6.2.2 Experimental details.....	170
6.2.3 Ultra-small Au cluster characterization	171
6.2.4 Conclusions.....	177
6.3 Pd/TiO ₂ CHARACTERIZATION BY HAADF STEM	177

6.3.1 Introduction.....	177
6.3.2 Experimental details.....	178
6.3.3 Pd cluster characterization	180
6.3.3.1 Pd cluster characterization: before catalysis test	180
6.3.3.2 Pd cluster characterization: after catalysis test.....	182
6.4 CONCLUSIONS.....	185
REFERENCE:	187
CHAPTER 7 MULTILAYER DEPOSITION OF SIZE-SELECTED AU CLUSTERS AND POLYMER LAYERS	192
7.1 INTRODUCTION	192
7.2 EXPERIMENTAL DETAILS	194
7.3 RESULTS AND DISCUSSION	196
7.3.1 Supported Au clusters from multilayer deposition	196
7.3.1.1 Multilayer deposition	196
7.3.1.2 Dicing process of multilayer hybrid material.....	200
7.3.1.3 Release in solution.....	203
7.3.2 Size-selected colloidal cluster.....	205
7.3.2.1 PVP layer deposition: spray and evaporation.....	206
7.3.2.2 Formation and characterization of colloidal clusters.....	207
7.5 CONCLUSIONS.....	212
REFERENCE:	214
CHAPTER 8 CONCLUSION.....	220
APPENDIX I EXTRACTION OF INTEGRATED HAADF INTENSITY	224
APPENDIX II SIMULATION ATLAS OF AU₅₅ CLUSTERS.....	226
APPENDIX III SIMULATION ATLAS OF AU₃₀₉ CLUSTERS	231
APPENDIX IV VALIDITY TEST OF GEOMETRIC ANALYSIS.....	234

List of Figures

Figure 1.1	The “magic number” peaks in the mass spectrum of zinc and cadmium clusters.	3
Figure 1.2	The turnover frequency as a function of the average Au cluster size in the reaction of carbon monoxide oxidation at 0°C.	5
Figure 1.3	(a) Schematic of the nanocluster based single-electron transistor. (b) The scanning electron microscopy image of the single-electron transistor. (c) The conductance of the single cluster transistor as a function of gate voltage with the temperature of 4.2K.	7
Figure 1.4	The experimental data of the: (a) ionization potential and (b) electron affinity of a series of nanoclusters as a function of $1/R$.	8
Figure 1.5	(a) Mass spectrum of the sodium clusters in the size range of 4 to 100 sodium atoms. (b) The change in the electronic energy difference as a function of number of sodium atoms in the clusters.	11
Figure 1.6	The vertical ionization potentials of Cu_n clusters in the range of $n = 1-123$.	12
Figure 1.7	The mass spectrum of the sodium cluster in the: (a) small size range, and (b) large size range.	14
Figure 1.8	Structure model of the typical fcc type twelve-vertex polyhedral structure: (a) cuboctahedron, (b) Marckey-icosahedron and (c) Ino-decahedron.	15
Figure 1.9	Common fcc crystalline structures: (a) Octahedron, (b) cuboctahedron and (c) truncated octahedron.	17
Figure 1.10	Structure model of Mackay-icosahedron.	18
Figure 1.11	Structure models of decahedral structures: (a) regular decahedron, (b) Ino-decahedraon and (c) Marks-decahedron.	19
Figure 1.12	The Δ calculated for the different elemental clusters.	22
Figure 1.13	(a) The atomic structure of the $\text{Au}_{102}(\text{p-MBA})_{44}$ cluster. Yellow is gold, cyan is sulfur, grey is carbon and oxygen is red. The red network is the electron density map. (b) The TEM image of $\text{Au}_{102}(\text{p-MBA})_{44}$ clusters, showing a relative mono-dispersive size distribution. (c) The atomic structure of the Au core in the $\text{Au}_{102}(\text{p-MBA})_{44}$ cluster. Yellow are the 49-atom Marks-Decahedron, green are the two 20-atom caps and blue is the 13-atom band.	25

Figure 1.14	(a) Example electron microscopy image of the colloidal Au clusters. The magnification of the image is 50,000 \times . (b) The size distribution of the colloidal Au clusters with the condition: 0.5ml sodium citrate (up), 1ml sodium citrate (middle) and 2.5ml sodium citrate (lower). (c) The size distribution of colloidal Au clusters with different dilutions of reagents.	30
Figure 1.15	(a) A HAADF-STEM image of a Pd cluster supported on TiO ₂ , where the flat shape can be clearly seen. (b) Single crystal X-ray crystallography determined the atomic structure of Au ₃₈ (SR) ₁₈ cluster, showing the aspherical feature.	31
Figure 1.16	(a) HAADF-STEM image of Re ₈ clusters. (b) The integrated HAADF intensity distribution of the Re ₈ clusters.	32
Figure 1.17	The representable HAADF-STEM image of size-selected: (a) Au ₁₄₇ , (b) Au ₂₀₅₇ , and (c) Au ₆₅₂₅ clusters. (d) The cluster's integrated HAADF intensity as a function of cluster size. The inset is the log fit of the HAADF intensity against the cluster size.	33
Figure 1.18	Schematic of cluster weighing with size-selected clusters. (a) The monolayer-protected clusters and size-selected clusters were deposited separately on the same TEM grid. The representative HAADF-STEM images of (b) size-selected cluster and (c) monolayer-protected cluster. The integrated HAADF intensity distribution of monolayer-protected cluster with: (d) Au ₃₈ clusters, and (e) Au ₂₅ clusters	36
Figure 1.19	Representative TEM images of: (a) Mg clusters, (b) Al clusters, and (c) Cr clusters, showing their hexagonal, spherical and cubic shapes, respectively.	37
Figure 1.20	Representative EM images of: (a) decahedral cluster, and (b) icosahedral cluster. In (c), two parallel lines were employed to show the lattices are not parallel. (d) The irregular shape clusters. (e) The representative EM image of small Au clusters, showing the multiply-twinned structure that confirmed the growth of the cluster started from a small nucleus.	38
Figure 1.21	(a) An internal slice of the Pt cluster 3D image. The yellow box highlights the dislocation. (b) The zoomed-in image of the highlighted dislocation. (c)-(e) The finer sections of the slice in (b). (f) An image of the Pt cluster. (g) An internal slice of the Pt cluster image in (f), showing the atomic steps that are not observed in (f).	40

Figure 1.22	(a) A 3D plot of the HAADF intensity of a Au_{309} cluster with Ino-decahedral structure. (b) Line profile of the experimental image of an Ino-decahedral structure Au_{309} cluster. (c) Line profile of the simulated image of an Ino-decahedral structure Au_{309} cluster. (d) The representative HAADF-STEM images of clusters with different shapes.	42
Figure 1.23	(a) The representative images of $\text{Au}_{68}(\text{SH})_{32}$ clusters. The left column is the reconstructed images, whereas the middle column contains the class average TEM images, and the right column contains the experimental TEM images. (b) The electron density map of the $\text{Au}_{68}(\text{SH})_{32}$ cluster from the reconstruction software. (c) The comparison between the TEM obtained $\text{Au}_{68}(\text{SH})_{32}$ structure (up) and the DFT relaxed structure (lower).	43
Figure 1.24	The structure distribution of the Au clusters as a function of cluster diameter with different annealing temperature: (a) No annealing, (b) 1173 K, (c) 1223 K, (d) 1273 K, and (e) 1373 K.	44
Figure 1.25	The statistical results of the structure transformation from icosahedral, decahedral and fcc structures, with the corresponding representative images.	47
Figure 2.1	(a) The first electron microscope built by Ernst Ruska (Stored in Deutsches Museum, Munich, Germany). ³ (b) Ernst Ruska and Max Knoll with the electron microscope they built. ⁴ (c) Ernst Ruska received the Nobel Prize in Physics for his contribution in developing the electron microscope in 1986.	63
Figure 2.2	The first STEM image that observed single atoms. The new technique was demonstrated by the ADF-STEM images of pairs of single U atoms in: (a) low magnification, and (b) high magnification, with the Th long chain in (c) at low magnification and (d) high magnification.	65
Figure 2.3	A schematic of the aberration corrected STEM and the picture of the JEM 2100F STEM we used in our lab.	68
Figure 2.4	Schematic of a field emission electron source.	70
Figure 2.5	Schematic of a magnetic electron lens.	72
Figure 2.6	The schematic of the astigmatism of the lens.	74
Figure 2.7	Schematic of the magnetic electron lens's positive spherical aberration.	75
Figure 2.8	The schematic of: (a) the hexapole magnetic electron lens, and (b) the double hexapole lens system.	77

Figure 2.9	Schematic of the coherent and incoherent imaging by TEM and STEM.	81
Figure 2.10	The schematic of the magnetron sputtering, gas condensed cluster source with lateral time-of-flight mass selector.	83
Figure 2.11	Schematic of the time-of-flight mass selector.	86
Figure 2.12	Schematic of the multislice simulation.	89
Figure 2.13	Schematic of the structure determination with STEM image simulation atlas.	91
Figure 3.1	(a) The low magnification HAADF STEM image of: (a) Schmid method prepared clusters, and (b) size-selected Au_{309} clusters prepared with magnetron sputtering cluster source.	104
Figure 3.2	Cluster weighing for the clusters prepared by the Schmid method. (a) The integrated HAADF intensity distribution of Schmid clusters and size-selected Au_{309} clusters. (b) Fine core size distribution of Schmid clusters. The fourth peak at $\sim 54 \pm 1.5$ is assigned as the $\text{Au}_{55}(\text{PPh}_3)_{12}\text{Cl}_6$ clusters.	105
Figure 3.3	Maximum length of the assigned $\text{Au}_{55}(\text{PPh}_3)_{12}\text{Cl}_6$ clusters. The Gaussian peak value is 1.406.	107
Figure 3.4	The example of the STEM simulation atlas of the hybrid chiral structure (from $\alpha=0^\circ$, $\theta=0^\circ$ to $\alpha=60^\circ$, $\theta=0^\circ$), the icosahedral structure (from $\alpha=40^\circ$, $\theta=0^\circ$ to $\alpha=40^\circ$, $\theta=36^\circ$), the cuboctahedral structure (from $\alpha=0^\circ$, $\theta=0^\circ$ to $\alpha=60^\circ$, $\theta=0^\circ$), and the icosidodecahedral structure (from $\alpha=0^\circ$, $\theta=0^\circ$ to $\alpha=60^\circ$, $\theta=0^\circ$).	108
Figure 3.5	Typical high resolution HAADF-STEM images of the $\text{Au}_{55}(\text{PPh}_3)_{12}\text{Cl}_6$ clusters which are assigned to have hybrid structure and orientations of: (a) $\alpha=70^\circ$, $\theta=40^\circ$, (b) $\alpha=30^\circ$, $\theta=30^\circ$, (c) $\alpha=60^\circ$, $\theta=80^\circ$, and (d) $\alpha=100^\circ$, $\theta=0^\circ$. The insets are the corresponding best matched simulated images. From (e) to (h) are the high resolution HAADF-STEM images of the $\text{Au}_{55}(\text{PPh}_3)_{12}\text{Cl}_6$ clusters with an amorphous structure.	110
Figure 3.6	The integrated HAADF intensity of one $\text{Au}_{55}(\text{PPh}_3)_{12}\text{Cl}_6$ cluster as a function of scanning time. The HAADF integrated intensity was obtained in a series of continuous recorded HAADF STEM images of the same $\text{Au}_{55}(\text{PPh}_3)_{12}\text{Cl}_6$ cluster.	112
Figure 4.1	(a) Example images taken before and after the beam shower. (b) HAADF intensity ratio of each cluster in the STEM images taken after and before the beam shower.	124

Figure 4.2	Histogram of: (a) HAADF integrated intensity, and (b) Au-Ag core nuclearity (obtained from the measured diameters) for 202 individual thiolate protected $(\text{Au}_x\text{Ag}_{1-x})_{312\pm55}$ clusters. Both (a) and (b) show the distributions are consistent with the discrete multiples of monomers.	127
Figure 4.3	(a) MALDI mass spectrometry of the thiol-protected Au-Ag alloy clusters prepared using a 1:1 molar ratio of $\text{HAuCl}_4:\text{AgNO}_3$ starting materials. The 2+ peak at around 30 kDa is assigned to be the double charged peak of the molecular ions. The single charged peak is around 59 kDa. (b) The mass distribution of the same thiolate Au-Ag alloy clusters based on the analysis on the STEM data. The Gaussian fit of the main peak is at 59.68 kDa.	129
Figure 4.4	Typical HAADF STEM images of thiolated $(\text{Au}_x\text{Ag}_{1-x})_{312\pm55}$ clusters. (a)-(c), (g)-(i), and (m)-(o) are clusters assigned to the cuboctahedral, Ino-decahedral or icosahedral structures, based on the corresponding simulated images (for bare Au_{309} clusters) displayed in (d)-(f), (j)-(l) and (p)-(r), respectively.	131
Figure 4.5	The proportion of the fcc, ino-decahedral and icosahedral motifs for thiolated $(\text{Au}_x\text{Ag}_{1-x})_{312\pm55}$ clusters with the composition varying from pure Ag (left) to pure Au (right).	133
Figure 5.1	Schematic of intercellular Fe behavior. The Fe is imported into the cell with several medias such as divalent metal ion transporter 1 (DMT1), transferrin (Tf) and transferrin receptor (TfR). The imported Fe is utilized in many processes like oxygen transport, cell division and DNA replications. Excess ferrous Fe is harmful in the body and results in DNA and protein damage. The ferritins transfer the ferrous Fe to ferric, which is then crystalized into a protein to store the excess Fe to prevent possible damage to the body.	144
Figure 5.2	3D crystal structure of ferritin protein shell viewed from” (a) 4-fold symmetry axis, (b)3-fold symmetry axis, and (c) 2-fold symmetry axis.	145
Figure 5.3	Test of the Integrity of the ferritin protein. (a) SDS PAGE 12% gel loaded with ferritin (15, 30 and 45 μg) and stained with Coomassie blue. (b) SDS PAGE 12% gel loaded with ferritin (15, 30 and 45 μg) and subject to Western blotting with a polyclonal; antibody specific for the ferritin light chain.	148
Figure 5.4	(a) Plot of the maximum length of the ferritin mineral cores. (b)-(e) Examples of HAADF STEM images in which the maximum lengths of the cores are all similar for different core morphologies.	150
Figure 5.5	(a) Crystal structure analysis of ferritin Fe core. The d-spacing and angles labelled are consistent with the ferrihydrite crystal structure. Inset, lower right: the corresponding FFT. (b) Distribution of Fe loading in ferritin cores.	152

Figure 5.6	Ferrozine calibration curve created with standard Fe concentrations (0-10 mM) and estimated Fe concentrations of ferritin tabulated. Error denotes the standard deviation.	153
Figure 5.7	The morphology “atlas” of the ferritin Fe core with different Fe loading regions. From (a) to (z) are the representative images for every type of morphology observed in different size ranges. For example, there is only one morphologic “small circle” found in the size range of ~500 Fe atoms, as shown in (a), while all four types of morphology, (j) “doughnut”, (k) “crescent”, (l) “dumbbell” and (m) “full raft”, are observed in the size range ~2500 Fe atoms. The frame size of the ferritin example image is 8.24×8.24 nm.	156
Figure 6.1	Examples of the TEM images of different batches (A:A1, B:B1, C:C1) of Au/TiO ₂ clusters and their corresponding size histogram.	169
Figure 6.2	Representative STEM image of Au/TiO ₂ catalyst in: (a) bright field, and (b) high angle annular dark field mode.	172
Figure 6.3	Representative HAADF STEM images of Au/TiO ₂ catalysts batch: A1 ((a)-(c)), and batch B1 ((d)-(f)).	173
Figure 6.4	(a) Size distribution of the ultra-small Au clusters. The representative images of the mass balance Au clusters are shown in (b) and (c).	174
Figure 6.5	3D plot of the HAADF-STEM images of ultra-small Au clusters on the TiO ₂ support.	176
Figure 6.6	Representative HAADF STEM images of the Pd/TiO ₂ catalysts from A1 ((a)-(d)), and B1 ((e)-(f)).	180
Figure 6.7	(a) Size distribution of the Pd clusters, obtained by the cluster weighing method. The representative images of the Pd clusters used as mass balance in the cluster weighing are shown in (b) and (c).	181
Figure 6.8	Representative HAADF-STEM images of A1 tested Pd/TiO ₂ catalysts. Both the regular small and large Pd clusters can be found in (a)-(c). The large irregular Pd clusters are shown in (d)-(f).	183
Figure 6.9	Representative HAADF-STEM images of tested B1 Pd/TiO ₂ catalysts.	184
Figure 7.1	Schematic of the multilayer deposition process.	196

Figure 7.2	Schematic of the through-focal HAADF STEM analysis on the multilayer sample. The electron beam was focused on: (a) upper cluster, and (b) lower cluster, respectively. The cluster's centres were estimated in their corresponding focal plane 1 and 2. Therefore, the defocus difference between these two planes corresponds to the depth of the whole C-cluster-PVP sandwich.	197
Figure 7.3	(a)-(f) Through-focal HAADF STEM images of a multilayer sample comprising eight carbon-cluster-PVP sandwiches deposited under identical conditions. The clusters which were focused are marked by the red circles. (g) A schematic diagram of the 3D structure of the multilayer sample with the thickness values determined from the through-focal STEM analysis.	199
Figure 7.4	(a)-(d) HAADF STEM images of the diced sample's edge at different magnification, showing the successful dicing with good morphology of the edge and the conservation of the multilayer structure after dicing. The imaging of the small diced piece was achieved by sandwiching the diced sample between two copper grids, as show in (e).	202
Figure 7.5	The representative HAADF STEM images of the dicing edge after laser dicing a multilayer sample. The frame sizes in (a), (b) and (c) are $2.57\ \mu\text{m} \times 2.57\ \mu\text{m}$, $1.03\ \mu\text{m} \times 1.03\ \mu\text{m}$ and $256.5\ \text{nm} \times 256.5\ \text{nm}$, respectively.	203
Figure 7.6	The HAADF STEM images of platelets with single, double and triple layers were shown in (a), (b) and (c), respectively. A platelet with part single layer, part double layer is shown in (d).	204
Figure 7.7	Instrument setup for the deposition of PVP layers in conjunction with size-selected clusters on the magnetron sputter inert gas aggregation source.	206
Figure 7.8	(a) HAADF intensity distribution of the size-selected Au_{923} colloidal clusters, where the PVP layer was deposited by the pulse valve spray method. Representative high resolution HAADF STEM images of the colloidal clusters are shown in (b) an (c).	208
Figure 7.9	(a) HAADF intensity distribution of the size-selected Au_{923} colloidal clusters, where the PVP layers were deposited by the thermal evaporation. Representative high resolution HAADF STEM images of the colloidal clusters are shown in (b) an (c).	209
Figure 7.10	The diameter distribution and the corresponding representative HAADF STEM images of the clusters from: (a) the normal as-deposited size-selected Au_{923} clusters, the Au colloidal clusters with PVP deposited by (b) the pulse valve spray method and (c) thermal evaporation method.	210

List of Tables

Table 5.1	The estimation of the Fe content with a ferrozine assay.	153
Table 6.1	Different temperatures and solvent variations for synthesis of the Au/TiO ₂ catalyst.	167

Abbreviations

STEM	Scanning Transmission Electron Microscope/Microscopy
TEM	Transmission Electron Microscope/Microscopy
MP	Monolayer Protected
HOMO	Highest Occupied Molecular Orbital
LUMO	Lowest Occupied Molecular Orbital
ESI-MS	Electrospray Ionization Mass Spectrum
TGA	Thermogravimetric Analysis
XPS	X-ray Photo-electron Spectrum
Cs	Spherical Aberration
TOF	Time-of-flight
BF	Bright Field
EXAFS	Extended X-ray Absorption Fine Structure
WAXS	Wide-angle X-ray Scattering
XANES	X-ray Absorption Near Edge Structure
DTA	Differential Thermoanalysis
AUC	Analytical Ultracentrifugation
HPC	High Performance Computer
HAADF	High Angle Annular Dark Field
ADF	Annular Dark Field
EELS	Electron Energy Loss Spectrum
EDX	Energy Dispersive X-ray Spectroscopy

Fcc	Face Centered Cubic
Bcc	Body Centered Cubic
FEG	Field Emission Gun
MALDI-MS	Matrix-assisted Laser Desorption/ionization Mass Spectrum
FFT	Fast Fourier Transformation
Tf	Transferrin
TfR	Transferrin Receptor
DMT1	Divalent Metal Ion Transporter 1
SDS PAGE	Sodium Sodecyl Sulfate Polyacrylamide Gel Electrophoresis
PVA	Polyvinylacohol
PVP	Polyvinylpyrrolidone
MACS	Matrix Assembly Cluster Source
p-MBA	p-mercaptobenzoic acid
DNA	Deoxyribonucleic acid

CHAPTER 1

INTRODUCTION AND BACKGROUND

1.1 Nanoclusters

1.1.1 Introduction

Nanoscience is a new area of research that has exhibited marvelous developments in the last 30 years. The word “nanoscience” is a combination of the word “nano”, meaning one billionth and “science”. Nanoscience is defined as a branch of science that is on the scale of nanometers, generally 1-100nm in at least two dimensions. It is a cross-disciplinary branch of science that includes physics, chemistry, biology and material science.¹⁻⁵ One person that cannot be ignored in an introduction of nanoscience is Dr. Richard Feynman, who was the first person to predict the rise of nanoscience. In his famous talk “There’s Plenty of Room at the Bottom” at the annual meeting of the American Physics Society in 1959,⁶ he painted a fantastic picture of the future: “By the improvement of technology, people can see, manipulate, control and make things on a much smaller scale, for use in the research of biology, computer science, materials science and others, all with the aim of completely changing the world.”

In nanoscience, the study of nanoclusters is of great interest due to their unique

properties due to their special size between small molecules and bulk materials.^{7–10}

The nanocluster is normally defined as an aggregation of atoms containing from 2 to 10^6 atoms. It can consist of either the same species of atoms as a homo-atomic cluster, or different species as a hetero-atomic cluster. Atoms of almost every element can aggregate and form clusters, from the rare gas helium to the radioactive element uranium.^{11–14} Although studies of nanoclusters became popular only in the last 30 years, the earliest study talking about a “cluster” can be traced back to 350 years ago, when Robert Boyle stated a cluster in his book “*The Sceptical Chymist*”.¹⁵

The most interesting feature of nanoclusters is their unique size and the consequent special position between molecules and bulk materials. The size of nanoclusters is a very important parameter for the clusters’ properties. Unlike molecules that can only have certain composition, nanoclusters can contain any number of atoms, which give us the opportunity to tune the nanoclusters’ properties by varying their size.⁷ In the 1980’s, spectroscopy scientists found that, in their spectrum studies on the clusters,^{16–19} there were strong intensity peaks at certain sizes, which is normally called a “magic number” now. An example is given in Figure 1.1, in which the mass spectrum of zinc and cadmium clusters is given.¹⁶ The high intensity peaks were found at $N=10, 20, 28, 35, 46, 54$ and 69 . The clusters with “magic number” sizes are normally considered to be more stable than other sizes of clusters, which is based on experimental operating conditions such as temperature, pressure, etc.^{17,19–24}

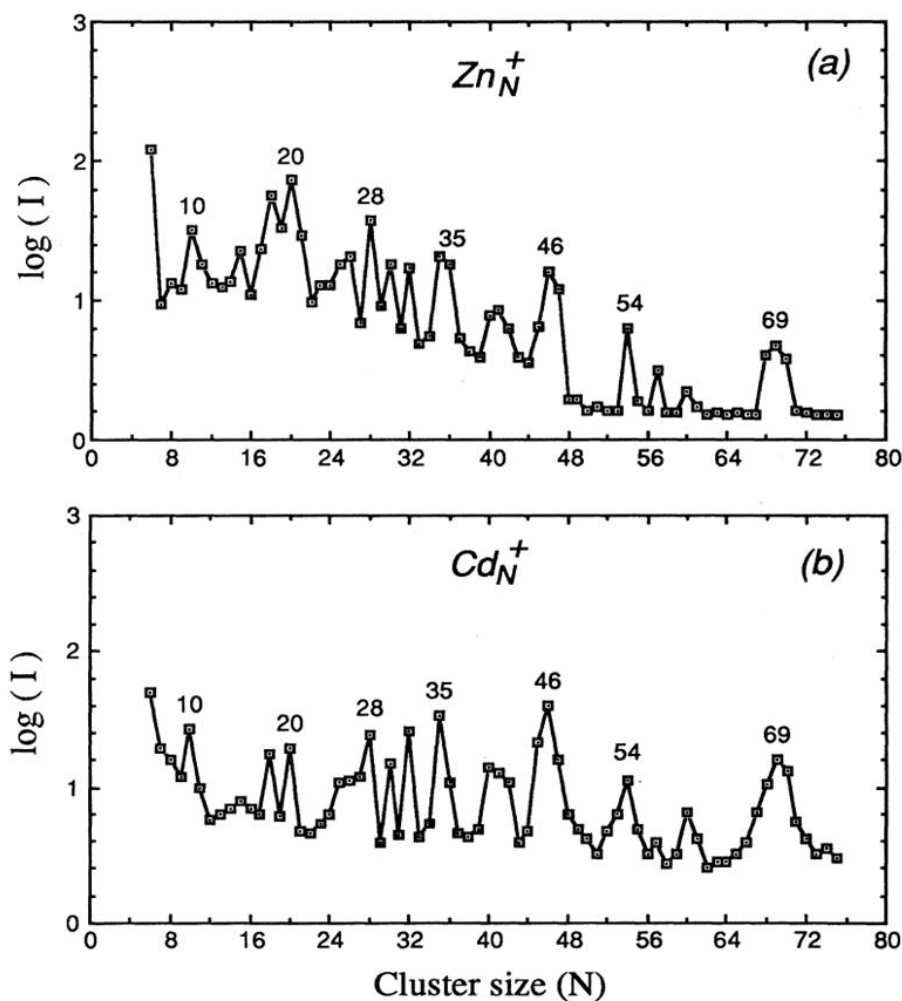


Figure 1.1 The “magic number” peaks in the mass spectrum of zinc and cadmium clusters.¹⁶ The figure is from ref [16].

The unique properties of nanoclusters lead to a great number of applications. The history of nanocluster applications is also longer than people normally think. In the middle ages, people found the colour of glass can be tuned by adding different metal powders, resulting in the resplendent stained glass windows in great old buildings.²⁵ Lord Rayleigh investigated this and suggested that the stained glass’s colour is due to small particles in the glass scattering the light.²⁶

Due to their high ratio of surface to volume, nanoclusters drew a great deal of interest in catalysis applications. As the low-coordinated atoms are believed to be the active site in the reaction, the smaller-sized nanoclusters with a higher percentage of these kinds of atoms in steps, edges or corners, are ideal catalysts in many reactions.^{27,28}

Gold is a good example of how properties change when an element material transfers its form from bulk solid to nanocluster. Gold has long been regarded as an inert element, showing no reactivity in most reactions. This property, combined with its rareness, made gold the standard unit of accounting and formed the gold standard in the monetary system. However, in 1970, Parravano et al. found that gold has reactivity in oxygen transfer between carbon monoxide and carbon dioxide and hydrogen transfer between cyclohexane and benzene, with MgO and Al₂O₃ as support.^{29,30} Further studies on the gold catalysis were carried out by Haruta et al.^{31–36} The Au clusters supported on the different metal oxides like Fe₂O₃, Co₃O₄, NiO, Al₂O₃ and TiO₂ were found to be catalytically active in many reactions like carbon monoxide oxidation, hydrogen oxidation, carbon dioxide hydrogenation and nitrogen monoxide reduction.^{28,31–44} The most active Au catalysts were found to be fairly small with diameters smaller than 5nm.³⁵ A study on the catalytic activity of Au clusters supported by three different oxides, Fe₂O₃, Co₃O₄, and TiO₂, was carried out to investigate the influence of size on their catalytic activity.³¹ The Au clusters on these three oxide supports were found to have different catalytic activities for carbon

monoxide oxidation; the clusters on the Co_3O_4 supports showed the highest activity, a lower activity appeared with the Fe_2O_3 and the clusters on the TiO_2 supports were least active. But the influence of the cluster size is more dominant. As shown in Figure 1.2, all the catalysts showed strong dependence on the Au cluster size. The smaller the size, the higher turnover frequency becomes, which means higher catalytic activity.

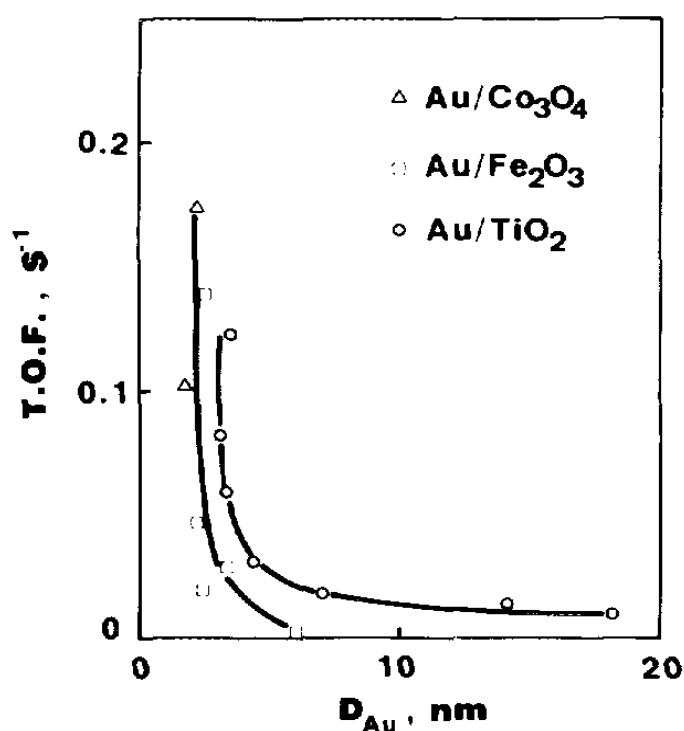


Figure 1.2. The turnover frequency as a function of the average Au cluster size in the reaction of carbon monoxide oxidation at 0°C .³¹ The figure is from ref [31].

Single-electron transistor is another potential application of nanoclusters. The principle of single-electron transistor comes from Coulomb blockade. When an electron tunnels into a small nanocluster that has a very low capacitance, the charging energy will be extremely large, requiring an extremely high corresponding bias

voltage. So, if the applied bias voltage is lower than this voltage, the electron transfer will not exist and behave like a “blockade” around the nanocluster. Klein et al. developed a single-electron transistor with cadmium selenide nanoclusters.⁴⁵ The schematic and a scanning electron microscopy image of their single-electron transistor are shown in Figure 1.3.⁴⁵ The cadmium selenide nanoclusters, with an average size of 5.5 nm, were deposited onto a pair of closely positioned Au leads. These leads are mounted on a silicon dioxide/silicon substrate as the gate. A gate voltage was applied to the substrate while another voltage was applied to the leads. Their conductance can therefore be measured and is shown in Figure 1.3(c). The single peak of the conductance indicates the changed charge state of the nanoclusters by single electron transition.⁴⁵

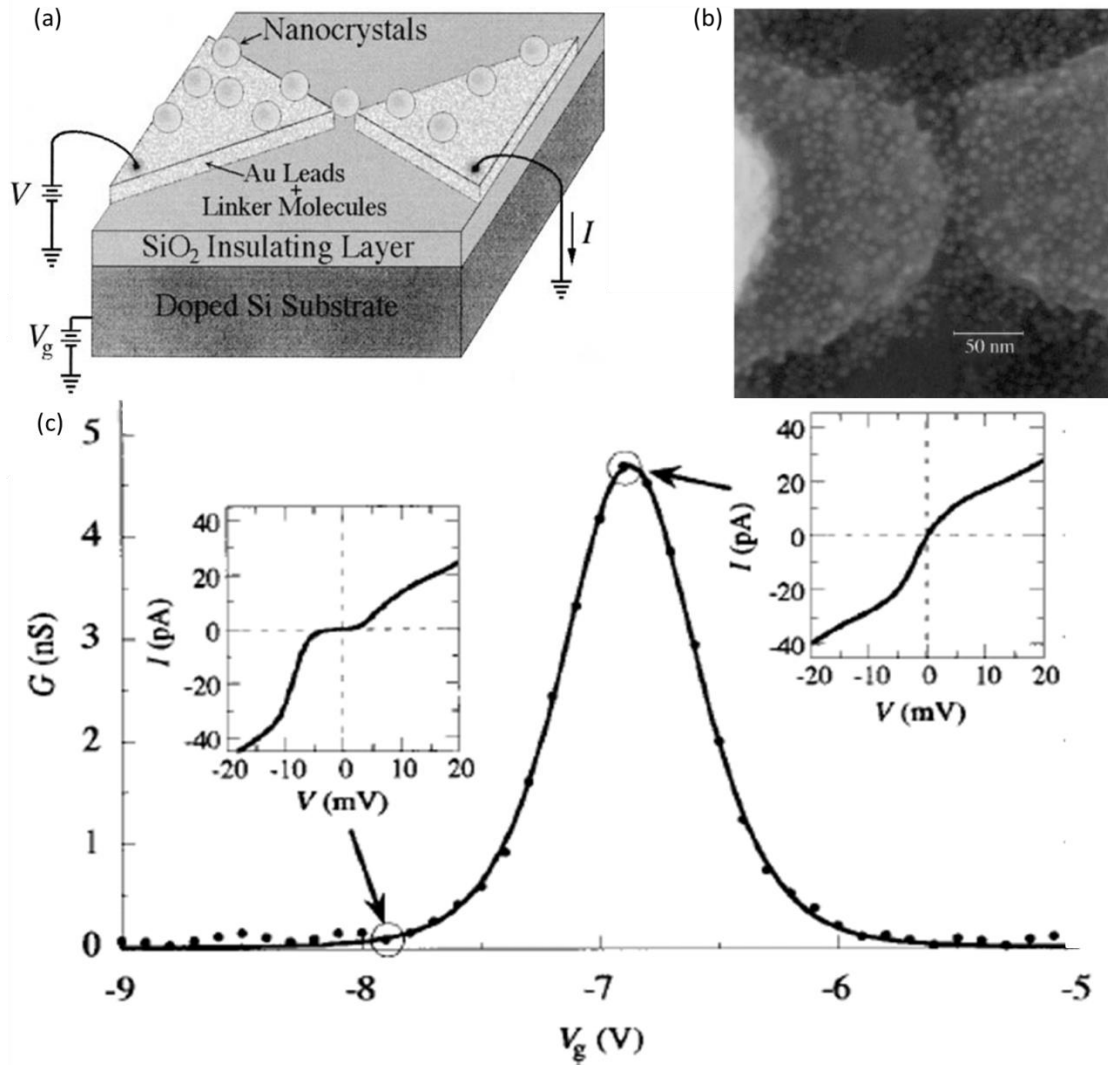


Figure 1.3 (a) Schematic of the nanocluster based single-electron transistor. (b) The scanning electron microscopy image of the single-electron transistor. (c) The conductance of the single cluster transistor as a function of gate voltage with the temperature of 4.2 K.⁴⁵ The figure is from ref [45].

1.1.2 Magic number clusters: electronic shell structure

To have a better understanding of nanoclusters, various theoretical models were presented. The liquid-drop model is one of the models used for metal clusters, which is based on classic electrostatics.⁴⁶ The nanocluster in this model is regarded as a

sphere with uniform conductivity. Based on this model, with the increasing size of the cluster, the cluster's ionization potential will decrease while its electron affinity will increase. The equation of the cluster's ionization potential (IP) and electron affinity (EA) can be described as below⁴⁶:

$$\begin{aligned} IP &= W + \left(\frac{3}{8} \times \frac{1}{4\pi\epsilon_0 R} \right) \\ EA &= W - \left(\frac{5}{8} \times \frac{1}{4\pi\epsilon_0 R} \right) \end{aligned} \quad (1.1)$$

Here, W is the work function of the bulk material, R is the radius of the cluster which is equivalent to $N^{1/3}$ (N is the number of atoms in the cluster).

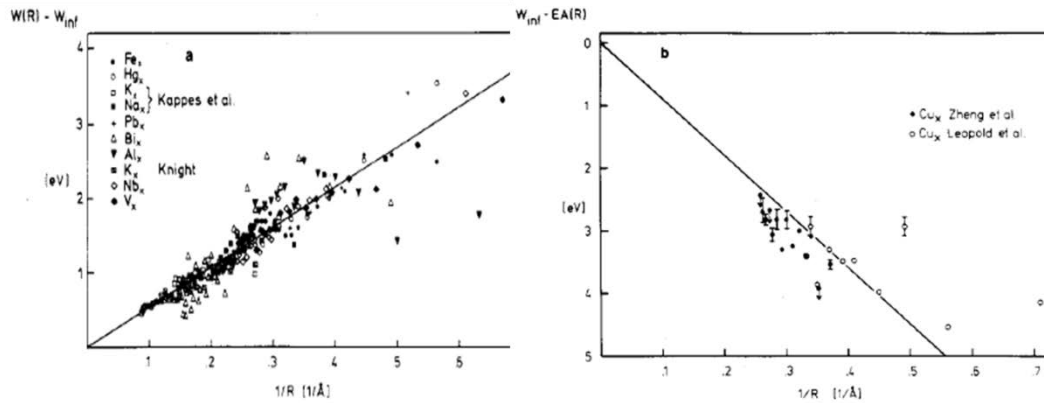


Figure 1.4 The experimental data of the: (a) ionization potential and (b) electron affinity of a series of nanoclusters as a function of $1/R$.⁴⁶ The figure is from ref [16].

A series of nanoclusters were experimentally studied through their ionization potential and electron affinity. Kappes concluded these data and found trends for each with the variation of $1/R$.⁴⁶ The clusters' ionization potential and electron affinity as a function of $1/R$ are shown in Figure 1.4. Kappes demonstrated that the liquid drop model can explain these trends well, especially for clusters bigger than 10 atoms.⁴⁶ However, for smaller ($N < 10$ atoms) clusters, the data showed a relatively large deviation from the

liquid drop model predictions, which is due to the quantum size effect.⁴⁶

Although the liquid drop model can give a reasonably good description of many nanocluster's size dependent properties (at least for the large size region), it still has drawbacks. As mentioned above, a series of experiments on the mass spectrum of nanoclusters found the isolated strong peaks in certain, highly reproducible size regions.^{11,16–19,21–24} The numbers corresponding to the strong peak were called magic numbers. However, the classical liquid drop model cannot explain this phenomenon, which indicates a new model that can take into consideration the cluster's discrete electronic states. Therefore, the jellium model was presented.

The spherical jellium model is the simplest jellium model and has been successfully explained through the magic numbers found in the mass spectrum of sodium clusters.^{18,23} In a spherical jellium model, the nanocluster is regarded as a positive uniformly charged sphere with electron gas inside. The electron gas is formed by the valance electrons of the atoms in the nanocluster. In other words, the nanocluster is treated like a “super atom”. The “super atom” also has quantum numbers like the normal atomic quantum number: principle quantum number n , angular momentum quantum number l and magnetic quantum number m_l . When the super “atomic” electron shells are fully filled, the super “atom” is more stable and the number of atoms in the super “atom” is the magic number.^{8,20,47}

The most commonly used empirical jellium potential used in the spherical jellium

model calculation is the Woods-Saxon potential, which is shown as¹⁸:

$$U(r) = - \frac{U_0}{\exp \left[\frac{r - r_0}{\sigma} \right] + 1} \quad 1.2$$

Here, U_0 is the combination of the work-function and Fermi energy of the bulk material, r_0 is the radius of the assumed cluster sphere, which is determined by¹⁸:

$$r_0 = r_{WS} \sqrt[3]{n} \quad 1.3$$

where r_{WS} is the Wigner-Seitz radius and n is the number of atoms in the nanocluster. σ is a parameter that can define the potential variation at the sphere edge.¹⁸

In the case of the sodium cluster studied by Knights et al, the electronic energy of each size cluster was obtained by solving the Schrodinger equation and found to be discrete with a different angular momentum quantum number l .¹⁸ When the electronic energy difference increases discontinuously, this means that the electron shell is fully filled and the next additional atom will result in a new higher energy orbital. The change of the electronic energy difference was plotted as a function of the number of sodium atoms in the cluster in Figure 1.5(b). The peak occurred in the close-shell number of atoms in the cluster and is consistent with the peaks in the experimental abundance mass spectrum of the sodium clusters in the size range of 4 to 100 sodium atoms in Figure 1.5 (a).¹⁸

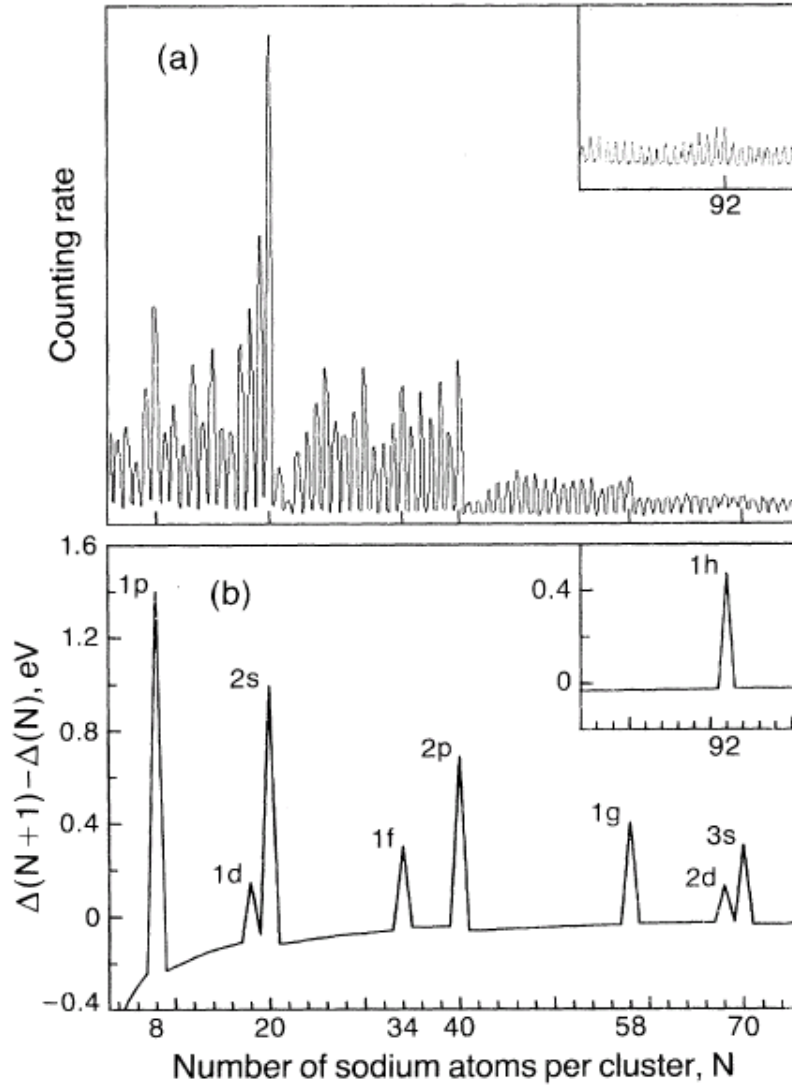


Figure 1.5 (a) Mass spectrum of the sodium clusters in the size range of 4 to 100 sodium atoms. (b) The change in the electronic energy difference as a function of number of sodium atoms in the clusters.¹⁸ The figure is from ref [18].

Although the spherical jellium model has successfully predicted the main peaks in the mass spectrum of the alkali metal clusters, it cannot explain the fine structure in the mass spectrum, such as the small peaks occurring in the mass spectrum of the sodium nanoclusters, shown in Figure 1.5. An ellipsoidal shell structure model was employed by Clemenger based on the Nilsson's nuclei model.^{48,49} In this model, the spherical

cluster was distorted in one direction when the jellium shell was not fully filled. In this situation, the degeneracy of the orbital will decrease and the jellium shell will be split to the subshell, resulting in the small peak between the close-shell peaks in the mass spectrum.⁴⁸

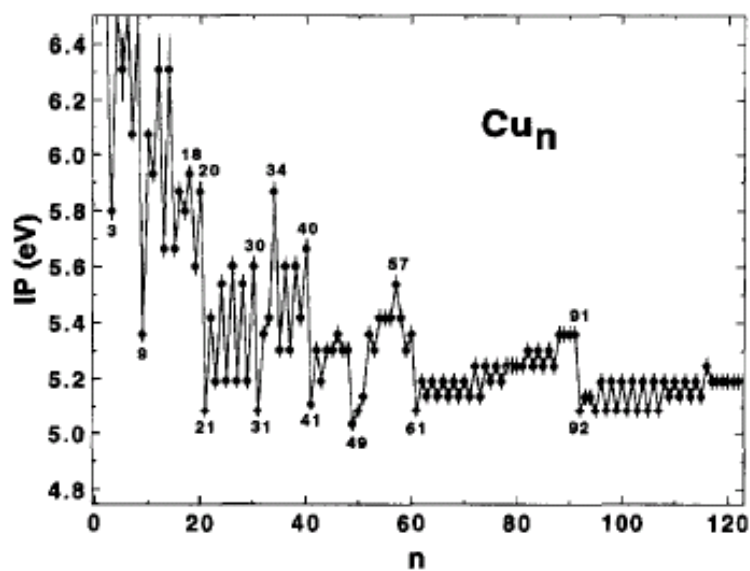


Figure 1.6 The vertical ionization potentials of Cu_n clusters in the range of $n = 1-123$.²¹ The figure is from ref [21].

A study of the copper cluster's ionization potential was carried out by Knickelbein, for which the Cu_n clusters' vertical ionization potentials were obtained precisely with the size range, $n = 1-150$.²¹ The vertical ionization potentials of the copper clusters were shown in Figure 1.6 as a function of number of atoms, n in the cluster. We can see the significant decrease after $n = 8, 18, 20, 34$ and 40 , which is consistent with the prediction by the spherical jellium model. The decrease after $n = 10, 14, 16, 18$, etc. can be predicted by the subshell in the ellipsoidal shell structure model. However, in the bigger size range ($n > 42$), the close-shell peak cannot be observed, suggesting the

geometric effect perturbs the electronic shell effect.²¹

1.1.3 Magic number clusters: geometric shell structure

The abundant mass spectrum studies of the magic number nanoclusters shown above are all in the small size region.^{16,18,21,48} So, what will happen in the bigger size range? Will the spectrum still obey the electronic shell structure? The answer seems to be no. Martin et al. employed the mass spectrum study on sodium clusters with sizes of up to 22000 atoms.¹⁹ The mass spectrum, which is shown in Figure 1.7, has a very large mass range. In the size range smaller than 1500, as shown in Figure 1.7(a), the features occurring in the mass spectrum matched well with the prediction based on the electronic shell structure. Based on the result and the jellium model, the electronic shells of the sodium clusters have the same value of $3n+1$ are degenerate. The number of atoms that need to fully fill the electronic shells, k , with the maximum shell number, K , can be explained as¹⁹:

$$N_k = \sum_{k=1}^K \sum_{l=0}^{L(K)} 2(2l+1) \quad 1.4$$

Here, l is the angular momentum quantum number, $L(K)$ is the highest angular momentum sub-shell in the K shell.¹⁹

However, in the bigger size range, as shown in Figure 1.7(b), the features did not follow the electronic shell structure. The features found in 1980, 2820, 3800, etc. have nothing to do with the electronic shell, but instead form a geometric, atom close

packed 12-vertex polyhedral structure (including mackay-icosahedron, icosahedron and cuboctahedron). The number of atoms in the k shell close-packed 12-vertex polyhedra structure cluster can be shown as:

$$N_k = \frac{1}{3}(10k^3 + 15k^2 + 11k + 3) \quad 1.5$$

Based on this, the 9 shell cluster will have 2057 atoms, 10 shell clusters will have 2869 atoms and 11 shell clusters will have 3871 atoms. We can see that these numbers are extremely close to the experimental data mentioned above. Also, the agreement between the theoretical prediction and experimental evidence continues as the cluster size increases to 22000, where there are 22227 atoms in the 19 shell 12 vertex polyhedra structure cluster with the experimental feature size 21300.¹⁹

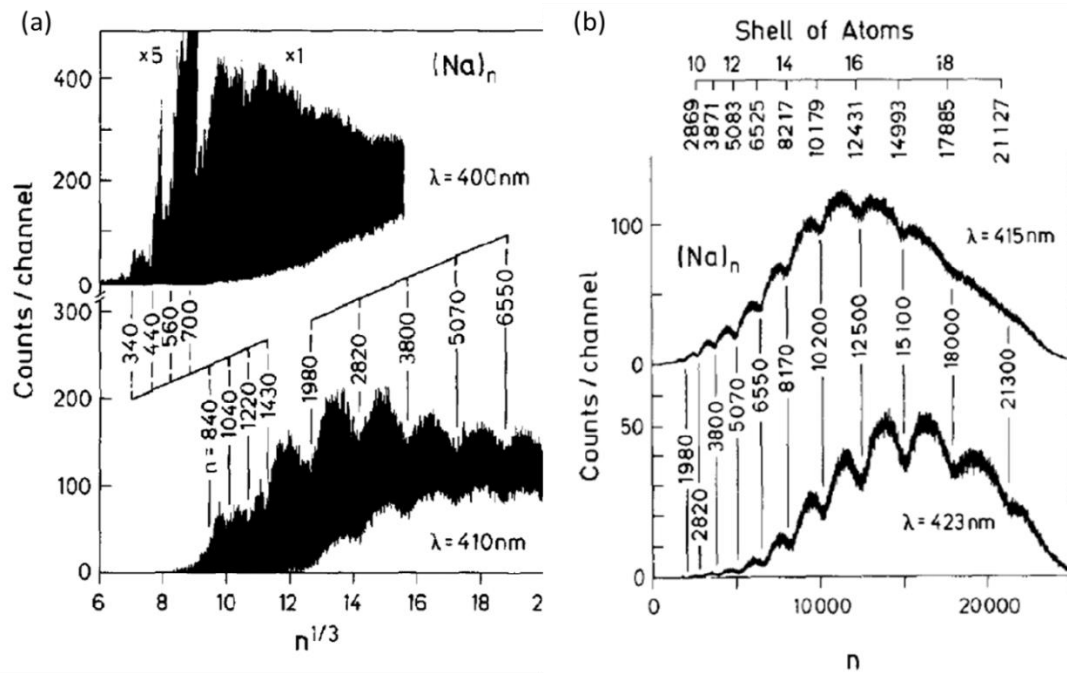


Figure 1.7 The mass spectrum of the sodium cluster in the: (a) small size range, and (b) large size range.¹⁹

The most common geometric structure of the cluster is the face center cubic (fcc) type

twelve-vertex polyhedral structure, e.g. Mackay-icosahedron, Ino-decahedron and cuboctahedron. The number of atoms for this full shell structure type can be calculated by equation 1.5. While there is also the body center cubic (bcc) type fourteen-vertex polyhedral structure like the rhombic dodecahedron. The full shell number of this type of structure can be described as:

$$N_k = 4k^3 + 6k^2 + 4k + 1 \quad 1.6$$

where k is the number of the geometric shells in the cluster.^{50,51}

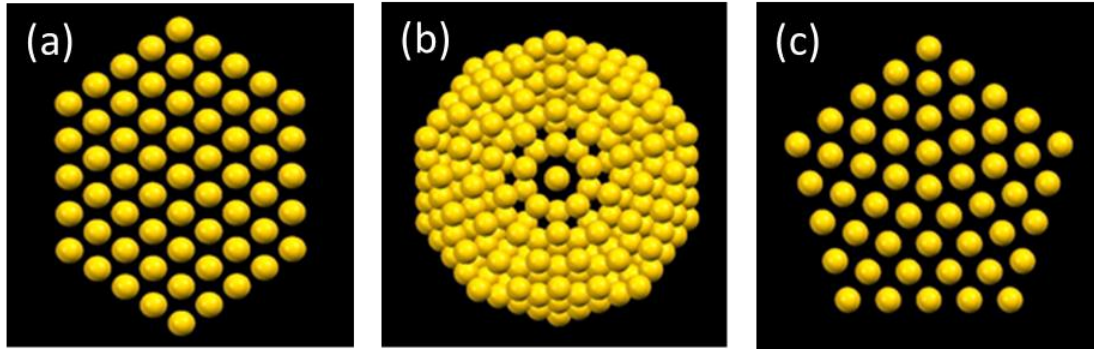


Figure 1.8 Structure model of the typical fcc type twelve-vertex polyhedral structure:

(a) cuboctahedron, (b) Mackay-icosahedron and (c) Ino-decahedron.

The phenomenon that the electronic shell structure dominates the magic number in the small size region of the clusters and the geometric shell structure dominates in the big size region can be explained by the melting temperature of the nanocluster. It is well known that the melting point temperature is dependent on the size of the nanocluster: the bigger the cluster is, the higher its melting point is.^{22,52,53} When the temperature is above the melting point, the cluster will exhibit a liquid-like form. The cluster will perform like a spherical liquid drop as suggested in the jellium model. In this situation,

there is no solid nucleus to maintain the geometric polyhedral structure, so the geometric shell structure cannot be observed and this affects the magic number of the cluster in the mass spectrum.⁵⁴ This can explain what happened in the mass spectrum of the sodium clusters, for certain temperatures, which above the melting point of small clusters and below the melting point of big clusters. Therefore, in conclusion, the electronic shell structure dominates the small, melting, liquid-like clusters, while the geometric shell structure dominates the large, solid, crystal-like clusters.^{7,54}

1.1.4 Atomic structures of metallic clusters and their transformation

The most common atomic structure (except for amorphous) of the metallic clusters are fcc-type structures, which include fcc crystalline, decahedron and Mackey-icosahedron. They were observed in many clusters and their percentage varies in different elements, composition and size. Normally, the clusters tend to have a low surface energy, which requires a close-packed structure with a more spherical shape to have the lowest surface to volume ratio.

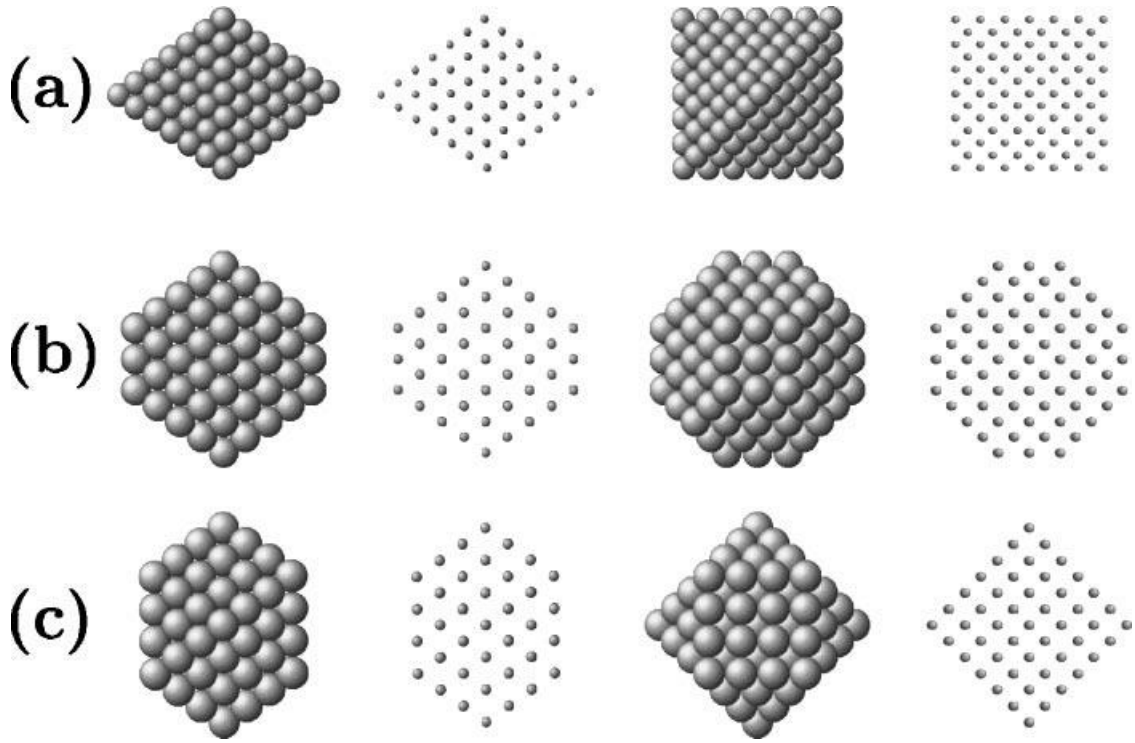


Figure 1.9 Common fcc crystalline structures: (a) Octahedron, (b) cuboctahedron and (c) truncated octahedron.²⁰ The figure is from ref [20].

The fcc crystalline structure clusters have the same structure as the bulk fcc crystal, but with optimized shape. The shapes are normally octahedron, cuboctahedron and truncated octahedron, as shown in Figures 1.9 (a), (b) and (c), respectively. An octahedral cluster has 8 triangular (111) facets that are close packed. Although the octahedral clusters are close packed, its non-spherical shape has a high surface to volume ratio, so the surface energy is relative high. To make the octahedral structure more spherical, we can cut its six vertexes to form a truncated octahedral structure. The truncated octahedral structure has 8 (111) facets and 6 (100) facets. When each vertex of the octahedral structure is cut with 1/3 edge length, the 8 close packed (111) facets are regular hexagons, and this structure is called the regular truncated

octahedral structure. If the half edge is cut, the 8 close packed (111) facets will be triangular, and this structure is the cuboctahedral structure.²⁰

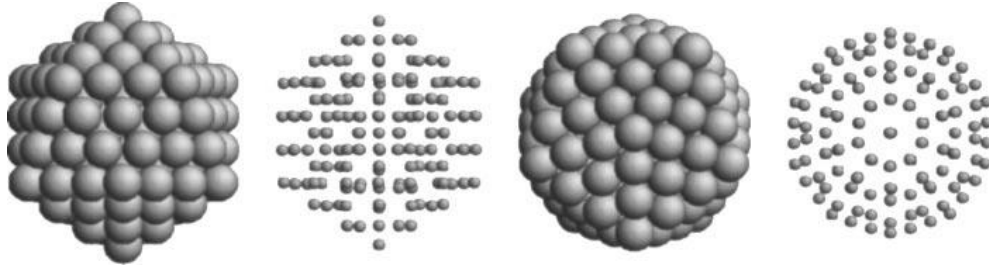


Figure 1.10 Structure model of Mackay-icosahedron.²⁰ The figure is from ref [20].

Neither regular truncated octahedral nor cuboctahedral are very close to the spherical structure. A more spherical shape was presented by Mackay, called the Mackay-icosahedron, as shown in Figure 1.10.⁵⁵ The Mackay-icosahedral structure has 30 edges, 12 vertexes and 20 regular triangular facets. All the facets in the Mackay-icosahedron are close packed (111) facets, so the surface energy is limited well. The drawback of the icosahedron is the relatively high volume and the high strain inside the structure. A Mackay-icosahedron can be regarded as consisting of 20 fcc tetrahedrons. However, the tetrahedrons cannot perfectly form the Mackay-icosahedron and spaces occur between them. To offset the spaces, these tetrahedrons need to be distorted, the inter-shell bond is compressed while the intra-shell bond is stretched. This distortion therefore generates high strain inside the structure.⁵⁵

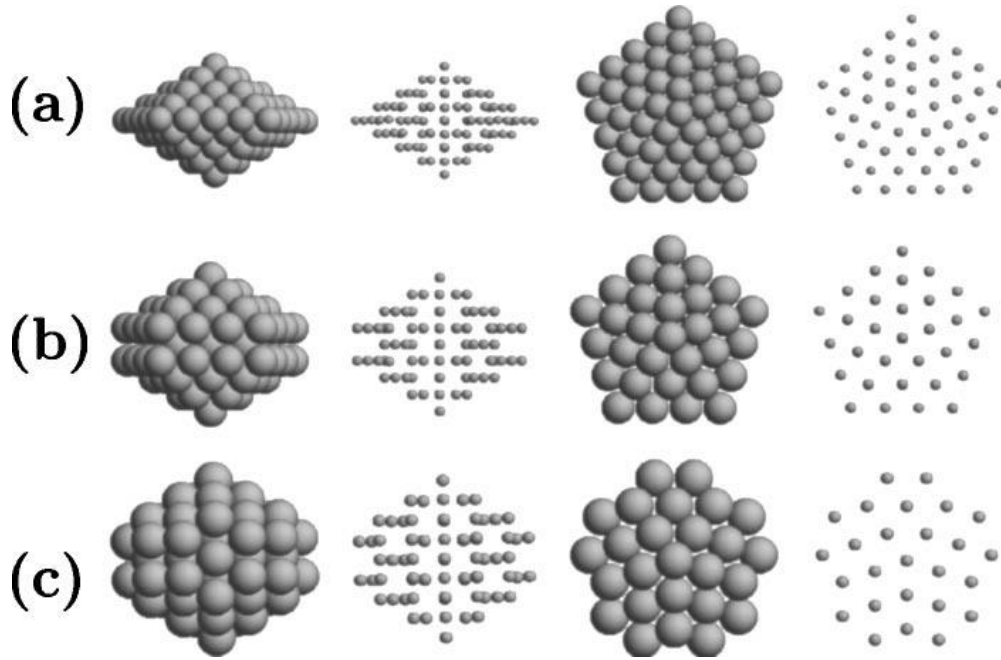


Figure 1.11 Structure models of decahedral structures: (a) regular decahedron, (b) Ino-decahedron and (c) Marks-decahedron.²⁰ The figure is from ref [20].

Another common atomic structure is the decahedron. The decahedral structure actually has three different types: regular decahedron, Ino-decahedron and Marks decahedron, as shown in Figures 1.11 (a), (b) and (c), respectively. The regular decahedron can be thought of consisting of 5 tetrahedrons with a shared edge in the fivefold axis. It has 15 edges, 7 vertexes and 10 regular triangular facets. All 10 facets are close packed (111) facets. Similar to the Mackay-icosahedron, these tetrahedrons also cannot perfectly form a decahedron. There are still spaces between them. To fill these spaces, the tetrahedrons also need to be distorted, which produces strains. The strains in the decahedron are smaller than those in the Mackay-icosahedron. The regular decahedron is not very spherical and has a very high surface-to-volume ratio. To overcome these factors, the edge on the side of the regular decahedron can be

truncated. This type of truncated decahedron was first presented by Ino, and therefore it was called the ‘Ino-decahedron’.⁵⁶ The Ino-decahedron has 25 edges, 12 vertexes and 15 facets. The 10 triangular (111) facets remain in the Ino-decahedron and 5 square (100) facets occur due to the truncation. Furthermore, there is another truncated decahedron proposed by Marks, which is called the ‘Marks-decahedron’.⁵⁷ This time, the vertical side edge in the Ino-decahedron is truncated and the re-entrant close packed (111) facets are exposed. The Marks-decahedron has 55 edges, 12 vertexes and 15 facets, 32 vertexes and 25 facets. The Marks-decahedron has a lower surface energy than the fcc type structure, but still has the strain inside.

In these motifs, the Mackay-icosahedral structure has the strongest internal strain, the Marks-decahedral has less strain, while the fcc crystalline structures don’t have any internal strain. As the internal strain is proportional to the volume, the Mackay-icosahedral is considered to be more stable in the small size region where the surface energy optimization can overcome the internal strain effect. The fcc crystalline structure is considered to be favored in the big size region, because it does not have the internal strain. The decahedron with the intermediate surface energy and strain is therefore more favorable in the middle size region. Therefore, there is a common view that clusters with small size prefer to have the Mackay-icosahedral structure. When the clusters grow, the favorable structure becomes decahedral and finally, for even bigger clusters, the preferred structure is the fcc structure.^{54,58}

The “favorableness” of the structures is actually the result of the comparison between the structures’ energetics. A commonly used index for the energetics comparison is Δ , which normally is explained as ⁵⁹:

$$\Delta(N) = \frac{E - NE_{coh}}{N^{2/3}} \quad 1.7$$

where N is the number of atoms in the cluster, E is the total energy of the cluster, E_{coh} is the cohesive energy per atom in the same elemental bulk.⁵⁸ The total energy of the cluster E can be expressed in the form ⁵⁹:

$$E = aN + bN^{2/3} + cN^{1/3} + d \quad 1.8$$

where the 4 terms are the contributions of volume, facet, edge and vertex, respectively.

Combine equation 1.7 and 1.8, we can get Δ in this form ⁵⁹:

$$\Delta(N) = \frac{a' + b'N^{1/3} + c'N^{2/3} + d'N}{N^{2/3}} \quad 1.9$$

Through 1.9, we can see that Δ will have a different trend with variation of the number of atoms in the different structures. With growing size, the Δ in the fcc structure will decrease and reach a limit, the Mackey-icosahedral and Marks-decahedral will decrease to a minimal point successively, then increase.^{20,58}

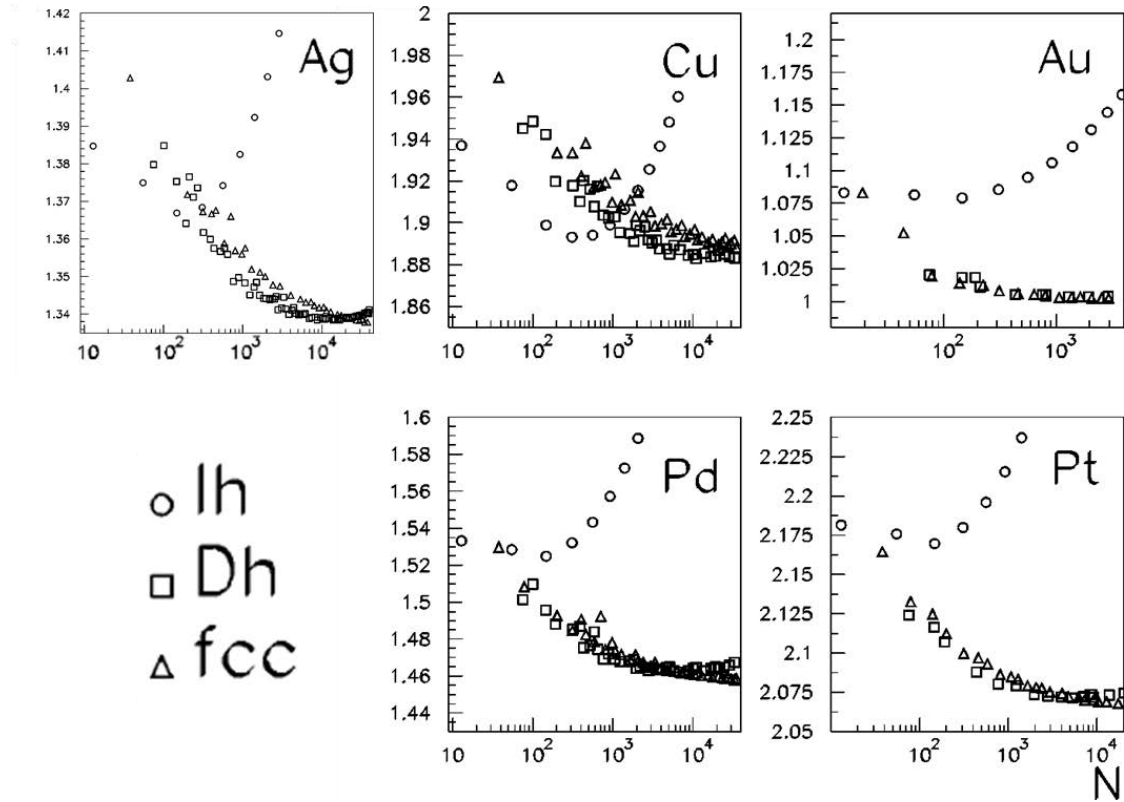


Figure 1.12 The Δ calculated for the different elemental clusters.⁵⁸ The figure is from ref [58].

The most stable structure trend of icosahedral-decahedral-fcc is the same in the clusters, but their crossover sizes are different with respect to the different elemental clusters. Ferrando et al, systematically studied the crossover size of different elemental clusters with two different potentials.⁵⁸ Five different elemental clusters were included: Au, Ag, Cu, Pd and Pt. The calculation results showed that the biggest crossover size from icosahedron to decahedron is found in the Cu cluster, which is about 1000 atoms, while the Ag cluster has the crossover size at around 300 atoms, the Au, Pd and Pt clusters have very small crossover size, all smaller than 100 atoms. The Δ for the decahedron structure and fcc structure (in this study, a truncated

octahedron) are very close over a large size range. The smallest decahedron-fcc crossover size is found in the Au cluster, which is approximately 500 atoms, while the crossover sizes of both Pt and Pd clusters are around 6500 atoms. The crossover size is quite big in Ag and Cu clusters: ~20000 and ~53000 atoms, respectively. The reason for this elemental dependency is due to the different energy needed to change the interatomic distances in different elements. The higher the energy needed, the smaller the crossover size.⁵⁸

1.1.5 Ligand-protected clusters

One of the most commonly used cluster synthesis methods is the chemical colloidal method. In this method, the cluster is synthesized in the solution, but the bare clusters in the solution tend to be aggregated with each other. To protect the cluster from the aggregation, a stabilizing agent is used to form a ligand shell over the cluster metal core. This type of clusters is called ligand-protected cluster.⁶⁰

Although metallic clusters were first synthesized quite a long time ago, the $\text{Au}_{55}(\text{PPh}_3)_{12}\text{Cl}_6$ first reported by Schmid in 1981 is important due to its unique 1.4nm size and a narrow size distribution.⁶¹ Due to its unique 1.4nm size, the $\text{Au}_{55}(\text{PPh}_3)_{12}\text{Cl}_6$ clusters have very special electronic properties that provide the potential for applications such as single electron switches and transistors in nanoscale electronic systems.⁹ The atomic structure of the $\text{Au}_{55}(\text{PPh}_3)_{12}\text{Cl}_6$ cluster metal core was firstly thought to be the cuboctahedron by Schmid, while some researchers

preferred an icosahedral structure.^{61–63} As we'll see in Chapter 3, a hybrid structure with both fcc and icosahedral features was observed to be dominant in nearly half of the clusters by the high-resolution STEM study.⁶⁴

Au₅₅(PPh₃)₁₂Cl₆ clusters have phosphine ligands, which have a relative weak Au-P bond. Beside this type of ligands, thiol ligands are widely used to form thiol-protected clusters, sometimes called monolayer protected clusters.^{65,66} Unlike the gold-phosphine bond, the gold-thiol bond is very strong and has significant effect on the surface of the cluster metal core. In 2006, Hakkinen et al theoretically predicted that the strong gold-thiol bond will form a gold-thiol cap on the surface of the pure gold core.⁶⁷ In 2007, this prediction was experimentally proved by Kornberg's beautiful X-ray crystallography work on Au₁₀₂ clusters.⁶⁸ Since then a series of studies also found this gold-thiol cap unit in the thiolate-protected gold clusters.^{68–79} Although numerous theoretical works have been carried out on the atomic structures of the ligand protected clusters, the experimental side was not satisfactory for a long time, mainly due to the unsuccessful single crystallization of the clusters for the single crystal X-ray structure analysis. The breakthrough in this area was made by Roger Kornberg.⁶⁸

Kornberg et al. successfully crystalized (p-MBA) protected Au₁₀₂ clusters and performed the single crystal X-ray diffraction structure analysis on them.⁶⁸ The determined atomic structure is shown in Figure 1.13. The atomic structure of the gold

core can be described as consisting of 4 parts: one 49-atom Marks-Decahedron, two 20-atom caps on the two poles of the five-fold axis in the Marks-Decahedron and one 13-atom band along the equator.⁶⁸ In this (p-MBA) protected Au_{102} cluster, only the 39 gold atoms in the core have pure Au-Au interaction. All the remaining 63 surface gold atoms have Au-S interactions, suggesting the strong influence of the thiol ligand on the cluster surface metallic atoms.⁶⁸ This Au-S staple was also found in other thiolate-protected clusters, which is now a common feature of this type of clusters.^{70,71,74,77,80,81}

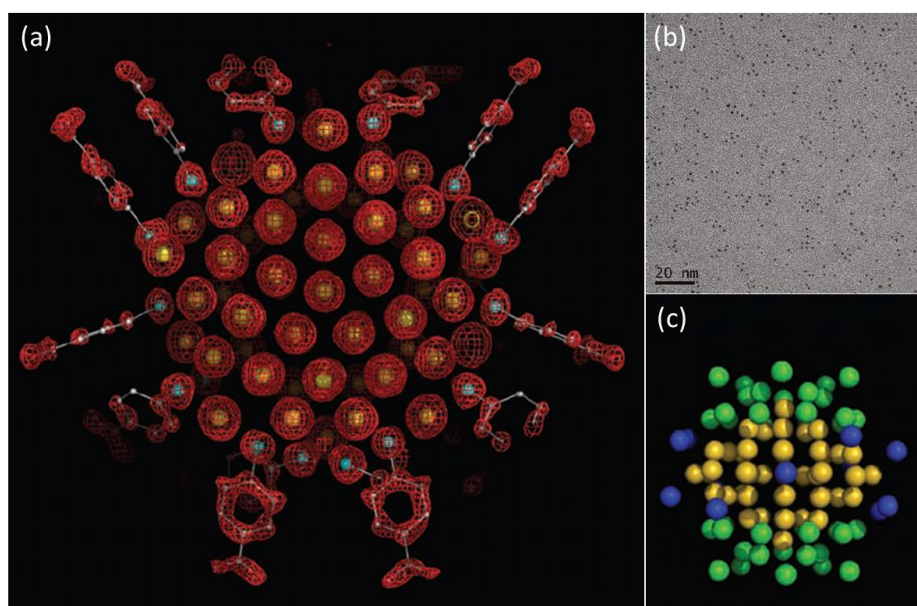


Figure 1.13 (a) The atomic structure of the $\text{Au}_{102}(\text{p-MBA})_{44}$ cluster. Yellow is gold, cyan is sulfur, grey is carbon and oxygen is red. The red network is the electron density map. (b) The TEM image of $\text{Au}_{102}(\text{p-MBA})_{44}$ clusters, showing a relative mono-dispersive size distribution. (c) The atomic structure of the Au core in the $\text{Au}_{102}(\text{p-MBA})_{44}$ cluster. Yellow are the 49-atom Marks-Decahedron, green are the two 20-atom caps and blue is the 13-atom band.⁶⁸ The figure is from ref [68].

As well as the experimentally determined atomic structure, another interesting point of this study is the high stability of the $\text{Au}_{102}(\text{p-MBA})_{44}$ clusters. This can be explained by the electronic shell structure with the jellium model. In the Au cluster, each gold atom will provide one valence electron, so there are 102 valence electrons from the gold atoms. Then, the 44 thiol ligands will accept 44 electrons from the gold, so there are 58 electrons left in total.⁶⁸ As mentioned in section 1.1.2, the 58 electrons can fully fill the 1g shell, resulting in high stability. This is confirmed by a theoretical electronic structure calculation study.⁸² In this study, the HOMO-LUMO gaps of the bare Au_{102} , $\text{Au}_{102}(\text{SCH}_3)_{44}$, $\text{Au}_{104}(\text{SCH}_3)_{46}$ and $\text{Au}_{102}(\text{SCH}_3)_{42}$ clusters were calculated by the DFT method. The bare Au_{102} cluster has an 0.16eV HOMO-LUMO gap which is significantly smaller than the thiol protected $\text{Au}_{102}(\text{p-MBA})_{44}$ cluster ($\sim 0.54\text{eV}$), which indicates a significant influence of the ligand on the electronic structure. To further test the electronic structure's effect on the cluster's stability, the $\text{Au}_{104}(\text{SCH}_3)_{46}$ cluster with 2 extra gold atoms and 2 extra thiol ligands was performed and the HOMO-LUMO gap is $\sim 0.51\text{eV}$. This also can be described as a 58 close electronic shell structure. Lastly, the $\text{Au}_{102}(\text{p-MBA})_{42}$ cluster (which has the same number of gold atoms, but 2 less thiol ligands) has a zero HOMO-LUMO gap, which is due to the open electronic shell structure.⁸²

Following Kornberg's work, more ligand protected clusters were successfully crystalized and their structures were determined by single crystal X-ray crystallography studies, such as $\text{Au}_{18}(\text{SR})_{14}$, $\text{Au}_{25-x}\text{Ag}_x(\text{SR})_{18}$, $\text{Au}_{12}\text{Ag}_{32}(\text{SR})_{30}$,

$\text{Ag}_{44}(\text{SR})_{30}$, and $\text{Au}_{133}(\text{SR})_{52}$. The single crystal X-ray crystallography is now routinely used to resolve the atomic structure of the protected metal clusters.^{80,83–85} However, this method requires very high single crystal purity to achieve the atomic resolution. The single crystal growth seems limited by the ligand type and the cluster size. Most successful crystallizations are found to have a ligand with a phenyl component.⁶⁰ Single crystallizations of the big size clusters also meet with difficulty. The biggest protected metal clusters are $\text{Au}_{133}(\text{SR})_{52}$.⁸⁵ It is very difficult to form a high-quality single crystal (cannot get good X-ray diffraction signal) of the next promising cluster, $\text{Au}_{144}(\text{SR})_{60}$,^{86,87} suggesting either the structures of the $\text{Au}_{144}(\text{SR})_{60}$ cluster is amorphous or the crystal has other size impurity.

As another powerful technique, high resolution electron microscopy does not require a high quality crystal or mono-dispersive size distribution, making it a more flexible structure characterization method. In the next section, we'll introduce this technique applied to the nanoclusters in detail.

1.2 Electron microscopy studies of nanoclusters

1.2.1 Introduction

To study nanoclusters, scientists have used almost every possible technique.^{62,65,88–91} Some techniques have achieved great success. For example, as mentioned above, single crystal X-ray crystallography has been successfully presented to determine the atomic structure of a series of ligand protected metal clusters.^{85,92–95} Among these

techniques, electron microscopy is one of the most common and powerful methods used for the study of nanoclusters.

There are advantages that electron microscopy has over other techniques. First, electron microscopy normally has the highest contemporary resolution. In the 1980's, the electron microscopy's highest resolution capability was challenged by the scanning probe microscopy.⁹⁶ However, through the development of the aberration correction and cold field emission gun, electron microscopy now has a slightly higher resolution than scanning probe microscopy.^{97,98} Second, electron microscopy has relatively high flexibility. The only requirement for successful use of electron microscopy applied to samples, is based upon the adequate thickness of the sample, which should be thin enough for electron transmission. Correspondingly, X-ray crystallography requires the sample should be a high quality single crystal, which is a requirement that very few species clusters can satisfy.⁶⁰ Third, electron microscopy can get different information about clusters. Electron microscopy can obtain more than just the geometric information of the cluster, such as size, shape or structure. When electrons are transmitted from the sample, they will lose an amount of energy that correspond to the sample's element and electronic state. Therefore, an electron energy loss spectroscopy detector can be used to detect these electrons and provide the electronic state and elemental information.⁹⁹ Some electrons may move very close to the atoms and be scattered by the atoms in a similar way to the Rutherford scattering. A donut-like, high angle annular dark field (HAADF) detector can detect

these scattered electrons and form a HAADF image, whose intensity is related to the atomic number of the materials, which can also be considered as chemical information of the samples.^{88,100–102}

There are also drawbacks to electron microscopy. As well as the economic issues like the high operation and maintenance expenses, the major drawback is electron beam induced damage.^{103–105} As an active detecting technique, the electron beam will transmit through the sample and this process will damage the sample. However, by applying a carefully designed experimental condition, the damage can be minimized and the useful information can still be obtained even from very small clusters.^{106–109}

The following sections will mainly focus on the imaging function of the electron microscopy study on the nanocluster. We will see that, by the development of electron microscopy, more and more detailed information can be obtained, from the approximate diameter in the past to the 3D atomic structure in the present.

1.2.2 EM studies of the size of clusters: diameter and mass

As one of the major parameters of the nanocluster, size can affect many of its properties, from its melting point and atomic structure to the catalytic activity.^{41,52,53,58,110} Therefore, size measurement is always an important part of the study on the cluster. Because of the low resolution requirement, the cluster or nanoparticle size measurement should be the earliest function of the electron

microscopy in cluster study.

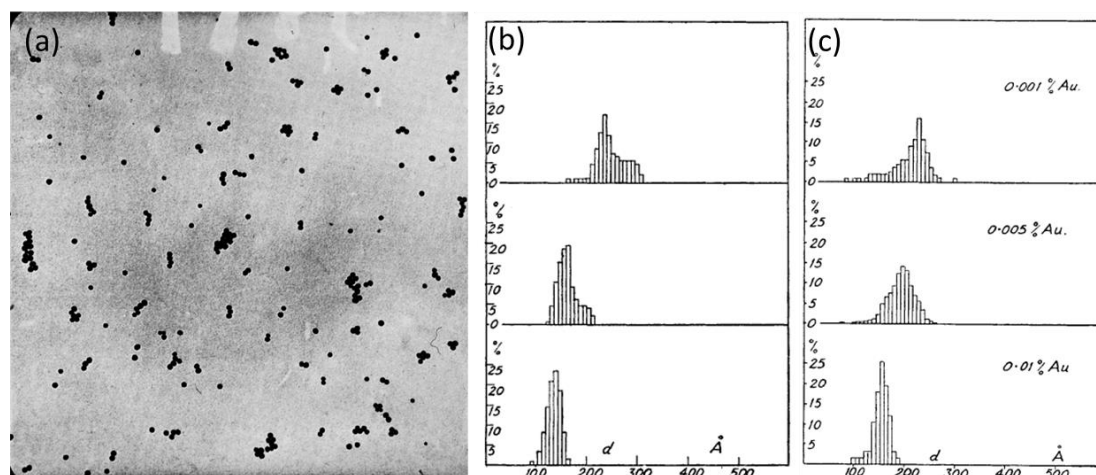


Figure 1.14 (a) Example electron microscopy image of the colloidal Au clusters. The magnification of the image is 50,000 \times . (b) The size distribution of the colloidal Au clusters with the condition: 0.5ml sodium citrate (up), 1ml sodium citrate (middle) and 2.5ml sodium citrate (lower). (c) The size distribution of colloidal Au clusters with different dilutions of reagents.¹¹¹ The figure is from ref [111].

In 1951, Turkevich et al. used electron microscopy to study the colloidal cold cluster's synthesis.¹¹¹ They detected the variation of the cluster size distribution with the different synthesis conditions. In the sodium citrate sols synthesis, the cluster's size is significantly affected by the synthesis temperature, sodium citrate amount and reagents dilution. The decreasing synthesis temperature results in a slightly smaller average cluster size, from $\sim 20\text{nm}$ at 100°C to $\sim 18\text{nm}$ at 70°C . As the amount of the sodium citrate decreases, the average cluster size decreases first, then rapidly

increases. For the reagent dilution's effect, the cluster mean size increases with the diluting reagents. The example of the gold cluster electron microscopy image and the distribution with the variable conditions are shown in Figure 1.14.¹¹¹

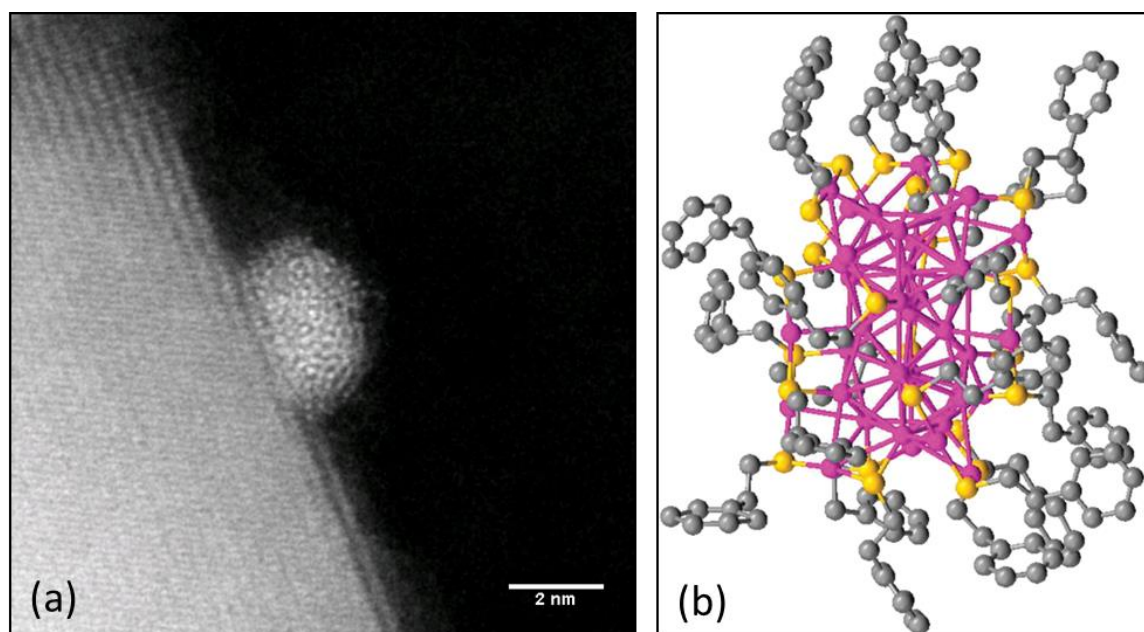


Figure 1.15 (a) A HAADF-STEM image of a Pd cluster supported on TiO_2 , where the flat shape can be clearly seen. (b) Single crystal X-ray crystallography determined the atomic structure of $\text{Au}_{38}(\text{SR})_{18}$ cluster, showing the aspherical feature.¹⁰⁷ The figure is from ref [107].

The diameter measurement by electron microscopy is a very common and fundamental method to determine the size now. It has been successfully employed in many different studies on nanoclusters. However, there is a significant disadvantage of this method. The diameter reflects that the cluster size is based on the assumption that the nanocluster has a spherical 3D shape. It works well for most situations,

however in some special cases, the cluster cannot be treated as spherical. Many studies reported that the support clusters (supported catalysts) tend to be flat on the support materials (as shown in Figure 1.15(a)). It can be recognized when we observe them on the side, but if the view point is above the clusters, we cannot easily identify whether they are spherical or flat. Another case is the very small cluster (<100 atoms). In this size region, the cluster's atomic structure is not always spherical, and the influence of the surface atoms on the diameter cannot be ignored. The example is shown in Figure 1.15(b).¹⁰⁷

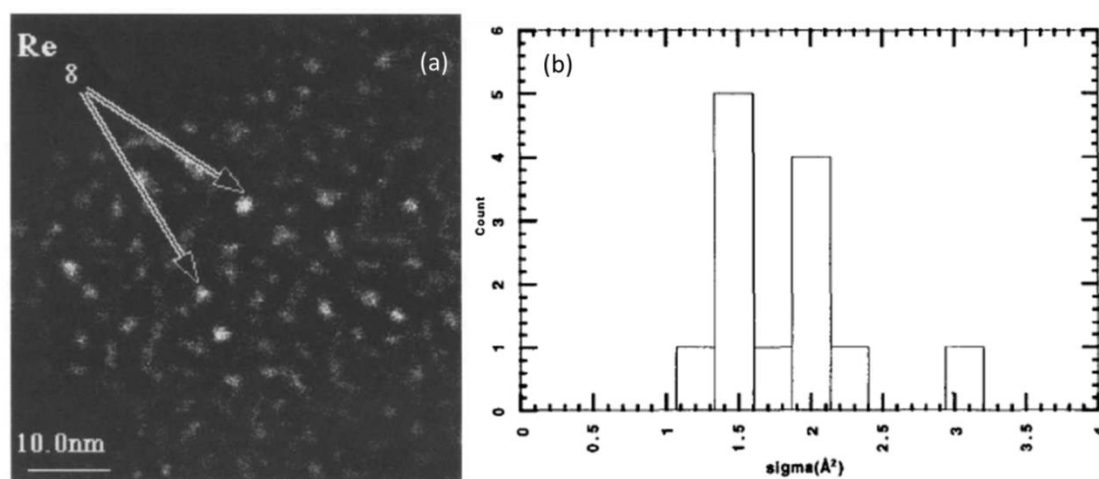


Figure 1.16 (a) HAADF-STEM image of Re₈ clusters. (b) The integrated HAADF intensity distribution of the Re₈ clusters. The figure is from ref [112].

To overcome these drawbacks, a new method of measuring the nanocluster's size is required. With the application of the field emission electron source, the scanning transmission electron microscopy (STEM) became a more practical technique. One of the most interesting parts of this technology is the HAADF imaging. In this

incoherent imaging mode, the intensity is only due to the high angle scattered electrons and it is dependent on the atomic number Z , so this mode is also called the Z -contrast imaging. So, for a mono-metallic nanocluster, its integrated HAADF intensity can directly reflect its mass. Yang et al. successfully employed the first HAADF-STEM analysis on the supported cluster in 1996.¹¹² The integrated HAADF intensities of Re clusters were measured, and the result matched well the theoretical calculation. The long time exposure was utilized to confirm the high stability of the Re_6 clusters under the electron beam. Figure 1.16 shows the example HAADF image of Re_8 clusters and the corresponding integrated HAADF intensity distribution.

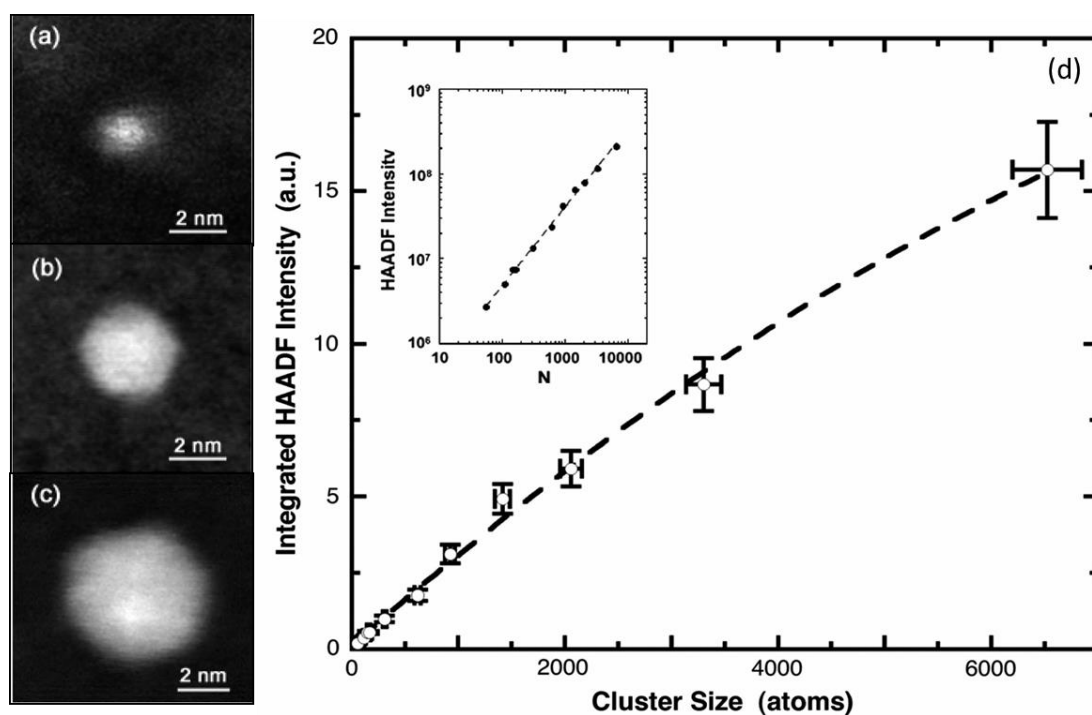


Figure 1.17 The representable HAADF-STEM image of size-selected: (a) Au_{147} , (b) Au_{2057} , and (c) Au_{6525} clusters. (d) The cluster's integrated HAADF intensity as a function of cluster size. The inset is the log fit of the HAADF intensity against the cluster size.¹¹³ The figure is from ref [113].

With the development of the size-selected cluster formation, the relationship between the integrated HAADF intensity of the clusters and the corresponding mass was studied by Young et al.¹¹³ They used the HAADF-STEM to image the size-selected Au clusters with a size range up to 30000 atoms. The integrated HAADF intensities of the clusters were measured after the background subtraction, due to the resolution limit, the measured area is big enough to include all the atoms in the HAADF intensity counting. The integrated HAADF intensity of the clusters as a function of the cluster size (number of atoms) is shown in Figure 1.17. We can see that the relationship between the integrated HAADF intensity and the cluster size displays good linearity in the small size range. For the bigger size clusters, their integrated HAADF intensity increases a little slower than the smaller clusters, which is mainly due to the multiple scattering.¹¹³ A similar study was carried out by Zhiwei et al, who used the different elemental size-selected cluster (Au and Pd) to find out the dependency of the integrated HAADF intensity on the size and element. The quantitative STEM analysis on the Pd cluster shows a good linear relationship between the integrated HAADF intensity and the cluster size. Such a similar linearity also suggests the relationship is not element-specific.¹¹⁴

The finding of the linear relationship between the cluster's integrated HAADF intensity and size provides the possibility to use the known size clusters as the mass standards to calculate the other cluster size in the HAADF-STEM study. Zhiwei et al.

reported using the size-selected Au clusters as mass balances to weigh the monolayer-protected Au₃₈ cluster.¹¹⁵ Three different sized clusters (Au₂₅, Au₃₈ and Au₅₅) were utilized to eliminate the possible size effect on the quantitative analysis. The ligand's contribution on the integrated HAADF intensity must be taken account of. With the calibrated exponent “n” in the Z^n dependent intensity, the ligands' contribution was calculated as 8.7 Au atoms. After the subtraction of the ligand contribution, the numbers of Au atoms in the monolayer-protected Au₃₈ clusters were calculated to be 38.6 ± 2.8 , 38.4 ± 2.9 and 37.5 ± 2.9 with the corresponding Au₂₅, Au₃₈ and Au₅₅ clusters, respectively, as the mass standard.¹¹⁵

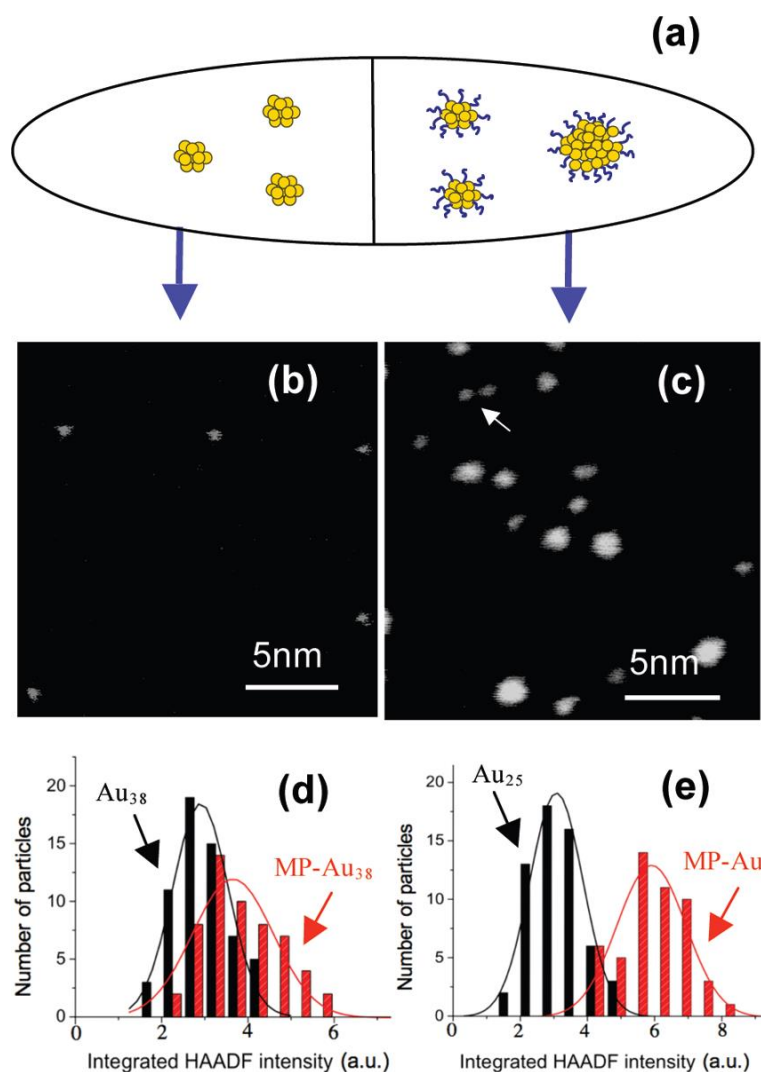


Figure 1.18 Schematic of cluster weighing with size-selected clusters. (a) The monolayer-protected clusters and size-selected clusters were deposited separately on the same TEM grid. The representative HAADF-STEM images of (b) size-selected cluster and (c) monolayer-protected cluster. The integrated HAADF intensity distribution of monolayer-protected cluster with: (d) Au_{38} clusters, and (e) Au_{25} clusters.¹¹⁵ The figure is from ref [115].

1.2.3 EM studies of the atomic structure of clusters

As Dr. Francis Crick said, “If you want to understand function, study structure.”¹¹⁶

The determination of the nanocluster's atomic structure is crucial for a better understanding of the cluster's properties.^{117–119} Electron microscopy, due to its high resolution and high flexibility, plays a very important role in the research of nanocluster's atomic structure. With the development of the techniques, the electron microscopic study of nanocluster structure becomes more accurate and quantitative, giving us more detailed information: from shape to quantitative atomic arrangement.^{64,89,120,121}

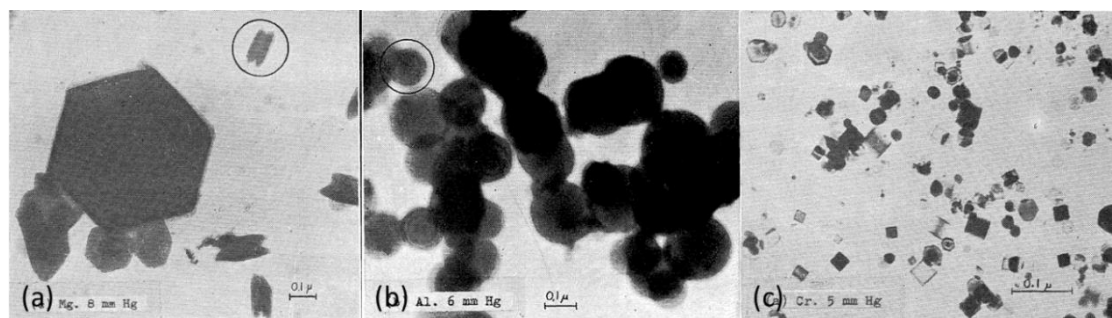


Figure 1.19 Representative TEM images of: (a) Mg clusters, (b) Al clusters, and (c) Cr clusters, showing their hexagonal, spherical and cubic shapes, respectively.¹²⁰ The figure is from ref [120].

In the early days, due to the resolution limitation, the study on the nanocluster structure was focused on the cluster's shape (by imaging) and crystal arrangement (by electron diffraction). Kimoto et al. performed electron microscopy research on the evaporated big metal clusters.¹²⁰ In their study, the geometric shapes of the clusters were obtained by electron microscopy. For example, they found the hexagonal and columnar shape of the Mg cluster, the spherical shape of the Al cluster and the cubic

shape of the Cr cluster. The representative images are shown in Figure 1.19.¹²⁰ As the electron microscope they used could not reach atomic resolution, they could not directly observe the crystal lattice structure of the clusters, so the electron diffraction pattern was used to help with the study of the crystal structure instead. The lattice of the Mg, Al and Cr clusters are hcp, fcc and bcc, respectively.¹²⁰

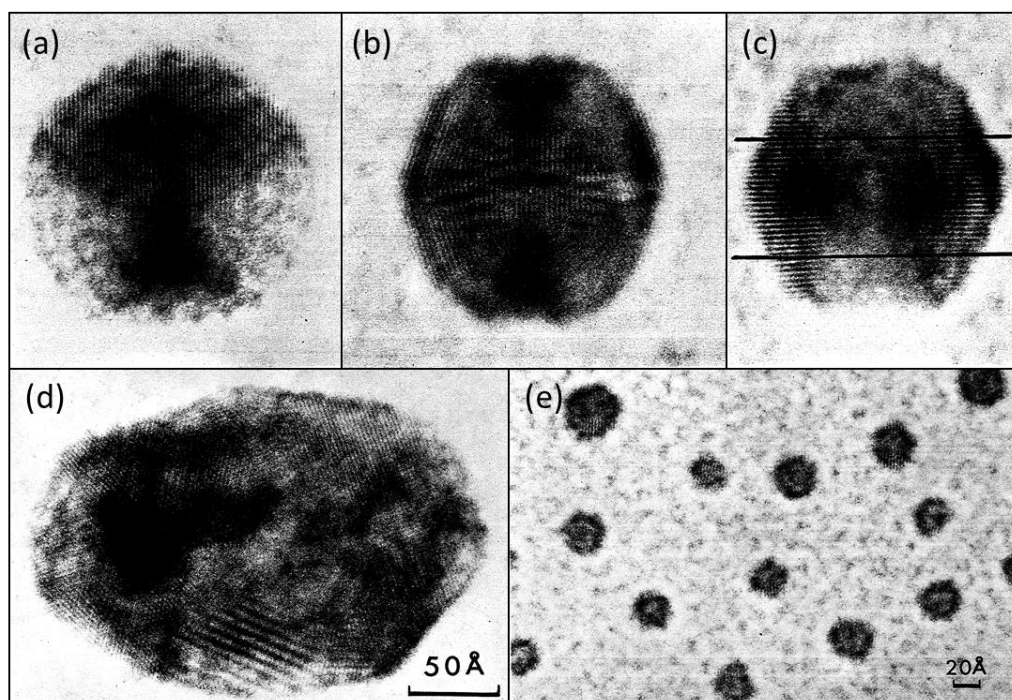


Figure 1.20 Representative EM images of: (a) decahedral cluster, and (b) icosahedral cluster. In (c), two parallel lines were employed to show the lattices are not parallel. (d) The irregular shape clusters. (e) The representative EM image of small Au clusters, showing the multiply-twinned structure that confirmed the growth of the cluster started from a small nucleus.¹²² The figure is from ref [122].

With the development of the instrument, Komoda studied the structure of evaporated Au clusters.¹²² The high resolution electron microscope allowed Komoda to study the

structure of the Au cluster directly through the imaging. With high resolution images (as shown in Figure 1.20), he observed the decahedral and icosahedral structure of the evaporated Au clusters that were consistent with Ino's research. The structure study with the different size Au clusters, suggesting the nanoclusters started from a small nucleus, then they grew with single close packed layers. Also, the lattices in the clusters were found to be not exactly parallel. The spacing between the lattices tended to be bigger in the outside part of the cluster, which suggested the existence of a strain inside the cluster. This can explain the change of the shape and structure of the clusters with sizes bigger than 15nm: the strain will increase with the bigger size, and when the cluster size was big enough, the effect of the strain induced internal energy will overcome the surface energy and force the cluster to change its structure in order to adapt to it.¹²²

Although the resolution of the electron microscope now is high enough to offer very clear images of clusters,^{89,117,123} its 2D nature still prevents us from resolving the 3D atomic structure of clusters. One solution to this is 3D electron tomography, the basic idea of this technique is to use a series of different orientation images of the nanocluster to reconstruct the 3D image of the nanoclusters. Chen et al. successfully employed HAADF-STEM tomography combined with the 3D Fourier filtering to obtain the 3D structure of a big Pt nanocluster at atomic resolution.¹²⁴ With this new technique, they found atomic steps and dislocations in the Pt cluster (as shown in Figure 1.21) that are invisible in 2D images, showing the advantages of this

technique.¹²⁴ However, this technique requires high stability of the clusters under the electron beam and sample tilting. This is not very practical to beam-sensitive small clusters, which are observed to rotate and change structure under the continuous electron beam radiation.^{79,89,106}

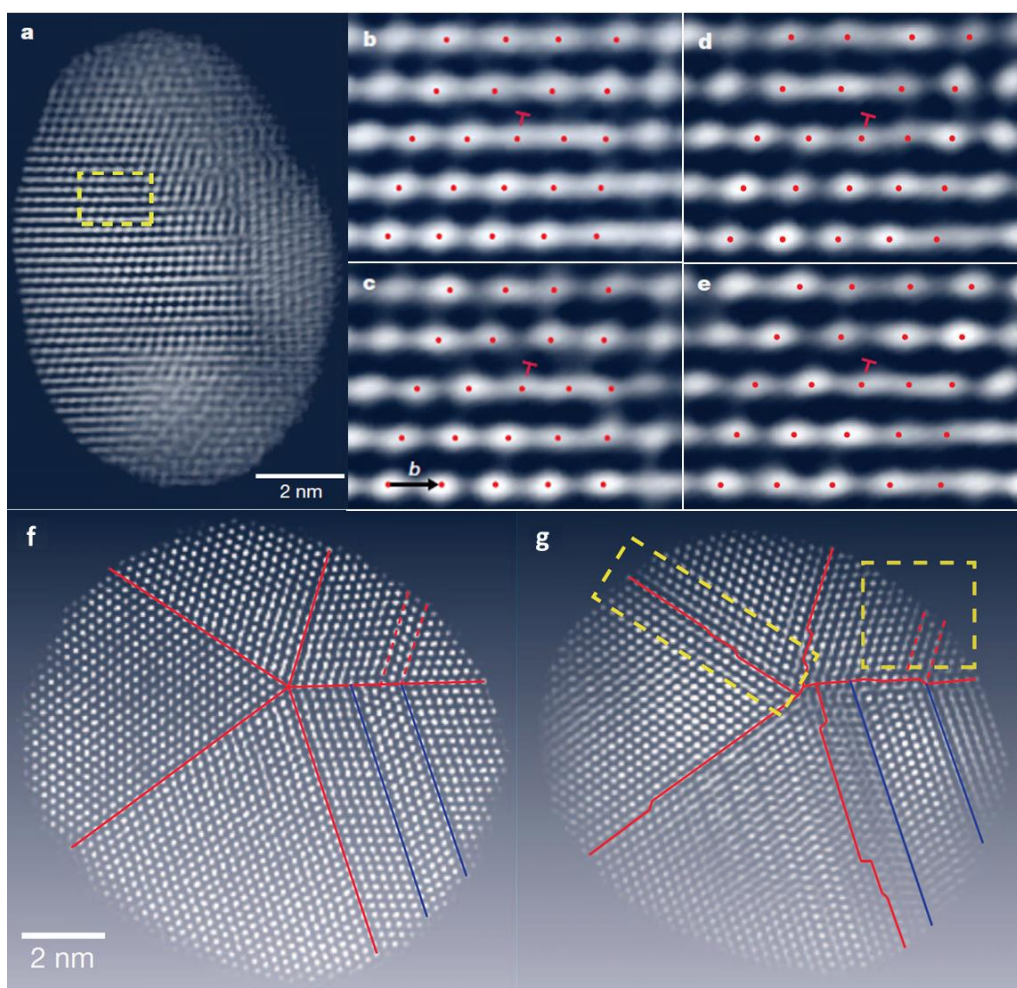


Figure 1.21 (a) An internal slice of the Pt cluster 3D image. The yellow box highlights the dislocation. (b) The zoomed-in image of the highlighted dislocation. (c)-(e) The finer sections of the slice in (b). (f) An image of the Pt cluster. (g) An internal slice of the Pt cluster image in (f), showing the atomic steps that are not observed in (f).¹²⁴

The figure is from ref [124].

As we discussed above, 3D electron tomography cannot be simply applied to a small nanocluster. Another 3D structure determination method based on a single image of the nanocluster was presented by Li et al⁸⁸ in our group. In this study, the aberration corrected HAADF STEM was utilized to investigate the 3D structure of size-selected Au₃₀₉ clusters. A quantitative HAADF intensity analysis was performed to confirm the Au cluster survives from landing on the carbon surface. The atomic structures of the Au clusters were determined by comparing them with simulated images of three structure models: cuboctahedron, Ino-decahedron and icosahedron. The result shows that 32% of the Au₃₀₉ clusters have an Ino-decahedral structure, 25% have a cuboctahedral structure and 8% have an icosahedral structure. The rest of the clusters did not show any ordered structure. Using this technique, only one high resolution image is needed for determination of the cluster's 3D structure, showing great practical potential for small clusters. The only drawback of this method is the size of the investigated cluster must be obtained in order to use the simulation of the correct size structure model. In Li's study, they used the size-selected cluster to avoid this issue. In chapter 3, we will show that with the combination of this technique and the cluster weighing, we can resolve the atomic structure of any size clusters we want.

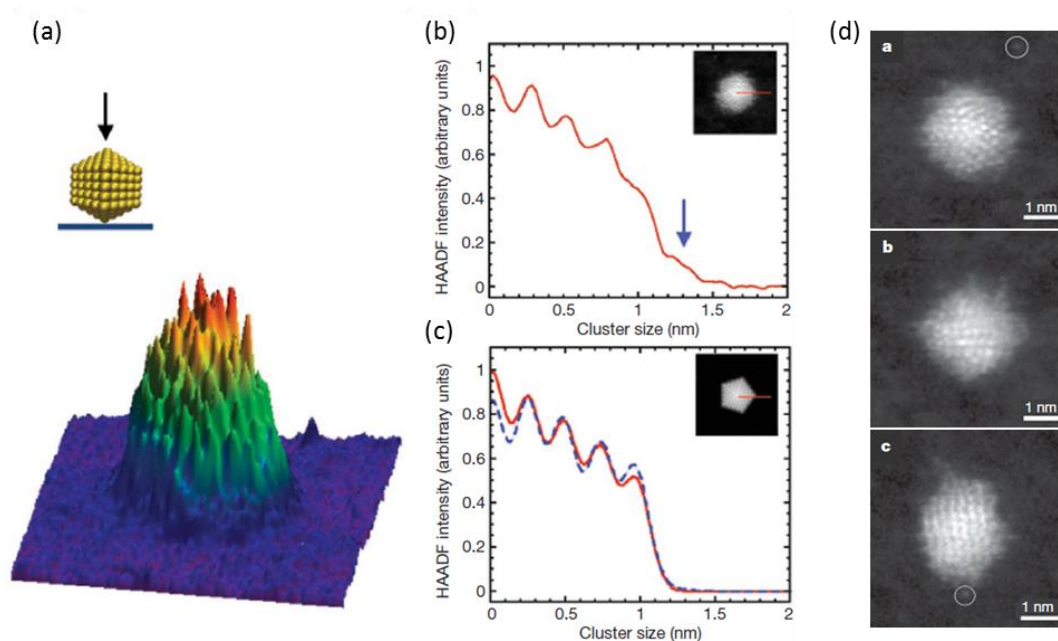


Figure 1.22 (a) A 3D plot of the HAADF intensity of a Au_{309} cluster with icosahedral structure. (b) Line profile of the experimental image of an icosahedral structure Au_{309} cluster. (c) Line profile of the simulated image of an icosahedral structure Au_{309} cluster. (d) The representative HAADF-STEM images of clusters with different shapes.⁸⁸ The figure is from ref [88].

It has long been argued by the researchers that the electron beam will affect the cluster's structure.¹²⁵ Recently, the application of the low dose single molecule TEM approach applied in molecule biology on the small clusters was carried out by Azubel et al.¹²¹ The sample they used was crystallized mono-dispersive $\text{Au}_{68}(\text{SH})_{32}$ clusters with high solubility and stability, which was confirmed by electrospray ionization mass spectrum (ESI-MS), thermogravimetric analysis (TGA) and x-ray photo-electron spectrum (XPS). Aberration corrected TEM images of nearly one thousand clusters were taken with a low electron dose of around $800 \text{ electron}/\text{\AA}^2$.

Then, the images of the clusters were put into the 3D structure reconstruction software. The reconstruction result showed a 68-peak electron density map corresponding to the 3D atomic structure of the $\text{Au}_{68}(\text{SH})_{32}$ cluster's metal core. This structure was confirmed by a DFT calculation. The model of the $\text{Au}_{68}(\text{SH})_{32}$ cluster based on the Au core structure obtained from the TEM images was relaxed to the minimum energy. The relaxed structure showed a great match with the structure from the TEM, only very few surface atoms moved from the previous position. This low electron dose TEM with 3D reconstruction technique shows great ability on the 3D structure determination of the small clusters. While we should notice this technique requires very high mono-dispersive samples, all the clusters in this technique should have the exact same size and atomic structure.

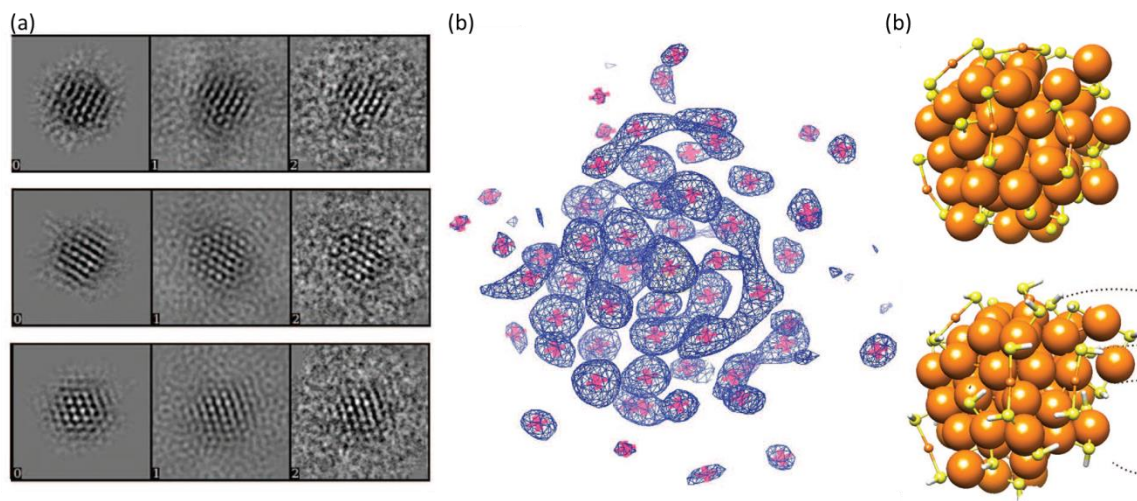


Figure 1.23 (a) The representative images of $\text{Au}_{68}(\text{SH})_{32}$ clusters. (b) The electron density map of the $\text{Au}_{68}(\text{SH})_{32}$ cluster from the reconstruction software. (c) The comparison between the TEM obtained $\text{Au}_{68}(\text{SH})_{32}$ structure (up) and the DFT relaxed structure (lower).¹²¹ The figure is from ref [121].

1.2.4 Dynamical studies of cluster structure transformation with EM

The atomic structure of the nanocluster was strongly influenced by parameters such as temperature, size and energy^{47,54,58,126–128} Therefore, studying the parameter-dependent atomic structure of the clusters is of great importance in better understanding the nature of the cluster structure. Electron microscopy, due to its high flexibility, is a suitable tool to perform this type of study.

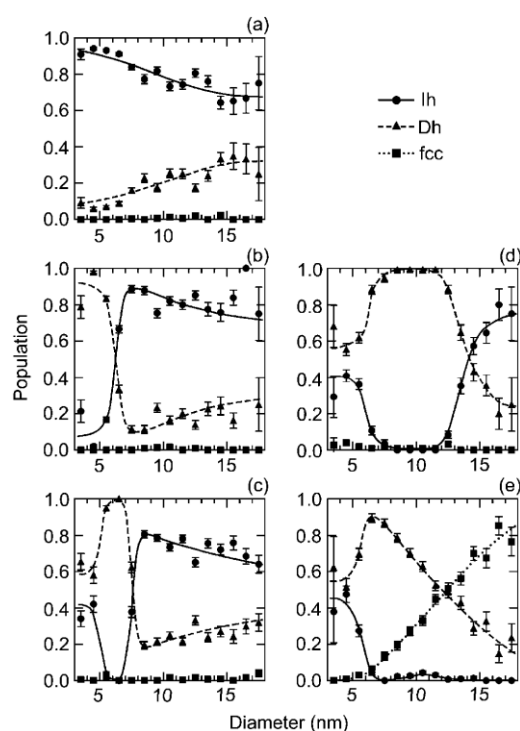


Figure 1.24 The structure distribution of the Au clusters as a function of cluster diameter with different annealing temperature: (a) No annealing, (b) 1173 K, (c) 1223 K, (d) 1273 K, and (e) 1373 K.¹²⁹ The figure is from ref [129].

An experimental study of the atomic structure of the Au nanocluster with variation of size and annealing temperature was employed by Koga et al, with high resolution

electron microscopy.¹²⁹ The Au cluster samples were prepared by gold evaporation with helium cooling. Before the helium-cooled Au cluster deposition, the clusters were passed through a heating zone with different temperatures from room temperature to above Au bulk melting point. Then the deposited clusters were analyzed by high resolution electron microscopy. Each cluster was tilted to a series of angles in order to better identify the structures. Next, the structure distribution of the cluster with different sizes and annealing temperatures were obtained as shown in Figure 1.24. The results show clearly the effect of the annealing temperature and size on the structure distribution. The study confirmed the energy barriers between structures, which has great influence on the structure distribution of the clusters with certain sizes and temperatures.¹²⁹ However, we should notice the special high percentage of icosahedral clusters observed in the condition without the annealing as shown in Figure 1.24 (a). This result shows contradictory to previous theoretical and experimental studies which suggest much lower percentage of icosahedral structures and higher percentage of decahedral and fcc structures in small size region. Koga et al suggested that the observation of these large icosahedral clusters is due to the kinetic trapping effect, the large icosahedral clusters were formed shell by shell from small icosahedral cluster “seed”. We cannot rule out this possibility, especially as the cluster formation conditions can change the structure proportion significantly. But a further study on this result can be performed for a better understanding on the mechanism of cluster structure formation.

In the electron microscopy studies, the electron beam irradiation is normally regarded as a “bad” factor due to its potential “damage” to the sample. However, in a series of electron microscopy studies employed by Zhiwei et al., the electron beam was no longer a potential damage-inducing factor, but a manipulation probe, which can be used to study the most stable structure of the Au nanoclusters.^{89,106,109} In the study on the size-selected Au₉₂₃ clusters,⁸⁹ the clusters were continually scanned and imaged by the aberration corrected STEM. The structures of the clusters were confirmed by comparing them with the simulated images of different structure motifs: Mackay-icosahedral, Ino-decahedral and cuboctahedral. Under the continuous electron beam scanning, as shown in Figure 1.25, the icosahedral structure was the least stable structure, as nearly all the icosahedral structured clusters transformed to decahedral or fcc structures after long-standing electron beam irradiation.⁸⁹ The decahedral structure seems the most stable structure: all the decahedral structured clusters retain the same structure after electron irradiation, though the direction of the structure was changed. The fcc structure also showed great stability, only one fcc structured cluster transferred to the decahedral structure. Based on these results, the icosahedral structured clusters should have a higher energy than the decahedral or fcc structured clusters. The decahedral structure may have the lowest energy as more of the icosahedral structure transferred to the decahedral structure. This result showed agreement with the theoretical prediction that in this medium size range, the decahedral should have the lowest energy, while the fcc structure has a slightly higher energy than the decahedral structure.⁵⁸ In another study on the size-selected Au₂₀

clusters, a similar method was employed and tetrahedral and unidentified structures were observed during the structure fluctuation under the continuous electron irradiation, showing the ability of this method applied to small clusters.¹⁰⁶

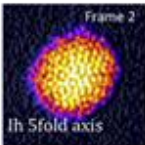
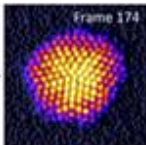
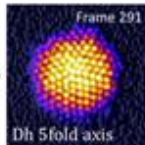
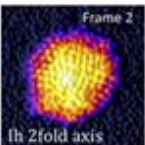
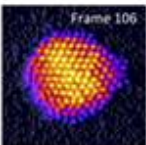
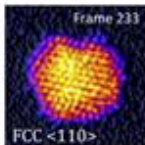
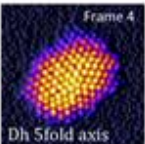
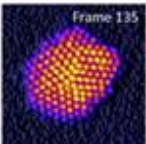
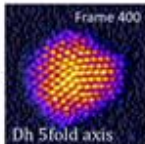
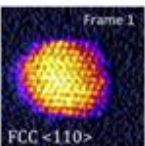
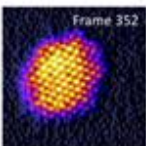
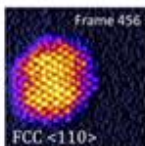
Initial state	After irradiation	Examples			
Ih: 42	Dh: 29 FCC: 12 Ih: 1	Ih->Dh			
		Ih->FCC			
Dh: 18	Dh: 18	Dh unchanged			
FCC: 19	FCC: 18 Dh: 1	FCC unchanged			

Figure 1.25 The statistical results of the structure transformation from icosahedral, decahedral and fcc structures, with the corresponding representative images.⁸⁹ The figure is from ref [89].

1.3 Aims and objectives

The main objective of this thesis has been to develop a more precise method to study the structure of nanoparticles by using aberration corrected HAADF-STEM. To

achieve this objective, using the incoherent nature of the HAADF-STEM imaging, the size-selected clusters produced from a magnetron sputtering, gas condensation cluster source were used to calibrate the integrated HAADF intensity. The sizes of the nanoparticles were then obtained from the calibrated integrated HAADF intensity. Using this method, the nanoparticle samples can be “purified”, and the structure of the nanoparticle studied in a much more precise size range.

Four different systems were investigated by the method mentioned above: phosphite protected monometallic Schmid Au clusters, thiol protected bimetallic AuAg cluster, TiO₂ supported PVA protected ultrasmall Au and Pd cluster and biological ferritin iron core. For the first system, the aim is to study the atomic structure of the Au₅₅(PPh₃)₁₂Cl₆ without the other size clusters' influence. For the second system, the aim is to study the atomic structure of the AuAg alloy clusters with the consideration of their composition. For the third system, the objective is to characterize the ultra small clusters in the TiO₂ supported Au and Pd catalysts to explain the unexpected high catalysis performance. For the fourth system, we aimed to study the ferritin iron core growth process by investigating the ferritin iron core morphologies with different iron loading.

Reference:

1. Schaefer, H.-E. *Nanoscience: The Science of the Small on Physics, Engineering, Chemistry, Biology and Medicine. Media* (2010). doi:10.1007/978-3-642-10559-3
2. Epstein, I. R. *Nanochemistry: a chemical approach to nanomaterials*. **89**, (Royal Society of Chemistry, 2009).
3. De, M., Ghosh, P. S. & Rotello, V. M. Applications of Nanoparticles in Biology. *Adv. Mater.* **01003**, 4225–4241 (2008).
4. Iijima, S. Helical microtubules of graphitic carbon. *Nature* **354**, 56–58 (1991).
5. Hoffmann, R. Small but strong lessons from chemistry for nanoscience. *Angew. Chemie - Int. Ed.* **52**, 93–103 (2013).
6. Feynman, R. *There's plenty of room at the bottom*. *Engineering and Science* **23**, (1960).
7. Johnston, R. L. *Atomic and molecular clusters*. (Taylor & Francis, 2002).
8. De Heer, W. A. The physics of simple metal clusters: Experimental aspects and simple models. *Rev. Mod. Phys.* **65**, 611–676 (1993).
9. Schmid, G. The relevance of shape and size of Au₅₅ clusters. *Chem. Soc. Rev.* **37**, 1909–30 (2008).
10. Schmid, G., Baumle, M., Geerkens, M., Heim, I., Osemann, C. & Sawitowski, T. Current and future applications of nanoclusters. *Chem. Soc. Rev.* **28**, 179–185 (1999).
11. Buchenau, H., Knuth, E. L., Northby, J., Toennies, J. P. & Winkler, C. Mass spectra and time-of-flight distributions of helium cluster beams. *J. Chem. Phys.* **92**, 6875 (1990).

12. Jarrold, M. F. & Constant, V. Silicon Cluster Ions: Evidence for a Structural Transition. *Physical Review* **67**, 2994–2997 (1991).
13. Reetz, M. & Helbig, W. Size-selective synthesis of nanostructured transition metal clusters. *J. Am. Chem. Soc.* **116**, 7401–7402 (1994).
14. Duval, P. B., Burns, C. J., Clark, D. L., Morris, D. E., Scott, B. L., Thompson, J. D., Werkema, E. L., Jia, L. & Anderson, R. A. Synthesis and Structural Characterization of the First Uranium Cluster Containing an Isopolyoxometalate Core. *Angewandte Chemie (International ed. in English)* **13**, 3357–3361 (2001).
15. Boyle, R. The Sceptical Chymist. (1661).
doi:<http://dx.doi.org/10.1017/CBO9780511703966.010>
16. Katakuse, I. *et al.* Correlation between mass distributions of zinc, cadmium clusters and electronic shell structure. *Int. J. Mass Spectrom. Ion Process.* **69**, 109–114 (1986).
17. Katakuse, I., Ichihara, T., Fujita, Y., Matsuo, T., Sakurai, T. & Matsuda, H. Mass distributions of copper, silver and gold clusters and electronic shell structure. *Int. J. Mass Spectrom. Ion Process.* **67**, 229–236 (1985).
18. Knight, W. D., Clemenger, K., de Heer, W. A., Saunders, W. A., Chou, M. Y. & Cohen, M. L. Electronic Shell Structure and Abundances of Sodium Clusters. *Phys. Rev. Lett.* **52**, 2141–2143 (1984).
19. Martin, T. P., Bergmann, T., Gohlich, H. & Lange, T. Observation of electronic shells and shells of atoms in large Na clusters. *Chem. Phys. Lett.* **172**, 209–213 (1990).
20. Baletto, F. & Ferrando, R. Structural properties of nanoclusters: Energetic, thermodynamic, and kinetic effects. *Rev. Mod. Phys.* **77**, 371–423 (2005).

21. Knickelbein, M. B. Electronic shell structure in the ionization potentials of copper clusters. *Chem. Phys. Lett.* **192**, 129–134 (1992).
22. Martin, T. P., Näher, U., Schaber, H. & Zimmermann, U. Evidence for a sizedependent melting of sodium clusters. *J. Chem. Phys.* **100**, 2322 (1994).
23. Winter, B. J., Parks, E. K. & Riley, S. J. Copper clusters: The interplay between electronic and geometrical structure. *J. Chem. Phys.* **94**, 8618 (1991).
24. H.Gohlich, T.Lange, T.Bergmann & T.P, M. Electronic Shell Structure in Large Metallic Clusters. *Phys. Rev. Lett.* **65**, 748–751 (1990).
25. Louis, C. & Bond, G. *Gold Nanoparticles for Physics, Chemistry and Biology*. (London: Imperial College Press, 2012).
26. Strutt, J. W. On the Scattering of Light by small Particles. *Scientific Papers* **1**, 1869–1881 (1899).
27. Norskov, J. K., Bligaard, T., Hvolbaek, B., Abild-Pederen, F., Chorkendorff, I. & Christensen, C. H. The Nature of the Active Site in Heterogeneous Metal Catalysis. *Chem. Soc. Rev.* **37**, 2163–2171 (2008).
28. Janssens, T. V. W., Clausen, B. S., Hvolbaek, B., Falsig, H., Christensen, C. H., Bligaard, T. & Norskov, J. K. Insights into the reactivity of supported Au nanoparticles: Combining theory and experiments. *Top. Catal.* **44**, 15–26 (2007).
29. Parravano, G. Surface reactivity of supported gold. II. Hydrogen transfer between benzene and cyclohexane. *J. Catal.* **18**, 320–328 (1970).
30. Cha, D. Y. & Parravano, G. Surface Reactivity of Supported Gold. I. Oxygen Transfer Between Carbon Monoxide and Carbon Dioxide. *J. Catal.* **18**, 200–211 (1970).

31. Haruta, M. Low-Temperature Oxidation of CO over Gold Supported on TiO₂, α-Fe₂O₃, and Co₃O₄. *Journal of Catalysis* **144**, 175–192 (1993).
32. Haruta, M., Kobayashi, T., Sano, H. & Yamada, N. Novel gold catalysts for the oxidation of carbon monoxide at a temperature far below 0.DEG.C. *Chem. Lett.* 405–408 (1987). doi:10.1246/cl.1987.405
33. HARUTA, M. Gold catalysts prepared by coprecipitation for low-temperature oxidation of hydrogen and of carbon monoxide. *J. Catal.* **115**, 301–309 (1989).
34. Sakurai, H., Tsubota, S. & Haruta, M. Hydrogenation of CO₂ over gold supported on metal oxides. *Appl. Catal. A, Gen.* **102**, 125–136 (1993).
35. Haruta, M. Size- and support-dependency in the catalysis of gold. *Catal. Today* **36**, 153–166 (1997).
36. Sakurai, H. & Haruta, M. Synergism in methanol synthesis from carbon dioxide over gold catalysts supported on metal oxides. *Catal. Today* **29**, 361–365 (1996).
37. Burch, R. Gold catalysts for pure hydrogen production in the water-gas shift reaction: activity, structure and reaction mechanism. *Phys. Chem. Chem. Phys.* **8**, 5483–500 (2006).
38. Edwards, J. K., Ntainjua, E., Carley, A. F., Herzing, A. A., Kiely, C. J. & Hutchings, G. J. Direct synthesis of H₂O₂ from H₂ and O₂ over gold, palladium, and gold-palladium catalysts supported on acid-pretreated TiO₂. *Angew. Chemie - Int. Ed.* **48**, 8512–8515 (2009).
39. Guzman, J. & Gates, B. Catalysis by supported gold: Correlation between catalytic activity for CO oxidation and oxidation states of gold. *J. Am. Chem. Soc.* 2672–2673 (2004).
40. Lemire, C., Meyer, R., Shaikhutdinov, S. K. & Freund, H. J. CO adsorption on

- oxide supported gold: From small clusters to monolayer islands and three-dimensional nanoparticles. *Surf. Sci.* **552**, 27–34 (2004).
41. Molina, L. M. & Hammer, B. Some recent theoretical advances in the understanding of the catalytic activity of Au. in *Applied Catalysis A: General* **291**, 21–31 (2005).
42. Valden, M., Lai, X. & Goodman, D. W. Onset of catalytic activity of gold clusters on titania with the appearance of nonmetallic properties. *Science* **281**, 1647–50 (1998).
43. Pasquato, L., Rancan, F., Scrimin, P., Mancin, F. & Frigeri, C. N-Methylimidazole-functionalized gold nanoparticles as catalysts for cleavage of a carboxylic acid ester. *Chem. Commun.* **2**, 2253–2254 (2000).
44. Ueda, A., Oshima, T. & Haruta, M. Reduction of nitrogen monoxide with propene in the presence of oxygen and moisture over gold supported on metal oxides. *Appl. Catal. B Environ.* **12**, 81–93 (1997).
45. Klein, D. L., Roth, R., Lim, A. K. L., Alivisatos, A. P. & McEuen, P. L. A single-electron transistor made from a cadmium selenide nanocrystal. *Nature* **389**, 699–701 (1997).
46. Kappes, M. M. Experimental Studies of Gas-Phase Main-Group Metal Clusters. *Chem. Rev.* **88**, 369 (1988).
47. Brack, M. The physics of simple metal clusters: Self-consistent jellium model and semiclassical approaches. *Reviews of Modern Physics* **65**, 677–732 (1993).
48. Clemenger, K. Ellipsoidal shell structure in free-electron metal clusters. *Phys. Rev. B* **32**, 1359–1362 (1985).
49. Gustafson, C.; Lamm, I.L.; Nilsson, B.; Nilsson, S. G. Nuclear deformabilities in the rare-earth and actinide regions with excursions off the stability line and

- into the super-heavy region. *Ark. Fys.* **36**, 613 (1967).
50. Martin, T. P., Bergmann, T., Goehlich, H. & Lange, T. Shell structure of clusters. *J. Phys. Chem.* **95**, 6421 (1991).
 51. Martin, T. P. Shells of atoms. *Phys. Rep.* **273**, 199–241 (1996).
 52. Chushak, Y. G. & Bartell, L. S. Melting and freezing of gold nanoclusters. *J. Phys. Chem. B* **105**, 11605–11614 (2001).
 53. Buffat, P. & Borel, J. P. Size effect on the melting temperature of gold particles. *Phys. Rev. A* **13**, 2287–2298 (1976).
 54. Baletto, F. & Ferrando, R. Structural properties of nanoclusters: Energetic, thermodynamic, and kinetic effects. *Rev. Mod. Phys.* **77**, 371–423 (2005).
 55. Mackay, A. L. A dense non-crystallographic packing of equal spheres. *Acta Crystallogr.* **15**, 916–918 (1962).
 56. Ino, S. Stability of multiply-twinned particles. *J. Phys. Soc. Japan* **27**, 941–953 (1969).
 57. Marks, L. D. Surface structure and energetics of multiply twinned particles. *Philos. Mag. A* **49**, 81–93 (1984).
 58. Baletto, F., Ferrando, R., Fortunelli, A., Montalenti, F. & Mottet, C. Crossover among structural motifs in transition and noble-metal clusters. *J. Chem. Phys.* **116**, 3856 (2002).
 59. Cleveland, C. & Landman, U. The energetics and structure of nickel clusters: Size dependence. *J. Chem. Phys.* **94**, 7376 (1991).
 60. Goswami, N., Li, J. & Xie, J. *Protected Metal Clusters - From Fundamentals to Applications. Frontiers of Nanoscience* **9**, (2015).

61. Schmid, G., Pfeil, R., Boese, R., Bandermann, F., Meyer, S., Calis, G. H. M. & van der Velden, J. W. A. $\text{Au}_{55}[\text{P}(\text{C}_6\text{H}_5)_3]_{12}\text{Cl}_6$ — ein Goldcluster ungewöhnlicher Größe. *Chem. Ber.* **114**, 3634–3642 (1981).
62. Marcus, M. A., Andrews, M. P., Zegenhagen, J., Bommanavar, A. S. & Montano, P. Structure and vibrations of chemically produced Au_{55} clusters. **42**, 3312–3316 (1990).
63. Vogel, W., Rosner, B. & Tesche, B. Structural Investigations of Au_{55} Organometallic Complexes by X-ray Powder Diffraction and Transmission Electron Microscopy. *J. Phys. Chem.* **97**, 11611–11616 (1993).
64. Jian, N., Stapelfeldt, C., Hu, K.-J., Fröba, M. & Palmer, R. E. Hybrid atomic structure of the Schmid cluster $\text{Au}_{55}(\text{PPh}_3)_{12}\text{Cl}_6$ resolved by aberration-corrected STEM. *Nanoscale* **7**, 885–888 (2015).
65. Templeton, A. C., Wuelfing, W. P. & Murray, R. W. Monolayer-protected cluster molecules. *Acc. Chem. Res.* **33**, 27–36 (2000).
66. Hostetler, M. J., Zhong, C., Yen, B. K. H., Andereg, J., Gross, S. M., Evans, N. D., Porter, M. & Murray, R. W. Stable, Monolayer-Protected Metal Alloy Clusters. *J. Am. Chem. Soc.* **120**, 9396–9397 (1998).
67. Hakkinen, H., Walter, M. & Gronbeck, H. Divide and Protect Capping Gold Nanoclusters with Molecular Gold - Thiolate Rings. *J. Phys. Chem. B* **110**, 9927–9931 (2006).
68. Jadzinsky, P. D., Calero, G., Ackerson, C. J., Bushnell, D. a & Kornberg, R. D. Structure of a thiol monolayer-protected gold nanoparticle at 1.1 Å resolution. *Science* **318**, 430–3 (2007).
69. Yang, H., Wang, Y., Huang, H., Gell, L., Lehtovaara, L., Malola, S., Hakkinen, H. & Zheng, N. All-thiol-stabilized Ag_{44} and $\text{Au}_{12}\text{Ag}_{32}$ nanoparticles with

- single-crystal structures. *Nat. Commun.* **4**, 1–8 (2013).
70. Zeng, C., Liu, C., Chen, Y., Rosi, N. L. & Jin, R. Gold-thiolate ring as a protecting motif in the Au₂₀(SR)₁₆ nanocluster and implications. *J. Am. Chem. Soc.* **136**, 11922–11925 (2014).
71. Harkness, K. M., Tang, Y., Dass, A., Pan, J., Kothalawala, N., Reddy, V. J., Cliffel, D. E., Demeler, B., Stellacci, R., Bakr, O. M. & Mclean, J. A. Ag₄₄(SR)₃₀⁴⁻: a silver-thiolate superatom complex. *Nanoscale* **4**, 4269–74 (2012).
72. Li, Y., Galli, G. & Gygi, F. Electronic structure of thiolate-covered gold nanoparticles: Au₁₀₂(MBA)₄₄. *ACS Nano* **2**, 1896–1902 (2008).
73. Zeng, C., Chen, Y., Li, G. & Jin, R. Synthesis of a Au₄₄(SR)₂₈ nanocluster: structure prediction and evolution from Au₂₈(SR)₂₀, Au₃₆(SR)₂₄ to Au₄₄(SR)₂₈. *Chem. Commun. (Camb)*. **50**, 55–7 (2014).
74. Xu, Q., Kumar, S., Jin, S., Qian, H., Zhu, M. & Jin, R. Chiral 38-gold-atom nanoclusters: synthesis and chiroptical properties. *Small* **10**, 1008–14 (2014).
75. Pei, Y., Lin, S., Su, J. & Liu, C. The Structure Prediction of Au₄₄(SR)₂₈: A Chiral Superatom Cluster The Structure Prediction of Au₄₄(SR)₂₈: A Chiral Superatom Cluster. **44**, (2013).
76. Pei, Y., Lin, S., Su, J. & Liu, C. The Structure Prediction of Au₄₄(SR)₂₈: A Chiral Superatom Cluster. *J. Am. Chem. Soc.* **44**, (2013).
77. Das, A., Liu, C., Zeng, C., Li, G., Li, T. Rosi, N. L. & Jin, R. Cyclopentanethiolato-protected Au₃₆(SC₅H₉)₂₄ nanocluster: Crystal structure and implications for the steric and electronic effects of ligand. *J. Phys. Chem. A* **118**, 8264–8269 (2014).
78. Zeng, C., Chen, Y., Li, G. & Jin, R. Magic Size Au₆₄(Sc-C₆H₁₁)₃₂ Nanocluster

- Protected by Cyclohexanethiolate. *Chem. Mater.* **64**, (2014).
79. Malola, S., Lehtovaara, L., Knoppe, S., Hu, K., Palmer, R. E., Burgi, T. & Hakkinen, H. Au₄₀(SR)₂₄ Cluster as a Chiral Dimer of 8-Electron Superatoms: Structure and Optical Properties. *J. Am. Chem. Soc.* **40**, 8–11 (2012).
80. Yang, H., Wang, Y., Huang, H., Gell, L., Lehtovaara, L., Malola, S., Hakkinen, H. & Zheng, N. All-thiol-stabilized Ag₄₄ and Au₁₂Ag₃₂ nanoparticles with single-crystal structures. *Nat Commun* **4**, (2013).
81. Das, A., Li, T., Nobusada, K., Zeng, C., Rosi, N. L. & Jin, R. Crystal structure and electronic properties of a thiolate-protected Au₂₄ nanocluster. *Nanoscale* **6**, 6458–62 (2014).
82. Han, Y. K., Kim, H., Jung, J. & Choi, Y. C. Understanding the magic nature of ligand-protected gold nanoparticle Au₁₀₂(MBA)₄₄. *J. Phys. Chem. C* **114**, 7548–7552 (2010).
83. Das, A., Liu, C., Byen, H. Y., Nobusada, K., Zhao, S., Rosi, Nathaniel, R. & Jin, R. Structure Determination of [Au₁₈(SR)₁₄]. *Angew. Chemie* **54**, 3140–3143 (2015).
84. Kumara, C., Aikens, C. M. & Dass, A. X-ray Crystal Structure and Theoretical Analysis of Au_{25-x}Ag_x(SCH₂CH₂Ph)₁₈⁻ Alloy. *J. Phys. Chem. Lett.* **5**, 461–466 (2014).
85. Dass, A., Theivendran, S., Nimmala, P. R., Kumara, C., Jupally, V. R., Fortunelli, A., Sementa, L., Barcaro, G., Zuo, X. & Noll, B. C. Au₁₃₃(SPh-tBu)₅₂ Nanomolecules: X-ray Crystallography, Optical, Electrochemical, and Theoretical Analysis. *J. Am. Chem. Soc.* **137**, 4610–4613 (2015).
86. Qian, H. & Jin, R. Ambient synthesis of Au₁₄₄(SR)₆₀ nanoclusters in methanol.

- Chem. Mater.* **144**, 2209–2217 (2011).
87. Koivisto, J., Salorinne, K., Mustalahti, S., Lahtinen, T., Malola, S., Hakkinen, H. & Pettersson, M. Vibrational Perturbations and Ligand–Layer Coupling in a Single Crystal of Au₁₄₄(SC₂H₄Ph)₆₀ Nanocluster. *J. Phys. Chem. Lett.* **144**, 1–6 (2014).
 88. Li, Z. Y., Young, N. P., Di Vece, M., Palomba, S., Palmer, R. E., Bleloch, A. L., Curley, B. C., Johnston, R. L., Jiang, J. & Yuan, J. Three-dimensional atomic-scale structure of size-selected gold nanoclusters. *Nature* **451**, 46–8 (2008).
 89. Wang, Z. W. & Palmer, R. E. Determination of the ground-state atomic structures of size-selected Au nanoclusters by electron-beam-induced transformation. *Phys. Rev. Lett.* **108**, 245502 (2012).
 90. Emmrich, M., Huber, F., Pielmeier, F., Welker, J., Hofmann, T., Schneiderbauer, M., Meuer, D., Polesya, S., Mankovsky, S., Kodderitzsch, D., Ebert, H. & Giessibl, F. J. Subatomic resolution force microscopy reveals internal structure and adsorption sites of small iron clusters. *Science* **348**, 308–311 (2015).
 91. Reinhard, D., Hall, B. D., Ugarte, D. & Monot, R. Size-independent fcc-to-icosahedral structural transition in unsupported silver clusters: An electron diffraction study of clusters produced by inert-gas aggregation. *Phys. Rev. B* **55**, 7868–7881 (1997).
 92. Zeng, C., Qian, H., Li, T., Li, G., Rosi, N. L., Yoon, B., Barnett, R. N., Whetten, R. L., Landman, U. & Jin, R. Total Structure and Electronic Properties of the Gold Nanocrystal Au₃₆(SR)₂₄. *Angew. Chemie* **124**, 13291–13295 (2012).
 93. Zeng, C., Li, T., Das, A., Rosi, N. & Jin, R. Chiral structure of thiolate-protected 28-gold-atom nanocluster determined by X-ray crystallography. *J. Am. Soc.* **135**, 10011–10013 (2013).

94. Qian, H. & Eckenhoff, W. Total structure determination of thiolate-protected Au₃₈ nanoparticles. *J. Am. Chem. Soc.* **25**, 8280–8281 (2010).
95. Zhu, M. & Aikens, C. Correlating the crystal structure of a thiol-protected Au₂₅ cluster and optical properties. *J. Am. Chem. Soc.* **130**, 5883–5885 (2008).
96. G.Binnig and H.Rohrer. Scanning Tunneling Microscopy. *Surf. Sci.* **126**, 236–244 (1983).
97. Crewe, A. V. & Wall, J. A scanning microscope with 5 Å resolution. *J. Mol. Biol.* **48**, (1970).
98. Dellby, N., Krivanek, O. L., Nellist, P. D., Batson, P. E. & Lupini, A. R. Progress in aberration-corrected scanning transmission electron microscopy. *Reprod. Syst. Sex. Disord.* **50**, 177–185 (2001).
99. Hirata, A., Fujita, T., Wen, Y. R., Schneibel, J. H., Liu, C. T. & Chen, M. W. Atomic structure of nanoclusters in oxide-dispersion-strengthened steels. *Nat. Mater.* **10**, 922–926 (2011).
100. Langlois, C., Wang, Z. W., Pearmain, D., Ricolleau, C. & Li, Z. Y. HAADF-STEM imaging of CuAg core-shell nanoparticles. *J. Phys. Conf. Ser.* **241**, 012043 (2010).
101. Midgley, P. A., Weyland, M., Thomas, J. M. & Johnson, B. F. G. Z-Contrast tomography: a technique in three-dimensional nanostructural analysis based on Rutherford scattering. *Chem. Commun.* 907–908 (2001). doi:10.1039/b101819c
102. Dahmen, U., Erni, R., Radmilovic, V., Kisielowski, C., Rossell, M. & Denes, P. Background, status and future of the Transmission Electron Aberration-corrected Microscope project. *Phil. Trans. A* **367**, 3795–3808 (2009).
103. Egerton, R. F., Li, P. & Malac, M. Radiation damage in the TEM and SEM. in

- Micron* **35**, 399–409 (2004).
104. Garvie, L. & Buseck, P. Determination of $\text{Ce}^{4+}/\text{Ce}^{3+}$ in electron-beam-damaged CeO_2 by electron energy-loss spectroscopy. *J. Phys. Chem. Solids* **60**, 1943–1947 (1999).
 105. Pan, Y., Brown, A., Brydson, R., Warley, A., Li, A. & Powell, J. Electron beam damage studies of synthetic 6-line ferrihydrite and ferritin molecule cores within a human liver biopsy. *Micron* **37**, 403–411 (2006).
 106. Wang, Z. W. & Palmer, R. E. Direct atomic imaging and dynamical fluctuations of the tetrahedral Au(20) cluster. *Nanoscale* **4**, 4947–9 (2012).
 107. Wang, Z. W., Toikkanen, O., Quinn, B. M. & Palmer, R. E. Real-space observation of prolate monolayer-protected Au₃₈ clusters using aberration-corrected scanning transmission electron microscopy. *Small* **7**, 1542–1545 (2011).
 108. Han, Y., He, D. S., Liu, Y., Xie, S. Tsukuda, T. and Li, Z. Y. Size and shape of nanoclusters: Single-shot imaging approach. *Small* **8**, 2361–2364 (2012).
 109. Wang, Z. W. & Palmer, R. E. Experimental evidence for fluctuating, chiral-type Au₅₅ clusters by direct atomic imaging. *Nano Lett.* **12**, 5510–5514 (2012).
 110. Li, H., Li, L., Pedersen, A. & Gao, Y. Magic-Number Gold Nanoclusters with Diameters from 1 to 3.5 nm: Relative Stability and Catalytic Activity for CO Oxidation. *Nano Lett.* **15**, 682–688 (2014).
 111. Turkevich, J., Stevenson, P. C. & Hillier, J. A Study of the Nucleation and Growth Processes in the Synthesis of Colloidal Gold. *Discuss. Faraday Soc.* **11**, 55–75 (1951).
 112. Yang, J.C., Singhal, A., Bradley, S. & Gibson, J.M. A Novel Stem-Based Mass Spectroscopic Technique: Applications to Catalytic Materials. *MRS Proc.* **466**,

- 227 (1996).
113. Young, N. P., Li, Z. Y., Chen, Y., Palomba, S., Di Vece, M. & Palmer, R. E. Weighing supported nanoparticles: Size-selected clusters as mass standards in nanometrology. *Phys. Rev. Lett.* **101**, 246103 (2008).
 114. Wang, Z. W. & Palmer, R. E. Intensity calibration and atomic imaging of size-selected Au and Pd clusters in aberration-corrected HAADF-STEM. *J. Phys. Conf. Ser.* **371**, 012010 (2012).
 115. Wang, Z. W. Toikkanen, O., Yin, F., Li, Z. Y., Quinn, B. M. & Palmer, R. E. Counting the atoms in supported, monolayer-protected gold clusters. *J. Am. Chem. Soc.* **132**, 2854–2855 (2010).
 116. Francis, C. *What mad pursuit.* (Basic Books, 1988). doi:10.1016/S1359-1789(02)00068-X
 117. Van Aert, S., Batenburg, K. J., Rossell, M. D., Erni, R. & Van Tendeloo, G. Three-dimensional atomic imaging of crystalline nanoparticles. *Nature* **470**, 374–377 (2011).
 118. May, C. A., Crady, J. K., Laue, T. M., Poli, M., Arosio, P. & Chasteen, N. D. The sedimentation properties of ferritins. New insights and analysis of methods of nanoparticle preparation. *Biochim. Biophys. Acta - Gen. Subj.* **1800**, 858–870 (2010).
 119. Wang, Z. Transmission electron microscopy of shape-controlled nanocrystals and their assemblies. *J. Phys. Chem. B* **104**, 1153–1175 (2000).
 120. Kimoto, K. & Nishida, I. Crystal habit and crystal structure of fine chromium particles: an electron microscope and electron diffraction study of fine metallic particles prepared by evaporation in argon at low pressures (III). *Thin Solid Films* **23**, 179–189 (1974).

121. Azubel, M. Koivisto, J., Malola, S., Bushnell, D., Hura, G. L., Koh, A. L., Tsunoyama, H., Tsukuda, T., Pettersson, M., Hakkinen, H. & Kornberg, R. D. Electron microscopy of gold nanoparticles at atomic resolution. *Science* (80-.). **345**, 909–912 (2014).
122. Komoda, T. Study on the Structure of Evaporated Gold Particles by Means of a High Resolution Electron Microscope. *Jpn. J. Appl. Phys.* **7**, 27–30 (1968).
123. Barnard, A. S., Young, N. P., Kirkland, A. I., Van Huis, M. A. & Xu, H. Nanogold: A quantitative phase map. *ACS Nano* **3**, 1431–1436 (2009).
124. Chen, C.-C., Zhu, C., White, E. R., Chiu, C.-Y., Scott, M. C., Regan, B. C., Marks, L. D., Huang, Y. & Miao, J. Three-dimensional imaging of dislocations in a nanoparticle at atomic resolution. *Nature* **496**, 74–7 (2013).
125. Williams, D. B. & Carter, C. B. *Transmission Electron Microscopy—A Textbook for Materials Science*. Micron (Springer, 2008).
126. Ekardt, W. Dynamical polarizability of small metal particles: Self-consistent spherical jellium background model. *Phys. Rev. Lett.* **52**, 1925–1928 (1984).
127. Seidl, M. & Brack, M. Liquid drop model for charged spherical metal clusters. *Ann. Phys. (N. Y.)* **245**, 275–310 (1996).
128. Garzón, I., Michaelian, K., Beltran, M. R., Posada-Amarillas, A., Ordejon, R., Artacho, E., Sanchez-Portal, D. & Soler, J. M. Lowest Energy Structures of Gold Nanoclusters. *Phys. Rev. Lett.* **81**, 1600–1603 (1998).
129. Koga, K., Ikeshoji, T. & Sugawara, K. I. Size- and Temperature-Dependent Structural Transitions in Gold Nanoparticles. *Phys. Rev. Lett.* **92**, 115507–1 (2004).

CHAPTER 2

EXPERIMENTAL METHODS

2.1 Scanning transmission electron microscopy

2.1.1 A brief history of electron microscopy

It was a momentous time when the first electron was transmitted through a sample in the first electron microscope designed and built by Dr. Ernst Ruska and Dr. Max Knoll in late 1933.¹ From that time, the human being's observation ability marched to the nanoscale world.

The principle of electron microscopy can date back to 1924, when Louis de Broglie introduced his theory of the matter wave in his famous PhD thesis, "Research on the theory of the quanta".² In this new theory, all small particles, not only photons, can have wave-particle duality. So, the wavelength of the electron beam can be described as:

$$\lambda = \frac{h}{p} = \frac{h}{[2m_0eV(1 + \frac{eV}{2m_0c^2})]^{1/2}} \quad 2.1$$

where h is the Plank constant, m_e is the rest mass of the electron, V is the acceleration voltage applied to the electron, e is the charge of the electron and c is the speed of light. Note that relativistic effects must be considered because the velocity of the accelerated electron in the TEM can be very high (electrons accelerated by 200 kV

can be faster than the half of the speed of light!). The mass of the electron is much larger than that of the photon, therefore accelerated electrons can have a much smaller wavelength than light. As the resolution of a microscope is limited by its probe wavelength, hence, it shows the great potential of the electron microscope to resolve the features in a much lower scale than the normal visible light microscope.

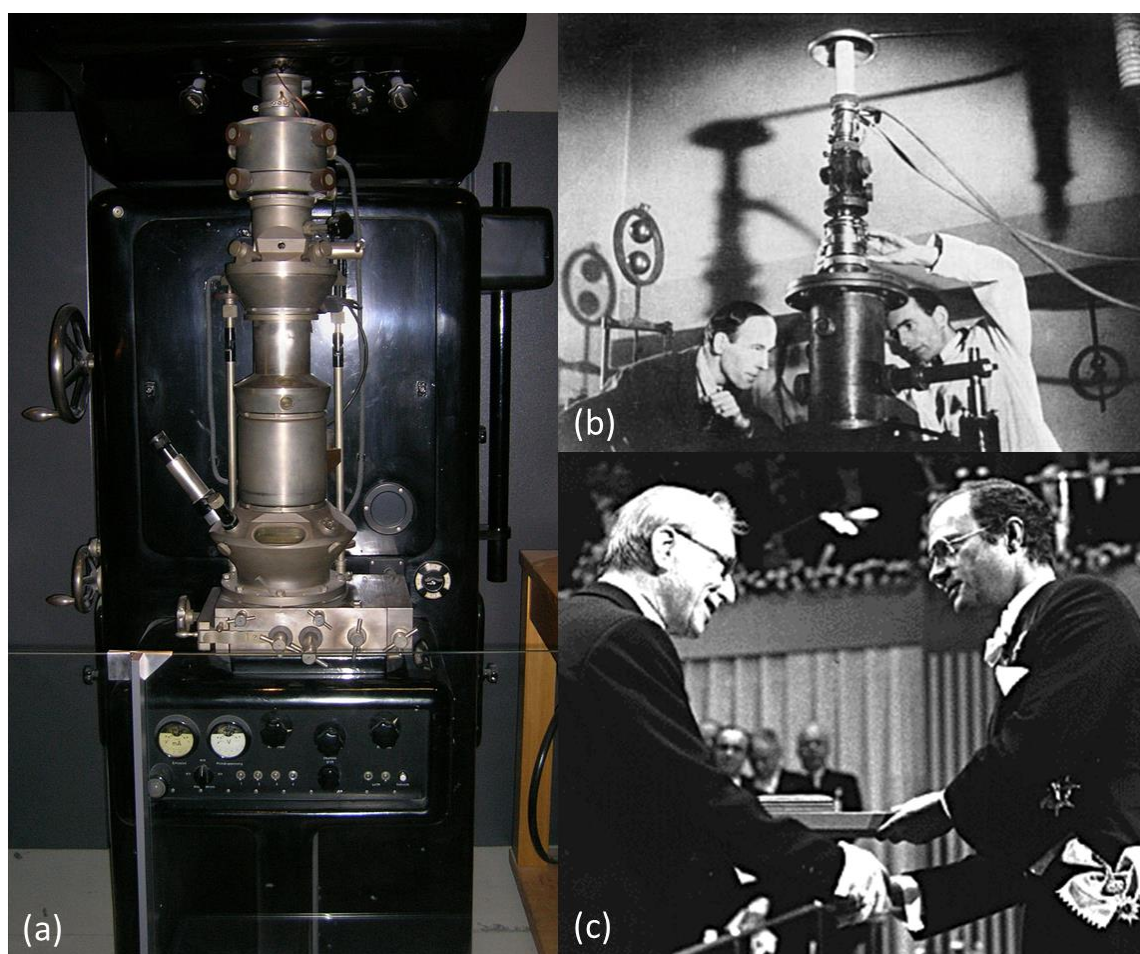


Figure 2.1 (a) The first electron microscope built by Ernst Ruska (Stored in Deutsches Museum, Munich, Germany).³ (b) Ernst Ruska and Max Knoll with the electron microscope they built.⁴ (c) Ernst Ruska received the Nobel Prize in Physics for his contribution in developing the electron microscope in 1986.⁵

In 1927, Hans Busch first demonstrated how to focus the electron beam by a magnetic

electron lens, which is the foundation of the electron microscope.⁶ In 1933 the first complete electron microscope with a magnification of 12,000 times was built by Ernst Ruska and Max Knoll.^{1,5,7} It is very interesting, that at first, Ernst Ruska was unaware of Louis De Broglie's new theory, but he soon realized the electrons in his new instrument would have a much smaller wavelength than light, and would be capable of achieving angstrom scale resolution. Two years later, in 1935, the first scanning electron microscopy image was published by Knoll.⁸ Manfred von Ardenne designed and built the first STEM in 1937. He realized that the transmitted electrons could be directly detected to form the image rather than refocused to form the image, avoiding the chromatic aberration of the lens.^{9,10} However, because of the limitation on the brightness of the electron source and the spherical aberration of the electron lens, the resolution of the first generation STEM showed no advantage compared with the conventional TEM.⁹

The next significant development of the STEM was nearly 30 years later, when Albert Crewe equipped his STEM with a field emission electron gun (FEG) to solve the low brightness problem. In 1970, Crewe et al. reported the visualization of single heavy atoms on thin carbon film by the new STEM equipped with a cold field emission electron source and an annular dark field (ADF) detector.^{11,12} The newly developed instrument gave them a resolution of 0.5 nm.¹¹ They suggested that the annular detector can be utilized to collect most of the elastically scattered electrons and form a high contrast image, while the inelastically scattered electrons and unaffected

electrons that pass through the hole of the annular detector can be separated and analyzed by an energy analysis spectrum.^{11,12}

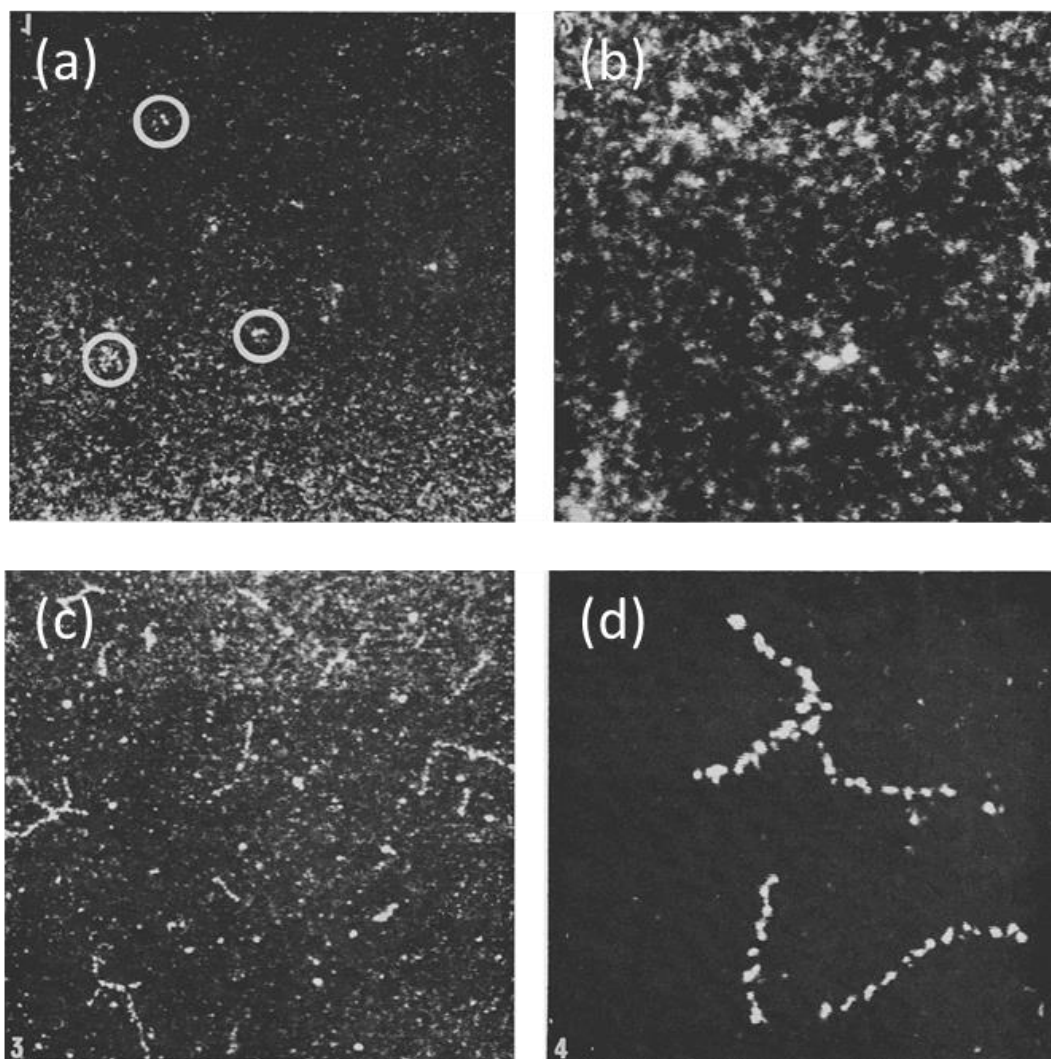


Figure 2.2. The first STEM image that observed single atoms. The new technique was demonstrated by the ADF-STEM images of pairs of single U atoms in: (a) low magnification, and (b) high magnification, with the Th long chain in (c) at low magnification and (d) high magnification.¹² The figure is from ref[12].

With the brightness issue having been solved by usage of the field emission electron gun, the aberration of the electron lens became the most significant limitation of the

instrument. Since the development of the first electron microscope, the aberration of the electron lens was considered to be a limit on the resolution. In Otto Schezer's famous 1936 paper he demonstrated that the spherical aberration is positive for round electron lenses and that it is impossible to completely eliminate.¹³ Many scientists were inspired to find a way to solve this problem. However, despite some brilliant physicists proposing elegant ideas on the aberration correction, such as high-frequency lens, using space charge or foil lens to correct the spherical aberration, round electron lens and mirror or the idea of the multipole system correctors, all aberration correction projects were essentially unsuccessful until the 1990's due to the complication of the system and the absence of a high performance operation and diagnostic system.¹⁴⁻²² The breakthrough in aberration correction was finally made in the 1990's by two different groups, Haider et al. developed the first capable sextupoles type corrector for the TEM,²³⁻²⁵ while Krivanek et al. worked out the first successful quadrupole-octopole type correction for the STEM.²⁶⁻²⁸

With the scientists' more than a half century endeavor, the resolution of the electron microscope finally achieved the sub-angstrom scale seen today. Currently, it is reported that the best resolution is as low as 0.35 angstrom and is achieved by a Hitachi HF3300v STEM equipped with a 300kV cold field emission gun and a spherical&chromatic aberration corrector.²⁹ The scanning transmission electron microscope equipped with a field emission electron source and cs-corrector is becoming a sort of "standard configuration" and is being distributed throughout

laboratories in the world to improve the studies in the areas of physics, chemistry, material science etc.

2.1.2 Overview of the STEM

All electron microscopy work contained in this thesis were carried out using a JEOL JEM2100F STEM in our group. The general schematic of how the STEM works is shown in Figure 2.3. Electron beam, the media between the sample and the microscopy image, was generated by a Schottky field emission electron source. The electrons from the electron source tip are extracted by the first anode in the electron source, then accelerated by the second anode. The acceleration voltage applied is 200kV. The details of the electron source will be discussed in section 2.1.3.

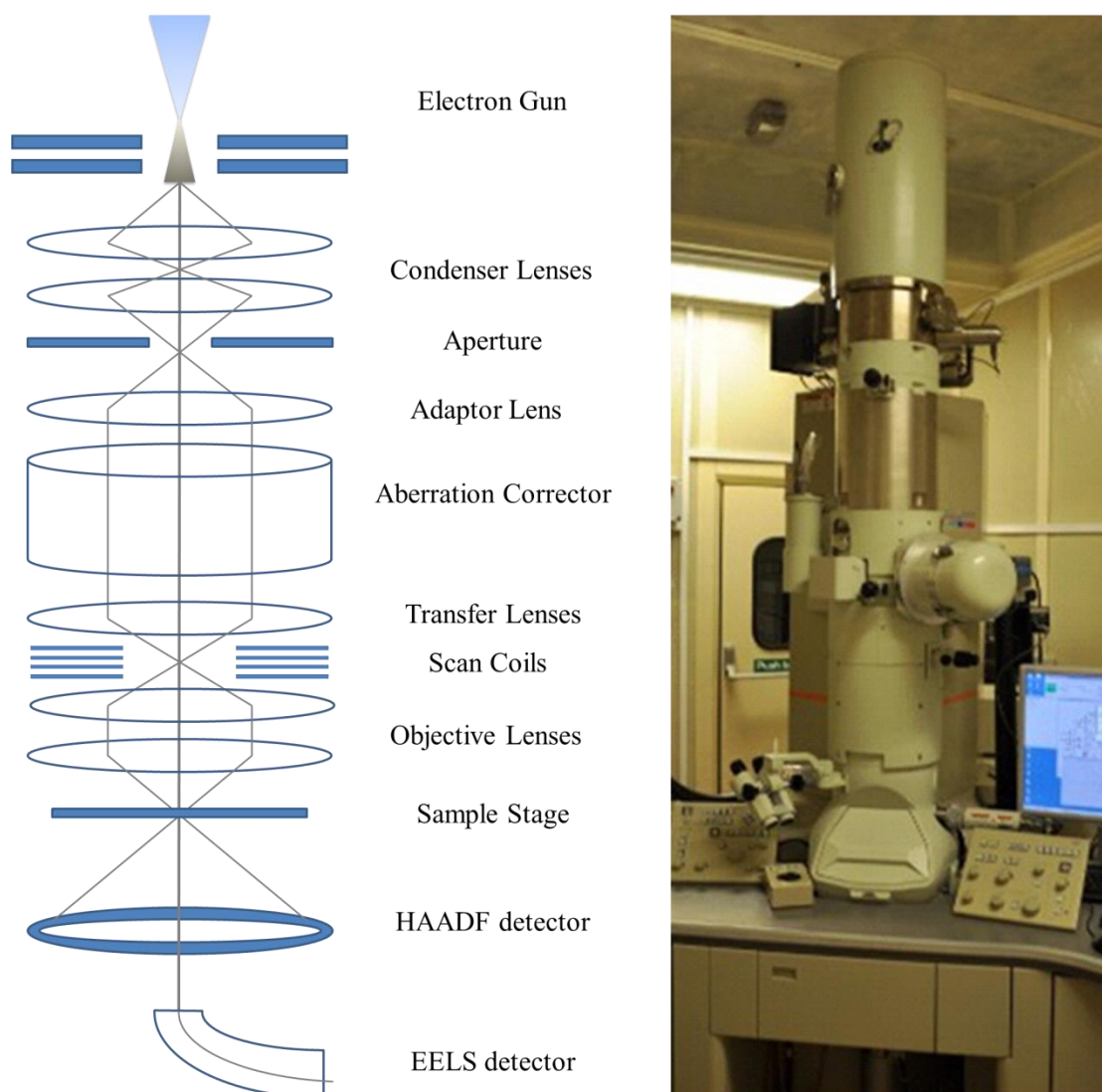


Figure 2.3 A schematic of the aberration corrected STEM and the picture of the JEM 2100F STEM we used in our lab.

After the generation, the accelerated electron beam is adjusted and focused by the condenser lenses. An aperture is inserted to remove the wider scattered electrons. The size is chosen by the compromise between the beam intensity and beam quality. After aperture, the electron beam passes through the CEOS cs-corrector which can compensate for most of the spherical aberration of the electron beam. Then the spherical aberration corrected electron beam is formed to be an electron probe by the

objective lens. The electron probe is controlled by the scan coil to scan over the selected region of the sample. In our STEM, the size of the electron probe can be achieved to 0.1nm and the beam current is around 30pA. Below the sample, the high angle annular dark field (HAADF), bright field (BF) and electron energy loss detectors are positioned to collect different electron signal. On the contrary, an energy dispersive X-ray (EDX) detector is placed above the sample to collect the characteristic X-ray emitted from the sample.

2.1.3 Electron source

A bright and reliable electron source is of great importance to the TEM. There are two major types of electron sources: the thermionic emission electron source and the field emission electron source. There is also another type, called the Schottky source, which combines both thermionic and field emission features.⁴

If the free electrons of a material are given energy which is greater than the material's work function, then the electrons will escape from the surface of the material to the outside. A thermionic emission electron source uses this idea by heating the material to a reasonably high temperature to give the electrons a high thermal energy to overcome the energy barrier of the material.⁴ Through the Richardson's law, we can have a better understanding of the thermionic emission³⁰:

$$J = AT^2 e^{-\frac{W}{kT}} \quad (2.2)$$

Here, J is the emission current density, A is the Richardson's constant which is dependent on the electron source materials, T is the temperature of the material, W is

the work function of the material and k is Boltzmann's constant. Through this equation, we can see that if we want high emission current density, we must heat the material to a high temperature in order to give the electrons enough thermal energy. However, this requires that the materials have special properties, either the material must have a very high melting point or a reasonably low work function. There are not many materials available that meet these requirements, the only common material used in the thermionic electron sources are Tungsten and LaB_6 .⁴

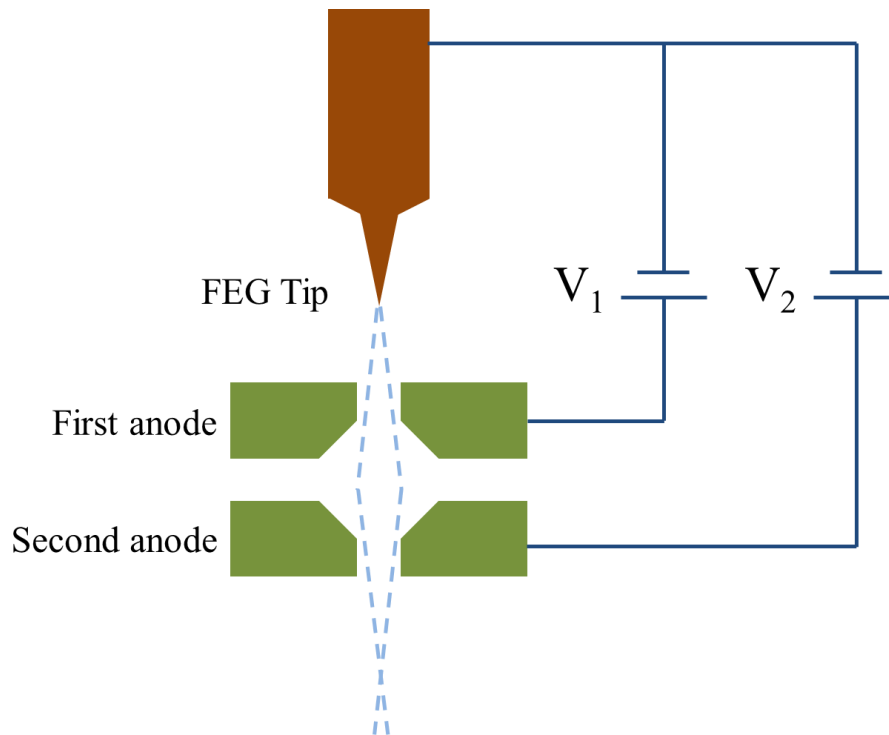


Figure 2.4 Schematic of a field emission electron source.

Unlike the thermionic source, the field emission electron source uses an electronic field to extract the electrons from the source materials. If a voltage, V is applied to a round point with a radius of r , then we can find the electron field,

$$E = \frac{V}{r} \quad (2.3)$$

Hence, through using a super small needle tip, a very large electron field is generated to lower the work function of the tip material, the electrons can then be emitted from the tip due to the tunneling effect. There are two anodes below the small needle tip. The first anode always has several kV applied to “extract” the electron from the tip material, While a much higher voltage is applied to the second anode to accelerate the electrons to form a high energy electron beam.^{4,31}

When field emission occurs at room temperature, the electron source is called a cold field emission electron source. However, the cold field emission electron source requires a very smooth surface which needs an ultra-high vacuum ($<10^{-9}$ Pa) environment.^{4,31} If the tip material is heated to a higher temperature, the thermal energy will enhance the electron emission, and a lower vacuum condition ($<10^{-6}$ Pa) is required. This type of electron source is called the Schottky field emission electron source.³² The Schottky field emission electron source is more reliable as it requires a lower vacuum (compared with the cold field emission source) but still maintains a reasonably high performance in brightness and electron energy dispersion (compared with the thermionic emission source). It is now the most popular electron source used in the electron microscope^{4,33}

2.1.4 Magnetic electron lenses

To converge or diverge the electron beam on electron microscope, electron lenses must be used. A schematic of the magnetic electron lens is shown in Figure 2.5.⁴

There are two major parts in a magnetic electron lens. The first is a current that passes through a copper wire coil, which forms the magnetic field. The second is soft iron core inside the copper coil called a pole piece. Normally there are two pole pieces (one is up and one is down), with holes in the pole pieces called bores. The distance between the upper and lower pole pieces is called the gap. The ratio between bore and gap decides the magnetic lens's ability for convergence of the electron beam. The pole piece's function is to form and strengthen the magnetic field in a relatively small range, which is helpful in focusing the electron beam. In general, the magnetic electron lens will form an inhomogeneous magnetic field which is symmetric to the axis. A water cooling system is normally applied in the magnetic electron lens due to the resistant heat from the copper wire.⁴

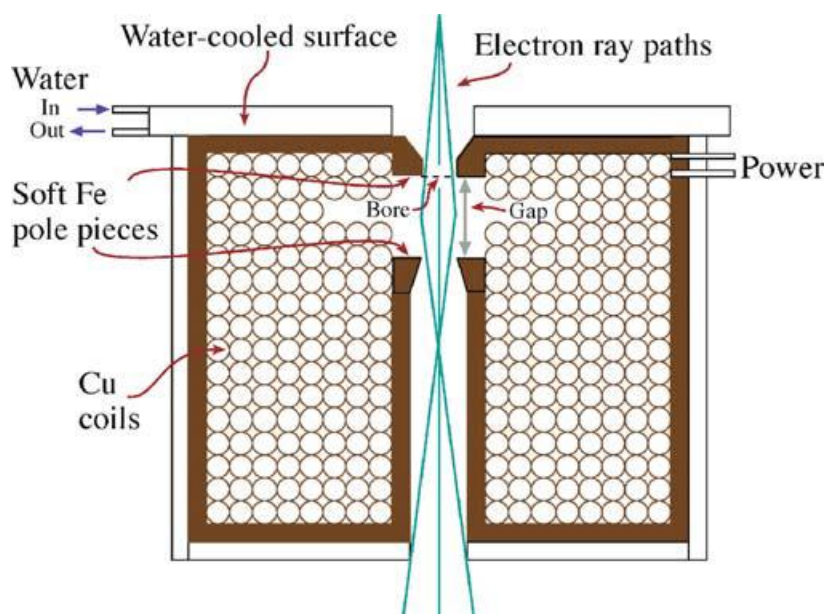


Figure 2.5 Schematic of a magnetic electron lens.⁴ The figure is from ref[4].

A schematic of the workings of a magnetic electron lens is shown in Figure 2.5. When the electron beam passes through the magnetic lens, the electrons will experience the Lorentz force, F due to the magnetic field, B from the lens and the electron's velocity,

v. To make the description clear, we will divide the magnetic field and velocity into two direction components: the axis directions, B_z and v_z and the radial directions, B_r and v_r . In the upper part of the magnetic field in the electron lens, the radial velocity, v_r will experience a Lorentz force due to the axial magnetic field, B_z , whose direction is into the paper. The Lorentz force produced by the axial velocity, v_z and radial magnetic field, B_r has the same direction. So a tangential velocity from the axial rotation, v_t is formed. Then the v_t will cause a Lorentz force, F_c with a direction to the axis, in which the electron beam will converge. When the electron goes into the lower part of the magnetic field, the tangential velocity will decrease due to the different direction of the velocity and the magnetic field, while the direction will remain the same. So, the direction of F_c will also not be changed and keeps converging the electron beam until the magnetic field is weak enough due to the long distance from the lens.⁴

2.1.5 Aberration and aberration correction

If we only count the influence of the electron's wavelength, the maximum spatial resolution of a 200kV STEM can be as high as 0.003 nm. This is much higher than the resolution of the most advanced STEM in the world (0.035 nm, as we mentioned above). The reason for the gap between these two resolutions is the difference between the perfect lens and the realistic electron lens, which is called optical aberration.

There are two major types of aberration: chromatic and monochromatic. For an optical (light) lens, chromatic aberration occurs because the refractive index of the lens varies for different colour of light (wavelength of the electromagnetic wave). In the electron microscope, chromatic aberration is due to the convergence ability of the magnetic electron lens differing for electrons with different energy (wavelength of the mass wave). In our STEM, FEG electron source has a very small energy spread, which reduces the effect of chromatic aberration. Additionally, the STEM mode does not need the image forming lens, so the enhanced energy spread due to the electron energy loss will not affect the STEM image as it does on the TEM.

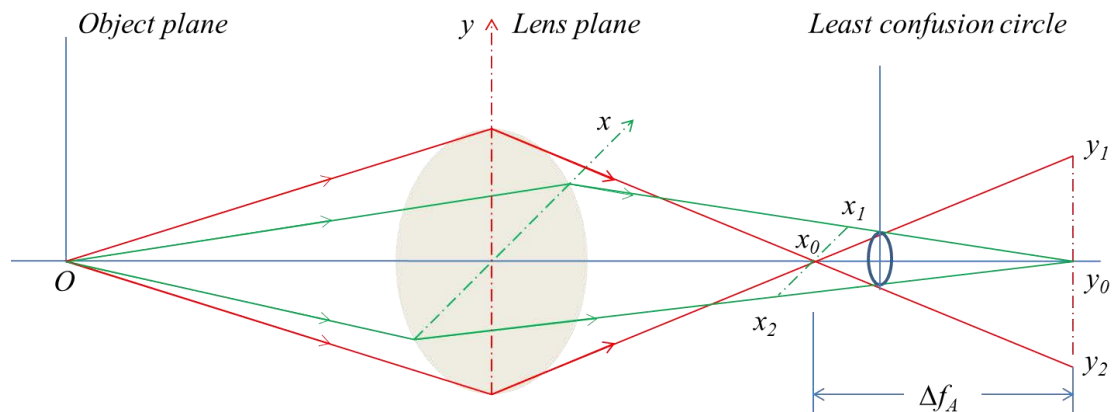


Figure 2.6 The schematic of the astigmatism of the lens.

The other type of aberration is called monochromatic aberration, which includes several species: most importantly astigmatism and spherical aberration. The astigmatism aberration is due to the lens having a different convergence ability for different directions. In the electron microscope, astigmatism is mainly due to the magnetic field being asymmetric to the axis in the magnetic electron lens. This

asymmetric magnetic field can result from the imperfect production of the soft-iron pole piece, the inhomogeneity of the material, the un-centred apertures and even the contamination in the STEM.⁴ A schematic describing astigmatism has been shown in Figure 2.6. In Figure 2.6, we can see that in the y-direction, the convergent ability is stronger than in the x-direction. The electron beam from O in the direction y is focused in the line $x_1 x_2$, while in the direction x, it is focused in the line $y_1 y_2$. Hence, no matter how we change the focusing condition, we cannot focus the image in both x and y directions. There will always be an astigmatism focus difference, Δf_A between x_0 and y_0 . However, there is a point between x_0 and y_0 where the electrons from different directions have the same defocus, which we call the circle of least confusion.

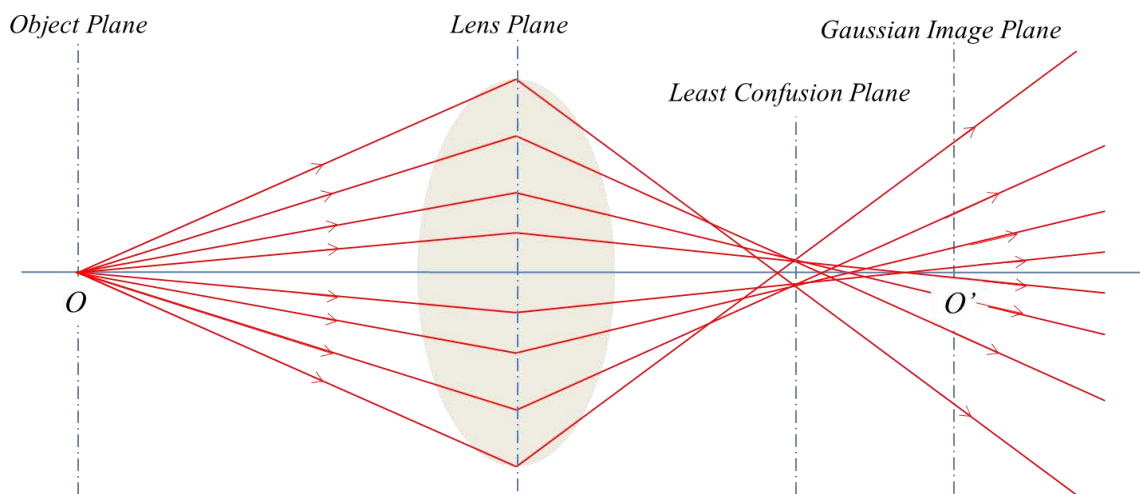


Figure 2.7. Schematic of the magnetic electron lens's positive spherical aberration.

When the convergent ability of a lens is dependent on the distance from the centre of the lens, it is called spherical aberration.^{18,22,28} In the magnetic electron lens, the magnetic field strength is different dependent on the distance to the optical axis, the outside of the lens always has stronger convergent ability than the near-centre part. So

the incident electron beam from one point will be focused on different points on the axis, the focus point of the off-axis incident ray will be closer to the lens, while the near-axis ray will be further away from the lens. This spherical aberration is called “positive spherical aberration”. So, a point object, “O” before the lens will form a circle image with a limited diameter. There is always a plane that can be found where the circle’s diameter will be the smallest, this is called the plane of least confusion plane. In practical STEM operation, the plane of least confusion is often picked as the “focus point”. A schematic of the spherical aberration is shown in Figure 2.7.

For a STEM equipped with a field emission electron source, the main limitation to the resolution is spherical aberration. Therefore, a spherical aberration correction is required to improve the performance of the STEM. As mentioned above, all the ordinary round electron magnetic lenses have “positive” spherical aberration. The principle of a spherical aberration corrector is to form a lens with “negative” spherical aberration to compensate for the positive spherical aberration of the other lens. There are two types of spherical aberration correction systems, both with different configurations of multipole lens: one is the quadrupole-octupole based system, and the other is the hexapole based system.^{22–24,26,28} The CEOS corrector used in our JEOL 2100F is a hexapole based system. Here, the hexapole magnetic lens system will be described. A schematic of the hexapole magnetic lens is shown in Figure 2.8 (a). When electrons move down into the plane of the paper, they experience the Lorentz force, $F = eqv$ with a direction parallel to the plane of the paper. All the electrons, that

along the same line which is parallel to the plane of the paper and across the axis of the hexapole lens, will experience the Lorentz force in the same direction due to the hexapole lens, and will be deflected. The power of the Lorentz force is dependent on the distance between the electron and the central axis of the hexapole. The closer the electron is to the central axis, the weaker the Lorentz force will be. If we introduce the depth of the lens, it will be a little different. When the electrons go through the hexapole lens, those that positioned in the side which the Lorentz force point to will be more deflected compared to the electrons in the other side. The effect of this is that the hexapole lens will diverge the electron beam; the further the beam is from the axis, the stronger the beam divergence will be. Through this hexapole structure a lens with “negative” spherical aberration is formed, which is required to compensate the “positive” spherical aberration of the magnetic electron lens.

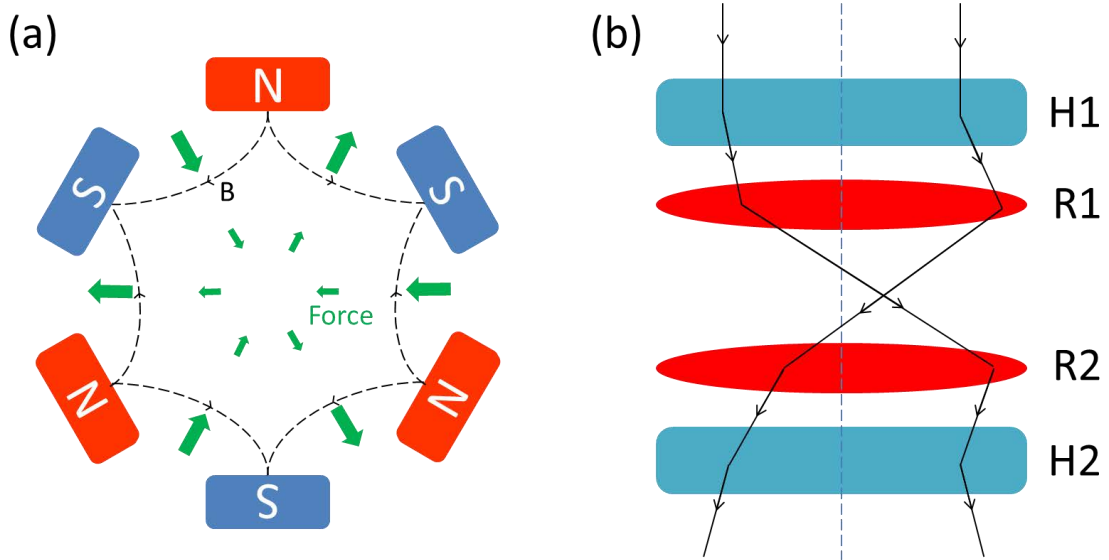


Figure 2.8. The schematic of: (a) the hexapole magnetic electron lens, and (b) the double hexapole lens system.

However, the hexapole lens will form three-fold astigmatism due to the hexapole

structure. To solve this problem, a double hexapole system was developed by combining two hexapole magnetic lenses to offset the three-fold astigmatism. The schematic of a double hexapole system is shown in Figure 2.8 (b). When the parallel electrons go through the first hexapole magnetic lens, H1, they will be diverged with a three-fold astigmatism. The electrons will then pass through a doublet of round lenses R1 and R2 with a magnification of -1 to make a point inversion of the electron beam. Next, the inversed electrons go through the second hexapole lens, H2. The electrons will experience another divergence with an inverse three-fold distortion. So the electrons will be diverged further while the inverse three-fold distortion will compensate for the previous three-fold distortion. So a double hexapole lens system can perform as a lens with negative spherical aberration to correct the positive spherical aberration, and without the three-fold astigmatism which is caused by the single hexapole magnetic lens.

2.1.6 Detectors and image formation

When the high energy incident electron beam scans over the specimen, there are different signals emanating from the sample. In the STEM, there are normally three types of signals being collected by different detectors.⁴ If the electrons pass through the specimen and are scattered to a very low angle, they can be detected by either a BF detector to form a BF image, or an electron energy loss spectrum (EELS) detector and be used to analyse the chemical information of the sample.^{34,35} When high energy electrons hit the atoms of the sample material, they may transfer energy to the inner

shell electrons, ejecting them from the atoms and leaving the atom in an excited state. An outer shell electron give excited atom will then fill the hole in the inner shell and emit the characteristic X-ray. The emission energy depends on the energy difference between the inner and outer shells, which is different for different elements. So the X-ray signal is characteristic of a given material and can be used in chemical analysis.³⁶ In practice, an energy dispersive X-ray detector is installed above the sample to detect the X-ray signal efficiently.

If an incident electron is close to the atomic nucleus, then it will be elastically scattered. Electrons that are scattered to a relatively high angle can be detected by a HAADF detector to form a HAADF image.^{12,37} As most of the STEM studies in this thesis were performed using this HAADF mode, we will discuss this in detail below.

A HAADF-STEM image is normally formed by electrons scattered through angles greater than 50 mrad.^{4,1238} Within this scattering angle range, electrons that are elastically scattered from the nucleus dominate the signal. Elastic scattering by the nucleus is often described by Rutherford scattering. The differential cross-section of the classic Rutherford scattering equation is expressed as:

$$\sigma_R(\theta) = \frac{e^4 Z^2}{16(4\pi\epsilon_0 E_0)^2 \sin^4 \frac{\theta}{2}} d\Omega \quad (2.4)$$

Here, θ is the scattering angle of the electron, Z is the proton number in the nucleus, E_0 is the energy of the electron, and Ω is the solid angle of scattering. In Equation 2.4, the screening effect (the effect of the electron cloud around the nucleus) is not

considered. However, in practical conditions, the electron screening effect cannot be ignored. To consider the screening effect in the cross-sectional equation, the term $\sin^4 \frac{\theta}{2}$ should be corrected to $[\sin^2 \frac{\theta}{2} + (\frac{\theta_0}{2})^2]^2$.⁴ Here θ_0 is given by:

$$\theta_0 = \frac{0.117Z^{1/3}}{E_0^{1/2}} \quad (2.5)$$

As the normal acceleration voltage in the STEM is above 100kV, relativistic effect must be considered. By adding the relativity corrected wavelength (as shown in equation 2.1) and the Bohr radius, $a_0 = \frac{h^2 \epsilon_0}{\pi m_0 e^2}$ of the atom, the screening and relativity corrected cross-section of the Rutherford scattering is given by:

$$\sigma_R(\theta) = \frac{Z^2 \lambda_R^4}{64\pi^4 a_0^2 [\sin^2 \frac{\theta}{2} + (\frac{\theta_0}{2})^2]^2} d\Omega \quad (2.6)$$

Through equations 2.5 and 2.6, we find that the scattering intensity is proportional to Z^a , where a is no bigger than 2 (where the value of 2 is for the unscreened Rutherford scattering, as shown in equation 2.4).

Now, we discuss the incoherent nature of the HAADF-STEM. To simplify the condition, we assume the object here has a crystal structure with a low index direction. The standard that defines the image's coherency is if the Airy discs of each atom's columns have a phase relationship between each other.^{38–40} This is dependent on the comparison between the transverse coherent length and the interatomic spacing distance. The transverse coherence length is defined as $L_t = 0.61\lambda/\theta$.⁴⁰ To make the image incoherent, the transverse coherent length, L_t must be smaller than the interatomic spacing distance, d , as shown in Figure 2.9.⁴⁰ For a 200kV STEM, the

electrons have a wavelength of 0.00251 nm, the interatomic spacing distance, d is normally around 0.3 nm. A normal HAADF-STEM's detection angle is 50 – 150 mrad, the transverse coherent length is then calculated to be 0.01-0.03 nm, which is far smaller than the normal interatomic spacing distance. So the HAADF-STEM image is the incoherent image.

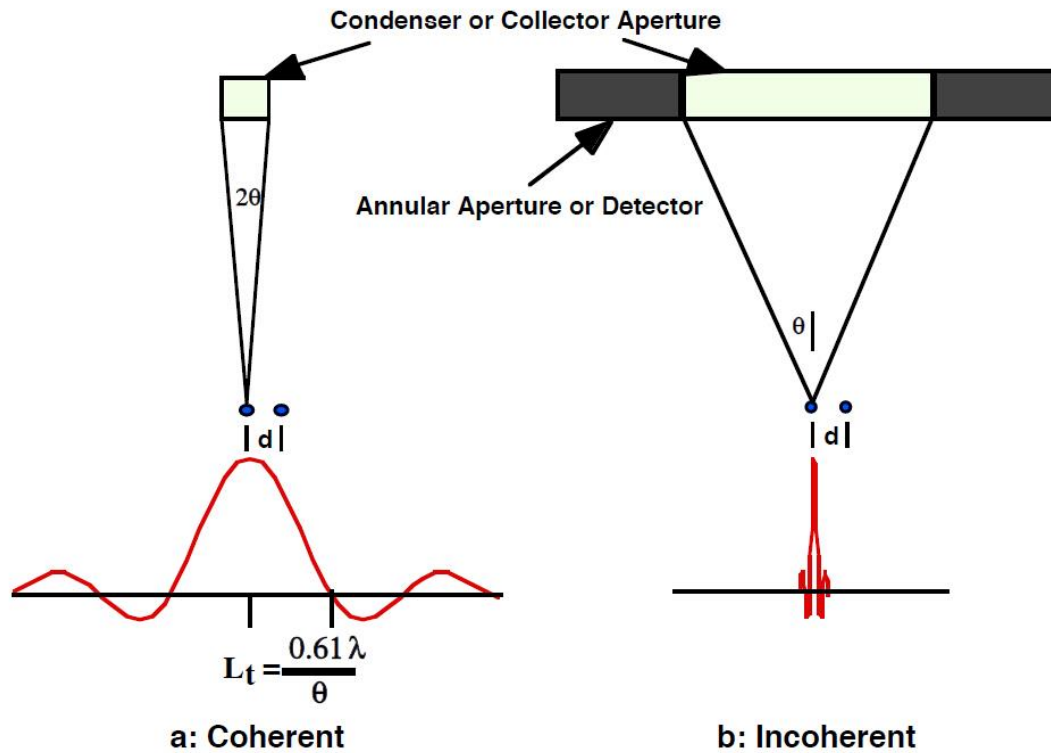


Figure 2.9 Schematic of the coherent and incoherent imaging by TEM and STEM.⁴⁰

The figure is from ref[40].

Because of the incoherent nature of HAADF-STEM, the HAADF image is solely formed by the total number of scattered electrons at each electron probe position. As mentioned above, the high angle scattering can be considered as Rutherford scattering, and the cross-section is described by equation 2.6. Therefore, the relationship of the

integrated HAADF intensity of different elemental clusters can be described as:

$$\frac{I_a}{I_b} = \frac{n_a}{n_b} * \left(\frac{Z_a}{Z_b}\right)^\alpha \quad (2.7)$$

Here, I is the integrated HAADF intensity, n is the number of atoms in the cluster, Z is the atomic number of the atom, and α is the parameter that can be tuned by changing the HAADF detection angle. In our STEM with the HAADF detection angle range of 62~164 mrad, α is 1.46 ± 0.18 .⁴¹

2.2 Cluster formation by magnetron sputtering and gas condensation

Cluster production has attracted research over the last 20 years due to the unique physical and chemical properties of nanoscale cluster materials, and their potential function in areas such as catalysis, medicine and electronics.^{42–53} The unique properties of the clusters are mainly a result of their size range. So satisfactory size-control of the clusters is important to enable investigation of the properties as functions of size, such as the catalytic activity.^{49,54,55} In this thesis, size-selected clusters are required as mass balances for atom counting. Here, a magnetron sputtering, gas condensation cluster source with a lateral time-of-flight mass selector is employed to produce the size-selected clusters.^{56,57} The schematic of the cluster source is shown in Figure 2.10

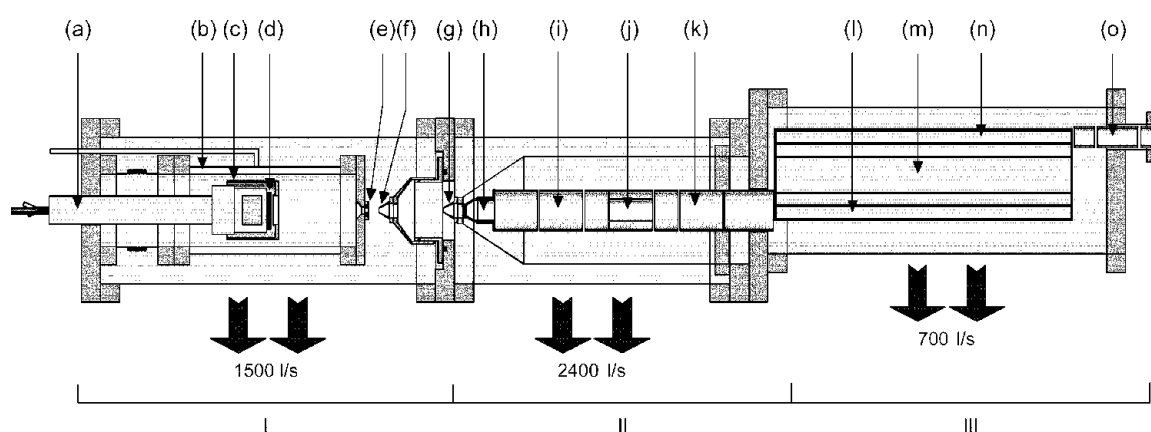


Figure 2.10 The schematic of the magnetron sputtering, gas condensed cluster source with lateral time-of-flight mass selector. The figure is from ref [56].

The cluster source can be separated into three different functional parts: cluster formation, cluster beam tuning and cluster mass selection. Here, we will explain these three parts sequentially.

2.2.1 Cluster formation

To achieve the size selection, the clusters must be ionized sufficiently. The magnetron sputtering method employed here produces ionized cluster materials. There are two main advantages of the magnetron sputtering method: First, the proportion of ionized clusters is relatively high (~30%), therefore, no further ionization step is required. Second, the strong magnet will enhance the plasma and improve the sputtering efficiency.⁵⁶

As shown in Figure 2.10, a magnetron gun is setup on a long axial mount. Argon is injected into the front of the magnetron and the gas flow rate is controlled by the exit nozzle. A pure material (e.g. 99.99% gold) disc is placed as the target in the

magnetron and a high RF voltage is applied to it. The Ar plasma is ignited by this RF voltage. Due to the nature of the RF voltage, the target attracts the electrons and repels to the Ar^+ when it is in the positive cycle and the contrary in the negative cycle. Because of the mass difference between electron and Ar^+ , the mobility of the electrons is much better than the Ar^+ . Hence, there is a negative bias voltage on the the target which induces the sputtering process. The strong magnet field behind the target improves the ionization of the Ar^+ by increasing the electron mobile trajectory, which can enhance the sputtering process.⁵⁶

When the Ar^+ ions hit the target, the energy of the Ar^+ will transfer to the target material surface. If the energy is high enough to overcome the binding energy of the target atoms, then the atoms will be ejected from the target. To generate larger clusters, He gas is injected to cool down the sputtered atoms and produce small “seed” clusters for further growth. The process can be regarded as a three-body collision between one He atom and two sputtered atoms. Because of their important role in the cluster production process, the Ar^+ and He pressures can significantly affect the cluster formation. A previous study showed that the cluster size can be increased a thousand times by introducing both Ar^+ and He gas, rather than Ar^+ gas only. Due to the important role in the “seed” production, the He pressure can be used to affect the cluster size distribution. In a certain range, the cluster size increases with increasing He pressure. However, if the He pressure keeps increasing, the size of the clusters will decrease, this is because the formation rate of a small “seed” clusters is higher than

the formation rate of big clusters. The small “seed” clusters can grow larger within the condensation chamber in two ways: one is the aggregation of “seed” cluster; the other is the condensation of atoms on the surface of the “seed” clusters. We can adjust the condensation chamber length to control the cluster growth time, which will also affect the size distribution of clusters.⁵⁶

2.2.2 Cluster beam optics

To ensure good performance regarding size selection and deposition, a well-focused cluster beam is necessary. The cluster condensation process ends at the nozzle. Following this, the clusters move to the ion optics, beam generation chamber through two skimmers due to the pressure difference between the two chambers. The two skimmers are used to remove the off-axis clusters and form a unidirectional beam. The clusters are first accelerated by the extraction lens, (only specific charged clusters can be extracted), then, the cluster beam is focused by two einzel lenses. There is a deflection plate between the two einzel lenses, which is used to finely tune the cluster beam trajectory. After passing through the ion optics chamber, the cluster beam is well-focused and ready to go into the mass selector chamber.⁵⁶

2.2.3 Time-of-flight mass selection

The mass selection of the clusters is achieved by a lateral time-of-flight mass selector. The principle of this time-of-flight mass selector is to give the ionized clusters momentum perpendicular to the beam direction by applying an electric field pulse.

Clusters with different masses will have different perpendicular velocities due to the same applied momentum. After the clusters move for a certain time, an opposite electric field is applied to remove the perpendicular momentum caused by the previous electric field. Clusters with different masses are separated by the different perpendicular movement.

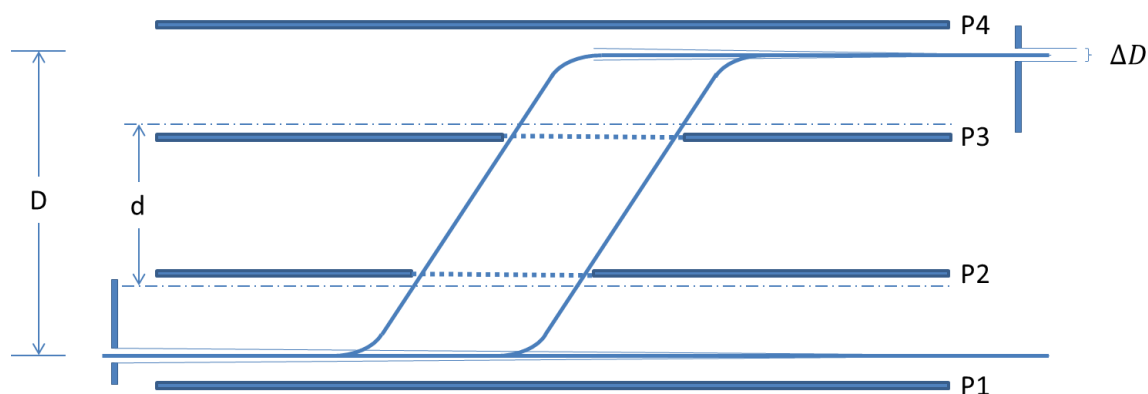


Figure 2.11 Schematic of the time-of-flight mass selector.

A schematic of the time-of-flight mass selector is shown in Figure 2.11. The clusters enter the mass selector through the entrance slit in the lower left. A short high voltage pulse is applied to the plate P1 to give the clusters an upward momentum. The duration of the pulse is designed to ensure no clusters leave the acceleration area (between plates P1 and P2), so that all the clusters are given the same upward momentum. There is an opening with mesh in P2 where the accelerated clusters can pass through to the field free region between P2 and P3. A similar opening in P3 allows the clusters to pass through P3. An equal but opposite voltage pulse is then applied to P4; giving the clusters a downward momentum, which offsets the previous upward momentum. The clusters will maintain their horizontal velocity to the right and move out of the mass selector from the exit slit.

The time that a cluster takes to travel from the acceleration region between P1 and P2 to the deceleration region between P3 and P4 is dependent on the perpendicular velocity of the clusters, which is dependent on its mass. The perpendicular momentum added to the cluster is $p=mv_p$, where m is the cluster's mass, and v_p is the perpendicular velocity after acceleration, and the vertical distance between the acceleration region and the deceleration region is d . Therefore, the time interval between the acceleration pulse and the deceleration pulse is:

$$T_i = \frac{d}{v_p} = \frac{md}{p_p} \quad (2.8)$$

As the perpendicular momentum, P_p and the distance, d are normally fixed, the interval time between the two pulses is used to select the cluster's mass.⁵⁷

The mass resolution of the mass selector is determined by the ratio of the entrance and exit slit aperture sizes and the perpendicular movement distance. If m_0 is the mass of a cluster, that can exactly transfer through the exit slit, for a cluster with mass m , the perpendicular velocity is⁵⁷:

$$v_m = v_{m_0} \frac{m_0}{m} \quad (2.9)$$

The perpendicular movement distance can be calculated by⁵⁷:

$$D_m = \frac{1}{2} v_m t_p + v_m t_d + \frac{1}{2} v_m t_p = \frac{m_0}{m} D \quad (2.10)$$

Here, t_p is the acceleration time, t_d is the field free flight time, and D is the total perpendicular movement distance of the exactly transmitted clusters. The change rate of the perpendicular movement distance with respect to the mass can be explained

as⁵⁷:

$$\frac{dD_m}{dm}_{m=m_0} = -\frac{m_0 D}{m^2}_{m=m_0} = -\frac{D}{m_0} \quad (2.11)$$

The exit slit has an opening size, ΔD , so clusters with a mass range will all be selected by the mass selector. The mass range can be calculated by⁵⁷:

$$\Delta m = \frac{dm}{dD_m} \Delta D = -\frac{m_0}{D} \Delta D. \quad (2.12)$$

So the mass resolution is given by:

$$R = \frac{m}{\Delta m} = \frac{D}{\Delta D} \quad (2.13)$$

In practical conditions, ΔD is not only the exit slit size, but a convolution of both the entrance and exit slit sizes.⁵⁷

2.3 Multislice STEM image simulation of clusters

Although the aberration corrected HAADF-STEM can provide a very high resolution image of a cluster, it is still the two dimensional projection of the three dimensional structure. Therefore, to investigate the atomic structure of the nanocluster, a high resolution simulation of the HAADF-STEM images is required. In this thesis, the QSTEM,⁵⁸ which is a free software package using multislice simulation, is utilized to simulate the STEM simulation images. The practical parameters of our STEM, such as acceleration voltage, HAADF detection angle range and spherical aberration, is uploaded to the software for more accurate STEM image simulations to help our structure identification.

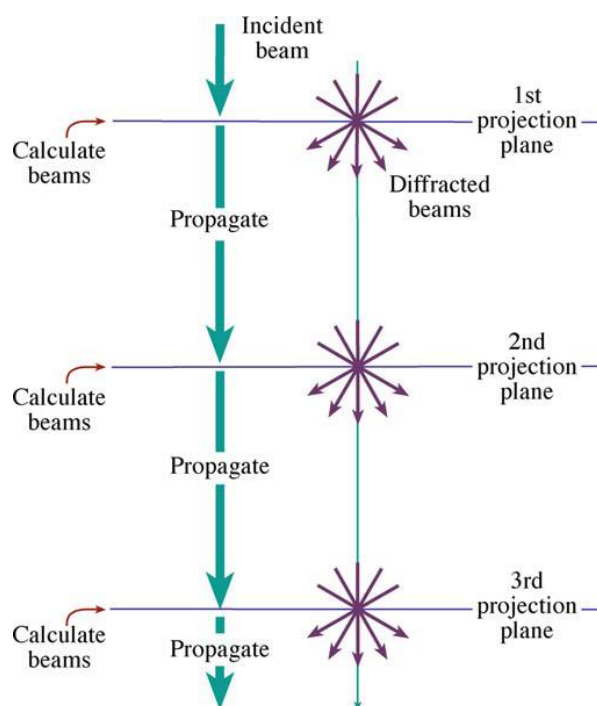


Figure 2.12 Schematic of the multislice simulation.⁴ The figure is from ref [4].

QSTEM is based on the multislice simulation method. The principle, as shown in Figure 2.12, is to divide the model structure that will be simulated into multiple slices, and then simulate the process slice by slice. For the multislice simulation of the electron microscope images, the model structure is sectioned into many small slices that are perpendicular to the incident electron beam. The potential of each slice will be projected onto one plane in the slice. The interaction between the incident electron wave function and the first slice is simulated first. The changes in both amplitude and phase of the electron beam after the interaction with the first slice are calculated and propagated to the projection plane of the next slice, as the new incident electron beam wave function. This process repeats until the last slice is simulated. The advantage of multislice simulation is high accuracy, as it can produce highly accurate STEM image simulations if a very small slice thickness is used.⁴ However, this method is fairly

computationally expensive. To overcome this, we used the high performance computing (HPC) system blue bear⁵⁹ to increase the computation efficiency and accuracy.

The purpose of the multislice simulation of the STEM image is to simulate STEM images of possible cluster structures and then compare the simulation images with the experimental images to investigate the clusters' 3D structures. Because the clusters land randomly on the surface and the clusters will rotate under the electron beam during scanning, the pattern of the clusters will change dramatically. So, every possible beam incident orientation must be considered in the simulation. The end result of the simulation process is a “map” of simulated STEM images for each possible structure, at different angles of orientation, that can be compared against HAADF STEM images to identify the atomic structure of clusters-we call this a simulation atlas. The comparison is processed by the author and cross-tested by other people for accuracy. In practice, some specific pattern features from the specific structures are used to help the comparison work. A schematic of the structure identification with the simulation atlas is shown in Figure 2.13.

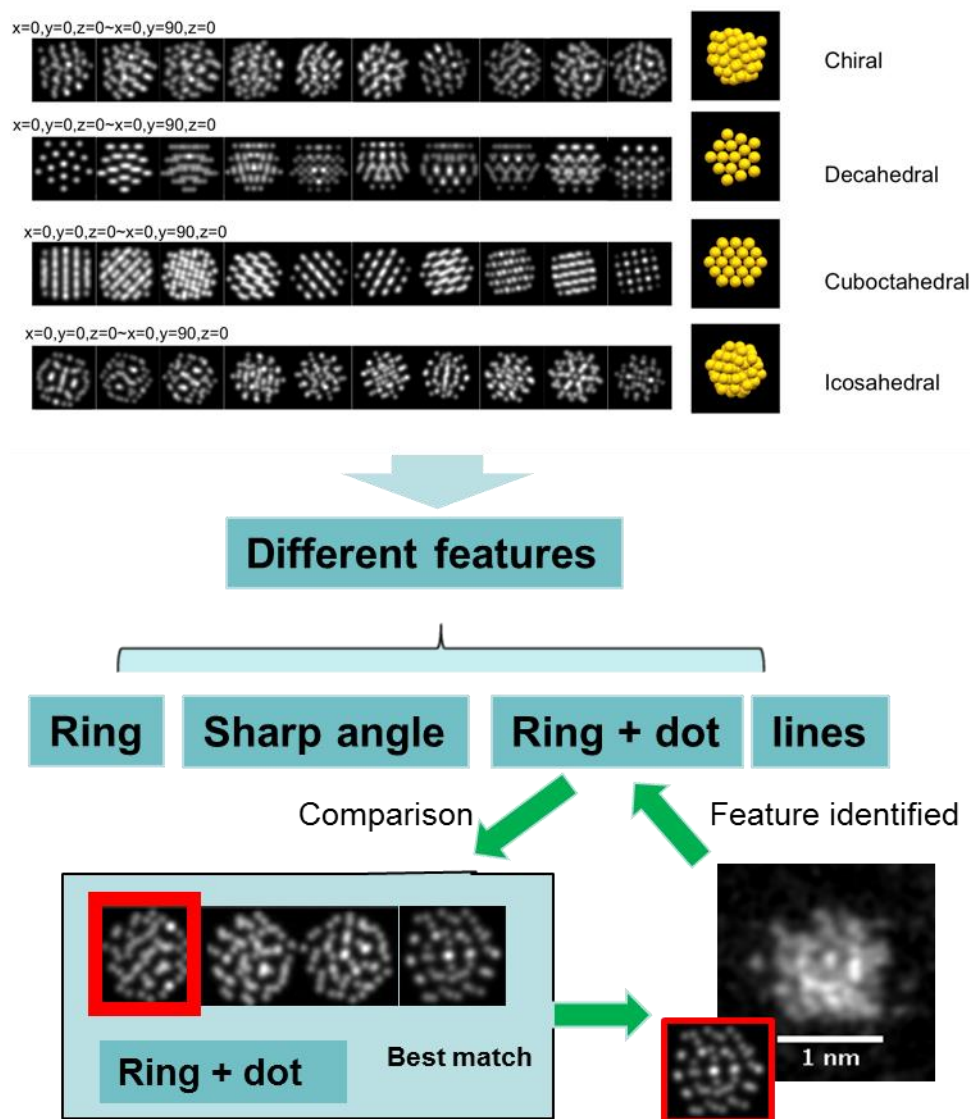


Figure 2.13 Schematic of the structure determination with STEM image simulation atlas.

In the research on Au_{55} clusters, the hybrid structure calculated by Garzon et al⁶⁰ and the three high-symmetry full-shell Au_{55} cluster structures: cuboctahedral, icosahedral and ino-decahedral, were simulated for every possible incident beam orientation. For the research on the thiolated $(\text{Au}_x\text{Ag}_{1-x})_{312\pm55}$ clusters, the cuboctahedral, icosahedral and ino-decahedral models for Au_{309} were used to perform the simulations. The

simulation atlases of these motifs are shown in the appendix.

Reference:

1. Ruska, E. Die elektronenmikroskopische Abbildung elektronenbestrahlter Oberflächen. *Zeitschrift für Phys.* **83**, 492–497 (1933).
2. Broglie, L. de. On the theory of the quanta. (University of Paris, 1924).
3. First Electron Microscope with Resolving Power Higher than that of a Light Microscope. *Electron Microscope Deutsches Museum* (2006).
4. Williams, D. B. & Carter, C. B. *Transmission Electron Microscopy—A Textbook for Materials Science*. Micron (Springer, 2008).
5. Nobelprize.org. Ernst Ruska - Autobiography. http://nobelprize.org/nobel_prizes/physics/laureates/1986/ruska-autobio.html
6. Pietzch, J. The Nobel Prize in Physics 1986: Life through a Lens. *Nobelprize.org*
7. Knoll, M. & Ruska, E. Das Elektronenmikroskop. *Zeitschrift für Physik* **79**, 699 (1932).
8. Knoll, M. Aufladepotential und sekundäremission elektronenbestrahlter körper. *Z tech Phys* **16**, 467–475 (1935).
9. Ardenne, M. von. Das Elektronen-Rastermikroskop. *Zeitschrift für Phys.* **109**, 553–572 (1938).
10. von Ardenne, M. Die durch Elektronenstreuung im Objekt verursachten Abbildungsfehler des Elektronenmikroskops und ihr Verhältnis zueinander. *Zeitschrift für Phys.* **111**, 152–157 (1938).
11. Crewe, A. V. & Wall, J. A scanning microscope with 5 Å resolution. *J. Mol. Biol.* **48**, (1970).
12. Crewe, A.V., Wall, J. & Langmore, J. Visibility of single atoms. *Science* **168**,

- 1338–1340 (1970).
13. Scherzer, O. Über einige Fehler von Elektronenlinsen. *Zeitschrift für Phys.* **101**, 593–603 (1936).
 14. Oldfield, L. Computer design of high frequency electron-optical systems. in *Image Processing and Computer-aided Design in Electron Optics* 370–399 (Academic Press, 1973).
 15. Ash, E. A. Use of space charge in electron optics. *J. Appl. Phys.* **26**, 327–330 (1955).
 16. Hanai, T., Hibino, M. & Maruse, S. Improvement of an Electron Probe Profile Using the Foil Lens. *Microsc.* **31**, 360–367 (1982).
 17. Kunath, W. Correction of a ring-shaped objective lens with the aid of two round lenses. in *%th European Congr. on Electron Microscopy* 70–71 (1972).
 18. Chen, E. & Mu, C. New development in correction of spherical aberration of electromagnetic round lens. *International Symposium on Electron Microscopy* 28–35 (1991).
 19. Crewe, A. V., Ruan, S., Tsai, F. & Korda, P. The first test on a magnetically focused mirror corrector. in *Conference series-institute of physics* 301–304 (1995).
 20. Baranova, L. A. B. & Yavor, S. Y. The Optics of Round and Multipole Electrostatic Lenses. *Adv. Electron. Electron Phys.* **76**, 1–207 (1989).
 21. Crewe, A. V., Cohen, D. & Meads, P. A multipole element for the correcting of spherical aberration. in *Proceedings of the Fourth Regional Conference on Electron Microscopy* (1968).
 22. Hawkes, P. W. Aberration correction past and present. *Philos. Trans. A. Math. Phys. Eng. Sci.* **367**, 3637–3664 (2009).

23. Haider, M., Rose, H., Uhlemann, S., Schwan, E., Kabius, B. & Urban, K. A spherical-aberration-corrected 200kV transmission electron microscope. *Ultramicroscopy* **75**, 53–60 (1998).
24. Haider, M., Rose, H., Uhlemann, S., Kabius, B. & Urban, K. Towards 0.1 nm resolution with the first spherically corrected transmission electron microscope. *J. Electron Microsc. (Tokyo)*. **47**, 395–405 (1998).
25. Uhlemann, S. & Haider, M. Residual wave aberrations in the first spherical aberration corrected transmission electron microscope. *Ultramicroscopy* **72**, 109–119 (1998).
26. Krivanek, O. L., Dellby, N. & Lupini, A. R. Towards sub-Å electron beams. **78**, (1999).
27. Dellby, N., Krivanek, O. L., Nellist, P. D., Batson, P. E. & Lupini, A. R. Progress in aberration-corrected scanning transmission electron microscopy. *Reprod. Syst. Sex. Disord.* **50**, 177–185 (2001).
28. Krivanek, O. L., Dellby, N., Spence, A. J., Camps, R. A. & Brown, L. M. Aberration correction in the STEM. *Inst. Phys. Conf. Ser. EMAG97* **153**, 35–40 (1997).
29. Herring, R. A. & Hoyle, D. The Ultra-stable Scanning Transmission Electron Holography Microscope. *Microsc. Microanal.* **19**, 347–348 (2013).
30. Richardson, O. W. *Thermionic Emission from Hot Bodies*. (2003).
31. Crewe, A. V., Eggenberger, D. N., Wall, J. & Welter, L. M. Electron gun using a field emission source. *Rev. Sci. Instrum.* **39**, 576–583 (1968).
32. Pollack, S. R. Schottky field emission through insulating layers. *J. Appl. Phys.* **34**, 877–880 (1963).
33. Bogner, A., Jouneau, P. H., Thollet, G., Basset, D. & Gauthier, C. A history of

- scanning electron microscopy developments: Towards ‘wet-STEM’ imaging. *Micron* **38**, 390–401 (2007).
34. Egerton, R. F. *Electron Energy-Loss Spectroscopy in the Electron Microscope. Third*, (Springer Science & Business Media, 2011).
 35. Browning, N. D., Chisholm, M. F. & Pennycook, S. J. Atomic-resolution chemical analysis using a scanning transmission electron microscope. *Nature* **366**, 143–146 (1993).
 36. Goldstein, J., Newbury, D. E., Echlin, P., Joy, D. C., Romig, A. D., Lyman, C. E., Fiori, C. & Lifshin, E. *Scanning electron microscopy and X-ray microanalysis. A text for biologists, material scientists and geologists. IJ 1.46r* (1992). doi:10.1016/0047-7206(83)90085-7
 37. Wang, Z. L. New Developments in Transmission Electron Microscopy for Nanotechnology. *Adv. Mater.* **15**, 1497–1514 (2003).
 38. Nellist, P. D. *The Principles and Interpretation of Annular Dark-Field Z-Contrast Imaging.* **113**, (2008).
 39. Pennycook, S. J. Z-contrast stem for materials science. *Ultramicroscopy* **30**, 58–69 (1989).
 40. Pennycook, S. J. & Nellist, P. D. in *Impact of electron scanning probe microscopy on materials research* 161–207 (1999). doi:10.1017/CBO9781107415324.004
 41. Wang, Z. W. & Palmer, R. E. Intensity calibration and atomic imaging of size-selected Au and Pd clusters in aberration-corrected HAADF-STEM. *J. Phys. Conf. Ser.* **371**, 012010 (2012).
 42. Schmid, G. Metal clusters and cluster metals. *Polyhedron* **7**, 2321–2329 (1988).
 43. Goswami, N., Li, J. & Xie, J. *Protected Metal Clusters - From Fundamentals*

- to Applications. *Frontiers of Nanoscience* **9**, (2015).
44. Ferrando, R., Jellinek, J. & Johnston, R. L. Nanoalloys : From Theory to Applications of Alloy Clusters and Nanoparticles. **108**, (2008).
 45. Walter, M., Akola, J., Lopez-Acevedo, O., Jadzinsky, P. D., Calero, G., Ackerson, C. J., Whetten, R. L., Gronbeck, H. & Hakkinen, H. A unified view of ligand-protected gold clusters as superatom complexes. *Pnas* **105**, 9157–62 (2008).
 46. Schmid, G. The relevance of shape and size of Au₅₅ clusters. *Chem. Soc. Rev.* **37**, 1909–1930 (2008).
 47. De Heer, W. A. The physics of simple metal clusters: Experimental aspects and simple models. *Rev. Mod. Phys.* **65**, 611–676 (1993).
 48. Caps, V., Arrii, S. & Morfin, F. Structures and associated catalytic properties of well-defined nanoparticles produced by laser vaporisation of alloy rods. *Faraday Discuss.* **138**, 241–256; discussion 317–335, 433–434 (2008).
 49. Molina, L. M. & Hammer, B. Some recent theoretical advances in the understanding of the catalytic activity of Au. in *Applied Catalysis A: General* **291**, 21–31 (2005).
 50. Baletto, F. & Ferrando, R. Structural properties of nanoclusters: Energetic, thermodynamic, and kinetic effects. *Rev. Mod. Phys.* **77**, 371–423 (2005).
 51. Schmid, G., Baumle, M., Geerkens, M., Heim, I., Osemann, C., & Sawitowski, T. Current and future applications of nanoclusters. *Chem. Soc. Rev.* **28**, 179–185 (1999).
 52. Janssens, T. V. W., Clausen, D. S., Hvolbaek, B., Falsig, H., Christensen, C. H., Bligaard, T. & Norskov, J. K. Insights into the reactivity of supported Au nanoparticles: Combining theory and experiments. *Top. Catal.* **44**, 15–26 (2007).

53. Klein, D. L., Roth, R., Lim, A. K. L., Alivisatos, A. P. & McEuen, P. L. A single-electron transistor made from a cadmium selenide nanocrystal. *Nature* **389**, 699–701 (1997).
54. Reetz, M. & Helbig, W. Size-selective synthesis of nanostructured transition metal clusters. *J. Am. Chem. Soc.* **116**, 7401–7402 (1994).
55. Haruta, M. Size- and support-dependency in the catalysis of gold. *Catal. Today* **36**, 153–166 (1997).
56. Pratontep, S., Carroll, S. J., Xirouchaki, C., Streun, M. & Palmer, R. E. Size-selected cluster beam source based on radio frequency magnetron plasma sputtering and gas condensation. *Rev. Sci. Instrum.* **76**, 045103 (2005).
57. von Issendorff, B. & Palmer, R. E. A new high transmission infinite range mass selector for cluster and nanoparticle beams. *Rev. Sci. Instrum.* **70**, 4497–4501 (1999).
58. Koch, C. DETERMINATION OF CORE STRUCTURE PERIODICITY AND POINT DEFECT DENSITY ALONG DISLOCATIONS. *Dissertation* (Arizona State University, 2002).
59. Linux Compute (BlueBEAR).
<https://intranet.birmingham.ac.uk/it/teams/infrastructure/research/bear/bluebear/index.aspx>.
60. Garzón, I., Michaelian, K., Beltran, M. R., Posada-Amarillas, A., Ordejon, R., Artacho, E., Sanchez-Portal, D. & Soler, J. M. Lowest Energy Structures of Gold Nanoclusters. *Phys. Rev. Lett.* **81**, 1600–1603 (1998).

CHAPTER 3

HAADF STEM STUDY ON THE ATOMIC STRUCTURE OF $Au_{55}(PPh_3)_{12}Cl_6$ SCHMID CLUSTERS

Most of the text and figures in this chapter have been used in my publication (with me as the first author): Jian, N., Stapelfeldt, C., Hu, K., Fröba, M. & Palmer, R. E. Hybrid atomic structure of the Schmid cluster $Au_{55}(PPh_3)_{12}Cl_6$ resolved by aberration-corrected STEM. *Nanoscale* **7**, 885–888 (2015).

3.1 Overview

In this chapter, The investigation of the atomic structure of the $Au_{55}(PPh_3)_{12}Cl_6$ Schmid cluster¹ by using aberration-corrected scanning transmission electron microscopy (STEM) combined with multislice simulation of STEM images is introduced. Atom counting is employed, with size-selected clusters as mass standards, to “fractionate” the correct cluster size in the image analysis. Systematic structure analysis shows that a hybrid structure,² predicted by density functional theory, best matches nearly half the clusters observed. Most other clusters are amorphous. I believe these conclusions are consistent with all the previous, apparently

contradictory structural studies of the Schmid cluster.

3.2 Introduction

The report of the ligand-stabilized Au₅₅(PPh₃)₁₂Cl₆ cluster by Schmid and colleagues in 1981¹ was a significant event in the emergence of nanotechnology. Its size (1.4nm), stability and electronic properties drew a great deal of attention.^{3–13} It was quickly seen as the basis of a future single electron transistor and, more generally, a potential building block of a nanostructured system.^{2–7} However, the atomic structure of Au₅₅(PPh₃)₁₂Cl₆ has long remained a mystery, not least because the cluster resisted the crystallization which is needed to allow single-crystal X-ray diffraction analysis.^{14–16}

The first Au₅₅(PPh₃)₁₂Cl₆ cluster structure model was proposed by Schmid et al in their first report of the clusters in 1981.¹ They used the Mossbauer spectrum and found 4 types of Au atoms, which is consistent with a full shell cuboctahedral structure (a shape of fcc structure). In 1990, people studied the average coordination number of Au atoms in Au₅₅(PPh₃)₁₂Cl₆ clusters with the extended X-ray absorption fine structure (EXAFS) method.^{9,10} The results best fit the cuboctahedral model, rather than the icosahedral or decahedral models. A combination of EXAFS, wide-angle X-ray scattering (WAXS) and X-ray absorption near edge structure (XANES) analysis reported in 2001, also support the cuboctahedral structure.¹¹ However, beside the cuboctahedral, an icosahedral model is also suggested to be the Au₅₅(PPh₃)₁₂Cl₆ clusters structure. The first report is by Vogel et al. in 1993, where the

powder diffraction curve of $Au_{55}(PPh_3)_{12}Cl_6$ agreed best with the icosahedral model.¹² In theoretical area, an *ab initio* research of $Au_{55}(PPh_3)_{12}Cl_6$ clusters in 2010 also support the icosahedral structure.¹³ Beyond these two assignments, the structure of the $Au_{55}(PPh_3)_{12}Cl_6$ cluster was considered to be heterogeneous by Rapoport and colleagues with an integrated analysis that included high resolution cryo transmission electron microscopy (TEM), thermogravimetry (TG), X-ray scattering (XRS), differential thermoanalysis (DTA) and analytical ultracentrifugation (AUC).¹⁴ The TEM was utilized to study the $Au_{55}(PPh_3)_{12}Cl_6$ clusters in the past, but it was mainly used to measure the diameter of the clusters and they all showed a diameter around 1.4 nm.^{12,14,15} There was no extensive TEM study on the atomic structure of the $Au_{55}(PPh_3)_{12}Cl_6$ clusters except for a few high resolution images.

In this chapter, the systematic experimental STEM investigation of the atomic structure of the $Au_{55}(PPh_3)_{12}Cl_6$ clusters are presented. The cluster weighing method was used to get the correct size of cluster to study. The high resolution aberration corrected HAADF-STEM combined with the multilayer simulation were used to investigate the clusters structure. A hybrid structure, which was predicted theoretically for the bare Au_{55} cluster, was found to match about half of the clusters, while the other half are amorphous.

3.3 Experimental details

The $Au_{55}(PPh_3)_{12}Cl_6$ clusters were synthesized by Christopher Stapelfeldt and Michael Froba in Humburg with the Schmid method, which dissolving Ph_3PAuCl in benzene then treated with gaseous B_2H_6 at 60 °C to form the Au clusters.¹ The clusters were sent to Birmingham in powder form, and redissolved in dichloromethane (CH_2Cl_2) and drop casting onto one half of a 400-mesh TEM grid covered with an amorphous carbon film. The size-selected Au_{309} clusters were deposited on the other half part of the same 400-mesh copper TEM grid (the half grid on which the $Au_{55}(PPh_3)_{12}Cl_6$ clusters were subsequently deposited was covered by a cap to prevent the deposition of the size-selected Au_{309} clusters, in case they affected the ligand-protected clusters) by a gas condensed, magnetron sputtering cluster source equipped with a lateral time-of-flight mass selector.¹⁷⁻¹⁹ The cluster beam current was 20A and the deposition time was 150 seconds, the number of the size-selected Au_{309} clusters was $\sim 1.9 \times 10^{10}$. The microscopy work was performed by a 200kV JEOL JEM2100F STEM with a CEOS spherical aberration corrector. The HAADF detector we used in this study had a 62 mrad inner collection angle and 164 mrad outer angle. All the images were taken within 2.7 s (with an equivalent electron dose up to 1.9×10^4 electron \AA^{-2}) and no beam shower was performed on the samples to minimize the beam effect.

3.4 Results and discussion

3.4.1 “Weighing” Clusters

Although the Schmid method can synthesize fairly mono-dispersive clusters, but like many other chemical synthesized clusters, there were also some similar size clusters produced during the synthesis process. So, when we try to figure out the atomic structure of the $Au_{55}(PPh_3)_{12}Cl_6$ clusters, the disturbance of the other size clusters must be overcome. As mentioned before, using the Z-contrast property of the HAADF intensity, we can “weigh” the clusters with size-selected clusters as the mass balance.^{20,21} The basic idea here is to measure the integrated HAADF intensity of the cluster and subtract the contribution of its background. To enhance the accuracy of the measurement of integrated HAADF-STEM intensity, the size-selected Au_{309} clusters were deposited onto half of the TEM grid, while the Schmid clusters, dissolved in dichloromethane, were drop cast onto the other half of the same TEM grid.

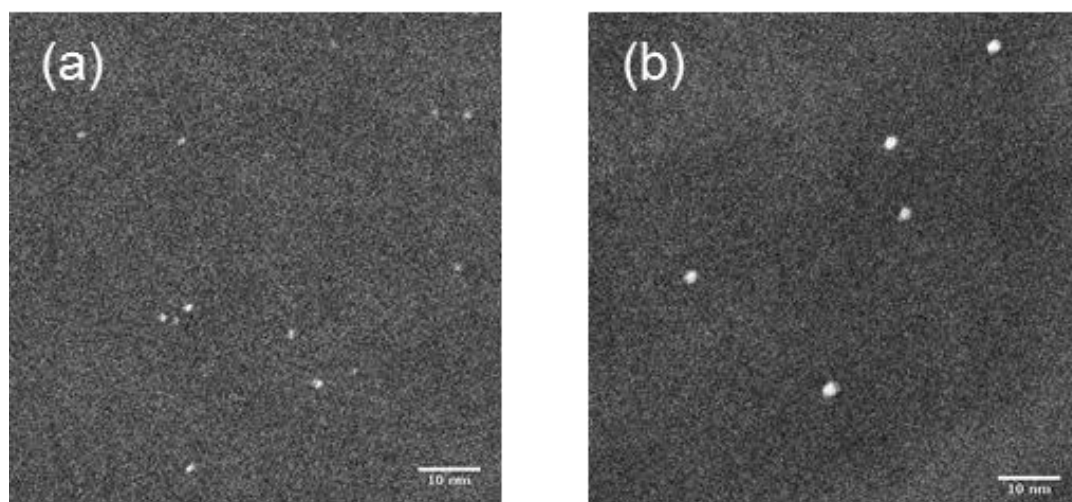


Figure 3.1 (a) The low magnification HAADF STEM image of: (a) Schmid method prepared clusters, and (b) size-selected Au_{309} clusters prepared with magnetron sputtering cluster source.

In Figure 3.1, we can see the HAADF STEM images of both Schmid clusters and the size-selected Au_{309} clusters. The size-selected Au_{309} clusters on the right side are evenly distributed on the TEM grid surface, while the Schmid clusters have a little higher concentration. We can see that some Schmid clusters in the image are obviously large aggregations, so to improve the efficiency of the work, only the clusters which were smaller than 1.8 nm were chosen to be included in the statistical analysis.

Comparison of the integrated HAADF STEM intensity of each cluster prepared by the Schmid method with the size-selected Au_{309} clusters shows that there is some variation in the nuclearity of the “Schmid clusters” beyond that of pure $Au_{55}(PPh_3)_{12}Cl_6$ clusters. But the same comparative intensity measurement enable us

to “fractionate” the chemically prepared sample to focus on the “ Au_{55} ” clusters which are of most interest. The relative integrated HAADF intensity of both Schmid clusters and size-selected Au_{309} clusters were shown in Figure 3.2(a).

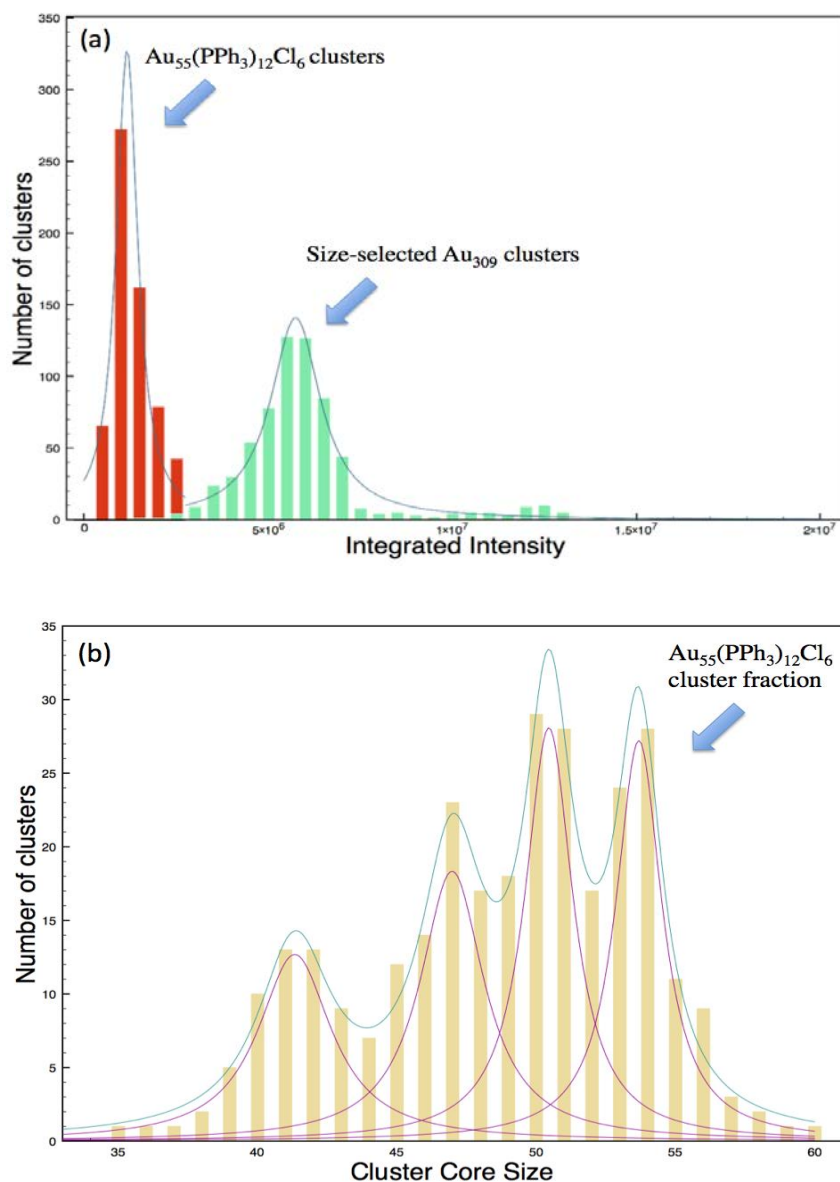


Figure 3.2 Cluster weighing for the clusters prepared by the Schmid method. (a) The integrated HAADF intensity distribution of Schmid clusters and size-selected Au_{309} clusters. (b) Fine core size distribution of Schmid clusters. The fourth peak at $\sim 54 \pm 1.5$ is assigned as the $\text{Au}_{55}(\text{PPh}_3)_{12}\text{Cl}_6$ clusters.²² The figure is from ref [22].

The integrated HAADF intensity of the Schmid clusters were dependent on both the Au core and the ligand .calculated to an equivalent number E of Au atoms:

$$E = N_H \left(\frac{Z_H}{Z_{Au}} \right)^n + N_C \left(\frac{Z_C}{Z_{Au}} \right)^n + N_{Cl} \left(\frac{Z_{Cl}}{Z_{Au}} \right)^n + N_P \left(\frac{Z_P}{Z_{Au}} \right)^n = 9.88 \pm 2.74$$

Here, N_H , N_C , N_{Cl} and N_P , are the number of H, C, Cl and P atoms. Also, Z represents the atomic number of each element and the value “n” is from the previous calibration of our STEM.²³ After removing the contribution of the ligands, the distribution of the Au core size of the Schmid clusters can be obtained. A high resolution plot from this distribution is shown in Figure 3.2(b). We can see 4 peaks at 41 ± 2 , 47 ± 1.5 , 50 ± 1.5 and 54 ± 1.5 for the Au atoms. The fourth peak at $\sim 54 \pm 1.5$ is closest to that of Au_{55} . The maximum length of clusters in the fourth peak were also measured. The distribution of the maximum length of the clusters is shown in Figure 3.3, and we can see a peak of 1.406 nm, which is also consistent with the previous study. Based on these, the fourth peak is assigned as the $Au_{55}(PPh_3)_{12}Cl_6$ clusters. Our atomic structure analysis will then focus on the clusters from this peak.

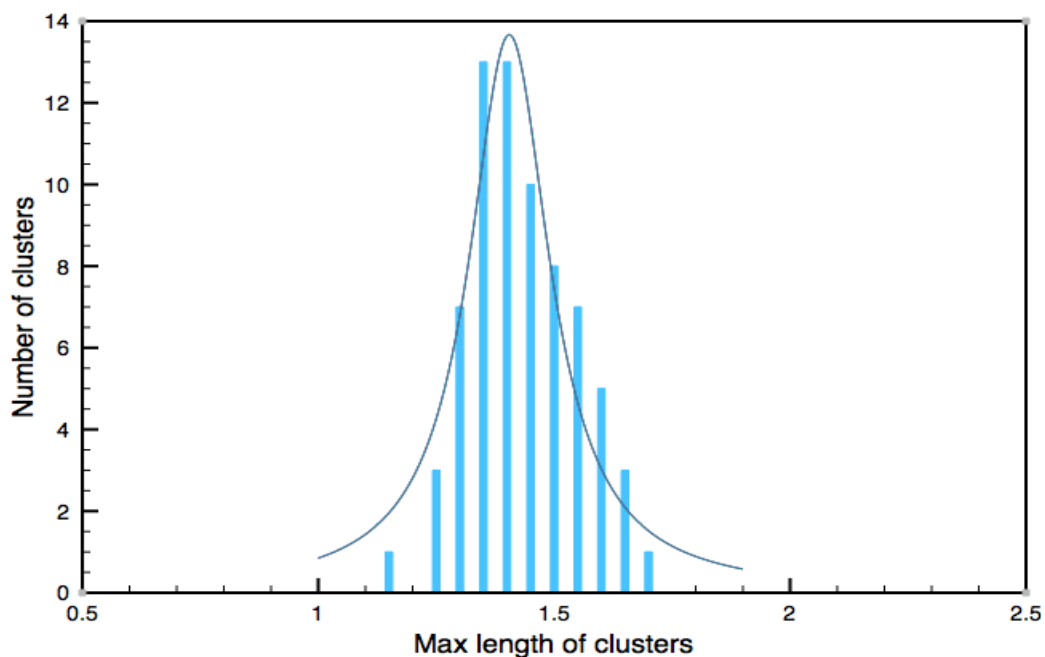


Figure 3.3. Maximum length of the assigned $\text{Au}_{55}(\text{PPh}_3)_{12}\text{Cl}_6$ clusters. The Gaussian peak value is 1.406.

3.4.2 Atomic structure of $\text{Au}_{55}(\text{PPh}_3)_{12}\text{Cl}_6$

3.4.2.1 Multislice simulation atlas

Comparing the experimental electron microscopy images with the simulation images of the predicted structure model is a common method to determine the atomic structure of nanomaterials.^{24–30} Here, the QSTEM software package was used to simulate the HAADF STEM image.³¹ The parameters in the simulation program were set as same as the parameters of the STEM operated in the experiment to enhance the accuracy of the simulation STEM images. There were four candidate models used to do the HAADF STEM simulation: cuboctahedral, icosahedral, icosidodecahedral and the hybrid chiral structure. The hybrid chiral structure was predicted by Garzon for bare

Au_{55} clusters.² In the density function theory (DFT) calculation, this structure has been found to have the lowest energy structure compares compare with many other structures, including the cuboctahedral and icosahedral.

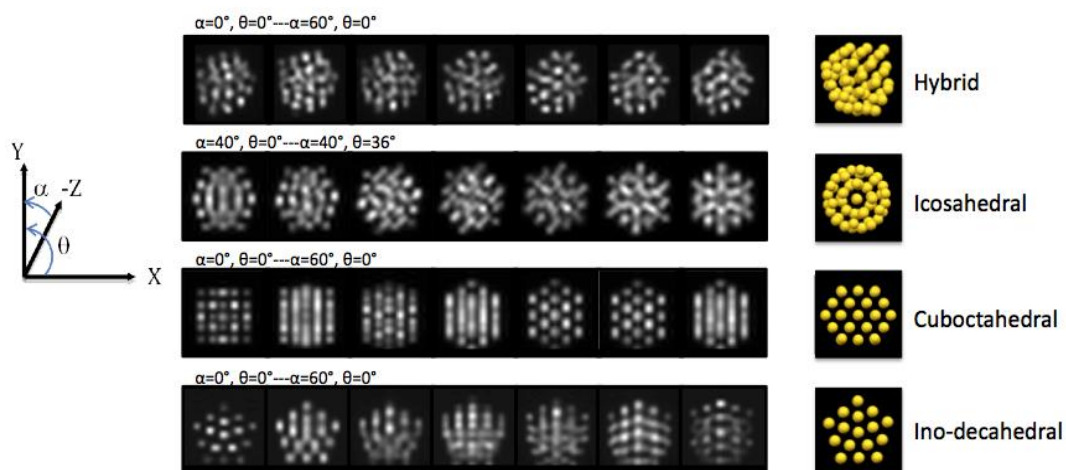


Figure 3.4 The example of the STEM simulation atlas of the hybrid chiral structure (from $\alpha=0^\circ$, $\theta=0^\circ$ to $\alpha=60^\circ$, $\theta=0^\circ$), the icosahedral structure (from $\alpha=40^\circ$, $\theta=0^\circ$ to $\alpha=40^\circ$, $\theta=36^\circ$), the cuboctahedral structure (from $\alpha=0^\circ$, $\theta=0^\circ$ to $\alpha=60^\circ$, $\theta=0^\circ$), and the ino-decahedral structure (from $\alpha=0^\circ$, $\theta=0^\circ$ to $\alpha=60^\circ$, $\theta=0^\circ$).²² The figure is from ref [22].

As the clusters landed on the TEM grid surface randomly, the same size clusters with the same structure can display differently in the STEM images. For example, in Figure 3.4, the simulated image of the ino-decahedral clusters with an orientation of $\alpha=0^\circ$, $\theta=0^\circ$, has a five-fold symmetric structure pattern which is rather different compared with the hybrid clusters at $\alpha=0^\circ$ and $\theta=60^\circ$, which has a two-fold symmetry structure pattern. So to systematically investigate the atomic structure of the Schmid

Au₅₅(PPh₃)₁₂Cl₆ clusters, the STEM image simulation of the candidate models from every possible incident electron beam orientation has been performed, as the "simulation atlas". The orientation range for the simulation depends on the symmetric properties of each of the structure models. The orientation range of the hybrid chiral structure is from $\alpha=0^\circ$, $\theta=0^\circ$ to $\alpha=180^\circ$, $\theta=180^\circ$; the icosahedral is from $\alpha=0^\circ$, $\theta=0^\circ$ to $\alpha=40^\circ$, $\theta=36^\circ$; the cuboctahedral is from $\alpha=0^\circ$, $\theta=0^\circ$ to $\alpha=60^\circ$, $\theta=45^\circ$, and the icosidodecahedral is from $\alpha=0^\circ$, $\theta=0^\circ$ to $\alpha=90^\circ$, $\theta=18^\circ$. The example of the simulation atlas is shown in Figure 3.4, where the whole simulation atlas is shown in the appendix.

3.4.2.2 Atomic structure analysis

The comparison between simulation and experimental STEM images is performed manually by identifying the different patterns from the cluster 2D image, like a ring with a central dot inside, parallel lines, or certain angle inside the pattern. The comparison method was described in detail in chapter 2. In this research, all the HAADF-STEM images of the clusters in the "true Au₅₅ fraction" were compared with all the simulated images of the four candidate models in the simulation atlas.

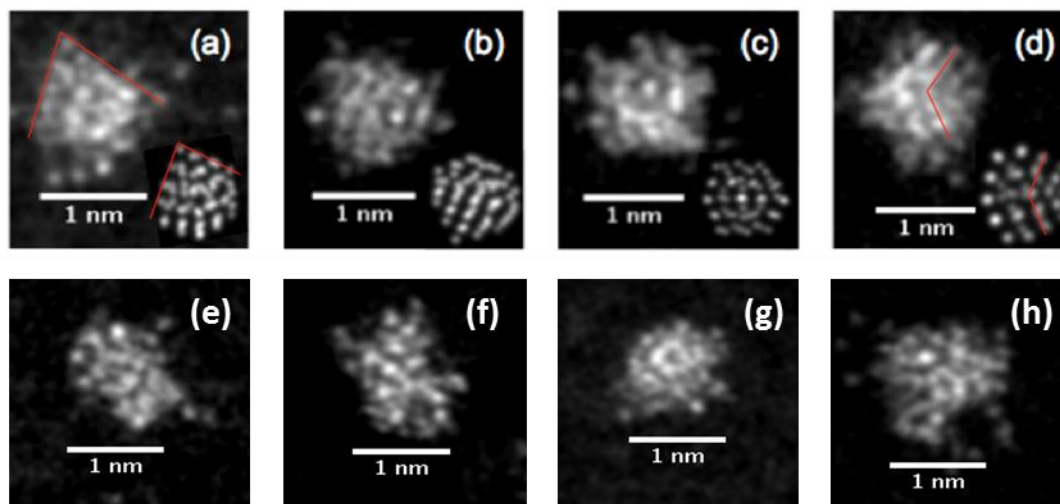


Figure 3.5 Typical high resolution HAADF-STEM images of the $\text{Au}_{55}(\text{PPh}_3)_{12}\text{Cl}_6$ clusters which are assigned to have hybrid structure and orientations of: (a) $\alpha=70^\circ$, $\theta=40^\circ$, (b) $\alpha=30^\circ$, $\theta=30^\circ$, (c) $\alpha=60^\circ$, $\theta=80^\circ$, and (d) $\alpha=100^\circ$, $\theta=0^\circ$. The insets are the corresponding best matched simulated images. From (e) to (h) are the high resolution HAADF-STEM images of the $\text{Au}_{55}(\text{PPh}_3)_{12}\text{Cl}_6$ clusters with an amorphous structure.²² The figure is from ref [22].

Figure 3.5 shows the examples of the high resolution HAADF-STEM images of the clusters from the $\text{Au}_{55}(\text{PPh}_3)_{12}\text{Cl}_6$ peak which are designated as the “true” $\text{Au}_{55}(\text{PPh}_3)_{12}\text{Cl}_6$ clusters. All 72 clusters in the “true $\text{Au}_{55}(\text{PPh}_3)_{12}\text{Cl}_6$ fraction” were analysed. Based on the results of the comparison between experimental and simulated HAADF-STEM images, we found no cluster that has either a cuboctahedral, icosahedral or icosahedral structure. However, there are 30 clusters best matched the hybrid chiral structure. For example, the cluster in Figure 3.5 (d) has a pattern of parallel fold lines, with an angle of 122° , which is very close to the parallel fold lines

in the STEM simulation image of the hybrid chiral structure model of orientation $\alpha=100^\circ$, $\theta=0^\circ$, with an angle of 128° . The slight difference may be due to two points. Firstly, the discrete distance between the orientations in the multislice simulation of the hybrid chiral structure is 10° . The cluster may not be at the exact angle of $\alpha=100^\circ$, $\theta=0^\circ$, which can cause a small deviation like this. Secondly, the electron beam may slightly affect the cluster structure and cause the atoms to move faintly from the original location. A deeper discussion on the electron beam effect will be presented later. The rest of the clusters, which is more than half of the Au₅₅(PPh₃)₁₂Cl₆ peak, are considered to have an amorphous structure. The example of the amorphous structure Au₅₅(PPh₃)₁₂Cl₆ clusters are shown in Figures 3.5 (e) to (h).

3.4.2.3 Electron beam damage

As mentioned above, the experimental images of the Au₅₅(PPh₃)₁₂Cl₆ clusters did not match the simulation images 100%. One of the reasons may be due to the effect of the incident electron beam. In many previous electron microscopy studies on small clusters, such as Au₂₀, MP-Au₃₈ and Au₄₀(SR)₂₄, people reported the electron beam can give rise to the atom motion inside the clusters during the imaging process.^{29,32,33} Can the electron beam break the clusters in our research? To answer this question, a serial integrated intensity test was performed by repetitively scanning one single cluster over and over again with the same experimental parameter we used in the atomic structure study. The results are shown in Figure 3.6.

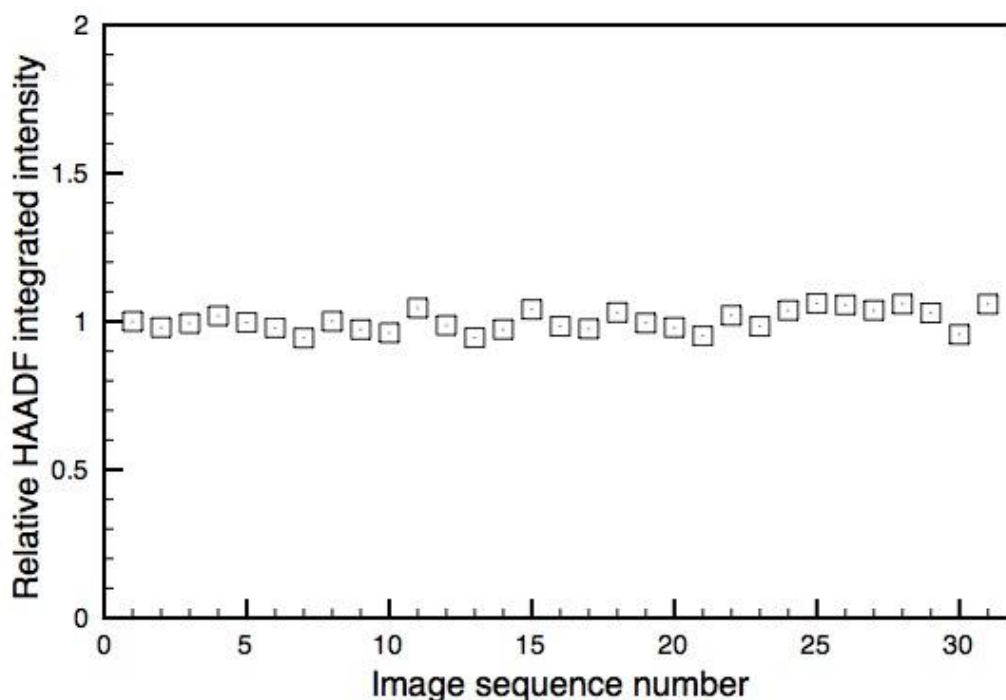


Figure 3.6. The integrated HAADF intensity of one $\text{Au}_{55}(\text{PPh}_3)_{12}\text{Cl}_6$ cluster as a function of scanning time. The HAADF integrated intensity was obtained in a series of continuous recorded HAADF STEM images of the same $\text{Au}_{55}(\text{PPh}_3)_{12}\text{Cl}_6$ cluster.²² The figure is from ref [22].

In Figure 3.6, we can see the cluster's integrated HAADF intensity in each image did not change significantly in the continuous imaging process. They are basically fluctuating around the first image's integrated HAADF intensity with a very small fluctuation. This small fluctuation can be due to the error of the STEM instrument. As there isn't any obvious change that occurred during the long time scanning, we concluded that the electron beam cannot break the clusters seriously under the current experimental condition, at least not in the first several scanning times. But the small variation of the atomic structure of the cluster during the electron beam scanning is

inevitable, especially after a long time scanning. So, using the STEM images recorded the first two scanning times to do the atomic structure analysis is very important in order to reduce the risk of the clusters structure being changed completely by the incident electron beam. Beside this, the effect of the electron beam may also be the reason of the amorphous structured clusters. Of course, the interaction between the cluster metal core, phosphine ligand and the amorphous carbon substrate surface can also be a possible reason for the slight change in structure of the cluster.

3.4.4.4 Discussion of the new assignment

It is quite different comparing our assignment for the atomic structure of the Au₅₅(PPh₃)₁₂Cl₆ clusters, which is a combination of the hybrid chiral motif and amorphous structures, with the previous assignments of the cuboctahedral or icosahedral structures. What's the reason for this? First, the hybrid chiral structure was initially proposed in 1998 as a bare cluster.² No one before has considered this hybrid structure as a candidate model for the Au₅₅(PPh₃)₁₂Cl₆ cluster. So, in the previous experimental study on the atomic structure of the Au₅₅(PPh₃)₁₂Cl₆ cluster, people didn't compare their data with this model.^{9,11,13,15} Second, the hybrid chiral structure can be considered to contain the structural elements from both cuboctahedral and icosahedral motifs. For example, from Figure 3.4 (b), we can see that the hybrid chiral configuration is like an assemblage of a closely packed fcc plane stick on an icosahedral cluster. This hybrid feature where the cluster has both cuboctahedral and icosahedral motifs, can explain the cuboctahedral feature found in the previous

EXAFS researches, and the icosahedral-like diffraction peak found in the previous XRD research. Furthermore, the mean coordination number of the hybrid chiral structure is 7.78, which is very close to the mean coordination number of the cuboctahedral structure, that is, 7.85. The previous EXAFS data also support well the hybrid chiral structure as the average coordination number obtained in the previous cuboctahedral assigned EXAFS studies (7.8⁹ and 7.3¹⁰) is closer to the hybrid chiral structure (7.78) than the cuboctahedral structure (7.85).^{11,13}

Another issue is the high percentage of the “amorphous” structure. In this research, the term “amorphous” is used to explain the structures that didn’t match with the hybrid, fcc, icosahedral or decahedral structure. These structures showed asymmetric pattern with a relatively wide range of aspect ratios. However, as the lowest energy structure of the Au₅₅ cluster is also asymmetric, we cannot rule out the possibility that there are other asymmetric structures with a medium energy between the hybrid structure and the ordered structure like fcc and icosahedral. In another word, the “amorphous” clusters can be considered as the “unassigned” clusters.

3.5 Conclusion

In conclusion, we find that the Schmid synthetic route does produce passivated clusters consistent with the formula for the Au₅₅(PPh₃)₁₂Cl₆ clusters as well as clusters containing from about 35 to 60 Au atoms. The fraction of clusters containing

54±1.5 Au atoms, as fractionated by the cluster “mass balance” (and assuming the standard ligand number), presents atomic structures, measured by aberration-corrected STEM which fit best the hybrid model (42%) and amorphous structures (58%). We found no evidence of the previously proposed cuboctahedral and icosahedral structures. However, the hybrid structure, first proposed for bare Au₅₅, contains both close-packed and icosahedral-type motifs and appears to rationalize the previous contradictory assignments. Looking forward, the combination of size-fractionation by the STEM mass balance method and atomic structure determination in the aberration-correction regime holds promise to reveal the isomeric structures of other nanoparticles.

Reference:

1. Schmid, G., Pfeil, R., Boese, R., Bandermann, F., Meyer, S., Calis, G. H. M. & van der Velden, J. W. A. $Au_{55}[P(C_6H_5)_3]_{12}Cl_6$ — ein Goldcluster ungewöhnlicher Größe. *Chem. Ber.* **114**, 3634–3642 (1981).
2. Garzón, I., Michaelian, K., Beltran, M. R., Posada-Amarillas, A., Ordejon, R., Artacho, E., Sanchez-Portal, D. & Soler, J. M. Lowest Energy Structures of Gold Nanoclusters. *Phys. Rev. Lett.* **81**, 1600–1603 (1998).
3. Schmid, G. & Chi, L. F. Metal clusters and colloids. *Adv. Mater.* **10**, 515–526 (1998).
4. Schmid, G. The relevance of shape and size of Au_{55} clusters. *Chem. Soc. Rev.* **37**, 1909–1930 (2008).
5. Chi, L., Hartig, M., Drechsler, T., Schwaack, Th., Seidel, C., Fuchs, H. & Schmid, G. Single-electron tunneling in Au_{55} cluster monolayers. *Appl. Phys. A Mater. Sci. Process.* **190**, 187–190 (1998).
6. Schmid, G., Baumle, M., Geerkens, M., Heim, I., Osemann, C., & Sawitowski, T. Current and future applications of nanoclusters. *Chem. Soc. Rev.* **28**, 179–185 (1999).
7. Schmid, G., Liu, Y. & Schumann, M. Quasi one-dimensional arrangements of $Au_{55}(PPh_3)_{12}Cl_6$ clusters and their electrical properties at room temperature. *Nano Lett.* **55**, 6–8 (2001).
8. Simon, U., Schön, G. & Schmid, G. The Application of Au_{55} Clusters as Quantum Dots. *Angew. Chemie Int. Ed. Engl.* **32**, 250–254 (1993).
9. Schmid, G., Pugin, R. & Sawitowski, T. Transmission electron microscopic and small angle X-ray diffraction investigations of $Au_{55}(PPh_3)_{12}Cl_6$ microcrystals. *Chem. Commun.* **55**, 1303–1304 (1999).

10. Marcus, M. A., Andrews, M. P. & Zegenhagen, J. Structure and vibrations of chemically produced Au_{55} clusters. *Phys. Rev. B* **42**, 3312–3316 (1990).
11. Fairbanks, M. C., Benfield, R. E., Newport, R. J. & Schmid, G. An EXAFS Study of the Cluster Molecule $Au_{55}(PPh_3)_{12}Cl_6$. *Solid State Commun.* **73**, 431–436 (1990).
12. Benfield, R. E., Grandjean, D., Kro, M., Pugin, R. & Sawitowski, T. Structure and Bonding of Gold Metal Clusters, Colloids, and Nanowires Studied by EXAFS, XANES, and WAXS. *J. Phys. Chem. B.* **105**, 1961–1970 (2001).
13. Vogel, W., Rosner, B. & Tesche, B. Structural Investigations of Au_{55} Organometallic Complexes by X-ray Powder Diffraction and Transmission Electron Microscopy. *J. Phys. Chem.* **97**, 11611–11616 (1993).
14. Pei, Y., Shao, N., Gao, Y. & Zeng, X. C. Investigating active site of gold nanoparticle $Au_{55}(PPh_3)_{12}Cl_6$ in selective oxidation. *ACS Nano* **4**, 2009–2020 (2010).
15. Rapoport, D. & Vogel, W. Ligand-Stabilized Metal Clusters: Reinvestigation of the Structure of ' $Au_{55}[P(C_6H_5)_3]_{12}Cl_6$ '. *J. Phys. Chem. B* **101**, 4175–4183 (1997).
16. Wallenberg, L., Bovin, J. & Schmid, G. On the crystal structure of small gold crystals and large gold clusters. *Surf. Sci.* **156**, 256–264 (1985).
17. von Issendorff, B. & Palmer, R. E. A new high transmission infinite range mass selector for cluster and nanoparticle beams. *Rev. Sci. Instrum.* **70**, 4497 (1999).
18. Pratontep, S., Preece, P., Xirouchaki, C., Palmer, R. E., Sanz-Navarro, C. F., Kenny, S. D. & Smith, R. Scaling relations for implantation of size-selected Au, Ag, and Si clusters into graphite. *Phys. Rev. Lett.* **90**, 055503 (2003).
19. Pratontep, S., Carroll, S. J., Xirouchaki, C., Streun, M. & Palmer, R. E.

- Size-selected cluster beam source based on radio frequency magnetron plasma sputtering and gas condensation. *Rev. Sci. Instrum.* **76**, 045103 (2005).
20. Young, N. P., Li, Z. Y., Chen, Y., Palomba, S., Di Vece, M. & Palmer, R. E. Weighing supported nanoparticles: Size-selected clusters as mass standards in nanometrology. *Phys. Rev. Lett.* **101**, 246103 (2008).
 21. Wang, Z. W. Toikkanen, O., Yin, F., Li, Z. Y., Quinn, B. M. & Palmer, R. E. Counting the atoms in supported, monolayer-protected gold clusters. *J. Am. Chem. Soc.* **132**, 2854–2855 (2010).
 22. Jian, N., Stapelfeldt, C., Hu, K.-J., Fröba, M. & Palmer, R. E. Hybrid atomic structure of the Schmid cluster $\text{Au}_{55}(\text{PPh}_3)_{12}\text{Cl}_6$ resolved by aberration-corrected STEM. *Nanoscale* **7**, 885–888 (2015).
 23. Wang, Z. W. & Palmer, R. E. Intensity calibration and atomic imaging of size-selected Au and Pd clusters in aberration-corrected HAADF-STEM. *J. Phys. Conf. Ser.* **371**, 012010 (2012).
 24. Williams, D. B. & Carter, C. B. *Transmission Electron Microscopy—A Textbook for Materials Science*. Micron (Springer, 2008).
 25. Dwyer, C. Simulation of scanning transmission electron microscope images on desktop computers. *Ultramicroscopy* **110**, 195–198 (2010).
 26. Wang, Z. W. & Palmer, R. E. Experimental evidence for fluctuating, chiral-type Au_{55} clusters by direct atomic imaging. *Nano Lett.* **12**, 5510–5514 (2012).
 27. Plant, S. R., Cao, L., Yin, F., Wang, Z. W. & Palmer, R. E. Size-dependent propagation of Au nanoclusters through few-layer graphene. *Nanoscale* **6**, 1258–1263 (2014).
 28. Wells, D. M., Rossi, G., Ferrando, R. & Palmer, R. E. Metastability of the atomic structures of size-selected gold nanoparticles. *Nanoscale* **7**, 6498–6503

- (2015).
29. Wang, Z. W., Toikkanen, O., Quinn, B. M. & Palmer, R. E. Real-space observation of prolate monolayer-protected Au_{38} clusters using aberration-corrected scanning transmission electron microscopy. *Small* **7**, 1542–1545 (2011).
 30. Li, Z. Y., Young, N. P., Di Vece, M., Palomba, S., Palmer, R. E., Bleloch, A. L., Curley, B. C., Johnston, R. L., Jiang, J. & Yuan, J. Three-dimensional atomic-scale structure of size-selected gold nanoclusters. *Nature* **451**, 46–8 (2008).
 31. Koch, C. DETERMINATION OF CORE STRUCTURE PERIODICITY AND POINT DEFECT by. *Dissertation* (Arizona State University, 2002).
 32. Wang, Z. W. & Palmer, R. E. Direct atomic imaging and dynamical fluctuations of the tetrahedral $Au(20)$ cluster. *Nanoscale* **4**, 4947–9 (2012).
 33. Malola, S., Lehtovaara, L., Knoppe, S., Hu, K., Palmer, R. E., Burgi, T. & Hakkinen, H. $Au_{40}(SR)_{24}$ Cluster as a Chiral Dimer of 8-Electron Superatoms: Structure and Optical Properties. *J. Am. Chem. Soc.* **40**, 8–11 (2012).

CHAPTER 4

HAADF STEM STUDY OF THE VARIATION OF THE CORE ATOMIC STRUCTURE OF THIOLATED $(\text{Au}_x\text{Ag}_{1-x})_{312\pm55}$ NANOCCLUSERS WITH COMPOSITION

Most of the text and figures in this chapter have been used in my publication (with me as the first author): Jian, N. & Palmer, R. E. Variation of the Core Atomic Structure of Thiolated $(\text{Au}_x\text{Ag}_{1-x})_{312\pm55}$ Nanoclusters with Composition from Aberration-Corrected HAADF STEM. *J. Phys. Chem. C* **119**, 11114–11119 (2015).

4.1 Overview

In this chapter, the atomic structure of thiol-protected $(\text{Au}_x\text{Ag}_{1-x})_{312\pm55}$ clusters is investigated as a function of different composition (x) by using aberration-corrected scanning transmission electron microscopy (STEM), on high angle annular dark field (HAADF) mode, combined with multislice electron scattering simulations of the STEM images. Three structural motifs are considered: icosahedral, fcc and icosahedral. A combination of STEM intensity and diameter measurements is used to “fractionate” the deposited sample according to composition for atomic resolution imaging. We find that the structure depends critically on composition: the icosahedral

structure dominates the Ag-rich clusters, while the fcc structure dominates the Au-rich clusters. The icosahedral structure was only observed in clusters with Au content greater than 30% Au. The result should be relevant to the catalytic application of this new class of nanosystems.

4.2 Introduction

Nanoclusters are extensively studied because of their unique physical, chemical and catalytic properties.¹⁻⁵ Small alloy nanoclusters are of increasing interest⁶⁻¹¹ due to their distinctive size and compositional effects,^{6,12} which suggest a number of applications in catalysis, optics, engineering and electronics. In recent years, the syntheses of alloy nanoclusters become more efficient and accurate in size and composition, from sub-10 nm AuAg alloy nanoparticles to size-selected $Au_{25-n}Ag_n(SR)_{18}$, $Au_{38-n}Ag_n(SR)_{24}$, $Au_{144-n}Ag_n(SR)_{60}$, etc.¹³⁻²⁰ Cu-Au, and Pd-Au analogues of 25-atom and 144-atom species are also reported.²¹⁻²⁴ Monolayer-protected alloy nanoparticles are an emerging target of several researches.²⁵⁻²⁸ Thus, the atomic structures of alloy nanoclusters need to be investigated in order to correlate their properties with their structures. The optimum structure of alloy nanoclusters (up to 50 metal atoms) have been investigated, which found that the clusters' optimum structure was not trivial and was highly affected by their material, size and composition.²⁹ The x-ray crystal structure of smaller $Au_{25-n}Ag_n(SR)_{18}$ and $Ag_{44-n}Au_n(SR)_{30}$ have been determined,³⁰ but the structure of the larger alloy clusters are yet to be determined. Another research for the lowest energy

structure of Ag-Pd nanoclusters with specific size and composition, shows a strong dependence of structure on the composition.³¹

Here we present the atomic structure of phenylethanethiolate-protected ($-\text{SCH}_2\text{CH}_2\text{Ph}$) $\text{Au}_x\text{Ag}_{1-x}$ bimetallic nanoclusters containing 312 ± 55 atoms, with size and composition determined from STEM. Samples of variable composition are imaged using aberration-corrected STEM and compared with multislice simulation atlases. The projected area of the cluster in the STEM images is utilized to determine the total metal nuclearity, while calibrated HAADF-STEM integrated intensity measurements were employed to obtain the bimetallic cluster composition. Our results show that the atomic structures of MP- $(\text{Au}_x\text{Ag}_{1-x})_{312\pm55}$ nanoclusters are completely dependent on the composition: most Au-rich cluster structures are fcc, while most Ag-rich clusters are icosahedral. The icosahedral structure was only found in clusters with less than 30% Au.

4.3 Experimental details

The clusters investigated were provided by Dr. Amala Dass and Dr. Chanaka Kumara in Mississippi University. The detailed synthesis of 59 kDa, $(\text{Au}_x\text{Ag}_{1-x})_{312\pm55}$ involves three major steps. The first step: an aqueous solution (30 mL) containing 0.45 mmol of HAuCl_4 and 0.45 mmol of AgNO_3 (1:1 molar ratio) was mixed with a toluene solution (30 mL) of tetraoctylammonium bromide, TOABr. After stirring for 30 minutes, the turbid organic phase was separated and the phenylethanethiol was added. This mixture was then stirred for another 30 minutes at room temperature and then

cooled to 0°C with ice for 30 minutes. An aqueous solution of NaBH₄ (20 mmol/20 mL of distilled water) at 0°C was rapidly added to the reaction mixture under vigorous stirring. After 3 hours, the organic layer was separated and dried by rotary evaporation. This product was washed with methanol several times to remove any thiol and other by-products. In the second step, 150 mg of the crude product was subjected to thermochemical treatment at 80°C with excess phenylethanethiol (0.8 mL) to remove meta-stable nanoparticles. This process was time monitored by matrix-assisted laser desorption/ionization mass spectrometry (MALDI MS). After 5 hours, the reaction was stopped and the product washed with methanol several times to remove any excess thiol and other by-products. This step narrows down the size distribution of the nanoparticles. In the third step, the product was extracted with toluene and subjected to solvent fractionation using a toluene/methanol mixture to isolate the nanoparticle at 59 kDa. The monometallic, Au-only product of the above synthesis was assigned a composition of Au₃₁₂(SCH₂CH₂Ph)₈₄, based on a peak at 76.3 kDa.^{32,33} The 1:1 molar ratio of the HAuCl₄:AgNO₃ starting materials used in this work yielded a peak at 59 (±4%) kDa, which is quite broad and does not lead to a unique nuclearity and ligand number assignment per se. (We will see below that the STEM data are able to demonstrate the range of core size and metal composition in the nanoparticle distribution after deposition). However, based on the assumption that the ligand number is the same as assigned previously to the monometallic species,³³ and that the average Au:Ag ratio is 1:1, we obtain from the 59 kDa peak a nuclearity of 312, and thus an estimated mean composition of Au₁₅₆Ag₁₅₆(SR)₈₄.

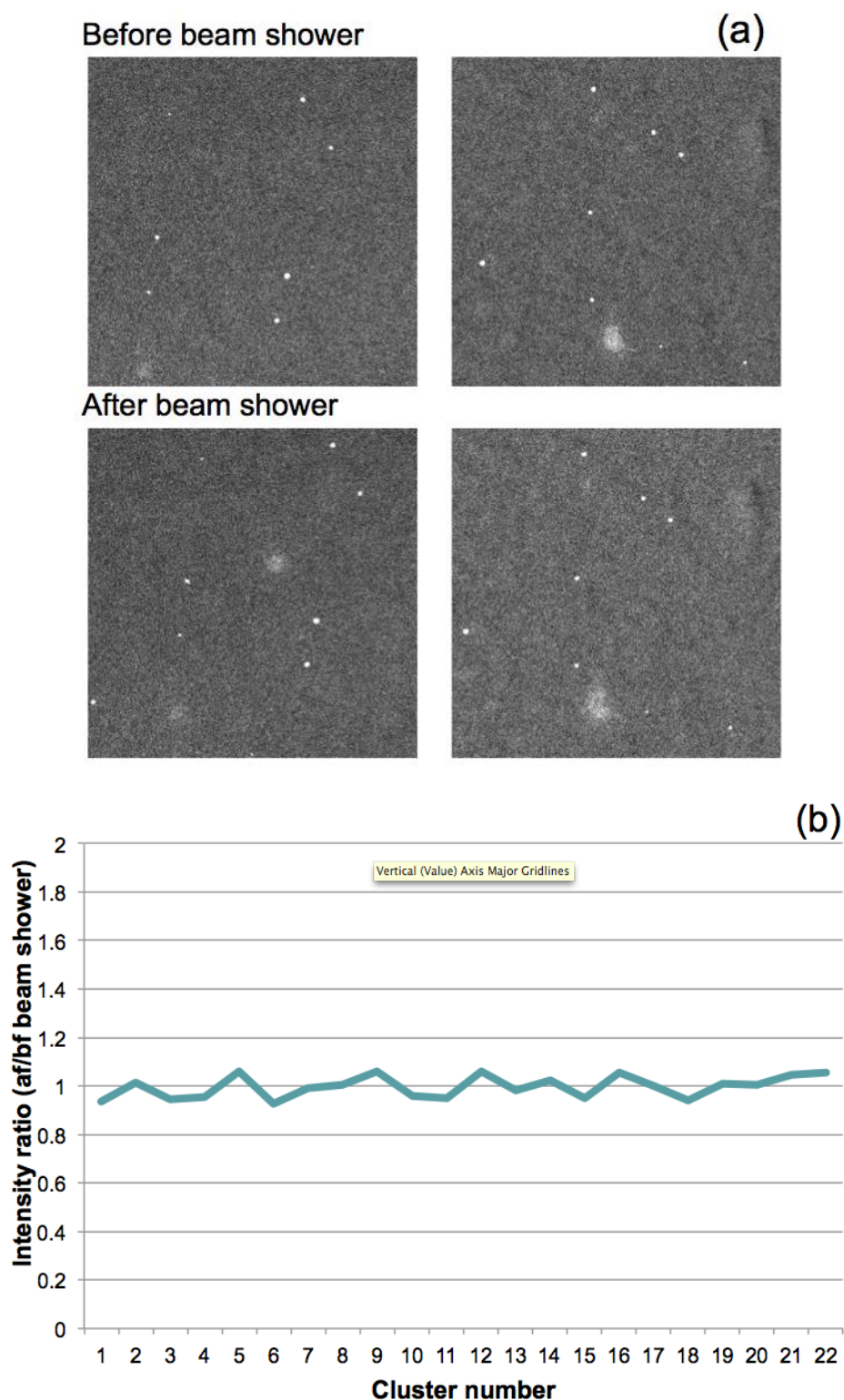


Figure 4.1. (a) Example images taken before and after the beam shower. (b) HAADF intensity ratio of each cluster in the STEM images taken after and before the beam shower.

The dried alloy cluster powder from the final synthetic product was dissolved in toluene and drop cast onto half of a 400-mesh TEM grid covered with an amorphous carbon film. Size-selected Au_{923} clusters (with an error of 5%), generated by magnetron sputtering, gas condensation cluster beam source and mass selected with a lateral time-of-flight (TOF) mass selector,^{34–36} were deposited onto the other half of the same TEM grid as a calibration tool. The cluster beam current was 50pA, deposition time was 60 seconds, and the number of clusters deposited was $\sim 1.9 \times 10^{10}$. Our 200 kV JEOL 2100F STEM with Cs corrector (CEOS) was equipped with an HAADF detector operating with inner angle of 62 mrad and outer angle 164 mrad. All images were typically taken in less than 2.7 seconds (equal to two scans over the whole image area) with an electron dose of $\sim 7.1 \times 10^3$ electrons \AA^{-2} at 12M magnification to minimize the beam damage. A 15-minute beam shower without enhanced electron beam at 400K magnification (total electron dose is $\sim 3.4 \times 10^4$ electrons \AA^{-2}) was employed to minimize the contamination. The beam shower did not damage the sample: images taken before and after the 15-minute beam shower are presented in Figure 4.1, where the results showed no evidence of cluster movement nor significant atom loss. The multislice simulations employed corresponded to bare magic-number Au_{309} clusters: cuboctahedral, icosahedral and icosidodecahedral structures were generated using the QSTEM software package³⁷ for comparison with the experimental results.

4.4 Results and discussion

4.4.1 Metal core size of thiolated $(\text{Au}_x\text{Ag}_{1-x})_{312\pm55}$ nanoclusters

Before we can investigate the thiolated $(\text{Au}_x\text{Ag}_{1-x})_{312\pm55}$ nanoclusters' atomic structure, the size (i.e. nuclearity) and composition of individual clusters, as found on the surface, are required. The HAADF integrated intensity distribution is shown in Figure 4.2 (a). There are three peaks in the distribution, forming a harmonic series, the first peak around 4×10^8 is assigned to be the peak of the monomer, while multiples are assigned to dimer and trimer produced by aggregation in the solution, or on the surface. Since the sample is an alloy, the atom counting method, based simply on the HAADF intensities as employed for mono-metallic clusters,^{38–40} cannot be applied. Thus, since most clusters observed are approximately circular in projection, we approximate the clusters to be spheres and convert the measured area in the STEM images into a volume, given the bond lengths of Au and Ag are very similar (288.4 pm and 288.9 pm), we can easily calculate the total number of metal atoms in the cluster. The validity of this method is demonstrated against size-selected Au_{561} and Au_{923} clusters, as detailed in the appendix.

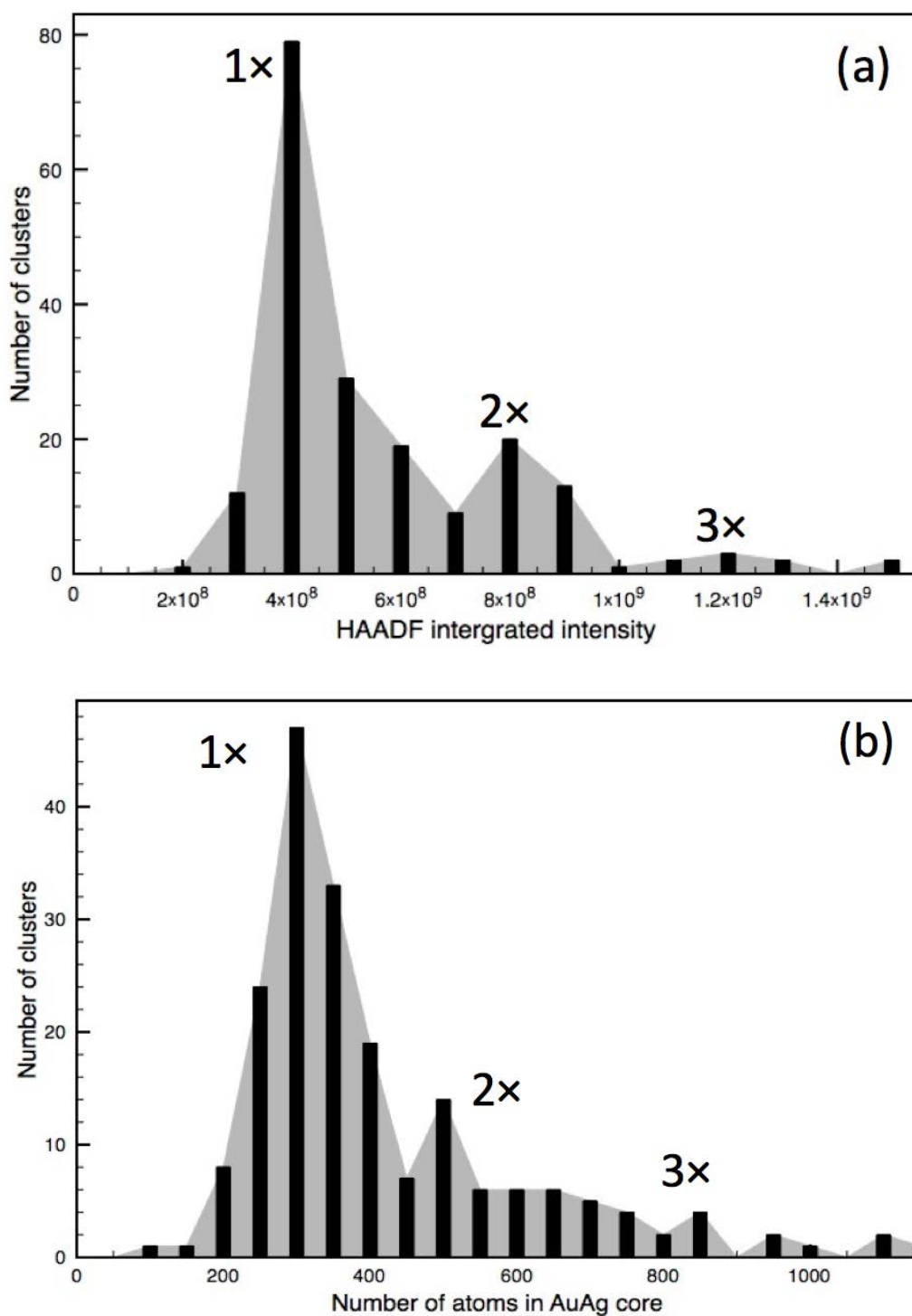


Figure 4.2. (a) Histogram of: (a) HAADF integrated intensity, and (b) Au-Ag core nuclearity (obtained from the measured diameters) for 202 individual thiolate protected $(Au_xAg_{1-x})_{312 \pm 55}$ clusters. Both (a) and (b) show the distributions are consistent with the discrete multiples of monomers.

4.4.2 Composition of thiolated $(Au_xAg_{1-x})_{312 \pm 55}$ nanocluster core

The number of atoms in each alloy cluster obtained by the method described above is shown in Figure 4.2 (b). With this size (nuclearity) information, we can now obtain the composition of each alloy cluster from the atom counting method,³⁸⁻⁴⁰ using size-selected Au clusters as the mass balance. The Au proportion is:

$$P_{Au} = \frac{N_{Au}}{N_T} = \frac{k}{k-1} - \frac{I_T - I_{ligand}}{I_{Au\ atom} (k-1) \times N_T}$$

$$k = \left(\frac{Z_{Ag}}{Z_{Au}}\right)^n \quad (1)$$

Here, N_T is the total number of atoms in one Au-Ag alloy cluster, N_{Au} is the number of Au atoms, Z_{Ag} and Z_{Au} are the atomic numbers for Ag and Au, respectively, I_T is the total HAADF integrated intensity of the cluster, I_{Au} is the intensity of one Au atom (obtained from the size-selected Au_{923} clusters), and I_{ligand} is the intensity of a ligand, based on the calibrated Z-contrast exponent, n .^{41,42} In the size region of 312 ± 55 , we use a tentative ligand number of 84, as previously assigned to the mono-metallic composition,³³ which is consistent with the MALDI data as noted above.

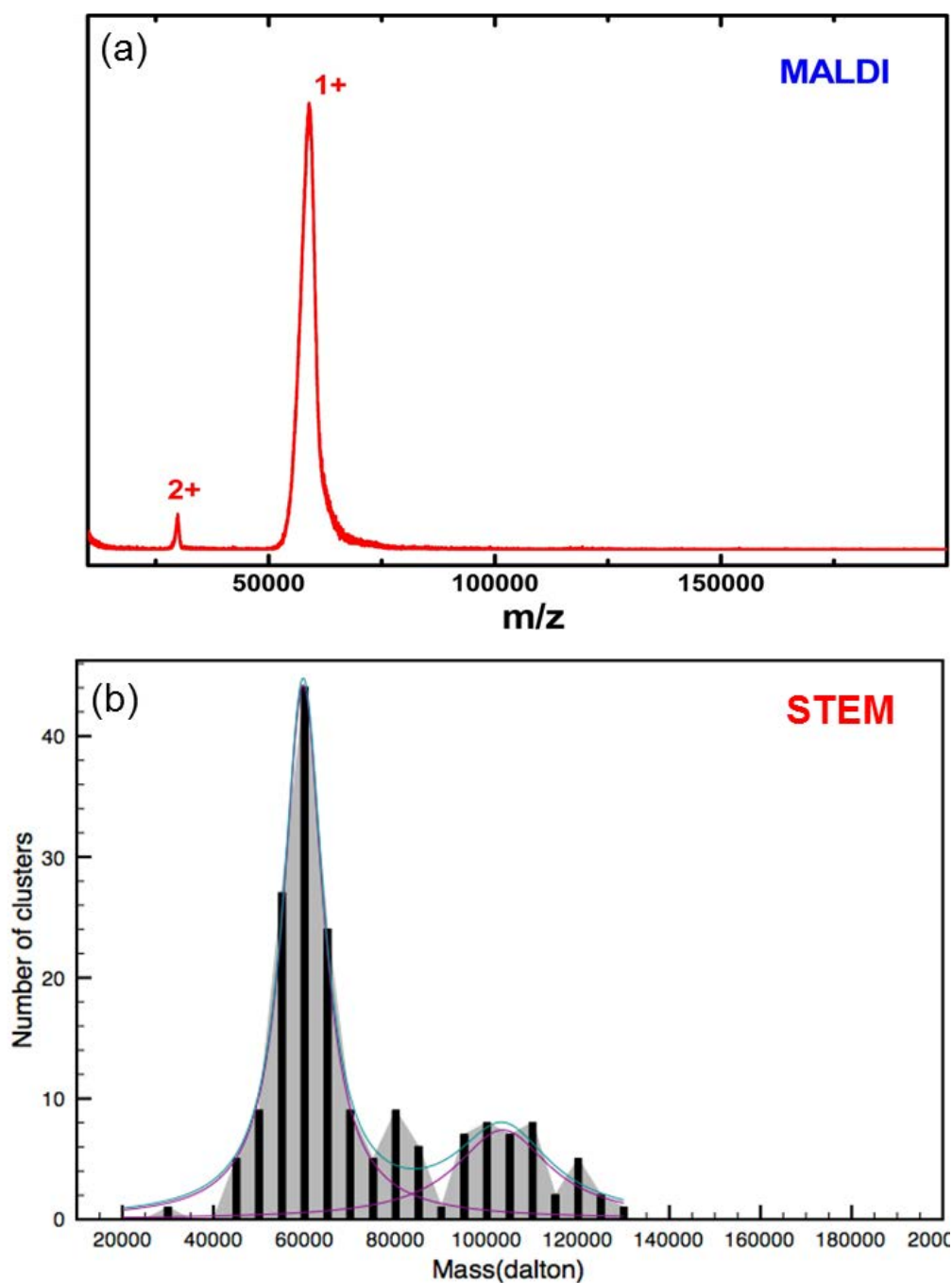


Figure 4.3. (a) MALDI mass spectrometry of the thiol-protected Au-Ag alloy clusters prepared using a 1:1 molar ratio of $HAuCl_4:AgNO_3$ starting materials. The 2+ peak at around 30 kDa is assigned to be the double charged peak of the molecular ions. The single charged peak is around 59 kDa. (b) The mass distribution of the same thiolate Au-Ag alloy clusters based on the analysis on the STEM data. The Gaussian fit of the main peak is at 59.68 kDa.

A mass distribution of the thiolated alloy clusters based on the analysis results from STEM data was built and compared with the MALDI mass spectrum of the same sample to test the accuracy of our method on the core size of alloy clusters. The MALDI mass spectrum is shown in Figure 4.3 (a). The 2+ peak, at approximately 30 kDa, is assigned to be the doubly charged peak of the molecular ions with a single charge. The single charged peak occurs at approximately 59 kDa. The number of atoms in the metal core and the Au-Ag composition of every single thiolated cluster in the STEM image can be obtained by analysis, as shown above. So a mass distribution of the clusters has been formed, which is shown in Figure 4.3 (b). The first Gaussian fit peak is at 59.68 kDa, which is very close to the 59 kDa value in the MALDI spectrum, showing the analysis method we used had very good accuracy. We can see that there are also other size clusters observed in the Figure 4.3 (b), and the 59.68 kDa peak is a little broader than in the MALDI mass spectrum. This can be the result of the aggregation of the original clusters during the experimental process, like dissolving or drying the sample. Also, there may be some size clusters that were not very efficiently ionized in the MALDI experiment. Beside these reasons, the error in the atom counting also cannot be ignored. The size selected clusters have an error of $\pm 5\%$ which will be propagated to the result of the atom counting method.

4.4.3 Atomic structure of thiolated $(Au_xAg_{1-x})_{312\pm55}$ nanocluster cores

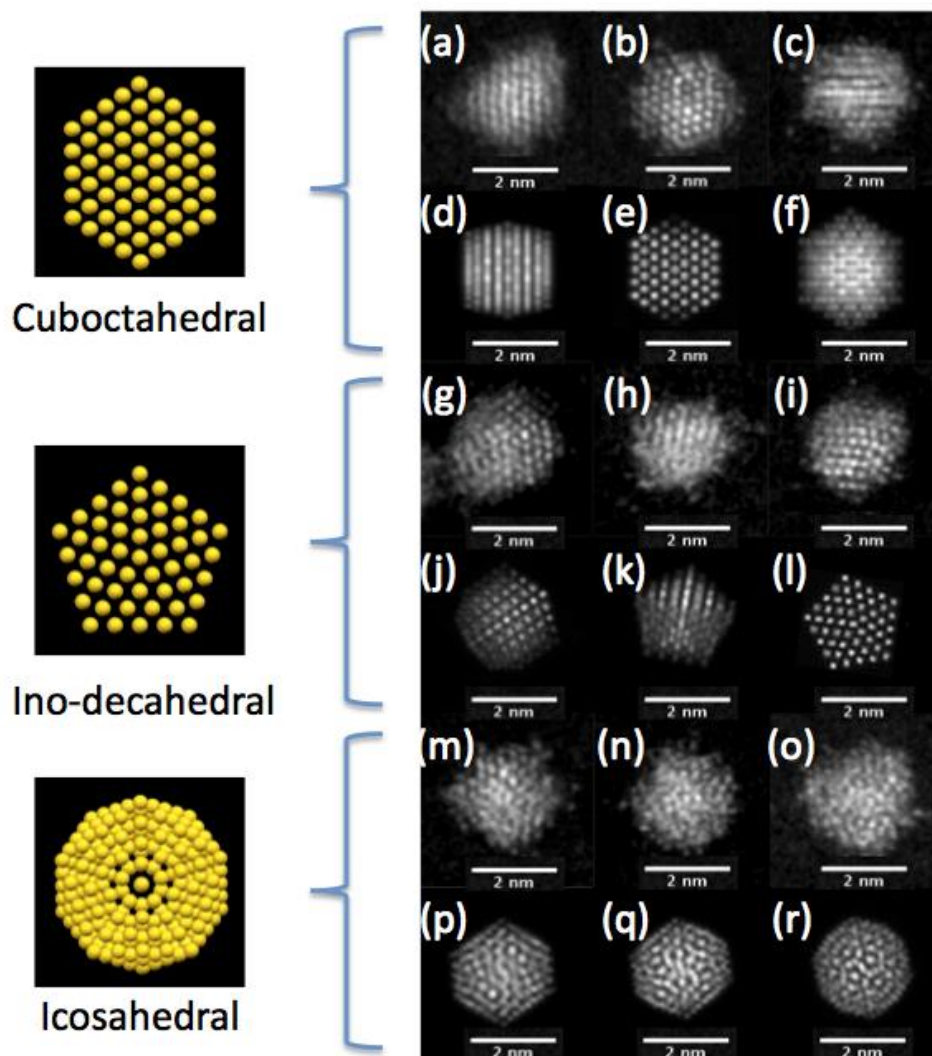


Figure 4.4. Typical HAADF STEM images of thiolated $(Au_xAg_{1-x})_{312\pm55}$ clusters. (a)-(c), (g)-(i), and (m)-(o) are clusters assigned to the cuboctahedral, Ico-decahedral or icosahedral structures, based on the corresponding simulated images (for bare Au_{309} clusters) displayed in (d)-(f), (j)-(l) and (p)-(r), respectively.

After obtaining the nuclearity and composition of the deposited alloy clusters, we can

investigate the atomic structure of the clusters $(\text{Au}_x\text{Ag}_{1-x})_{312 \pm 55}\text{SR}_{84}$ with the multislice simulation atlas^{43–46} as a function of composition (x). First, in the high-resolution HAADF STEM images, all the bimetallic clusters showed intermixing alloy formation, no significant core-shell, multishell or subcluster features were found. Figure 4.4 shows an illustrative set of HAADF STEM images of Au-Ag alloy clusters with their corresponding simulation images (for bare Au_{309} clusters). Thus, for example, Figures 4.4 (a) to (c) are the experimental images of clusters assigned to the fcc structures, and (d) to (f) are their corresponding simulation images. These show a good match with the experimental images. Images corresponding to the Ino-decahedral structures are shown in Figures 4.4 (g) to (i) whereas the icosahedral structure images are shown in Figures 4.4 (m) to (r). Some experimental images did not match the simulated images perfectly. We note that the models used for our simulations are ideal, symmetric, full shell structures, but many clusters grew asymmetrically.⁴⁷ For example, in Fig. 2(i), the central axis of decahedron is markedly off centre. Moreover, we know that the thiol ligands will have a strong effect on the surface of the clusters, with surface Au atom incorporated into the ligand shell.^{48,49} These displaced surface atoms will affect the match between the experimental STEM images and the corresponding simulated images. However, the core structure of the clusters can still be recognized,^{43,50} via distinctive motifs like the icosahedron's “circle with dot inside” or the five-fold symmetry of the decahedron, as shown in given specific panels.

4.4.4 Variation of Au-Ag metal core structure with composition

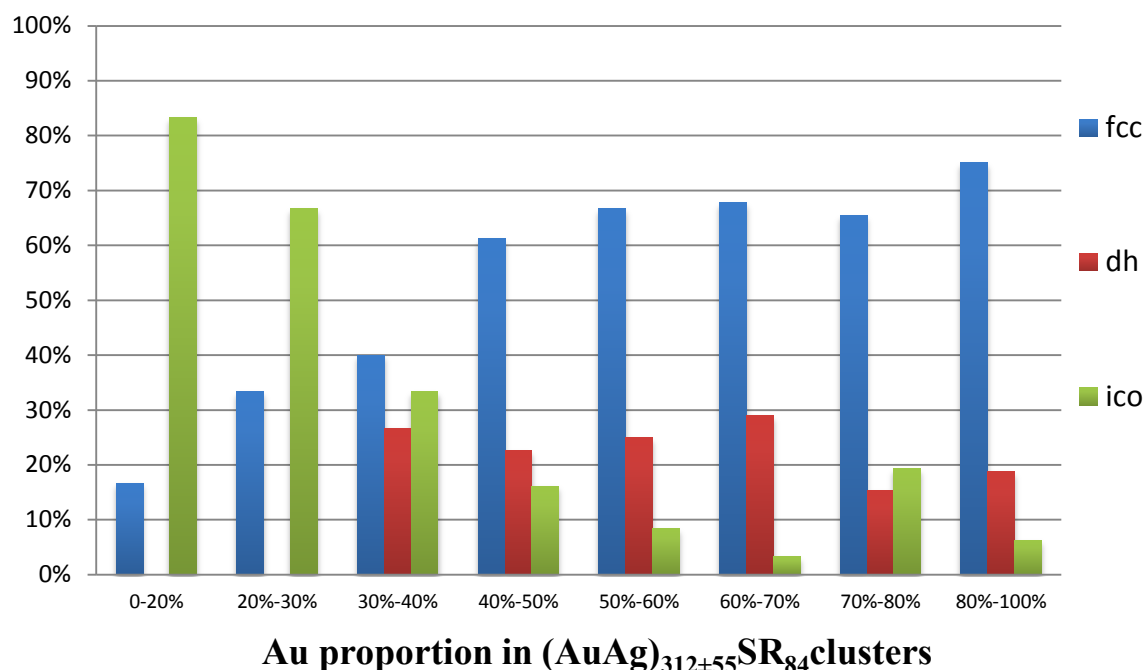


Figure 4.5. The proportion of the fcc, ino-decahedral and icosahedral motifs for thiolated $(\text{Au}_x\text{Ag}_{1-x})_{312 \pm 55}$ clusters with the composition varying from pure Ag (left) to pure Au (right).

Figure 4.5 shows the main outcome of the work, the relative proportion of different structural isomers of $(\text{Au}_x\text{Ag}_{1-x})_{312 \pm 55} \text{SR}_{84}$ as a function of the Au/Ag compositions. The amorphous or unidentified structure clusters ($\sim 42\%$ of all clusters) were removed from the statistics to focus on relative abundance of ordered structures with varying Au/Ag composition. From Figure 4.5, the Au/Ag composition has a profound impact on the proportion of the different isomers. There is a clear trend, namely, that in the Ag rich region, the icosahedral structure is dominant, with the percentage declining smoothly as the Au proportion increases, while in the fcc motif, which shows very

low abundance in the Ag rich clusters, rises continuously as the Au proportion increases. Their crossover is at a composition of around 40% Au. The decahedron was only found in clusters with an Au content greater than 30%, after which the percentage of decahedral clusters remains between 18% and 30% into the Au-rich region. A comparison analysis of the structure distribution of clusters with size, of above and below 312 atoms, has also been employed to avoid the possibility of a size effect on the cluster atomic structure. The results show no significant difference and remain the trend of the variation of the atomic structure. We also note that the wide range of the Ag-Au composition ratio, and indeed the relatively broad range of size, derived from STEM, are not reflected in the MALDI mass spectrum discussed above. Further work is warranted to explore this discrepancy in terms of the fundamental nature of the measurements.

4.4.5 Discussion of the atomic structure variation with composition

Theoretical prediction of the atomic structure of noble clusters as a function of size appears to vary widely.⁵¹⁻⁵³ The experimental results reported here are consistent with theoretical simulations which employed the Gupta potential for clusters. Specifically, this theoretical work finds a transition from the icosahedral to fcc structure with increasing size. For Au clusters, the crossover size is around 30 atoms, while for Ag the crossover size is much higher, around 300 to 400 atoms.^{51,52} This difference in behaviour is associated with the relative values of bulk modulus and cohesive energy

in Au and Ag. If we assume that the properties of Au-Ag alloy clusters vary monotonically from Au-rich to Ag-rich clusters, as previous research suggests,^{15,54} the theory is entirely compatible with our data for size 312 ± 55 atoms, showing high fcc and low icosahedral proportions in the Au-rich cluster, the opposite for the Ag-rich clusters.

4.5 Conclusions

In conclusion, we have exploited the capability of HAADF-STEM to determine the size of AuAg nanoalloy cluster from the projected areas and the Au-Ag composition from the HAADF intensities calibrated against size-selected clusters. The experimental atomic structures of thiolated $(\text{Au}_x\text{Ag}_{1-x})_{312\pm55}$ clusters deposited on amorphous carbon were compared with multislice image simulations for fcc, icosahedral and decahedral motifs. We found that in the size range of 312 ± 55 atoms, the isomer proportions vary smoothly with the change in composition from pure Ag to Au. The icosahedral structure dominates for Ag-rich composition and fcc dominates the Au-rich region, with the decahedron observed for Au-rich clusters. The work demonstrates the power of aberration-corrected STEM in revealing the atomic structure of bimetallic clusters as a function of composition. The data helps to distinguish between different theoretical approaches and may form a useful test case for future theoretical work. We believe that the experimental approach employed has much potential to be widely used to investigate the size, composition and atomic structures of other binary nanostructures.

Reference:

1. Baletto, F. & Ferrando, R. Structural properties of nanoclusters: Energetic, thermodynamic, and kinetic effects. *Rev. Mod. Phys.* **77**, 371–423 (2005).
2. De Heer, W. A. The physics of simple metal clusters: Experimental aspects and simple models. *Rev. Mod. Phys.* **65**, 611–676 (1993).
3. Schmid, G., Baumle, M., Geerkens, M., Heim, I., Osemann, C. & Sawitowski, T. Current and future applications of nanoclusters. *Chem. Soc. Rev.* **28**, 179–185 (1999).
4. Daniel, M. C. M. & Astruc, D. Gold Nanoparticles: Assembly, Supramolecular Chemistry, Quantum-Size Related Properties and Applications toward Biology, Catalysis and Nanotechnology,. *Chem. Rev.* **104**, 293–346 (2004).
5. Marks, L. D. Experimental Studies of Small Particle Structures. *Reports Prog. Phys.* **57**, 603–649 (1994).
6. Ferrando, R., Jellinek, J. & Johnston, R. L. Nanoalloys: From Theory to Applications of Alloy Clusters and Nanoparticles. *Chem. Rev.* **108**, 846–904 (2008).
7. Schmid, G., West, H., Malm, J., Bovin, J. & Grenthe, C. Catalytic Properties of Layered Gold- Palladium Colloids. *Inorg. Chem.* **2**, 1099–1103 (1996).
8. Caps, V., Arrii, S. & Morfin, F. Structures and associated catalytic properties of well-defined nanoparticles produced by laser vaporisation of alloy rods. *Faraday Discuss.* **138**, 241–256 (2008).
9. Ferrer, D., Torres-Castro, A., Gao, X., Sepulveda-Guzman, S., Ortiz-Mendez, U. & Jose-Yacaman, M. Three-layer core/shell structure in Au-Pd bimetallic nanoparticles. *Nano Lett.* **7**, 1701–1705 (2007).
10. Toshima, N. & Yonezawa, T. Bimetallic nanoparticles—novel materials for

- chemical and physical applications. *New J. Chem.* **22**, 1179–1201 (1998).
11. Yasuda, H., Kameoka, T., Sato, T., Kijima, N. & Yoshimura, Y. Sulfur-tolerant Pd–Pt/Al₂O₃–B₂O₃ catalyst for aromatic hydrogenation. *Appl. Catal. A Gen.* **185**, 199–201 (1999).
 12. Ruban, A., Skriver, H. & Nørskov, J. Surface segregation energies in transition-metal alloys. *Phys. Rev. B* **59**, 15990–16000 (1999).
 13. Li, Y., Wang, Z. W., Chiu, C-Y., Ruan, L., Yang, W., Yang, Y., Palmer, R. E. & Huang, Y. Synthesis of bimetallic Pt-Pd core-shell nanocrystals and their high electrocatalytic activity modulated by Pd shell thickness. *Nanoscale* **4**, 845 (2012).
 14. Mallin, M. & Murphy, C. Solution-phase synthesis of sub-10 nm Au-Ag alloy nanoparticles. *Nano Lett.* **2**, 10–12 (2002).
 15. Kariuki, N. N., Luo, J., Maye, M. M., Hassan, S. A., Menard, T., Naslund, H. R., Lin, Y., Wang, C., Engelhard, M. H. & Zhong, C-J. Composition-controlled synthesis of bimetallic gold-silver nanoparticles. *Langmuir* **20**, 11240–11246 (2004).
 16. Li, Z. Y., Wilcoxon, J. P., Yin, F., Chen, Y., Palmer, R. E. & Johnston, R. L. Structures and optical properties of 4–5 nm bimetallic AgAu nanoparticles. *Faraday Discuss.* **138**, 363–373 (2008).
 17. Kumara, C., Aikens, C. M. & Dass, A. X-ray Crystal Structure and Theoretical Analysis of Au_{25-x}Ag_x(SCH₂CH₂Ph)(18)(-) Alloy. *J. Phys. Chem. Lett.* **5**, 461–466 (2014).
 18. Kumara, C. & Dass, A. AuAg alloy nanomolecules with 38 metal atoms. *Nanoscale* **4**, 4084 (2012).
 19. Jupally, V. R. & Dass, A. Synthesis of Au₁₃₀(SR)₅₀ and Au_{130-x}Ag_x(SR)₅₀

- nanomolecules through core size conversion of larger metal clusters. *Phys. Chem. Chem. Phys.* **16**, 10473–9 (2014).
20. Kumara, C. & Dass, A. $(AuAg)_{144}(SR)_{60}$ alloy nanomolecules. *Nanoscale* **3**, 3064–3067 (2011).
 21. Negishi, Y., Munakata, K., Ohgake, W. & Nobusada, K. Effect of copper doping on electronic structure, geometric structure, and stability of thiolate-protected Au_{25} nanoclusters. *J. Phys. Chem. Lett.* **3**, 2209–2214 (2012).
 22. Negishi, Y., Kurashige, W., Niihori, Y., Iwasa, T. & Nobusada, K. Isolation, structure, and stability of a dodecanethiolate-protected Pd_1Au_{24} cluster. *Phys. Chem. Chem. Phys.* **12**, 6219–25 (2010).
 23. Dharmaratne, A. C. & Dass, A. $Au_{144-x}Cu_x(SC_6H_{13})_{60}$ nanomolecules: effect of Cu incorporation on composition and plasmon-like peak emergence in optical spectra. *Chem. Commun. (Camb)*. **50**, 1722–4 (2014).
 24. Kothalawala, N., Kumara, C., Ferrando, R. & Dass, A. $Au(144-x)Pd(x)(SR)_{60}$ nanomolecules. *Chem. Commun. (Camb)*. **49**, 10850–2 (2013).
 25. Hostetler, M. J., Zhong, C.-J., Yen, B. K. H., Andereg, J., Gross, S. M., Evans, N. D., Porter, M. & Murray, R. W. Stable, Monolayer-Protected Metal Alloy Clusters. *J. Am. Chem. Soc.* **120**, 9396–9397 (1998).
 26. Philip, R., Kumar, G. R., Sandhyarani, N. & Pradeep, T. Picosecond optical nonlinearity in monolayer-protected gold, silver, and gold-silver alloy nanoclusters. *Phys. Rev. B - Condens. Matter Mater. Phys.* **62**, 13160–13166 (2000).
 27. Shon, Y. S., Dawson, G. B., Porter, M. & Murray, R. W. Monolayer-protected bimetal cluster synthesis by core metal galvanic exchange reaction. *Langmuir* **18**, 3880–3885 (2002).

28. Fields-Zinna, C. a., Crowe, M. C., Dass, A., Weaver, J. E. F. & Murray, R. W. Mass spectrometry of small bimetal monolayer-protected clusters. *Langmuir* **25**, 7704–7710 (2009).
29. Ferrando, R., Fortunelli, A. & Johnston, R. L. Searching for the optimum structures of alloy nanoclusters. *Phys. Chem. Chem. Phys.* **10**, 640–9 (2008).
30. Yang, H., Wang, Y., Huang, H., Gell, L., Lehtovaara, L., Malola, S., Hakkinen, H. & Zheng, N. All-thiol-stabilized Ag_{44} and $\text{Au}_{12}\text{Ag}_{32}$ nanoparticles with single-crystal structures. *Nat. Commun.* **4**, 1–8 (2013).
31. Negreiros, F. R., Kuntova, Z., Barcaro, G., Rossi, G., Ferrando, R. & Fortunelli, A. Structures of gas-phase Ag-Pd nanoclusters: A computational study. *J. Chem. Phys.* **132**, 234703 (2010).
32. Dass, A. Faradaurate nanomolecules: A superstable plasmonic 76.3 kDa cluster. *J. Am. Chem. Soc.* **133**, 19259–19261 (2011).
33. Kumara, C. & Dass, A. $\text{Au}_{329}(\text{SR})_{84}$ nanomolecules: compositional assignment of the 76.3 kDa plasmonic faradaurates. *Anal. Chem.* **86**, 4227–32 (2014).
34. von Issendorff, B. & Palmer, R. E. A new high transmission infinite range mass selector for cluster and nanoparticle beams. *Rev. Sci. Instrum.* **70**, 4497 (1999).
35. Pratontep, S., Preece, P., Xirouchaki, C., Palmer, R. E., Sanz-Navarro, C. F., Kenny, S. D. & Smith, R. Scaling relations for implantation of size-selected Au, Ag, and Si clusters into graphite. *Phys. Rev. Lett.* **90**, 055503 (2003).
36. Pratontep, S., Carroll, S. J., Xirouchaki, C., Streun, M. & Palmer, R. E. Size-selected cluster beam source based on radio frequency magnetron plasma sputtering and gas condensation. *Rev. Sci. Instrum.* **76**, 045103 (2005).
37. Koch, C. DETERMINATION OF CORE STRUCTURE PERIODICITY AND POINT DEFECT by. *Dissertation* (Arizona State University, 2002).

38. Young, N. P., Li, Z. Y., Chen, Y., Palomba, S., Di Vece, M. & Palmer, R. E. Weighing supported nanoparticles: Size-selected clusters as mass standards in nanometrology. *Phys. Rev. Lett.* **101**, 246103 (2008).
39. Wang, Z. W. Toikkanen, O., Yin, F., Li, Z. Y., Quinn, B. M. & Palmer, R. E. Counting the atoms in supported, monolayer-protected gold clusters. *J. Am. Chem. Soc.* **132**, 2854–2855 (2010).
40. Jian, N., Stapelfeldt, C., Hu, K., Fröba, M. & Palmer, R. Hybrid atomic structure of the Schmid cluster $\text{Au}_{55}(\text{PPh}_3)_{12}\text{Cl}_6$ resolved by aberration-corrected STEM. *Nanoscale* DOI: 10.1039/c4nr06059h (2015). doi:10.1039/c4nr06059h. Please
41. Wang, Z. W., Li, Z. Y., Park, S. J., Abdela, A., Tang, D. & Palmer, R. E. Quantitative Z-contrast imaging in the scanning transmission electron microscope with size-selected clusters. *Phys. Rev. B - Condens. Matter Mater. Phys.* **84**, 073408 (2011).
42. Wang, Z. W. & Palmer, R. E. Intensity calibration and atomic imaging of size-selected Au and Pd clusters in aberration-corrected HAADF-STEM. *J. Phys. Conf. Ser.* **371**, 012010 (2012).
43. Wang, Z. W., Toikkanen, O., Quinn, B. M. & Palmer, R. E. Real-space observation of prolate monolayer-protected Au_{38} clusters using aberration-corrected scanning transmission electron microscopy. *Small* **7**, 1542–1545 (2011).
44. Wang, Z. W. & Palmer, R. E. Determination of the ground-state atomic structures of size-selected Au nanoclusters by electron-beam-induced transformation. *Phys. Rev. Lett.* **108**, 245502 (2012).
45. Wang, Z. W. & Palmer, R. E. Experimental evidence for fluctuating, chiral-type Au_{55} clusters by direct atomic imaging. *Nano Lett.* **12**, 5510–5514 (2012).

46. Plant, S. R., Cao, L., Yin, F., Wang, Z. W. & Palmer, R. E. Size-dependent propagation of Au nanoclusters through few-layer graphene. *Nanoscale* **6**, 1258–1263 (2014).
47. Ascencio, J. A., Perez, M. & Jose-Yacamán, M. Truncated icosahedral structure observed in gold nanoparticles. *Surf. Sci.* **447**, 73–80 (2000).
48. Häkkinen, H. Atomic and electronic structure of gold clusters: understanding flakes, cages and superatoms from simple concepts. *Chem. Soc. Rev.* **37**, 1847–59 (2008).
49. Yang, H., Wang, Y., Huang, H., Gell, L., Lehtovaara, L., Malola, S., Hakkinen, H. & Zheng, N. All-thiol-stabilized Ag_{44} and $\text{Au}_{12}\text{Ag}_{32}$ nanoparticles with single-crystal structures. *Nat Commun* **4**, (2013).
50. Malola, S., Lehtovaara, L., Knoppe, S., Hu, K., Palmer, R. E., Burgi, T. & Hakkinen, H. $\text{Au}_{40}(\text{SR})_{24}$ Cluster as a Chiral Dimer of 8-Electron Superatoms: Structure and Optical Properties. *J. Am. Chem. Soc.* **40**, 8–11 (2012).
51. Baletto, F., Ferrando, R., Fortunelli, A., Montalenti, F. & Mottet, C. Crossover among structural motifs in transition and noble-metal clusters. *J. Chem. Phys.* **116**, 3856–3863 (2002).
52. Wang, B., Liu, M., Wang, Y. & Chen, X. Structures and Energetics of Silver and Gold Nanoparticles. *J. Phys. Chem. C* **115**, 11374–11381 (2011).
53. Barnard, A. S., Young, N. P., Kirkland, A. I., Van Huis, M. a. & Xu, H. Nanogold: A quantitative phase map. *ACS Nano* **3**, 1431–1436 (2009).
54. Bente, W., Nilius, N., Ernst, N. & Freund, H. J. Photon emission spectroscopy of single oxide-supported Ag-Au alloy clusters. *Phys. Rev. B - Condens. Matter Mater. Phys.* **72**, 045403 (2005).

CHAPTER 5

INVESTIGATIONS OF THE IRON CORE OF FERRITIN BY ABERRATION-CORRECTED HAADF STEM

Most of the text and figures in this chapter have been used in my publication (with me as the first author): Jian, N., Dowle, M., Horniblow, R. D., Tselepis, C. & Palmer, R. E. Morphology of the ferritin iron core by aberration corrected scanning transmission electron microscopy. *Nanotechnology*, **27**, 46 (2016).

5.1 Overview

As the major iron storage protein, ferritin stores and releases iron for maintaining the balance of iron in fauna, flora, and bacteria. In this chapter, an investigation of the morphology and iron loading of ferritin (from equine spleen) using aberration-corrected high angle annular dark field scanning transmission electron microscopy is presented. In this chapter, the atom counting method, with size selected Au clusters as mass standards, was employed to determine the number of iron atoms in the nanoparticle core of each ferritin protein. Quantitative analysis shows that the nuclearity of iron atoms in the mineral core varies from a few hundred iron atoms to around 5000 atoms. Moreover, a relationship between the iron loading and iron core

morphology is established, in which mineral core nucleates from a single nanoparticle, then grows along the protein shell before finally forming either a solid or hollow core structure.

5.2 Introduction

Fe is an essential trace element in living organisms. A schematic of the intercellular Fe behavior is shown in Figure 5.1. From the schematic, we can see that Fe is vital to many fundamental cellular processes such as oxygen transport, DNA replication and cell division.¹⁻³ However, excess Fe in the body can create potential toxicity due to its capacity to promote the formation of reactive oxygen species, which can lead to damage of the protein and DNA.⁴ As such, all organisms need to regulate the amount of free Fe available for fundamental cellular processes whilst avoiding Fe-induced toxicity. Ferritin, the major Fe storage protein, is central to this regulatory mechanism. It can store Fe, in the ferric state, and upon cellular demand is mobilized.⁵⁻⁸ Thus, ferritin is a protein critical to health. A deficiency of ferritin is associated with many diseases, such as Still's disease, Parkinson's disease, sideroblastic anemia, Friedreich's Ataxia and restless legs syndrome.⁸⁻¹⁰ In addition, ferritin also commands a good deal of attention in the area of bionanotechnology due to its attractive architectural feature, such as its cage structure, stability, non-toxicity and the ability to mineralize other elements.^{8,11-13} Ferritin demonstrates potential for a number of applications, including drug delivery, magnetic recording, and quantum electronics.¹⁴⁻¹⁷ Thus, a deeper understanding of ferritin is required from the perspective of public health and for the development of bionanotechnology.

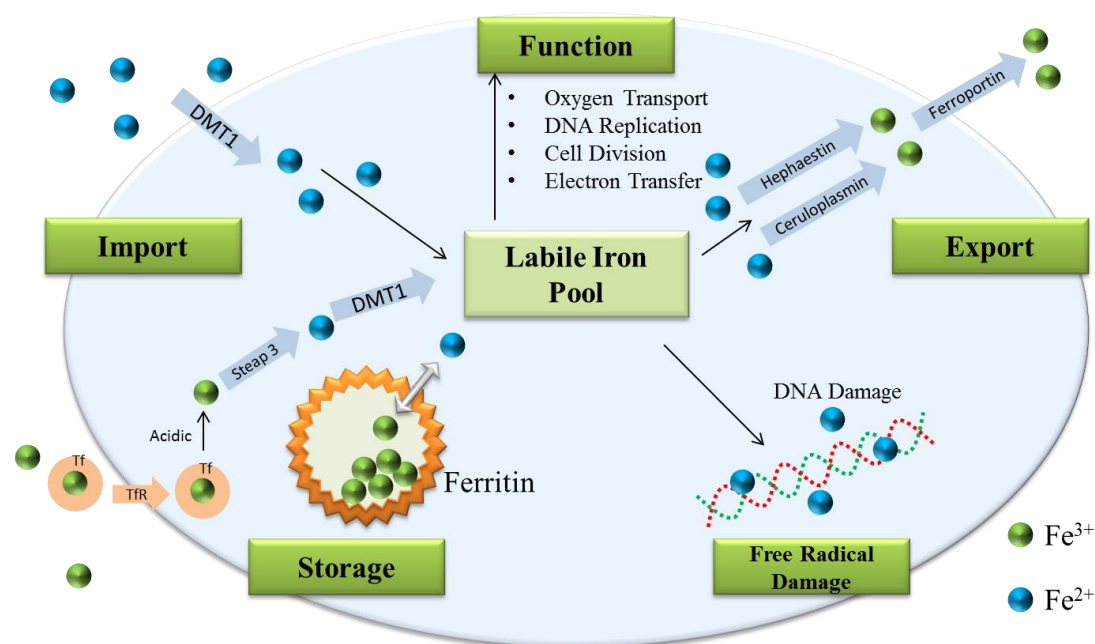


Figure 5.1. Schematic of intercellular Fe behavior. The Fe is imported into the cell with several medias such as divalent metal ion transporter 1 (DMT1), transferrin (Tf) and transferrin receptor (TfR). The imported Fe is utilized in many processes like oxygen transport, cell division and DNA replications. Excess ferrous Fe is harmful in the body and results in DNA and protein damage. The ferritins transfer the ferrous Fe to ferric, which is then crystalized into a protein to store the excess Fe to prevent possible damage to the body.

X-ray structures of the ferritin shell have been known since the 1980's, and show that ferritin molecules in different mammals have very similar structures.^{2,18–20} As shown in Figure 5.2, the apoferritin shell (Fe-free form of the ferritin protein) has a hollow symmetrical structure formed by 24 sub-units. There are two types of sub-units, H and L, with different amino acid sequences. Apoferritin has an outer diameter of 12 nm

and an 8 nm diameter hollow cavity inside, which is available to store mineralized Fe. There are 2-fold, 3-fold and 4-fold symmetry axes in the apoferritin molecule. The hydrophilic channels along the eight 3-fold symmetry axes are normally regarded as the major channels for Fe entrance.^{6–8} The composition of the mineralized Fe core is believed to be similar to ferrihydrite,^{20,21} a hydrous ferric oxyhydroxide mineral. As the mineralized Fe core varies in size and morphology from one ferritin molecule to the next, X-ray crystallography is not suitable for the characterisation of the ferritin core. Transmission electron microscopy is therefore especially useful in the study of the structure of the ferritin core.

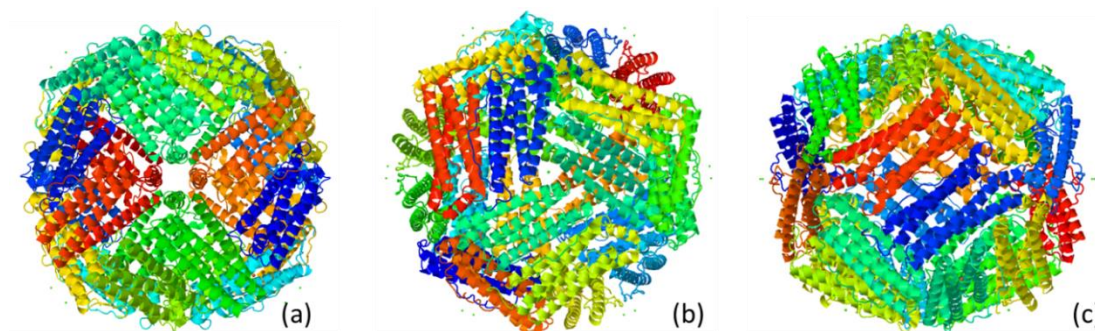


Figure 5.2. 3D crystal structure of ferritin protein shell viewed from” (a) 4-fold symmetry axis, (b) 3-fold symmetry axis, and (c) 2-fold symmetry axis.

Electron microscopic studies of ferritin can be traced right back to the 1950’s. In 1954, Farrant first observed the Fe-containing mineral core, reporting a 5.5 nm Fe core diameter and suggesting that it consisted of 4 sub-units, each 2.7 nm in diameter.²² Six years later, Muir presented a 6-sub-unit structure based on his TEM observations, in which the 6 sub-units sit at the corners of an octahedron.²³ In 1965, Haggis reported

several additional morphologies.²⁴ To achieve a higher resolution, in 1973, Massover et al. employed ultrahigh voltage (1-3 MeV) dark field electron microscopy on the horse spleen ferritin and showed that a single core can contain more than one crystallite with different sizes and shapes.²⁵ The first dark field scanning transmission electron microscopy study of the ferritin core was conducted in 1979 by Crewe and his group.²⁶ They observed the lattice spacing of the mineral core directly, which, combined with the electron diffraction studies, lead to the conclusion that the core structure is similar to ferrihydrite. A quantitative study with EELS in the STEM of individual cores was presented by Pan et al., who determined the range of core sizes and led to a proposal of a new Fe core morphology based on 8 sub-units growing from the 8 three-fold symmetry channels in the cavity.²⁷⁻²⁹

In this chapter, a study of ferritin's mineral core using aberration-corrected STEM in the high angle annular dark field (HAADF) mode is presented. Moreover, the atom counting method is employed, with size-selected Au clusters as the mass balance, to determine the number of Fe atoms in each Fe core. The Fe loading of the ferritin molecules varies from a few hundred atoms to about 5000 atoms. A relationship between the core morphology and the Fe loading is also observed, suggesting that the ferritin core grows from one small nanoparticle along the protein shell to finally form a full, either solid or hollow, Fe-containing mineral core.

5.3 Experimental details

The ferritin molecules investigated were sourced from Sigma Aldrich UK and are

purified from the equine spleen in saline solution. The integrity and quality of the ferritin utilised in this study was verified using SDS PAGE gel electrophoresis and western blotting using polyclonal antibodies to ferritin (1:10 000 dilution, Abcam, rabbit AB69090).³⁰ The Fe content of ferritin was estimated using a ferrozine assay, a colourimetric assay which determines total Fe concentrations post-protein degradation and acid liberation of protein-stored Fe.³¹ This ferritin solution was drop cast onto one half of a 300 mesh TEM copper grid. The TEM grid is covered with a holey carbon film and then a graphene oxide film (EM Solutions) to maximize the contrast. Size-selected Au_{923±46} clusters were deposited on the other half of the grid from a magnetron sputtering, gas condensation cluster beam source and mass filtered by a lateral time-of-flight mass selector.^{32–34} The cluster beam current was 30pA and the deposition time was 150 s. The number of size-selected clusters deposited was $\sim 2.8 \times 10^{10}$. Our 200kV JEOL JEM2100F Field Emission Gun (FEG) STEM with a spherical aberration corrector (CEOS) was utilized in HAADF mode to image both the ferritins and size-selected gold clusters. The HAADF detector was operated with an inner angle of 62 mrad and outer angle of 164 mrad. The electron dose for each image was 4×10^4 electrons \AA^{-2} at 12 million times magnification. No beam shower was performed on the samples in this research to prevent any damage resolving to the sample.

5.4 Results and discussion

5.4.1 Integrity of the ferritin protein shell

As the apoferritin shell of the ferritin is formed from low atomic number elements like

hydrogen, oxygen and carbon, the contrast is not high enough to see the protein shell in the HAADF STEM images. However, confirming the existence of the protein shell was crucial for this project. Both SDS PAGE gel electrophoresis (followed by Coomassie blue staining) and Western blotting confirmed the integrity of ferritin employed within this study. As shown in Figure 5.3, Coomassie blue staining revealed a single band at ca. 20 kDa, which corresponds to the ferritin sub-units (19 kDa ferritin L-chain and 21 kDa H-chain). The Western blotting revealed a single immunoreactive band, which corresponds to a ferritin light chain (L-chain) at ca. 19 kDa. From Figure 5.3, we can see the clear ferritin band and that ferritin degradation was not evident.

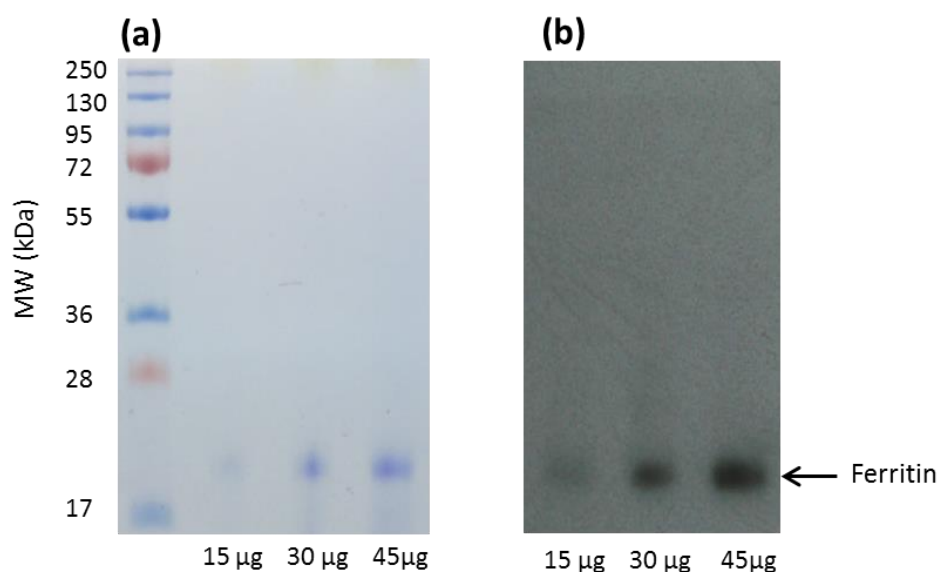


Figure 5.3. Test of the Integrity of the ferritin protein. (a) SDS PAGE 12% gel loaded with ferritin (15, 30 and 45 μ g) and stained with Coomassie blue. (b) SDS PAGE 12% gel loaded with ferritin (15, 30 and 45 μ g) and subject to Western blotting with a polyclonal; antibody specific for the ferritin light chain.³⁵ The figure is from ref [35]

The geometrical sizes of the ferritin cores were measured from the HAADF-STEM images. A histogram of the maximum lengths of a total of 114 mineral cores is shown in Figure 5.4 (a). We see a peak at 7.5 nm while no core is significantly longer than 8 nm. This implies that the molecule cavities have an inner diameter no greater than 8 nm, which is consistent with previous reports.^{2,7,18} Furthermore, the most ferritin iron cores have the relative high maximum length, even though their average iron loadings are just close to the half of the maximum capacity (will be shown below), suggesting the iron cores did not grow evenly from small ball to bigger, but grow along the protein shell, so the low loaded ferritin iron cores can also have higher maximum length. As shown in Figure 5.4 (b)-(e), the same maximum core length is found independent of the different core morphology. This suggests that all core shapes are limited in size by the protein shell which persists under electron beam irradiation. The lowest maximum length of the iron cores observed is around 2.5nm, but it doesn't mean no smaller iron core exists. The Z-contrast property of the HAADF-STEM limited the observation and characterization of the ultra-small and light elemental cores. The smaller average iron content of the ferritin from chemical analysis comparing with the result from the HAADF-STEM based atom counting also implies that the existence of very small iron cores which did not characterized by the HAADF-STEM.

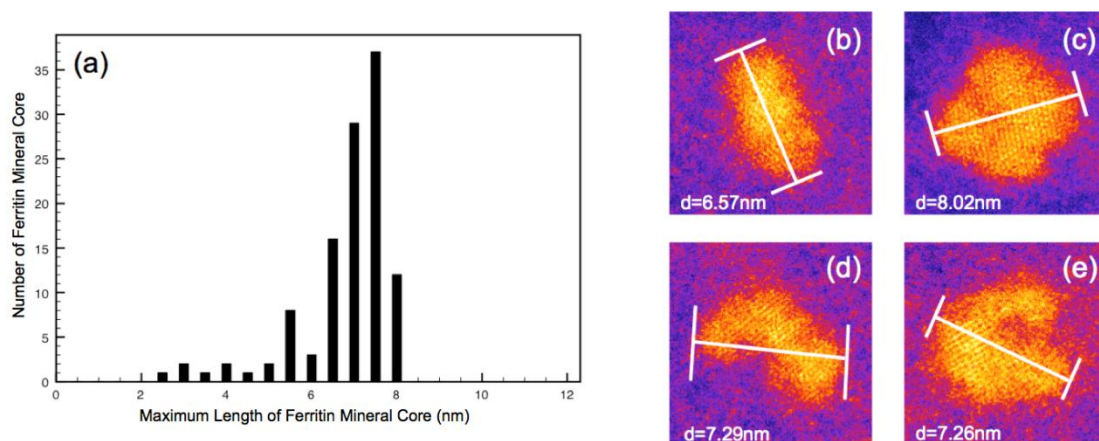


Figure 5.4. (a) Plot of the maximum length of the ferritin mineral cores. (b)-(e) Examples of HAADF STEM images in which the maximum lengths of the cores are all similar for different core morphologies.³⁵ The figure is from ref [35]

5.4.2 Iron loading of ferritin

The number of Fe atoms in the ferritin cores, that is, the Fe loading, has been obtained by the atom counting method, which compares the integrated HAADF intensity of Fe cores to that of size selected Au_{923} clusters deposited in the same grid, which functions as the mass standards. Background subtraction was carefully performed to include the region adjacent to the mineral core so as to remove the contribution of both the graphene oxide support and the protein shell itself assuming a 3D spherical protein shell of 2 nm thickness. The HAADF intensity contribution by a single proton was obtained through the HAADF intensity of the size selected Au_{923} cluster divided by the number of protons in each cluster. Then, the number of protons in the ferritin core can be calculated by comparing the integrated HAADF intensities between the

ferritin Fe core and single proton.^{36–38} The error in the Fe loading calculation is $\pm 4.36\%$, based on the mass resolution of size-selected clusters and the measurement error of the STEM intensity. A high resolution image of the Fe core crystal structure is shown in Figure 5.5 (a), with d-spacings of 2.54 Å, 2.51 Å and 2.61 Å and interplanar angles of 61.1°, 59.06° and 60.05°, respectively. These values are consistent with the ferrihydrite crystal structure.³⁹ Assuming that the mineral cores are indeed ferrihydrite, then the contribution of H and O atoms can be subtracted, and the actual number of Fe atoms in the ferritin cores obtained. The resulting distribution of the Fe loading of a total of 103 ferritin molecules is shown in Figure 5.5 (b), which shows that the number of Fe atoms varies from a few hundred to around 5000. This is a little higher than the maximum Fe loading capacity of 4500 Fe atoms suggested by many previous researches^{2,7,29,40}, but there were also studies that reported higher Fe loading of about 5000 or higher.^{10,41,42} This high maximum iron loading can be explained by: first, the 4500 iron capacity is from old experimental measurements, not a theoretical limit, so few hundreds iron atoms fluctuation on the maximum iron loading is acceptable; second, the error of the iron loading calculation also broadened the maximum iron loading about 200 iron atoms, which can also contribute the high maximum iron loading.

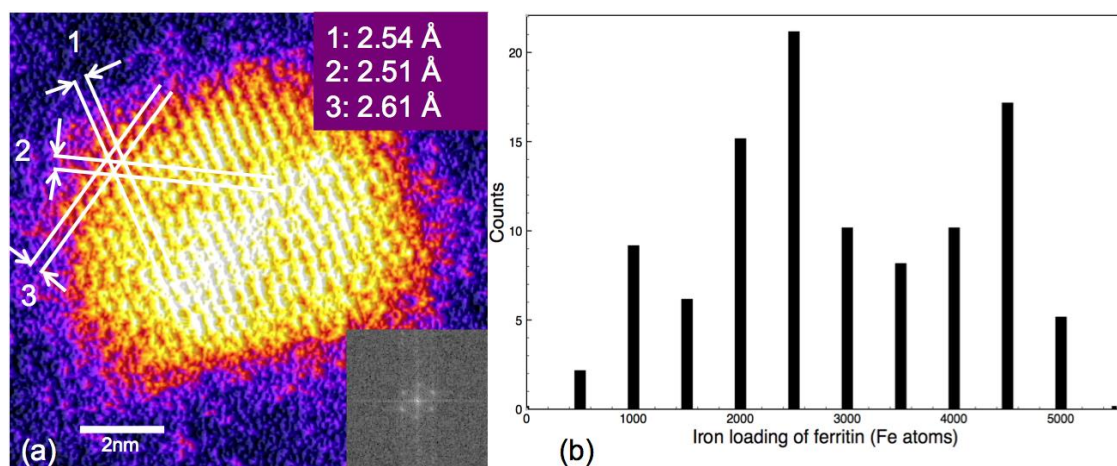


Figure 5.5. (a) Crystal structure analysis of ferritin Fe core. The d-spacing and angles labelled are consistent with the ferrihydrite crystal structure. Inset, lower right: the corresponding FFT. (b) Distribution of Fe loading in ferritin cores. The number of Fe atoms varies from around 500 to 5000.³⁵ The figure is from ref [35]

A chemical analysis of ferritin Fe content was also performed, which estimated an average Fe content of 2499 ± 9 (SD) Fe atoms per ferritin protein by using a ferrozine assay. The Ferrozine calibration curve which made from the standard Fe concentrations is shown in Figure 5.6. The detail of the estimation is performed in table 5.1. This value matches well with the average ferritin Fe content in the STEM analysis (~ 2922). The number of atoms estimated by the chemical analysis is slightly smaller, which is because the ferritin with very small Fe loading cannot be imaged by the HAADF-STEM method.

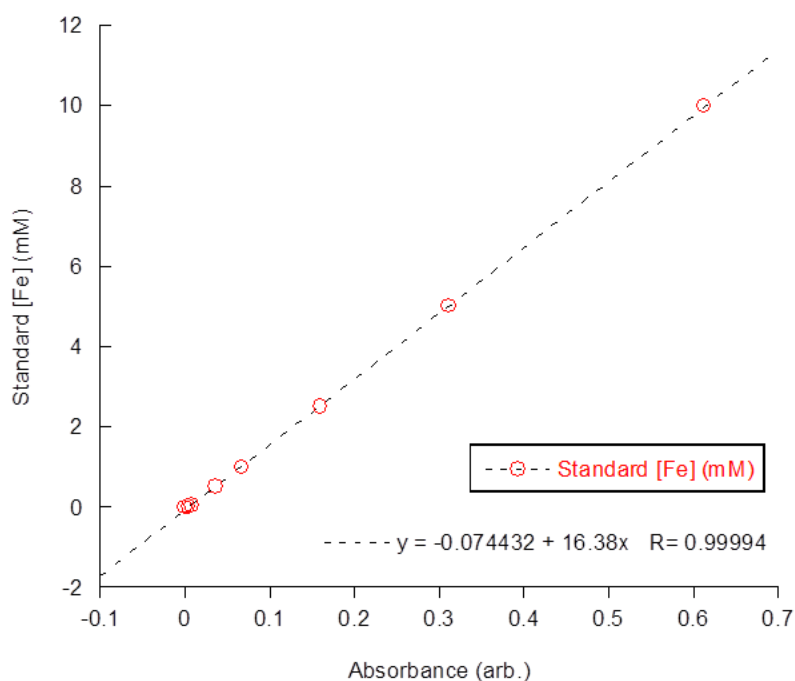


Figure 5.6. Ferrozine calibration curve created with standard Fe concentrations (0-10 mM) and estimated Fe concentrations of ferritin tabulated. Error denotes the standard deviation.³⁵ The figure is from ref [35]

Sample	A	B	C
Absorption Reading	0.08951	0.0891	0.08877
Iron concentration (mM)	1.39174	1.3850	1.3796
Fe atoms/ L	8.3810E+20	8.3406E+20	8.3080E+20
Fe atoms/ sample	1.3409E+17	1.3345E+17	1.3292E+17
Ferritin molecules/ sample	5.34E+13		
Iron/ ferritin (atoms)	2511	2499	2489
Average of triplicate	2499 \pm 9 iron atoms per ferritin molecule		

Table 5.1. The estimation of the Fe content with a ferrozine assay.³⁵ The figure is from ref [35]

5.4.3 Morphology of the ferritin iron core

As detailed above, different types of morphology are observed in the ferritin cores. We classify them by their 2D projection shape as follows: “small circle”, “dumbbell”, “crescent”, “doughnut” and “full raft”. The difference between “small circle” and “full raft” is simply the maximum length, with the maximum length of the “small circle” being lower than 4 nm, e.g. Figure 5.7 (a). The “dumbbell” type is defined as an Fe core with aspect ratio larger than 1.5, e.g. Figure 5.7 (c). The “crescent” type cores are the ones that have low intensity at the centre and an imperfect outer shell, e.g. Figure 5.7 (e). The “doughnut” types are the cores that also have low intensity at the centre, but in this case the outer shell is complete, e.g. Figure 5.7 (y). The different types of mineral cores are in the different regimes of Fe loading. The “small circle” cores are in the region of a few hundred to around one thousand Fe atoms, whereas the “dumbbell” cores contain from one thousand to three thousand Fe atoms, while the “crescent” cores contain from 1500 to 4000 Fe atoms, the “doughnut” cores contain from 2500 to 5000 Fe atoms, and the “full raft” cores contain from 1500 to 5000 Fe atoms. The data indicates that each morphology seems to dominate in a specific regime of Fe loading, which should be relevant to understanding the process of the growth of the mineral core. It should be noted that the regimes of different morphology overlap each other somewhat. This is because the STEM images have been classified by their 2D features, which means that in certain regimes of nuclearities, different morphology types can actually reflect the same 3D morphology with different 2D projections. For example, if a disk-like Fe core contains around

2500 Fe atoms (so the protein shell is half full) and has a hole in its centre, it will be considered as “doughnut”. However, if it stands vertically on the surface, the image will show a “dumbbell” type core.

5.4.4 Relationship between morphology and iron loading of the ferritin core

From the analysis of Fe loadings and morphologies of the ferritin mineral cores, a morphology “atlas” was generated and is shown in Figure 5.7. This shows how the morphologies change with Fe loadings. The smallest Fe loading corresponds to the “small circle” morphology, then as the Fe loading increases, the morphology changes in the following sequence: from 1000 Fe atoms, the “dumbbell” type morphology appears up to 3000 Fe atoms, from 1500 Fe atoms, the “crescent” type morphology emerges and persists up to 4000 Fe atoms, the “doughnut” is observed from 2500 to 4500 Fe atoms; finally the “full raft” appears from 1500 to 5000 Fe atoms, with the largest Fe loading matching the “full raft” morphology.

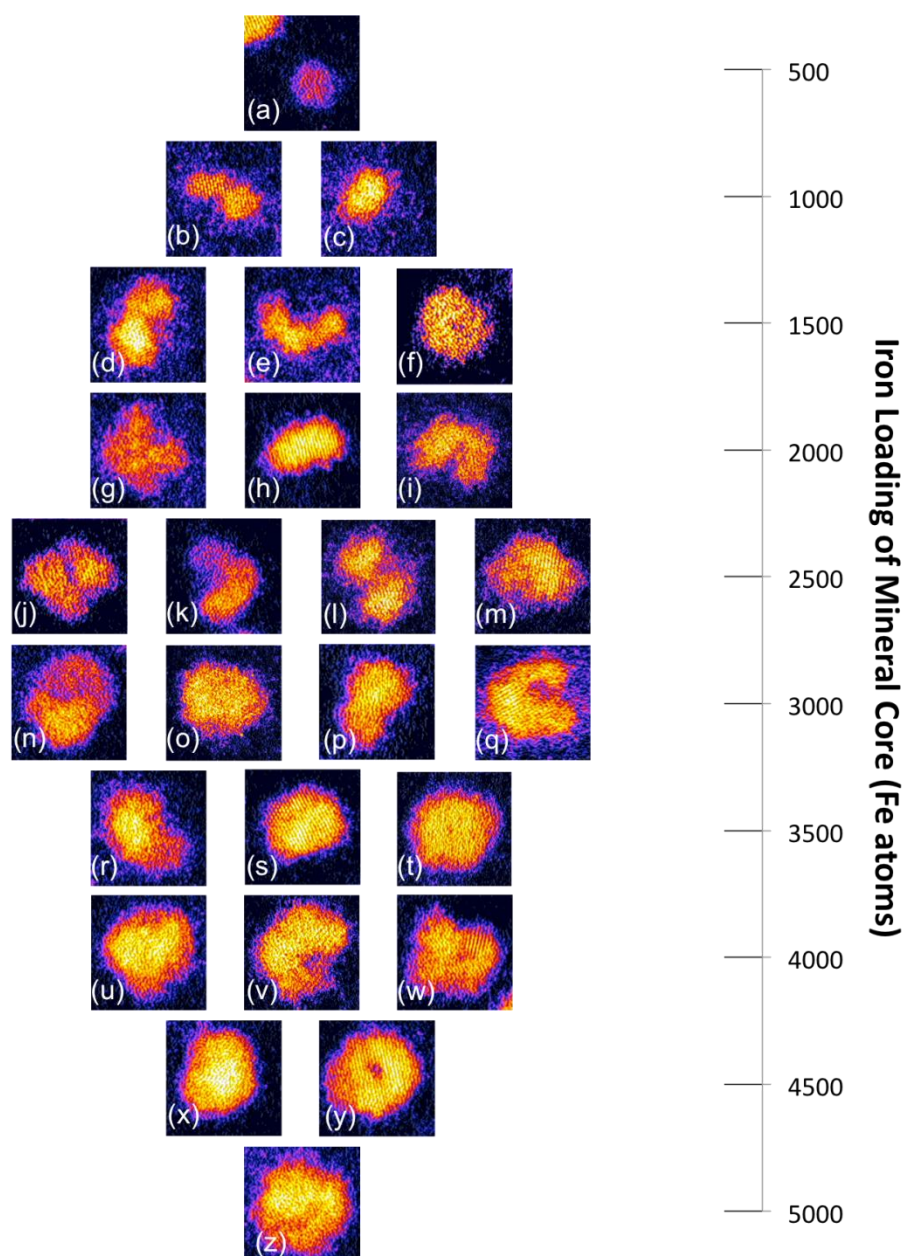


Figure 5.7. The morphology “atlas” of the ferritin Fe core with different Fe loading regions. From (a) to (z) are the representative images for every type of morphology observed in different size ranges. For example, there is only one morphologic “small circle” found in the size range of ~500 Fe atoms, as shown in (a), while all four types of morphology, (j) “doughnut”, (k) “crescent”, (l) “dumbbell” and (m) “full raft”, are observed in the size range ~2500 Fe atoms. The frame size of the ferritin example image is 8.24×8.24 nm.³⁵ The figure is from ref [35]

The 8 channels which correspond to the 3-fold symmetry axes of apoferritin are regarded as the main entrances for Fe mineralization. The dissolved Fe^{2+} ions are oxidized to form Fe^{3+} in the catalytic ferroxidase site, which is located in the centre of the helical bundle of ferritin sub-units and atom mineralization takes place on the H sub-unit of the protein shell to form the initial mineral core.^{2,7,11,19} Previous research suggests that when the mineral core is formed, the surface of the growing core will act as a site for oxidation deposition,^{2,42–45} such that deposition on the mineral core is faster than on the inside of the protein shell. This accounts for the well-defined quasi-spherical morphology of the cores at low Fe loading. Many of the mineral core structures in Figure 5.8 of higher mass can be rationalized as connected assemblies of these “small circle”, formed nucleation at two (Figure 5.7 (b)), three (Figure 5.7 (e)) or more (Figure 5.7 (w)) different sites within the protein cavity. Moreover, the “crescent” shapes observed, like in Figures 5.7 (e) and (q), suggest a tendency for these individual precipitates to nucleate on the inner surface of the protein shell. The observation of a quasi-hollow (almost) full mineral core can be seen as a further manifestation of the preferred nucleation in the inner wall of the protein shell.

5.4.5 Discussion of electron beam damage

In all electron microscopy research, there is the question of how much the electron beam itself affects the sample. In our work, the electron dose is 4×10^4 electrons \AA^{-2} . Research on the electron beam damage to ferritin^{27,29} used electron energy loss

spectra (EELS) to detect the valence change of Fe in the ferritin Fe core. At 200kV in the transmission electron microscope (TEM), Fe^{3+} began to be reduced to Fe^{2+} when the electron dose was above $\sim 10^5$ electrons \AA^{-2} , so our $\sim 10^4$ electrons \AA^{-2} can be seen as a “safe electron dose”. In a 100kV STEM study, the electron beam had no influence on the Fe valence state at an electron dose of 10^5 electrons \AA^{-2} , but the percentage of the Fe-O octahedral coordination did decrease from $\sim 75\%$ at 10^4 electrons \AA^{-2} to $\sim 63\%$ at the dose we employed in our research. Overall, it is reasonable to deduce that the electron beam effect is not very significant in our study. Furthermore, the maximum length analysis in Figure 5.4 showed that no ferritin core is larger than the ferritin protein shell inner diameter of 8 nm, which again suggests that the Fe core and protein cavity morphology is not changed significantly by the electron beam.

5.5 Conclusions

The morphology of the ferritin mineral core has been investigated via aberration-corrected HAADF STEM. The Fe loading of the ferritin cores has been determined by the atom counting method with size-selected Au clusters as mass balances. The number of Fe atoms in the core varies from a few hundred to ~ 5000 atoms. Analysis of the closest separation distances between the cores and their maximum length has confirmed the preservation of the ferritin protein shell. Different types of morphology of the Fe-containing cores were identified and classified as a function of their Fe loading. Growth of the mineral core begins with a small circle

morphology. Nucleation and growth of further such nanoparticles on the internal surface of the protein shell accounts for the “dumbbell” and “crescent” morphologies observed before near complete filling of the cavity with a solid or hollow, quasi-spherical core. The mineralization process we found will be helpful in a more accurate nanoparticle synthesis in ferritin protein and improve the performance of the ferritin based drug delivery system. The method we used to determine the Fe loading of ferritin can be extended to other metal containing proteins and can also be a new medical test method to develop more specific therapies for the ferritin-related diseases.

Reference:

1. Andrews, N. C. & Schmidt, P. J. Iron homeostasis. *Annu. Rev. Physiol.* **69**, 69–85 (2007).
2. Harrison, P. M. & Arosio, P. The ferritins: molecular properties, iron storage function and cellular regulation. *Biochim. Biophys. Acta - Bioenerg.* **1275**, 161–203 (1996).
3. Zhao, G., Ceci, P., Ilari, A., Giangiacomo, L., Laue, T. M., Chiancone, E. & Chasteen, N. D. Iron and hydrogen peroxide detoxification properties of DNA-binding protein from starved cells. A ferritin-like DNA-binding protein of *Escherichia coli*. *J. Biol. Chem.* **277**, 27689–27696 (2002).
4. Gutteridge, J. M. C. & Halliwell, B. Iron toxicity and oxygen radicals. *Baillieres. Clin. Haematol.* **2**, 195–256 (1989).
5. Liu, X. & Theil, E. C. Ferritins: Dynamic management of biological iron and oxygen chemistry. *Acc. Chem. Res.* **38**, 167–175 (2005).
6. Finazzi, D. & Arosio, P. Biology of ferritin in mammals: an update on iron storage, oxidative damage and neurodegeneration. *Arch. Toxicol.* **88**, 1787–1802 (2014).
7. Ford, G. C., Harrison, P. M., Rice, D. W., Smith, J. M. A., Treffry, A., White, J. L. & Yariv, J. Ferritin: design and formation of an iron-storage molecule. *Philos. Trans. R. Soc. Lond. B. Biol. Sci.* **304**, 551–565 (1984).
8. Theil, E. C. Ferritin: The protein nanocage and iron biomineral in health and in disease. *Inorg. Chem.* **52**, 12223–12233 (2013).
9. Barton, J. & Bertoli, L. Hemochromatosis: The genetic disorder of the twenty-first century. *Nat. Med.* **2**, 394–395 (1996).
10. Quintana, C., Bellefqih, S., Laval, J. Y., Guerquin-Kern, J. L., Wu, T. D., Avila,

- J., Ferrer, I., Arranz, R. & Patino, C. Study of the localization of iron, ferritin, and hemosiderin in Alzheimer's disease hippocampus by analytical microscopy at the subcellular level. *J. Struct. Biol.* **153**, 42–54 (2006).
11. Jutz, G., van Rijn, P., Santos Miranda, B. & Böker, A. Ferritin: A Versatile Building Block for Bionanotechnology. *Chem. Rev.* **115**, 1653–1701 (2015).
 12. Huard, D. J. E., Kane, K. M. & Tezcan, F. A. Re-engineering protein interfaces yields copper-inducible ferritin cage assembly. *Nat. Chem. Biol.* **9**, 169–76 (2013).
 13. Theil, E. C. & Turano, P. Metalloenzymes: Cage redesign explains assembly. *Nat. Chem. Biol.* **9**, 143–4 (2013).
 14. Yamashita, I. Fabrication of a two-dimensional array of nano-particles using ferritin molecule. *Thin Solid Films* **393**, 12–18 (2001).
 15. Jain, S. K., Chaurasiya, A., Gupta, Y., Jain, A., Dagur, P., Joshi, B. & Katoch, V. M. Development and characterization of 5-FU bearing ferritin appended solid lipid nanoparticles for tumour targeting. *J. Microencapsul.* **25**, 289–297 (2008).
 16. Miura, A., Tsukamoto, R., Yoshi, S., Yamashita, I., Uraoka, Y. & Fuyuki, T. Non-volatile flash memory with discrete bionanodot floating gate assembled by protein template. *Nanotechnology* **19**, 255201 (2008).
 17. Fujikawa, S., Muto, E. & Kunitake, T. Embedding of individual ferritin molecules in large, self-supporting silica nanofilms. *Langmuir* **23**, 4629–4633 (2007).
 18. Crichton, R. R. & Declercq, J. P. X-ray structures of ferritins and related proteins. *Biochim. Biophys. Acta - Gen. Subj.* **1800**, 706–718 (2010).
 19. Lewin, A., Moore, G. R. & Le Brun, N. E. Formation of protein-coated iron minerals. *Dalton Trans.* 3597–610 (2005). doi:10.1039/b506071k

20. Cowley, J. M., Janney, D. E., Gerkin, R. C. & Buseck, P. R. The structure of ferritin cores determined by electron nanodiffraction. *J. Struct. Biol.* **131**, 210–6 (2000).
21. Chasteen, N. D. & Harrison, P. M. Mineralization in ferritin: an efficient means of iron storage. *J. Struct. Biol.* **126**, 182–194 (1999).
22. Farrant, J. An electron microscopic study of ferritin. *Biochim. Biophys. Acta* **13**, 569–576 (1954).
23. Muir, A. R. The molecular structure of isolated and intracellular ferritin. *Q. J. Exp. Physiol. Cogn. Med. Sci.* **45**, 192–201 (1960).
24. Haggis, G. H. The iron oxide core of the ferritin molecule. *Journal of molecular biology* **14**, 598–602 (1965).
25. Massover, W. H., Lacaze, J. C. & Durrieu, L. The ultrastructure of ferritin macromolecules. I. Ultrahigh voltage electron microscopy (1-3 MeV). *J. Ultrastruct. Res.* **43**, 460–475 (1973).
26. Ohtsuki, M., Isaacson, M. S. & Crewe, A. V. Dark field imaging of biological macromolecules with the scanning transmission electron microscope. *Proc. Natl. Acad. Sci. U. S. A.* **76**, 1228–1232 (1979).
27. Pan, Y., Brown, A., Brydson, R., Warley, A., Li, A. & Powell, J. Electron beam damage studies of synthetic 6-line ferrihydrite and ferritin molecule cores within a human liver biopsy. *Micron* **37**, 403–411 (2006).
28. Pan, Y.-H., Brown, A., Sader, K., Brydson, R., Gass, M. & Bleloch, A. Quantification of absolute iron content in mineral cores of cytosolic ferritin molecules in human liver. *Mater. Sci. Technol.* **24**, 689–694 (2008).
29. Pan, Y. H., Sader, K., Powell, J., Bleloch, A., Gass, M., Trinick, J., Warley, A., Li, A., Brydson, R. & Brown, A. 3D morphology of the human hepatic ferritin

- mineral core: New evidence for a subunit structure revealed by single particle analysis of HAADF-STEM images. *J. Struct. Biol.* **166**, 22–31 (2009).
30. Horniblow, R. D., Dowle, M., Iqbal, T., Latunde-Dada, G. O., Palmer, R. E., Pikramenou, Z. & Tselepis, C. Alginate-iron speciation and its effect on in vitro cellular iron metabolism. *PLoS One* **10**, 1–14 (2015).
 31. Rebouche, C. J., Wilcox, C. L. & Widness, J. A. Microanalysis of non-heme iron in animal tissues. *J. Biochem. Biophys. Methods* **58**, 239–251 (2004).
 32. Pratontep, S., Carroll, S. J., Xirouchaki, C., Streun, M. & Palmer, R. E. Size-selected cluster beam source based on radio frequency magnetron plasma sputtering and gas condensation. *Rev. Sci. Instrum.* **76**, 045103 (2005).
 33. Pratontep, S., Preece, P., Xirouchaki, C., Palmer, R. E., Sanz-Navarro, C. F., Kenny, S. D. & Smith, R. Scaling relations for implantation of size-selected Au, Ag, and Si clusters into graphite. *Phys. Rev. Lett.* **90**, 055503 (2003).
 34. von Issendorff, B. & Palmer, R. E. A new high transmission infinite range mass selector for cluster and nanoparticle beams. *Rev. Sci. Instrum.* **70**, 4497 (1999).
 35. Jian, N., Dowle, M., Horniblow, R. D., Tselepis, C. & Palmer, R. E. Morphology of the ferritin iron core by aberration corrected scanning transmission electron microscopy. *Nanotechnology* (2016).
 36. Wang, Z. W., Toikkanen, O., Yin, F., Li, Z. Y., Quinn, B. M. & Palmer, R. E. Counting the atoms in supported, monolayer-protected gold clusters. *J. Am. Chem. Soc.* **132**, 2854–2855 (2010).
 37. Jian, N., Stapelfeldt, C., Hu, K., Fröba, M. & Palmer, R. Hybrid atomic structure of the Schmid cluster $\text{Au}_{55}(\text{PPh}_3)_{12}\text{Cl}_6$ resolved by aberration-corrected STEM. *Nanoscale* **7**, 885–888 (2015).
 38. Jian, N. & Palmer, R. E. Variation of the Core Atomic Structure of Thiolated

- (Au_xAg_{1-x})_{312±55} Nanoclusters with Composition from Aberration-Corrected HAADF STEM. *J. Phys. Chem. C* **119**, 11114–11119 (2015).
39. Drits, V. Structural Model for Ferrihydrite. *Clay Miner.* **28**, 185–207 (1993).
40. Rothen, A. Ferritin and Apoferritin in the Ultracentrifuge: Studies on the Relationship of Ferritin and Apoferritin; Precision Measurements of the Rates of Sedimentation of Apoferritin. *J. Biol. Chem.* **152**, 679–693 (1944).
41. Shuman, H. & Somlyo, A. P. Energy-filtered transmission electron microscopy of ferritin. *Proc. Natl. Acad. Sci. U. S. A.* **79**, 106–107 (1982).
42. Crichton, R. R., Ponce-Ortiz, Y., Koch, M. H., Parfait, R. & Stuhmann, H. B. Isolation and characterization of phytoferritin from pea (*Pisum sativum*) and Lentil (*Lens esculenta*). *Biochem. J.* **171**, 349–56 (1978).
43. Macara, I. G., Hoy, T. G. & Harrison, P. M. The formation of ferritin from apoferritin. Catalytic action of apoferritin. *Biochem. J.* **135**, 343–348 (1973).
44. Levi, S. & Luzzago, A. Mechanism of ferritin iron uptake: activity of the H-chain and deletion mapping of the ferro-oxidase site. *J. Biol. Chem.* **263**, 18086–18092 (1988).
45. Bauminger, E. R., Harrison, P. M., Nowik, I. & Treffry, A. Mössbauer spectroscopic study of the initial stages of iron-core formation in horse spleen apoferritin: evidence for both isolated Fe(III) atoms and oxo-bridged Fe(III) dimers as early intermediates. *Biochemistry* **28**, 5486–5493 (1989).
46. López-Castro, J. D., Delgado, J. J., Perez-Omil, J. A., Galvez, N., Cuesta, R., Watt, R. K. & Dominguez-Vera, J. M. A new approach to the ferritin iron core growth: influence of the H/L ratio on the core shape. *Dalt. Trans.* **41**, 1320 (2012).

CHAPTER 6

CHARACTERIZATION OF SMALL SUPPORTED CATALYST PARTICLES BY HAADF STEM

Some of the figure and text in section 5.2 of this chapter have been used in my publication (with me as a co-author who is responsible to all HAADF STEM related part): Rogers, S. M. , Catlow, C. R., Chan-Thaw, C. E., Gianolio, D., Gibson, E. K., Gould, A. L., Jian, N., Logsdail, A. J., Palmer, R. E., Prati, L., Dimitratos, N., Villa, A., Wells, P.. Tailoring Gold Nanoparticle Characteristics and the Impact on Aqueous-Phase Oxidation of Glycerol. *ACS Catal.* **5**, 4377–4384 (2015).

6.1 Overview

Heterogeneous catalysis is notable for its importance in the modern chemical industry and for its key role in pollution control.^{1–3} Nanocluster based catalysts are of great interest in heterogeneous catalysis due to their unique size, high surface-to-volume ratio and resulting high activity.^{4–9} In this chapter, the polyvinylalcohol (PVA) protected Au and Pd nanoclusters supported by TiO₂ were synthesized by colloidal methods under various conditions. Three solvents, H₂O, ethanol and their 1:1 mixed solution were used in the preparation, while different preparation temperatures were employed from -75°C to 75°C. The size ranges of the

metal catalyst particles, produced with different synthesis conditions, were determined by a BF TEM study. The catalytic activity of the nanoclusters with similar size but different synthesis conditions showed different catalytic activity, which suggests there is a difference, between the different active species, that was undiscovered by the BF TEM study. Therefore, in this work, the high resolution aberration-corrected HAADF STEM was employed to study these catalysts with atomic resolution.

6.2 Au/TiO₂ characterization by HAADF-STEM

6.2.1 Introduction

Until small Au nanoparticles supported on transition metal oxides were found to be active to CO oxidation, gold was not believed to have catalytic properties.¹⁰ Since then, a great deal of research has been performed on Au catalysis for many different reactions.^{1,4,5,11–20} The size of the Au particle is found to be critical to their catalytic properties.^{1,8,21,22} The smaller sized Au particles are normally thought to have a higher activity due to the high surface to volume ratio, and the high percentage of low coordinated atoms at the edges and corners of the particles. For the oxide supported Au clusters, the Au atoms that are adjacent to the support are also thought to be of great importance in the catalysis process.^{1,8,22}

The preparation of supported Au nanoparticles with tailored properties/conditions is a fast developing area in catalysis research.^{23–25} With the variation of synthesis

conditions, characteristics such as size, shape and structure can be tuned, which also affect their corresponding catalytic activities. Research on the systematic synthesis approach of PVA stabilized Au/TiO₂ catalysts with different preparation conditions were presented for increasing catalytic activity and durability. Two preparation conditions were modified during the synthesis of the PVA protected Au clusters supported on TiO₂: one is the ratio of water and ethanol in the solvent¹; the other is the colloidal generation temperature which was varied from -75°C to 75°C. The different solvents and temperatures employed for each batch of the Au/TiO₂ catalyst is shown in Table 6.1.

Sample abbreviation	Temperature (°C)	H ₂ O/Ethanol ratio	Average particle size(nm)
A1	1	100	2.0 ± 0.6
A2	25	100	2.3 ± 0.5
A3	50	100	2.8 ± 0.9
A4	75	100	3.3 ± 0.8
B1	-30	50	1.8 ± 0.5
B2	0	50	2.0 ± 0.6
B3	30	50	4.1 ± 1.8
C1	-75	0	2.4 ± 1.0
C2	-30	0	2.9 ± 1.2

Table 6.1 Different temperatures and solvent variations for synthesis of the Au/TiO₂ catalyst.

Bright field TEM was employed to investigate the size (diameter) of the Au nanoclusters in the catalyst system. The average sizes of the Au particles in each catalyst batch are shown in Table 6.1. It is very clear that for the same solvent, the average size of the Au particle will increase if the temperature is increased. Also,

higher temperature will broaden the size distribution of the Au particles. The influence of the solvent type on the particle size can also be obtained by comparing the batches with similar preparation temperatures, for example by comparing between A1 and B2, A2 and B3 or B1 and C2. We can see that there is almost no difference in size between A1 and B2. However a big difference has occurred between A2 and B3: the Au particles in the low H₂O/Ethanol ratio (batch B3) are significantly larger than Au particles in the high H₂O/Ethanol ratio (batch A2) (4.1 ± 1.8 nm in B3 compared to 2.3 ± 0.5 nm in A2). The trend continues when we compare B1 and C2, where C2 contains a lower H₂O/Ethanol ratio but has a much larger average particle size than B1. This suggests that the Au particle size increases when the H₂O/Ethanol ratio decreases. This may be due to the insolubility of PVA in ethanol, which will reduce the stabilization ability of PVA during the synthesis process.

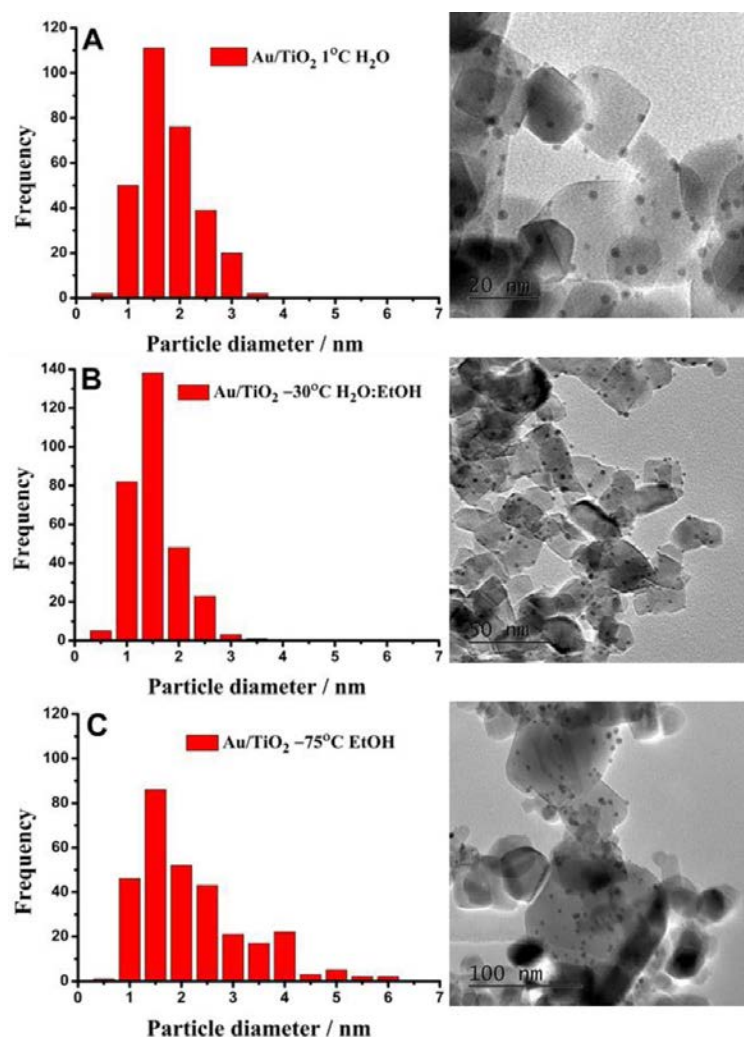


Figure 6.1. Examples of the TEM images of different batches (A:A1, B:B1, C:C1) of Au/TiO₂ clusters and their corresponding size histogram.²⁶ The figure is from ref [26].

All batches of the Au/TiO₂ catalyst were tested for catalytic activity in the liquid phase glycerol oxidation reaction. The catalytic activity is highly dependent on the temperature and solvent. The H₂O prepared Au/TiO₂ catalyst showed the highest activity. Batch A1, synthesized in H₂O with the lowest temperature is most active (TOF 915 h⁻¹). The catalyst in B2, which has the same Au particle size distribution but a different H₂O:ethanol ratio, showed a much lower activity (TOF 95 h⁻¹)

compared with A1. There are two possible reasons for this difference in catalytic activity: firstly, the stabilization agent (PVA) may be affected by the different preparation temperature and solvent systems; and second, there may be ultra-small Au clusters which are hard to detect by the bright field TEM method.

In this section, the aberration corrected HAADF-STEM is employed to investigate the existence of ultra-small Au clusters in the A1 and B1 catalyst systems. Although small Au clusters (smaller than 2 nm) were found in both catalyst systems, the ultra-small clusters, consisting of only a few Au atoms, were only found in the A1 Au/TiO₂ catalyst system. A quantitative integrated HAADF intensity analysis of the ultra-small Au clusters was prepared and it was found that these ultra-small clusters consist of between 1 and 5 Au atoms. This result can explain the extraordinarily high activity in the A1 system, compared with other catalyst batches of similar Au particle size.

6.2.2 Experimental details

The PVA protected Au/TiO₂ clusters were prepared by our collaborator, Scott Rogers, by the colloidal sol-immobilization method. Chloroauric acid (HAuCl₄·3H₂O) of a gold concentration of 1.26×10^{-4} M was dissolved in H₂O, ethanol or 1:1 H₂O/ethanol solution. The PVA solution (1wt% solution, $M_w = 9000 - 10000$ g/mol) was then added to make the molar ratio of PVA/Au 0.65. Red-brown sols were formed by adding the solution of 0.1M NaBH₄ dropwise to obtain a NaBH₄/Au ratio of 5:1.

Continuous stirring is performed during the addition process. After the reduction of the chloroauric acid, the colloidal solution was immobilized onto the quantitative support material TiO_2 , which formed the 1% weight ratio of Au and TiO_2 with strong stirring. Sulfuric acid was then used to acidify the resulting mixture to reduce the pH to 1.2. The mixture was then stirred for one hour before being filtered. After the filter is cleaned by washing with double distilled water, and dried over night at room temperature, the solid catalysts remains.

The Au/ TiO_2 catalysts were sent to our group in powder form. They were dissolved in pure ethanol then dispersed with sonication. The solution was then drop cast with a pipette onto a 400-mesh copper TEM grid covered with amorphous carbon film. The HAADF-STEM study was carried out using a 200kV JEOL JEM 2100F HAADF-STEM equipped with CEOS spherical aberration corrector. The HAADF detection angle used in this study is 62 mrad for the inner angle and 164 mrad for the outer angle.

6.2.3 Ultra-small Au cluster characterization

Through the representative BF and HAADF STEM images of the Au/ TiO_2 catalyst shown in Figure 6.2, it is very clear that the BF image is not suitable for detecting small Au clusters. This is because the phase contrast in the BF image gives the BF mode higher sensitivity to light elements, so we can see a very clear TiO_2 crystal lattice structure, but the pattern of the ultra-small clusters will not be distinguishable

from the TiO_2 and the carbon film. Within the HAADF STEM, the Z-contrast allows even single heavy atoms to have almost the same electron scattering ability as the whole support material and carbon film. So HAADF-STEM is clearly a better characterization tool for the small, high atomic number clusters (such as Au, Pt, etc).

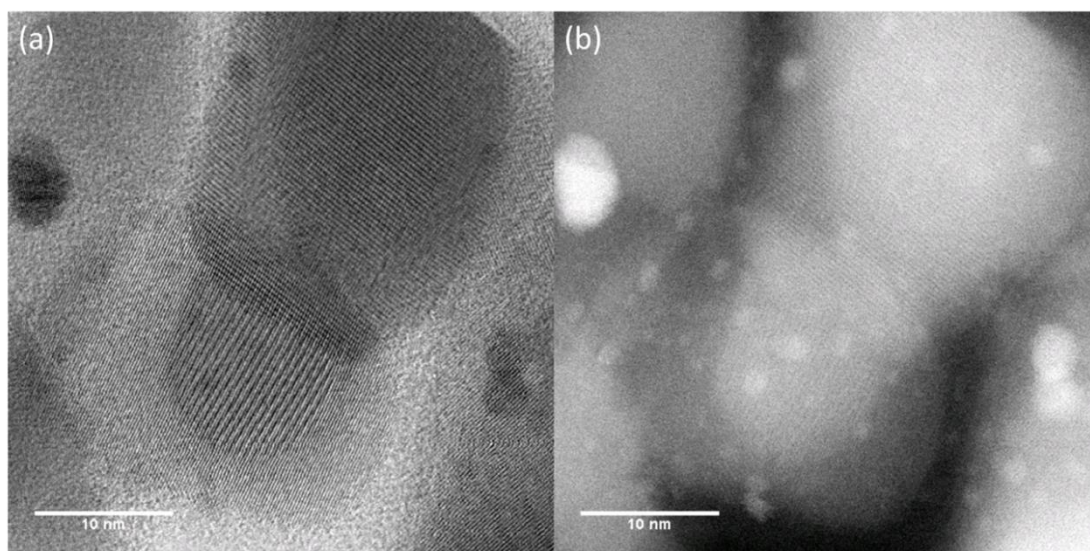


Figure 6.2. Representative STEM image of Au/ TiO_2 catalyst in: (a) bright field, and (b) high angle annular dark field mode.

The ability to detect the small Au clusters has been dramatically improved by using the HAADF-STEM method. The representative HAADF-STEM images of the Au/ TiO_2 catalysts from batches A1 and B1 are shown in Figure 6.3 (a)-(c) and (d)-(f), respectively. We can see that small Au clusters (around 1 nm), that cannot be seen in the BF TEM images, exist in both A1 and B1 samples. The image contrast of the large Au clusters on the thin TiO_2 support becomes slightly lower than in the BF TEM images, but their atomic structures can still be recognised. Only the clusters o

the thicker regions of the TiO_2 support are barely distinguishable. Through the TEM study, we already know that the average size of the large Au clusters in A1 and B1 batches are identical. The small size (around 1 nm) Au clusters from these two batches are identical. The small size (around 1 nm) Au clusters from these two batches in the HAADF-STEM images are also similarly distributed. Therefore, the ultra-small Au clusters (see Figure 6.3 (a)), that were only observed in the A1 sample, are the only difference between A1 and B1 and could be the explanation for the large gap between their catalytic activity towards the liquid phase glycerol oxidation reaction.

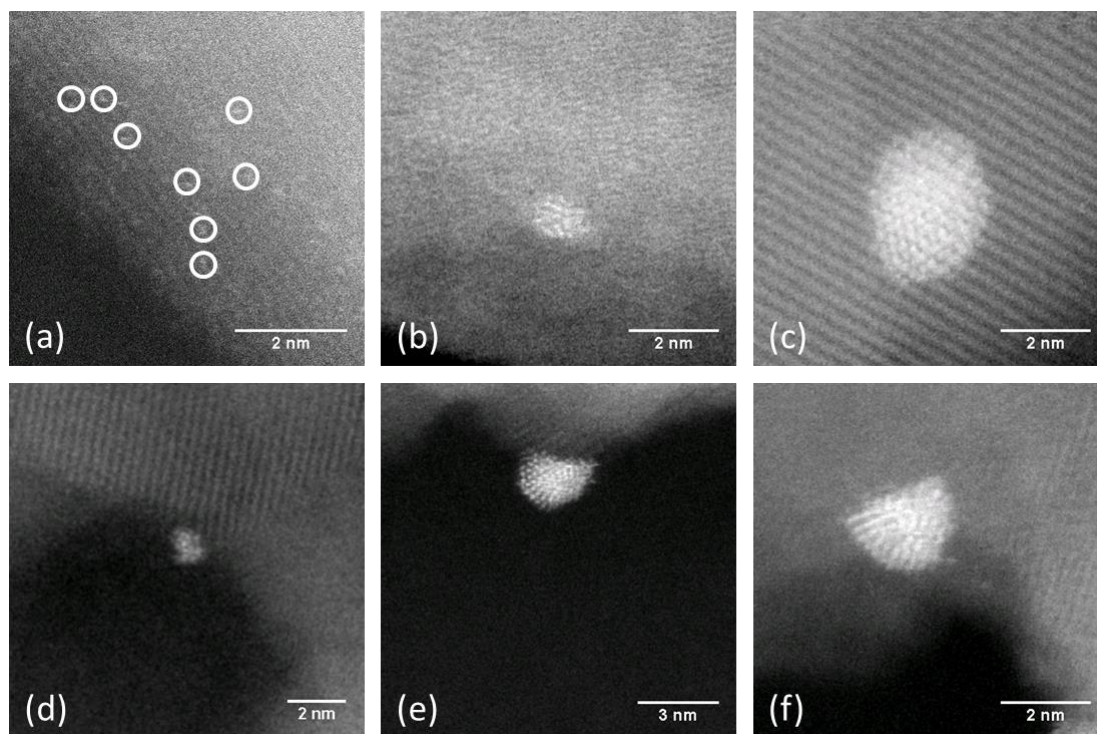


Figure 6.3. Representative HAADF STEM images of Au/TiO_2 catalysts batch: A1 ((a)-(c)), and batch B1 ((d)-(f)). The ultra-small cluster are circled.

A quantitative analysis was performed on the ultra-small Au clusters found in A1. The large Au clusters with clear background were used as mass balances,²⁷⁻²⁹ two

representative images of these clusters are shown in Figures 6.4 (b) and (c). Their sizes were calculated from their projected area with the method described in Chapter 4. Their integrated HAADF intensities were then obtained by a careful background subtraction. The integrated HAADF intensity of the ultra-small Au clusters were obtained and compared with the intensity of the Au clusters of known size (the mass balances). This analysis enabled the number of Au atoms in the ultra-small clusters to be determined and is called the atom counting method. The size distribution of the ultra-small Au clusters is shown in Figure 6.4 (a). Their size range is from 0.5 to 5 Au atoms. The appearance of the half number of Au atoms is due to the error in the background subtraction, influence of the PVA ligand and the STEM itself. But the majority of the clusters have an integer number of Au atoms, showing the relative accuracy of the atom counting method.

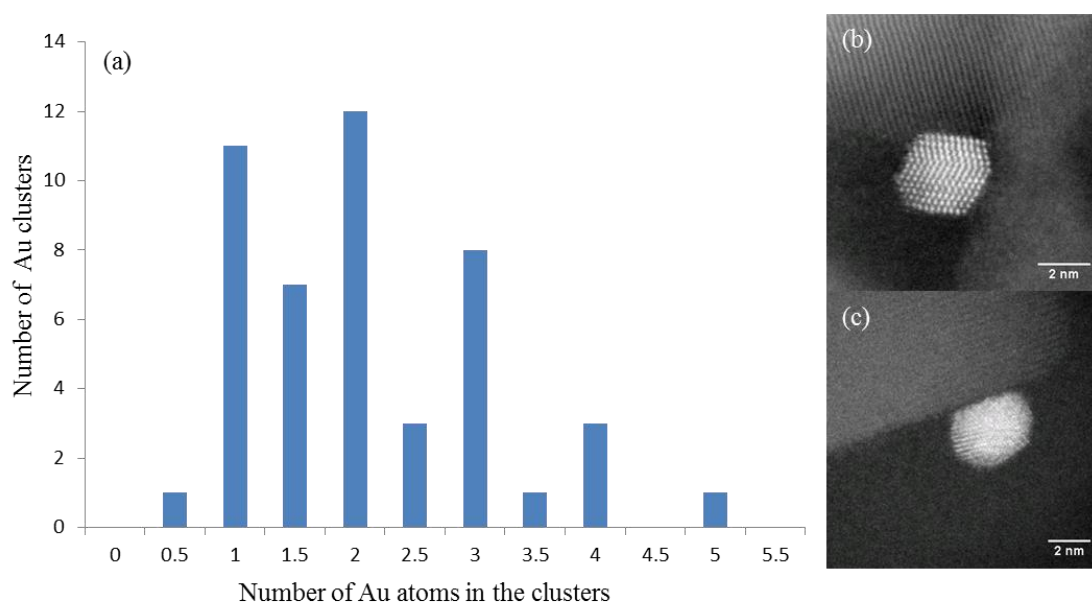


Figure 6.4. (a) Size distribution of the ultra-small Au clusters. The representative images of the mass balance Au clusters are shown in (b) and (c).

Figure 6.5 shows the ultra-small Au clusters with resolved number of atoms presented in the form of a 3D plot of the HAADF-STEM intensity. We can see that all five ultra-small Au clusters in Figure 6.5 look similar to a single atom in the 2D projection. However, the HAADF intensity analysis result indicates that they are actually clusters with different sizes. Three of them are single Au atoms, one is a Au₂ cluster and the last is a Au₃ cluster. This suggests that some of the ultra-small Au clusters are standing vertically on the TiO₂ surface.

The existence of the ultra-small Au clusters in the A1 catalyst can be regarded as the primary reason for its extraordinary catalytic activity. Many studies suggested that the Au atoms with low coordination numbers are the active sites in the Au catalyst, allowing for higher adsorption of oxygen and carbon monoxide.^{2,22,30–33} For the ultra-small Au clusters containing less than 5 atoms, all of the Au atoms have very low coordination number, which suggests an extremely high ratio of active site/mass for the A1 catalysts. Previous studies also suggest that for supported metal catalysts, there are special active sites at the boundary between the support and the Au clusters.^{22,34} For the ultra-small Au clusters observed here, nearly all the Au atoms are at the boundary, which may contribute to the high catalytic activity.

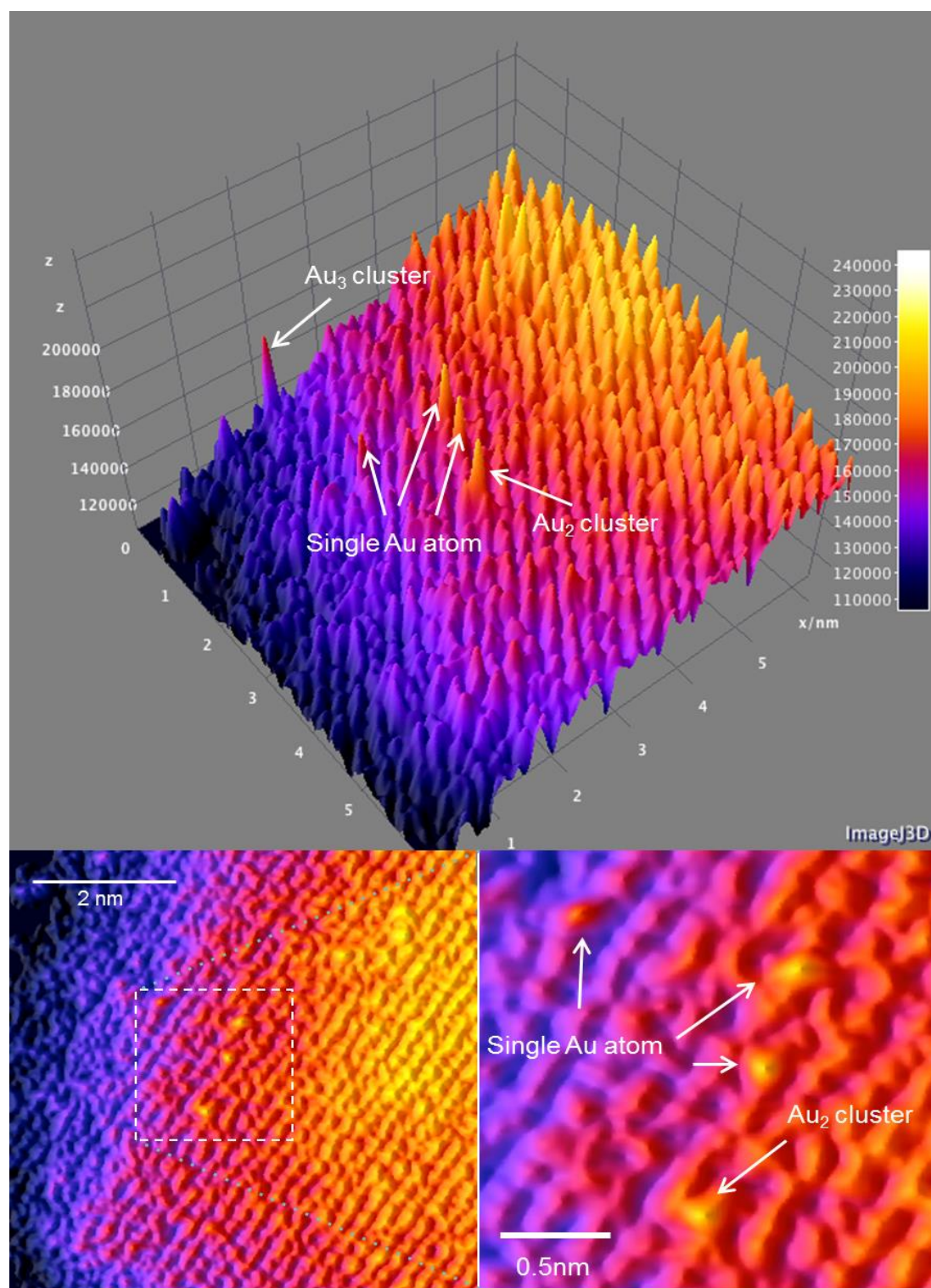


Figure 6.5. 3D plot of the HAADF-STEM images of ultra-small Au clusters on the TiO₂ support.²⁶ The figure is from ref [26]

6.2.4 Conclusions

In summary, the HAADF-STEM was successfully employed to investigate the small Au clusters in the Au/TiO₂ catalyst. The small Au clusters with size around 1 nm, that are difficult to detect in the BF TEM, are found in both A1 and B1 catalysts. While the ultra-small Au clusters were only observed in the A1 catalyst. The quantitative analysis of the ultra-small Au clusters in A1 is carried out by using the large Au clusters as a mass balance for atom counting. The ultra-small Au clusters are found to consist of 1 to 5 Au atoms. These ultra-small Au clusters can have very high catalytic activity due to the high percentage of low coordinated Au atoms and the large proportion of atoms at the Au-oxide boundary. Therefore, the existence of the ultra-small Au clusters in the A1 catalyst explain the A1 catalyst's extraordinarily high catalytic activity.

6.3 Pd/TiO₂ characterization by HAADF STEM

6.3.1 Introduction

Furfural, obtained directly from the acid-catalysed dehydration of xylose, is an important platform intermediate in the generation of various biofuels and chemical intermediates.^{35–37} The unsaturated molecule is reactive and generates a large product distribution, with the pathway depending on the type of catalyst used and reaction conditions. Furfuryl alcohol and tetrahydrofurfural are produced when furfural undergoes hydrogenation at the aldehyde group and furan ring, respectively. Furfuryl alcohol is used in the manufacturing of various chemical products including resins,

synthetic fibres and adhesives.³⁸ Further hydrogenation of furfuryl alcohol and tetrahydrofurfural yields tetrahydrofurfuryl alcohol, which is considered a green solvent, often found in printer inks as well as being commonly used for agricultural purposes.³⁹ Based on the success of the Au/TiO₂ catalysts with tailored synthesis conditions,²⁶ Pd/TiO₂ catalysts were also synthesised with varying conditions to find the most stable and selective catalyst to complete hydrogenation of furfural with minimal side product formation.

In this section, the aberration corrected HAADF-STEM was employed to investigate the morphology of the Pd/TiO₂ catalysts, focusing especially on the existence of ultra-small Pd clusters. Ultra-small clusters consisting of only a few Pd atoms were found in the A1 Pd/TiO₂ catalyst system, while was synthesized with a H₂O solution at 1 °C. While in the B1 Pd/TiO₂ catalyst system, which was synthesized with a 1:1 H₂O/EtOH solution at -30 °C, no ultra-small Pd cluster was observed. A quantitative integrated HAADF intensity analysis of the ultra-small Pd clusters was carried out and determined that these ultra-small clusters consist of from 1 to 3 Pd atoms. The catalysts were also imaged after the catalytic test. For the A1 catalyst, a significant amount of aggregation was observed, indicating low catalytic stability of the A1 catalyst.

6.3.2 Experimental details

The PVA protected Pd/TiO₂ catalysts were prepared using a standard

sol-immobilisation method similar to the Au nanoparticles preparation described above with controlled temperature during the reduction process.²⁶ The dipotassium tetrachloropalladate (K_2PdCl_4) with designed Pd amount (1.26×10^{-4} M) was dissolved in the ratio controlled H_2O /ethanol solution. The PVA solution (1wt% solution, $M_w = 9000 - 10000$ g/mol) was added while controlling the 0.65 PVA/Pd mass ratio. The dark brown/black sols were then formed by adding 0.1 M $NaBH_4$ solutions drop-wise to all different solutions within one minute, with continuous stirring. After the reduction of the Pd clusters, the colloidal solutions were immobilised onto a controlled mass of the TiO_2 support material, to form the 1% weight ratio of Pd and TiO_2 , with strong stirring. For temperatures above $50^\circ C$, the immobilisation process of the Pd clusters taken 15 minutes, while for temperatures lower than $50^\circ C$, the process taken 30 minutes. Sulphuric acid was added to the prepared mixtures to acidify them to 1-2 pH. The full immobilisation of the Pd clusters onto the TiO_2 support was then accomplished. The resulting solid was obtained from the filtered slurry. It was then washed with distilled water and dried over night at room temperature.

The Pd/ TiO_2 catalysts were sent to our group in powder form. They were dissolved in pure ethanol, then dispersed with sonication. The solution was drop cast with a pipette onto a 400-mesh copper TEM grid covered with amorphous carbon film. The HAADF-STEM study was carried out by using a 200kV JEOL JEM 2100F HAADF-STEM equipped with a CEOS spherical aberration corrector. The HAADF

detection angle used in this study is 62 mrad for the inner angle and 164 mrad for the outer angle.

6.3.3 Pd cluster characterization

6.3.3.1 Pd cluster characterization: before catalysis test

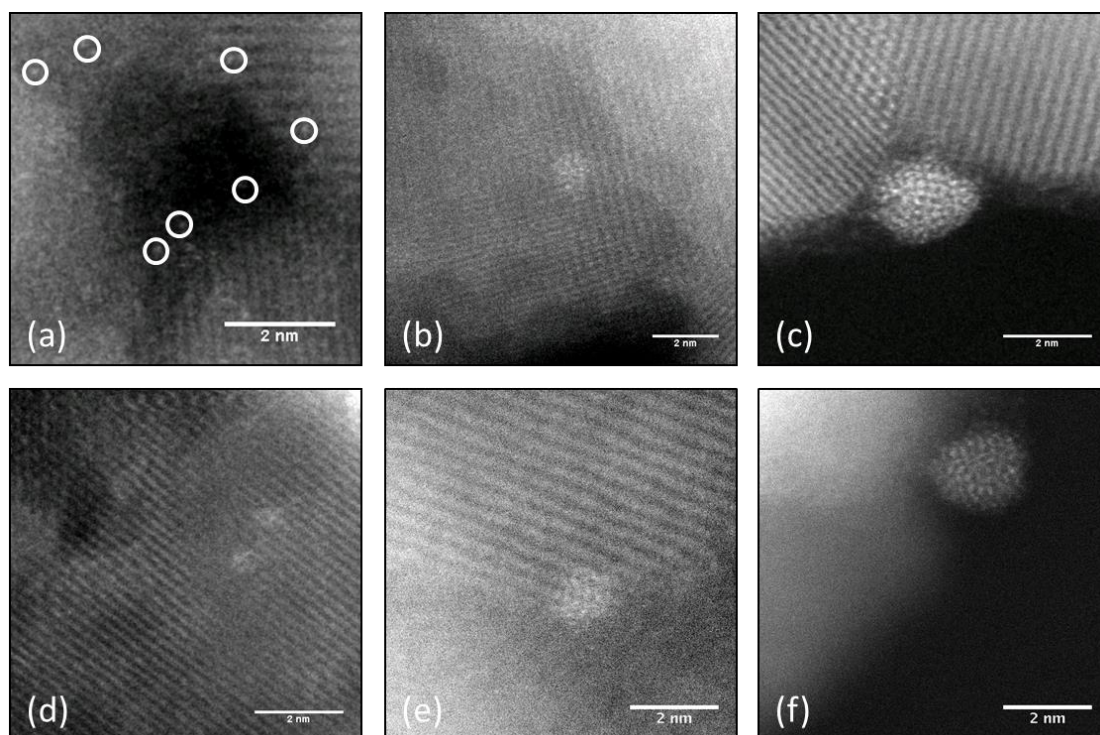


Figure 6.6. Representative HAADF STEM images of the Pd/TiO₂ catalysts from A1 ((a)-(d)), and B1 ((e)-(f)). The ultra-small cluster are circled.

Both A1 and B1 samples were imaged prior to the catalysis test by the aberration-corrected HAADF STEM. The small Pd clusters (smaller than 2 nm) can be found in both A1 and B1 samples. In the TEM analysis of these two samples, the average sizes of the A1 and B1 samples are 2.5 ± 0.8 nm and 1.4 ± 0.4 nm, respectively.

The ultra-small Pd clusters (consisting of a few atoms) are only found in the A1 sample, which compensates for the relatively high average particle size, resulting a similar catalytic activity in Furfural hydrogenation (A1: 464 and 620 mol (mol Pd)⁻¹h⁻¹ and at 25°C and 50°C; B1: 491 and 470 mol (mol Pd)⁻¹h⁻¹ and at 25°C and 50°C). The atomic number of Pd is 46, which is significantly smaller than that of Au (79), consequently, with the same TiO₂ support, the contrast of the Pd cluster is lower than that of the Au clusters studies on the previous section. Therefore, it is necessary that we image the Pd clusters at the edge of the TiO₂ support, or on the thinner regions of the TiO₂ support. The representative images of the Pd/TiO₂ catalysts are shown in Figure 6.6. We can see that the structural patterns of the Pd clusters on the TiO₂ support are not very clear due to the low contrast, while the Pd clusters on the edge of the TiO₂ support show a relatively clear structural pattern.

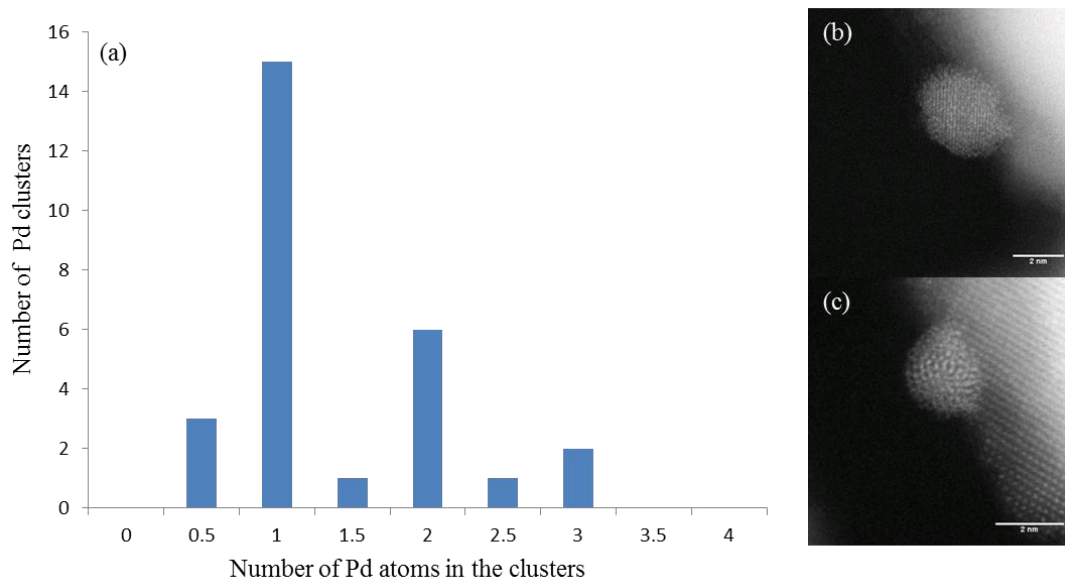


Figure 6.7. (a) Size distribution of the Pd clusters, obtained by the cluster weighing method. The representative images of the Pd clusters used as mass balance in the cluster weighing are shown in (b) and (c).

A quantitative analysis was performed on the ultra-small Pd clusters found in A1. The big Pd clusters with clear background were used as the mass balances in the cluster weighing, two representative images of these clusters are shown in Figures 6.7 (b) and (c). The size of the mass balance clusters was calculated from their projected area with the method described in Chapter 4. The integrated HAADF intensities of the clusters were obtained through a careful background subtraction. The integrated HAADF intensities of the ultra-small Pd clusters were obtained and then compared with the mass balance clusters' intensity. The numbers of Pd atoms in the ultra-small Pd cluster was therefore determined by the atom counting method. The size distribution of the ultra-small Pd clusters is shown in Figure 6.7 (a). Their size range is from 0.5 to 3 Au atoms. As discussed above, the appearance of the half number of Pd atoms is due to the error in the background subtraction, influence of the PVA ligand and instrument error. However, as we can see, the majority of the clusters have an integer number of Pd atoms, showing the relative accuracy of the atom counting method.

6.3.3.2 Pd cluster characterization: after catalysis test

The furfural hydrogenation was performed using a stainless steel reactor equipped with a heater, mechanical stirrer, gas supply system and thermometer. The furfural solution with suspended Pd/TiO₂ catalysts was added into the reactor and the hydrogenation reaction was performed. After the test, the catalyst was then dried and

imaged (for the second time) by the aberration corrected HAADF STEM.

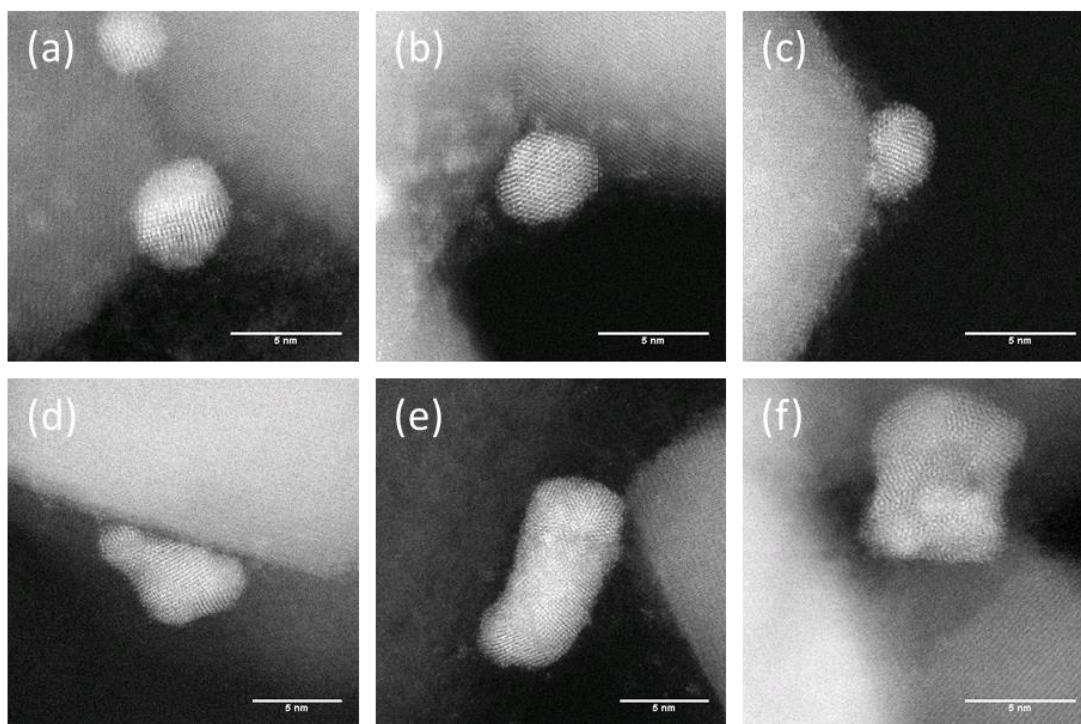


Figure 6.8. Representative HAADF-STEM images of A1 tested Pd/TiO₂ catalysts. Both the regular small and large Pd clusters can be found in (a)-(c). The large irregular Pd clusters are shown in (d)-(f).

The representative HAADF STEM images of the A1 Pd/TiO₂ catalysts that have undergone catalytic testing are shown in Figure 6.8. The small Pd clusters can still be observed in the tested A1 sample (as shown in Figures 6.8 (a)-(c)), showing the stability of the catalyst. Large Pd clusters, similar to the large ones in the untested sample, were also found. However, there were additional clusters observed that are larger and irregular in shape (as shown in Figures 6.8 (d)-(f)), which did not appear in the untested sample. Here, the large irregular clusters are defined by two features:

large geometric size, which should be bigger than 3 nm; and irregular shape differing from the normal quasi-spherical or quasi-elliptical shape of the untested Pd clusters. From the HAADF STEM images, we can see features in the large irregular clusters that suggest they are aggregations of the Pd clusters. For example, in Figure 6.8(d), it is obvious that the upper left part of the irregular cluster was a 2 nm quasi-spherical Pd cluster, its icosahedral structure is different from the crystal structure of the rest of the cluster.

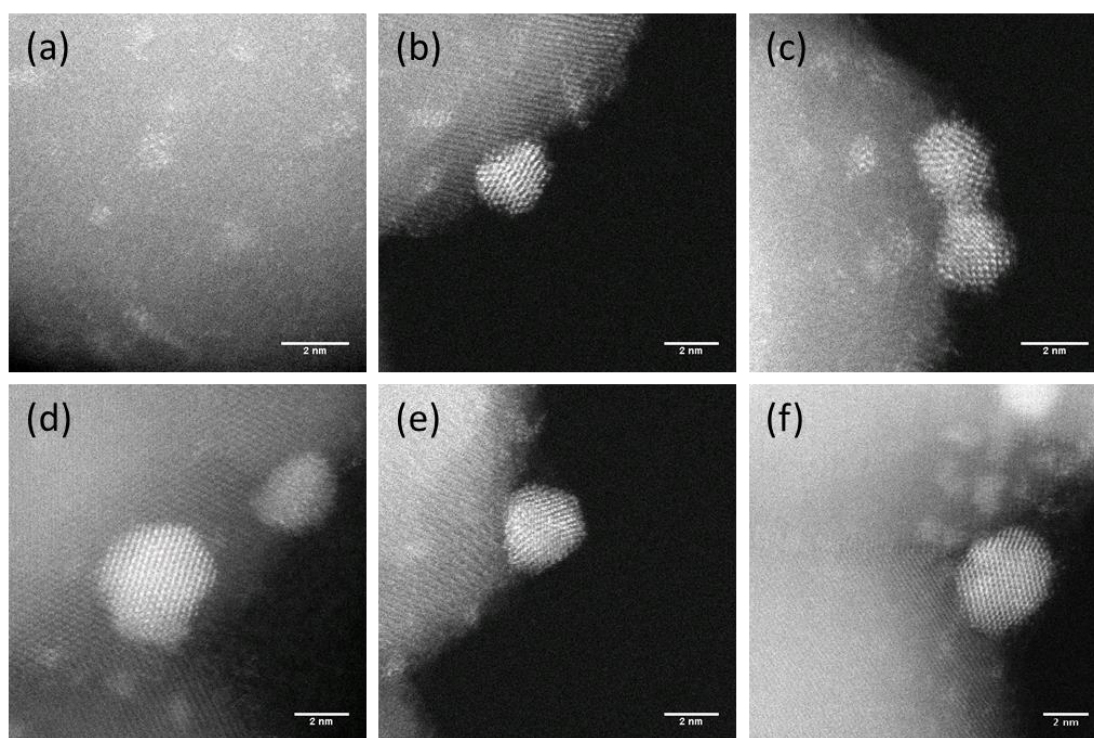


Figure 6.9. Representative HAADF-STEM images of tested B1 Pd/TiO₂ catalysts.

The representative HAADF STEM images of tested B1 Pd/TiO₂ catalysts are shown in Figure 6.9. Similar to the tested A1 sample, both regular small and large Pd clusters can be observed. However, unlike the tested A1, no large irregular clusters

were observed. Only two ~2 nm Pd clusters attached to each other were observed, as shown in Figure 6.9 (c), which may be due to the effect of the furfural hydrogenation process. The preserved small Pd clusters demonstrate the stability of the B1 Pd/TiO₂ catalyst. The presence and absence of the large irregular Pd clusters in the A1 and B1 samples respectively, combined with the catalysis stability test, signify that B1 has a better catalysis stability than A1.

6.4 Conclusions

In conclusion, the HAADF-STEM was successfully employed to investigate the small Pd clusters in the Pd/TiO₂ catalyst before and after the catalysis test. For the catalysts which were not tested in the furfural hydrogenation process, the small Pd clusters with size around 1 nm, that are difficult to detect in the BF TEM, are found in both the A1 and B1 samples. However, the ultra-small Au clusters were only characterized in the A1 catalyst. Quantitative atom counting analysis of the ultra-small Pd clusters in A1 was achieved by using the large Pd clusters as mass balances. The ultra-small Pd clusters were found to consist of 1 to 3 Pd atoms. The presence of these ultra-small and potentially higher catalytically active Pd clusters in the A1 catalyst explain why the catalytic activity of A1 and B1 are similar, despite A1 having a larger average size than B1. The existence of the small Pd cluster in both A1 and B1 samples after catalytic testing, shows the high stability of both catalysts. However, the large irregular Pd clusters that were only observed in the tested A1 sample suggest that the A1 catalyst has a lower catalytic stability than the B1

catalyst.

Reference:

1. Haruta, M. Size- and support-dependency in the catalysis of gold. *Catal. Today* **36**, 153–166 (1997).
2. Norskov, J. K., Bligaard, T., Hvolbaek, B., Abild-Pederen, F., Chorkendorff, I. & Christensen, C. H. The Nature of the Active Site in Heterogeneous Metal Catalysis. *Chem. Soc. Rev.* **37**, 2163–2171 (2008).
3. Satterfield, C. N. *Heterogeneous Catalysis in industrial Practice. Heterogenous Catalysis in Practice* (McGraw Hill Book Co, 1991). doi:TP156.C35S27
4. Burch, R. Gold catalysts for pure hydrogen production in the water-gas shift reaction: activity, structure and reaction mechanism. *Phys. Chem. Chem. Phys.* **8**, 5483–500 (2006).
5. Li, Z. Y., Young, N. P., Di Vece, M., Palomba, S., Palmer, R. E., Bleloch, A. L., Curley, B. C., Johnston, R. L., Jiang, J. & Yuan, J. Three-dimensional atomic-scale structure of size-selected gold nanoclusters. *Nature* **451**, 46–8 (2008).
6. Lewis, L. N. Chemical catalysis by colloids and clusters. *Chem. Rev. (Washington, DC, United States)* **93**, 2693–2730 (1993).
7. Judai, K., Abbet, S., Wörz, A. S., Heiz, U. & Henry, C. R. Low-Temperature Cluster Catalysis. *J. Am. Chem. Soc.* **126**, 2732–2737 (2004).
8. Janssens, T. V. W., Clausen, B. S., Hvolbaek, B. H., Falsig, H., Christensen, C. H., Bligaard, T. & Norskov, J. K. Insights into the reactivity of supported Au nanoparticles: Combining theory and experiments. *Top. Catal.* **44**, 15–26 (2007).
9. Ferrando, R., Jellinek, J. & Johnston, R. L. Nanoalloys: From Theory to Applications of Alloy Clusters and Nanoparticles. *Chem. Rev.* **108**, 846–904

- (2008).
10. Parravano, G. Surface reactivity of supported gold. II. Hydrogen transfer between benzene and cyclohexane. *J. Catal.* **18**, 320–328 (1970).
 11. Sakurai, H., Tsubota, S. & Haruta, M. Hydrogenation of CO₂ over gold supported on metal oxides. *Appl. Catal. A, Gen.* **102**, 125–136 (1993).
 12. HARUTA, M. Gold catalysts prepared by coprecipitation for low-temperature oxidation of hydrogen and of carbon monoxide. *J. Catal.* **115**, 301–309 (1989).
 13. Haruta, M., Kobayashi, T., Sano, H. & Yamada, N. Novel gold catalysts for the oxidation of carbon monoxide at a temperature far below 0.DEG.C. *Chem. Lett.* 405–408 (1987). doi:10.1246/cl.1987.405
 14. Haruta, M. Low-Temperature Oxidation of CO over Gold Supported on TiO₂, α -Fe₂O₃, and Co₃O₄. *Journal of Catalysis* **144**, 175–192 (1993).
 15. Ueda, A., Oshima, T. & Haruta, M. Reduction of nitrogen monoxide with propene in the presence of oxygen and moisture over gold supported on metal oxides. *Appl. Catal. B Environ.* **12**, 81–93 (1997).
 16. Caps, V., Arrii, S. & Morfin, F. Structures and associated catalytic properties of well-defined nanoparticles produced by laser vaporisation of alloy rods. *Faraday Discuss.* **138**, 241–256 (2008).
 17. Bamwenda, G. R., Tsubota, S., Nakamura, T. & Haruta, M. The influence of the preparation methods on the catalytic activity of platinum and gold supported on TiO₂ for CO oxidation. *Catal. Letters* **44**, 83–87 (1997).
 18. Sakurai, H. & Haruta, M. Synergism in methanol synthesis from carbon dioxide over gold catalysts supported on metal oxides. *Catal. Today* **29**, 361–365 (1996).

19. Pasquato, L., Rancan, F., Scrimin, P., Mancin, F. & Frigeri, C. N-Methylimidazole-functionalized gold nanoparticles as catalysts for cleavage of a carboxylic acid ester. *Chem. Commun.* **2**, 2253–2254 (2000).
20. Edwards, J. K., Ntainjua, E., Carley, A. F., Herzing, A. A., Kiely, C. J. & Hutchings, G. J. Direct synthesis of H₂O₂ from H₂ and O₂ over gold, palladium, and gold-palladium catalysts supported on acid-pretreated TiO₂. *Angew. Chemie - Int. Ed.* **48**, 8512–8515 (2009).
21. Li, G., Jiang, D., Kumar, S., Chen, Y. & Jin, R. Size Dependence of Atomically Precise Gold Nanoclusters in Chemoselective Hydrogenation and Active Site Structure. (2014).
22. Molina, L. M. & Hammer, B. Some recent theoretical advances in the understanding of the catalytic activity of Au. in *Applied Catalysis A: General* **291**, 21–31 (2005).
23. Cushing, B. L., Kolesnichenko, V. L. & O'Connor, C. J. Recent advances in the liquid-phase syntheses of inorganic nanoparticles. *Chem. Rev.* **104**, 3893–3946 (2004).
24. Taylor, M. G., Austin, N., Gounaris, C. E. & Mpourmpakis, G. Catalyst Design Based on Morphology- and Environment-Dependent Adsorption on Metal Nanoparticles. *ACS Catal.* **5**, 6296–6301 (2015).
25. Layan Savithra, G. H., Muthuswamy, E., Bowder, R. H., Carrillo, B. A., Bussell, M. E. & Brock, S. L. Rational design of nickel phosphide hydrodesulfurization catalysts: Controlling particle size and preventing sintering. *Chem. Mater.* **25**, 825–833 (2013).
26. Rogers, S. M. , Catlow, C. R., Chan-Thaw, C. E., Gianolio, D., Gibson, E. K., Gould, A. L., Jian, N., Logsdail, A. J., Palmer, R. E., Prati, L., Dimitratos, N., Villa, A., Wells, P. Tailoring Gold Nanoparticle Characteristics and the Impact

- on Aqueous-Phase Oxidation of Glycerol. *ACS Catal.* **5**, 4377–4384 (2015).
27. Wang, Z. W. Toikkanen, O., Yin, F., Li, Z. Y., Quinn, B. M. & Palmer, R. E. Counting the atoms in supported, monolayer-protected gold clusters. *J. Am. Chem. Soc.* **132**, 2854–2855 (2010).
28. Young, N. P., Li, Z. Y., Chen, Y., Palomba, S., Di Vece, M. & Palmer, R. E. Weighing supported nanoparticles: Size-selected clusters as mass standards in nanometrology. *Phys. Rev. Lett.* **101**, 246103 (2008).
29. Jian, N., Stapelfeldt, C., Hu, K., Fröba, M. & Palmer, R. Hybrid atomic structure of the Schmid cluster Au₅₅(PPh₃)₁₂Cl₆ resolved by aberration-corrected STEM. *Nanoscale* DOI: 10.1039/c4nr06059h (2015). doi:10.1039/c4nr06059h. Please
30. Lemire, C., Meyer, R., Shaikhutdinov, S. K. & Freund, H. J. CO adsorption on oxide supported gold: From small clusters to monolayer islands and three-dimensional nanoparticles. *Surf. Sci.* **552**, 27–34 (2004).
31. Garzón, I., Michaelian, K., Beltran, M. R., Posada-Amarillas, A., Ordejon, R., Artacho, E., Sanchez-Portal, D. & Soler, J. M. Lowest Energy Structures of Gold Nanoclusters. *Phys. Rev. Lett.* **81**, 1600–1603 (1998).
32. Guzman, J. & Gates, B. Catalysis by supported gold: Correlation between catalytic activity for CO oxidation and oxidation states of gold. *J. Am. Chem. Soc.* 2672–2673 (2004).
33. Pei, Y., Shao, N., Gao, Y. & Zeng, X. C. Investigating active site of gold nanoparticle Au₅₅(PPh₃)₁₂Cl₆ in selective oxidation. *ACS Nano* **4**, 2009–2020 (2010).
34. Pietron, J. J., Stroud, R. M. & Rolison, D. R. Using Three Dimensions in Catalytic Mesoporous Nanoarchitectures. *Nano Lett.* **2**, 545–549 (2002).

35. Nakagawa, Y., Takada, K., Tamura, M. & Tomishige, K. Total hydrogenation of furfural and 5-hydroxymethylfurfural over supported Pd-Ir alloy catalyst. *ACS Catal.* **4**, 2718–2726 (2014).
36. Lange, J. P., Van Der Heide, E., Van Buijtenen, J. & Price, R. Furfural-A promising platform for lignocellulosic biofuels. *ChemSusChem* **5**, 150–166 (2012).
37. Dutta, S., De, S., Saha, B. & Alam, M. I. Advances in conversion of hemicellulosic biomass to furfural and upgrading to biofuels. *Catal. Sci. Technol.* **2**, 2025 (2012).
38. Corma Canos, A., Iborra, S. & Velty, A. Chemical routes for the transformation of biomass into chemicals. *Chemical Reviews* **107**, 2411–2502 (2007).
39. Yan, K., Wu, G., Lafleur, T. & Jarvis, C. Production, properties and catalytic hydrogenation of furfural to fuel additives and value-added chemicals. *Renewable and Sustainable Energy Reviews* **38**, 663–676 (2014).

CHAPTER 7

MULTILAYER DEPOSITION OF SIZE-SELECTED AU CLUSTERS AND POLYMER LAYERS

7.1 Introduction

Understanding and tailoring the novel properties of nanoclusters has been a longstanding cornerstone of nanoscience research.¹⁻⁴ Nanoclusters display unique and size-dependent physical and chemical properties, providing great potential for use in electronics, optics, biology and catalysis applications.¹⁻⁹ There are three major cluster production routes: physical cluster beam deposition, chemical synthesis, and biological formation.^{5,10-18} Compared with the chemical and biological synthesis routes, cluster beam deposition has advantages in its precise size control, tuneable interaction with the deposition support, low contamination and convenience in producing multi-elemental clusters.¹⁸

However, despite such advantages, cluster beam technology has not been industrialized on a large scale. The greatest issue limiting the large-scale exploitation of cluster beam technology is the low cluster deposition flux, which to date has made this route uncompetitive compared with the chemical synthesis methods.^{11,18} To address this issue a new cluster beam technique, the “Matrix Assembly Cluster

Source”, has been developed at NPRL, which shows great potential for scaling up the cluster beam flux; from currently achievable beam currents of the order of nanoamps to the milliamp regime.^{19,20} The challenge is how to accommodate and process this large abundance of clusters. The current deposition method relies on depositing clusters onto planar substrates with a typical area of square centimetres.^{11,18} However, MACS can easily deposit sufficient clusters to cover an area of square metres to even square kilometres with a high density of clusters in a matter of hours, which is far beyond the ability of the normal cluster beam deposition methods. Therefore, a new deposition scheme, which is capable of accommodating the new high flux cluster source, is required.

Here, we present a new multilayer cluster deposition scheme. The key element of this scheme is the sequential deposition of a stack of three-layer sandwiches each comprising: (a) a thin support film, (b) a layer of clusters, and (c) a soluble release layer. The sandwich stack is then diced into small pieces and immersed in a solvent to dissolve the soluble release layers to create small platelets covered with clusters. For the proof of principle demonstration of this scheme, the support film was a carbon film produced using an e-beam evaporator, the soluble layer was a PVP layer (either spray-deposited using a pulse valve or vapour-deposited from an evaporator), and the cluster layer comprised size-selected Au₉₂₃ clusters generated by a magnetron sputtering inert gas aggregation cluster source. With the same instrument setup, we also demonstrate the ability to use PVP-cluster stacks to produce size-selected

colloidal clusters. The characterization of the multilayer structure was performed using through-focal aberration-corrected high angle annular dark field (HAADF) scanning transmission electron microscopy (STEM).

7.2 Experimental details

The carbon support layers were produced with a Mantis EBE-1 e-beam evaporator, which was added to the deposition chamber of the magnetron cluster source. The thickness of the carbon layer was controlled by the deposition flux measured by the integrated flux monitor. The carbon support film was simultaneously deposited on both a 1×1 cm silicon substrate and a 400-mesh TEM grid (for the STEM characterization of the multilayer structure). The size selected Au₉₂₃ clusters were deposited onto the carbon support layer from a gas condensation magnetron sputtering cluster source equipped with a lateral time-of-flight mass selector.^{11,21,22} The mass resolution of the cluster source is $M/\Delta M \approx 20$. The deposition energy of the clusters was set to 0.5eV per atom by controlling the bias applied to the substrate. The PVP layer was deposited on top of the cluster layer by either pulse valve spray deposition or thermal evaporation. The spray deposition was performed using a First Sensor series-9 high performance pulse valve, where the pulse time is as short as 160 μ s. The thermal evaporation is performed using a home-built thermal evaporator. The applied voltage was set to 1.2 V. The dicing of the samples was performed using either a diamond saw (DAD321 Automatic Dicer), or a laser cutting system (the Lasea laser micro machining centre). Then the diced samples were immersed in

isopropanol to dissolve the PVP release layers to produce the small supported cluster platelets. The multilayer deposited stacks, diced stacks and the released sample were analysed by a JEOL JEM 2100F HAADF STEM, equipped with an spherical aberration-corrector (CEOS GmbH). The acceleration voltage employed was 200 kV and the electron beam was produced using a field emission electron source. A HAADF detector was utilized with 62 mrad inner angle and 164 mrad outer angle. To minimize the effect of the sample's flatness level, the through focal analysis was performed in a region smaller than 31 nm \times 31 nm.

7.3 Results and discussion

7.3.1 Supported Au clusters from multilayer deposition

7.3.1.1 Multilayer deposition

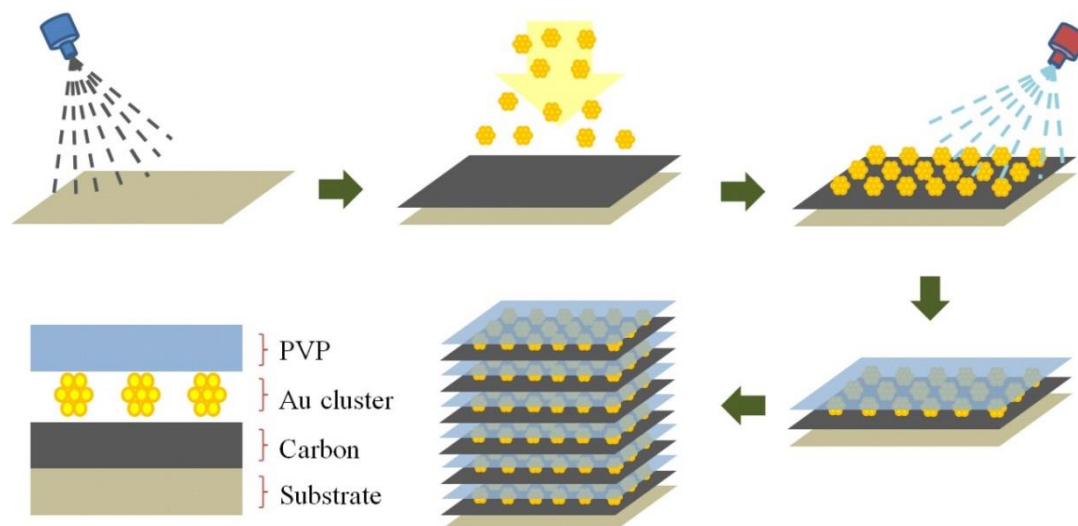


Figure 7.1. Schematic of the multilayer deposition process: First, the carbon layer was deposited onto the substrate by e-beam evaporation; then the Au clusters were deposited on top of the carbon layer; the PVP layer was formed on top of the cluster layer by either pulse valve spray deposition or thermal evaporation. This process was repeated to form a multilayer stack of carbon-cluster-PVP sandwiches.

A schematic illustration of the multilayer deposition is shown in Figure 7.1. First, the C support layer was deposited onto a Si substrate by e-beam evaporation. The size-selected Au_{923} clusters were deposited onto the deposited C support layer. The landing energy was set to 0.5 eV per atom to achieve the soft landing. After the cluster deposition, the PVP layer was either pulse valve sprayed or evaporated on top of the Au clusters to produce a C-cluster-PVP sandwich. These three steps were

repeated to form multilayer stacks of the C-cluster-PVP sandwiches.

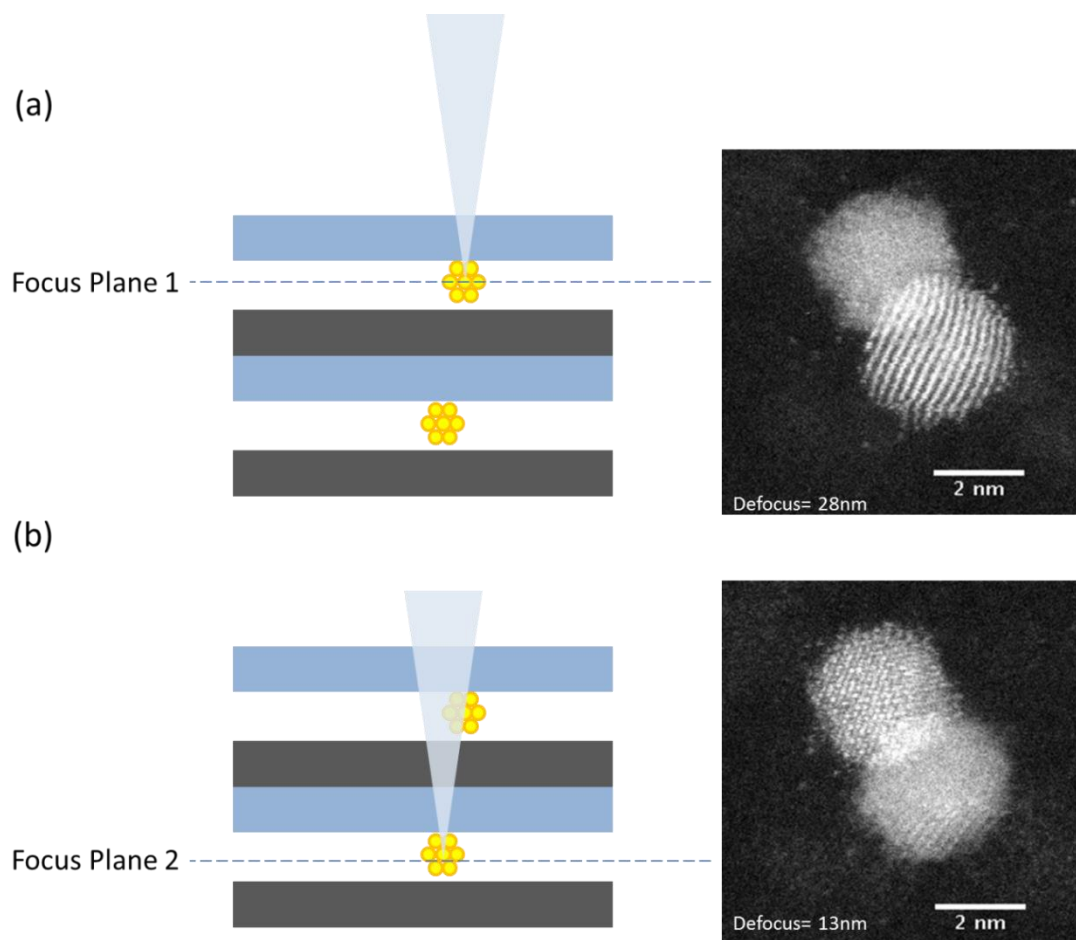


Figure 7.2. Schematic of the through-focal HAADF STEM analysis on the multilayer sample. The electron beam was focused on: (a) upper cluster, and (b) lower cluster, respectively. The cluster's centres were estimated in their corresponding focal plane 1 and 2. Therefore, the defocus difference between these two planes corresponds to the depth of the whole C-cluster-PVP sandwich.

Through the development of aberration correction technology, the vertical resolution of the aberration-corrected HAADF STEM has been dramatically improved. Experiments have been successfully employed to detect the 3D information on

dopants, buried defects and even single atoms using through-focal HAADF STEM analysis.^{23–26} Here, we employ a similar through-focal method to investigate the multilayer structure of the sample. An illustrative schematic and the corresponding experimental HAADF STEM images of the through-focal method are shown in Figure 7.2. In a sample comprising two carbon-cluster-PVP sandwiches, when the electron beam is focused on the upper Au cluster, an image of a clear upper Au cluster and blurry lower Au cluster is obtained. Then, the electron beam is focused on the lower cluster. Assuming the focal planes are located at the centre of the clearly imaged clusters, the focal difference between these two focal planes can be considered as the thickness of the whole C-cluster-PVP sandwich.

To test the reproducibility of the multilayer deposition, an 8-layer sample (where each ‘layer’ is a carbon-cluster-PVP sandwich) was produced using identical deposition conditions. The 8-layer sample deposited on the TEM grid was analysed by HAADF STEM. In the analysis, 6 layers of Au clusters were observed by the through-focal HAADF STEM, as shown in Figure 7.3. The focal range is from -28 nm to 13 nm. The focal differences between the neighbouring layers are 9 nm, 9 nm, 9 nm, 8 nm and 6 nm moving from the low defocus to high defocus values, which indicate the corresponding thicknesses of the sandwiches. The layer thickness is quite even especially for the first 4 layers. The reason for the slightly smaller 6 nm thickness layer may due to the following reasons. First, the error of the through-focal analysis, as the standard of judging whether the cluster under is focus or not depends

on whether the atomic structure of the cluster can be resolved clearly. This may give an error in the measured radius of the cluster, which for Au₉₂₃ is about 1.35 nm. Second, there are weak patterns in the background of the support, demonstrating that the layers are not exactly flat. So the clusters on either side of the 6 nm-thick layer may be in a locally “thin” region of the layer. But in general, the thicknesses of the successive layers are still reasonably uniform.

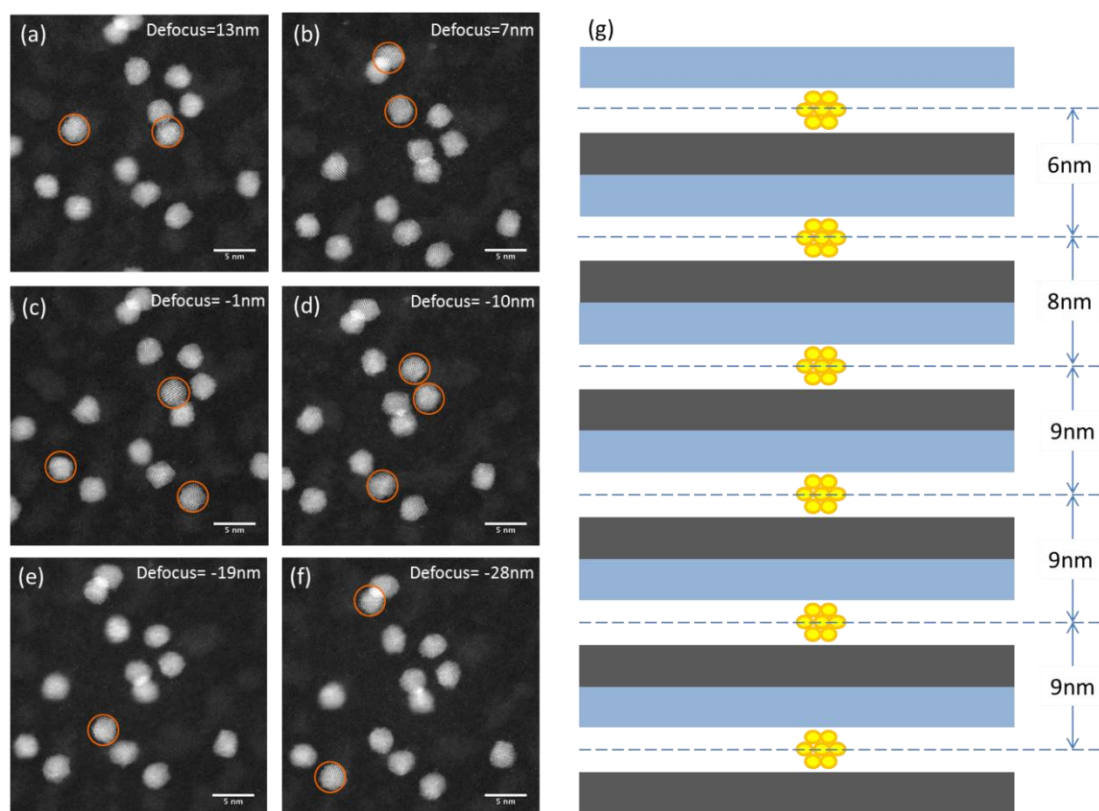


Figure 7.3. (a)-(f) Through-focal HAADF STEM images of a multilayer sample comprising eight carbon-cluster-PVP sandwiches deposited under identical conditions. The clusters which were focused are marked by the red circles. (g) A schematic diagram of the 3D structure of the multilayer sample with the thickness values determined from the through-focal STEM analysis.

It was not possible to identify clusters from all eight discrete layers in a single STEM image. At most, it was only possible to identify clusters from six discrete layers in a single STEM image. The reason for this can be due to the relatively small region we used for the through-focal analysis. Since the sample cannot be aligned exactly normal to the electron beam, and in order to minimize the effect of this, the analysis region is set to no larger than $31\text{ nm} \times 31\text{ nm}$. In this small region, it is hard to include all 8 layers of clusters. Evidence of the missing layers can be found in other series of the through-focal HAADF STEM images. In one series, only four layers of Au clusters were identified, but the focal difference between the highest and lowest cluster layers is 47 nm, which is even larger than the 41 nm difference in the 6-layer series. This suggests that there may be at least three more layers in this region that have not been identified by the through-focal analysis and this may be due to the lack of Au clusters in the small imaging region.

7.3.1.2 Dicing process of multilayer hybrid material

Two methods were adopted for the dicing process. The first is dicing by an automatic dicer with a diamond saw. This method has been successfully employed to produce powder-supported size-selected clusters.²⁷ Using this method, the multilayer sample can be diced into $0.5\text{ mm} \times 0.5\text{ mm}$ pieces. To check the effect of the dicing process on the multilayer sample, the multilayer sample deposited on the TEM grid (shown in Figures 7.2 and 7.3) was diced by the diamond saw into $0.5\text{ mm} \times 0.5\text{ mm}$ pieces.

One of these small pieces was then sandwiched between two copper TEM grids without any support layer, as shown in Figure 7.4 (e). The aberration-corrected HAADF STEM was used to image this sample. The HAADF STEM images of the dicing edge are shown in Figures 7.4 (a) to (d). From Figure 7.4 (a), we can see that the observation window is quite small, because we cannot match the two support copper grids perfectly. The observation window is actually where the two holes in the separate TEM grids overlap. The dicing edge appears to show good morphology from Figure 7.4s (a)-(c). The clusters were uniformly distributed in the sample even at the very edge of the diced piece, as seen in Figure 7.4 (c). Most significantly, it can be clearly seen in Figure 7.4 (d) that two clusters overlap each other without aggregation, which indicates that the multilayer structure was still conserved after dicing.

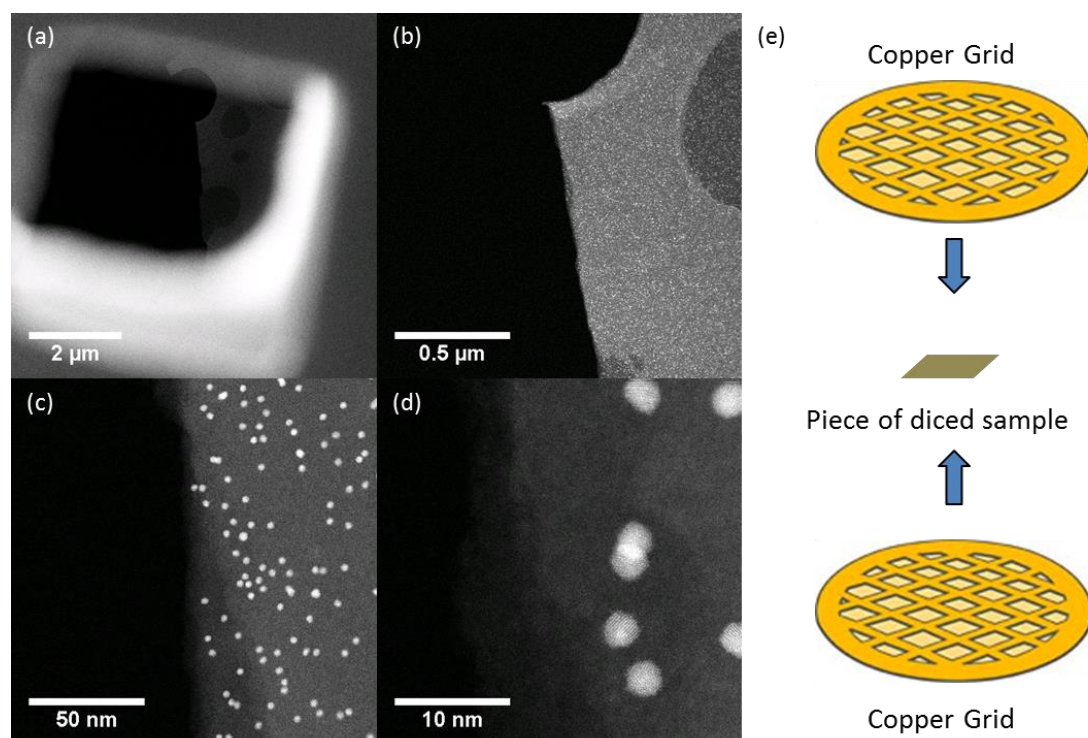


Figure 7.4. (a)-(d) HAADF STEM images of the diced sample's edge at different magnification, showing the successful dicing with good morphology of the edge and the conservation of the multilayer structure after dicing. The imaging of the small diced piece was achieved by sandwiching the diced sample between two copper grids, as show in (e).

The second method is laser dicing in a Lasea laser micro machining platform. A multilayer sample was diced with the laser to $105\mu\text{m} \times 105\mu\text{m}$ pieces. Then the HAADF STEM was employed to analyse the effect of laser dicing on the sample. The representative images are shown in Figure 7.5 (a), (b) and (c). We can see that the dicing edge also shows the good morphology with no significant damage to the sample. As shown in Figure 7.5 (c), the Au clusters survived even at the very edge of the diced sample without aggregation and that the mean cluster size is preserved.

Both laser and mechanical methods showed good performance in dicing the samples and had no significant effect on the diced cluster samples. In principle, the laser method is a more accurate and faster dicing process and will be helpful in the more precise micro process for our supported cluster samples in the future.

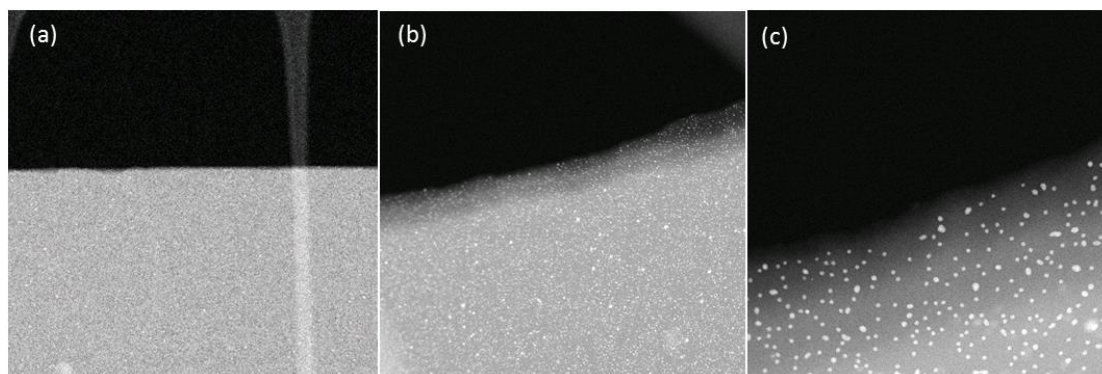


Figure 7.5 The representative HAADF STEM images of the dicing edge after laser dicing a multilayer sample. The frame sizes in (a), (b) and (c) are $2.57\ \mu\text{m} \times 2.57\ \mu\text{m}$, $1.03\ \mu\text{m} \times 1.03\ \mu\text{m}$ and $256.5\ \text{nm} \times 256.5\ \text{nm}$, respectively.

7.3.1.3 Release in solution

To demonstrate the release process multilayer samples comprising a stack of ten carbon-cluster-PVP sandwiches were prepared using the method described earlier. These samples were placed in isopropanol for 2 hours to dissolve the PVP layer and produce the small supported Au cluster platelets. After the platelets were released they were deposited onto the TEM grid to be imaged by HAADF STEM. The results are shown in Figure 7.6, where it can be seen that the supported Au cluster platelets

were successfully released from the multilayer samples. However, they do not appear to have been released as single layer platelets. Platelets comprising one, two and three layers can be seen in Figures 7.6 (a), (b) and (c), respectively. It seems that not all the carbon-supported Au clusters were successfully released. In Figure 7.6 (d), platelets with both single layer parts and double layer regions are observed. In general, we have proven that small C-supported Au cluster platelets can be released from the multilayer C-cluster-PVP stacks. The double and triple layer platelets suggest that either the PVP release layers were not completely dissolved, or the pulse valve sprayed PVP release layers may not be completely homogeneous. The colloidal experiment below seems to support the latter argument.

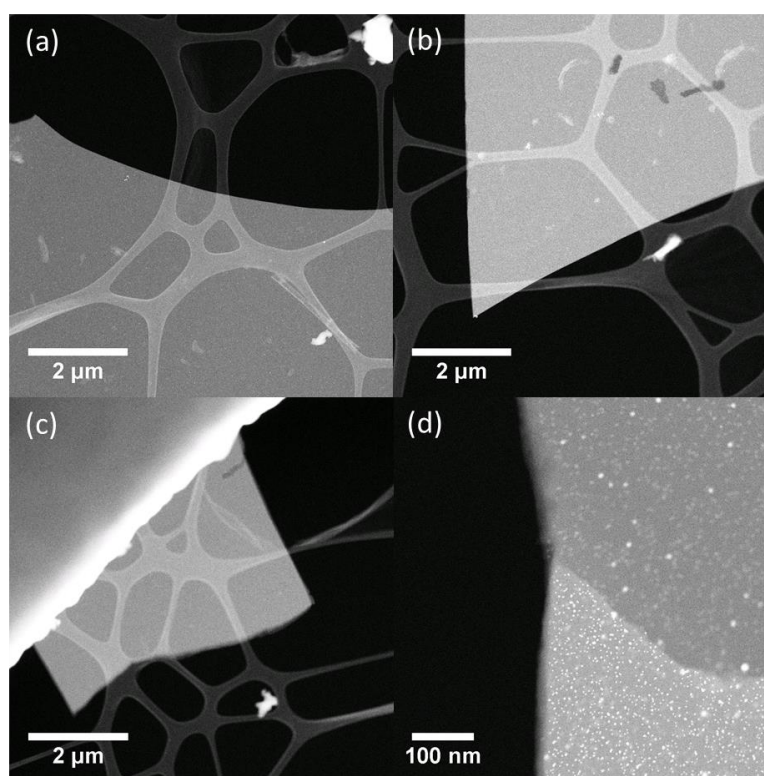


Figure 7.6. The HAADF STEM images of platelets with single, double and triple layers were shown in (a), (b) and (c), respectively. A platelet with part single layer, part double layer is shown in (d).

7.3.2 Size-selected colloidal cluster

Colloidal metal nanoclusters draw a great deal of attention due to their unique properties in catalysis, electronics and optics.^{28–31} In the area of catalysis, colloidal clusters were found to be active catalysts for many reactions in solution.^{32–35} The size of the cluster is one of the most important parameters that can significantly influence the catalytic activity.^{34,35} Therefore, the size control of the colloidal cluster is of great importance to their catalytic properties. Most colloidal clusters are produced via the chemical synthesis routes.^{7,36–38} The main drawback of chemical synthesis is the relative broad size distribution of the clusters (compare with the size-selected cluster source). Though some researchers have reported good size-control in chemically synthesized clusters, they can only be achieved for certain sizes with low flexibility.^{14,39–44}

With the approach for multilayer deposition described earlier, we can produce stacks of PVP-cluster layers, i.e. multilayer stacks of PVP-cluster layers without carbon support layers. After immersing the PVP-cluster multilayer samples into a solvent, the physically deposited size-selected clusters can be released into solution with PVP molecules surrounding them as a protection shell. Through this method, colloidal clusters that are size selected by the time-of-flight mass selector in the cluster beam source can be obtained.

7.3.2.1 PVP layer deposition: spray and evaporation

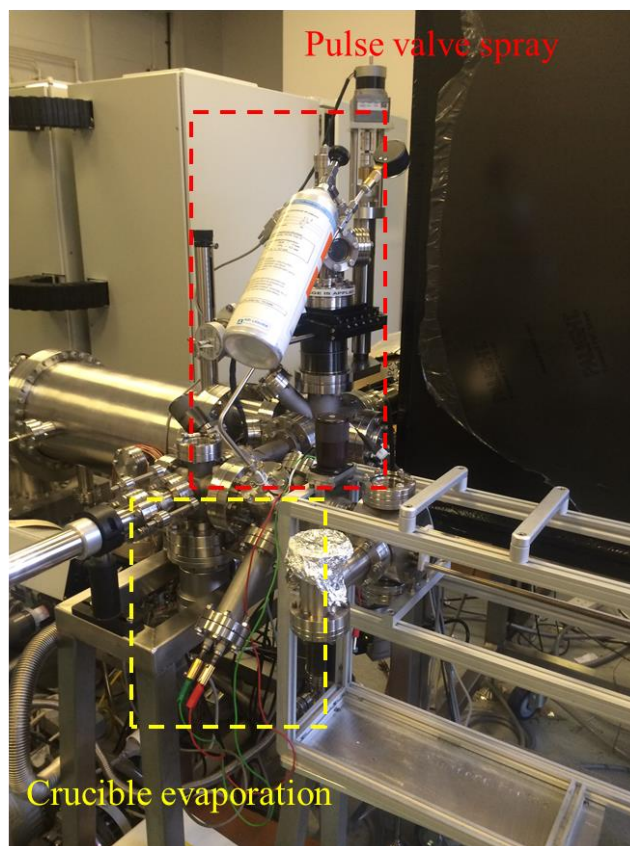


Figure 7.7. Instrument setup for the deposition of PVP layers in conjunction with size-selected clusters on the magnetron sputter inert gas aggregation source.

The deposition process can be seen as the multilayer deposition process described above without the C layer. Two PVP layer deposition methods were tested, i.e. pulse valve spray and evaporation. As shown in Figure 7.7, the pulse valve and evaporator were assembled in the same cluster deposition chamber in order to provide a better comparison under the same conditions. For the pulse spray method, the PVP (average molar weight 10000) solution (1g PVP+200 ml isopropanol) was sprayed onto the Si substrate in the cluster deposition chamber with the valve opened for a period of 1 ms, and 5 Hz frequency. The total deposition time is 5 mins. Then the size-selected Au₉₂₃

clusters were deposited on top of the PVP layer, and the whole process was repeated. For the thermal evaporation, the same molar weight for PVP was put into the crucible. The applied voltage was 0.6 V with a current of 5 A, the temperature is about 550°C. The total evaporation time was 120 s. The same coverage of size-selected Au clusters was deposited on each of the two samples for comparison purposes.

7.3.2.2 Formation and characterization of colloidal clusters

The two PVP-cluster multilayer samples were placed into separate 1 ml volumes of isopropanol for 1 hour. Then the solutions containing the samples were slightly shaken and stirred for 1 min. The clusters with the PVP layers were dissolved in isopropanol to form a colloidal solution. Then, 2 μL samples of each colloidal solution were drop cast onto two separate TEM grids. These two samples were then analysed by the HAADF STEM.

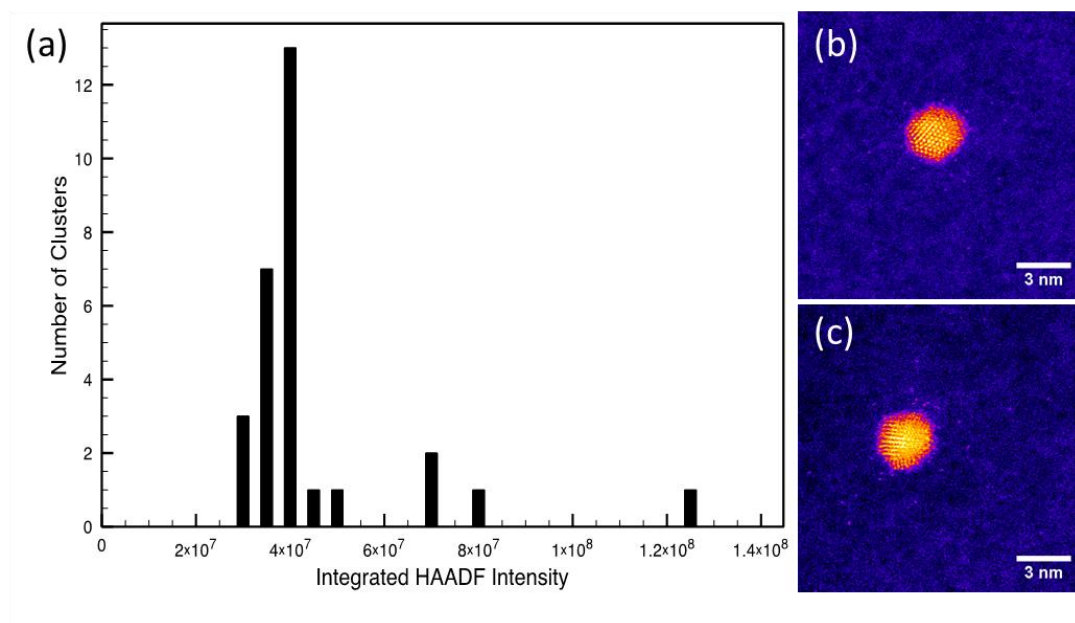


Figure 7.8 (a) HAADF intensity distribution of the size-selected Au₉₂₃ colloidal clusters, where the PVP layer was deposited by the pulse valve spray method. Representative high resolution HAADF STEM images of the colloidal clusters are shown in (b) and (c).

The analysis of the pulse valve sprayed sample is shown in Figure 7.8. The integrated HAADF intensity distribution of the clusters showed the size of the Au clusters was conserved in the colloidal solution. From the high resolution HAADF STEM images shown in Figures 7.8 (b) and (c), the colloidal clusters showed unchanged shapes and morphologies. This indicates that the clusters were surrounded and protected by the PVP ligands, which prevented the clusters from aggregating in the solution. A few peaks associated with dimer and trimer aggregation of the Au clusters were observed, but they cannot be confirmed to be the result of the clusters' aggregation in the solution. The dimer and trimer sized clusters were often observed in the sample from

the direct cluster beam deposition, where they were normally considered as the result of double- or triple-charged clusters. For cluster beam deposition with low landing energy, it is also possible to have different clusters deposited onto the same position resulting in aggregation.

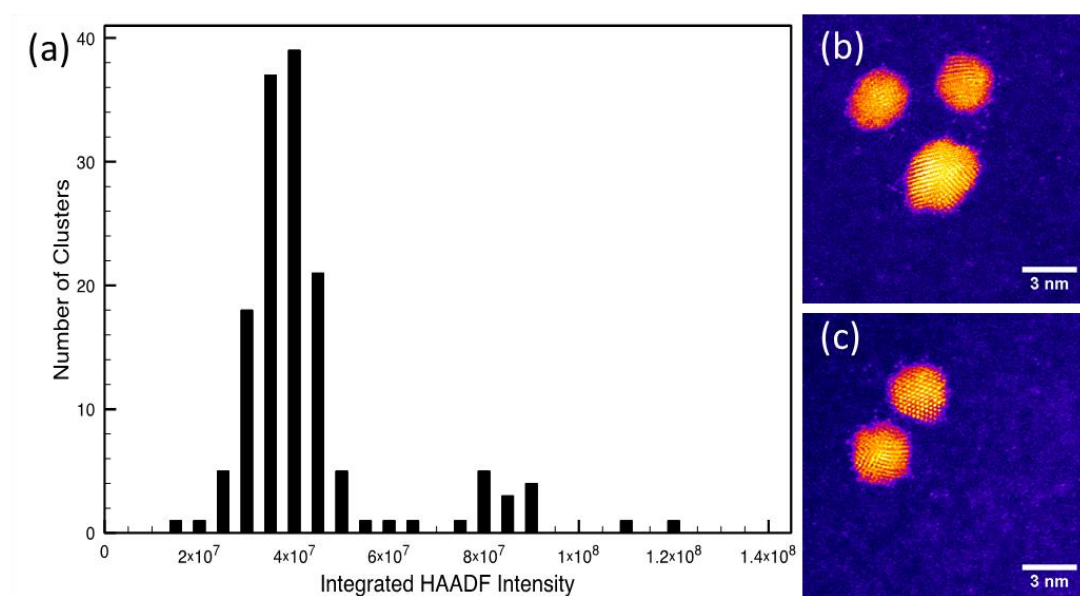


Figure 7.9 (a) HAADF intensity distribution of the size-selected Au_{923} colloidal clusters, where the PVP layers were deposited by thermal evaporation. Representative high resolution HAADF STEM images of the colloidal clusters are shown in (b) and (c).

Figure 7.9 shows the results of STEM measurements on colloidal clusters that were deposited between thermally evaporated PVP layers. Two discrete monomer and dimer peaks were observed in the integrated HAADF intensity distribution, showing that the size of the Au clusters was also conserved in the colloidal solution. It is

notable that the main peak of cluster monomers is slightly broader than that observed in the pulse valve spray sample. But, from the high resolution images (some representative examples of which are shown in Figure 7.9), the colloidal clusters have unchanged shapes and morphologies. Also, some images like Figure 7.9 (c) showed that the clusters were very close to each other without any aggregation. All of this suggests that the Au clusters were well protected by the PVP ligands in solution.

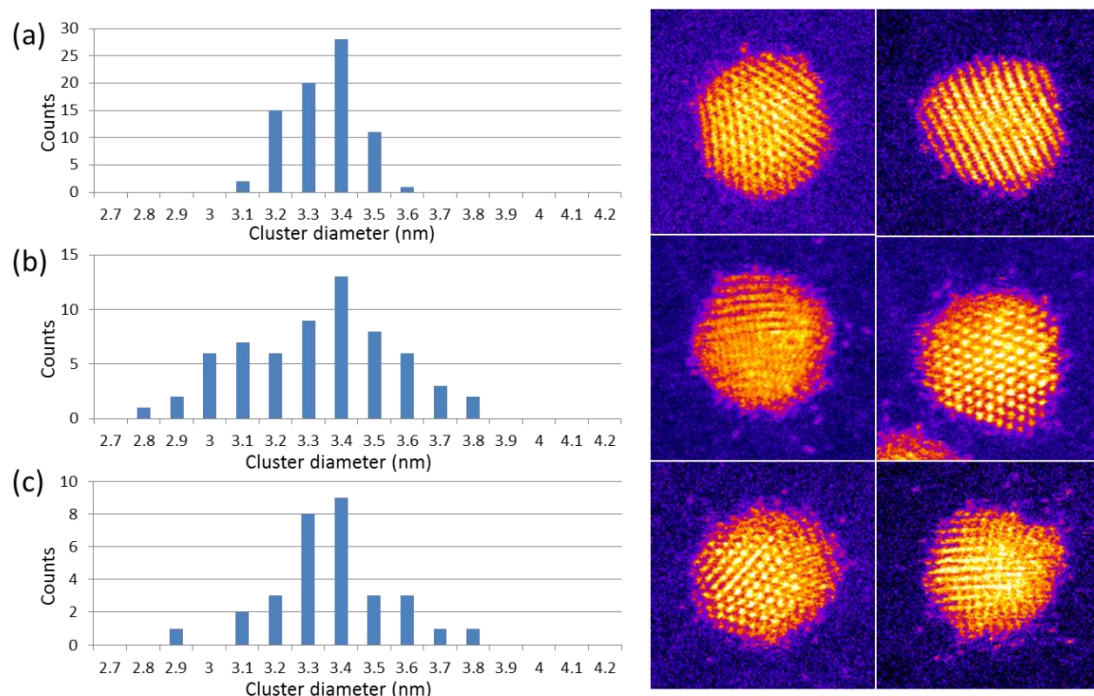


Figure 7.10. The diameter distribution and the corresponding representative HAADF STEM images of the clusters from: (a) the normal as-deposited size-selected Au₉₂₃ clusters, (b) the Au colloidal clusters with PVP deposited by the pulse valve spray method, and (c) the Au colloidal clusters with PVP deposited by the thermal evaporation method. The frame size of the representative HAADF STEM images is 5.04 nm × 5.04 nm.

The size (number of atoms inside the cluster) of the Au colloidal clusters cannot be obtained by the atom counting method utilized in chapter 3 due to the uncertain amount of the PVP ligands. Hence, the geometric sizes of the colloidal clusters from the monomer peak of their HAADF intensity distributions were measured to compare them with the value of the normal size-selected Au₉₂₃ clusters produced under the same cluster source experimental conditions. Their diameter distributions are shown in Figure 7.10. The peak sizes are very close, indicating that the clusters were well protected by the PVP ligands and the majority of the Au colloidal clusters remain the same size during the transfer process. However, the broadness of the size distributions for the three samples are different. The normal size-selected Au₉₂₃ clusters have the narrowest size distribution, while the Au colloidal with PVP deposited by the pulse valve spray has a somewhat broader distribution and the Au colloidal clusters with PVP deposited by the thermal evaporation have the broadest diameter distribution. The result of the geometric size distributions is consistent with their integrated HAADF intensity distribution, showing the different effect of the different PVP deposition methods on the mean cluster size.

As mentioned earlier, the cluster coverage for the two colloidal samples were set to be the same during cluster deposition. However, the density of the Au colloidal clusters measured by STEM was quite different. The colloidal sample, with PVP deposited by thermal evaporation, had a higher cluster density than the pulse valve

spray sample. This may suggest that the thermal evaporation method can produce a more homogeneous PVP layer than the pulse valve spray. This can also explain, that for the multilayer samples formed after dissolving in isopropanol (which the PVP layers were formed by pulse valve spray), the C-supported Au clusters were not completely released.

7.5 Conclusions

In summary, the multilayer deposition of multilayer stacks of C-cluster-PVP sandwiches has been demonstrated. The clusters survived during the multilayer deposition with conserved size and shape. Through-focal aberration-corrected HAADF STEM was employed to confirm the multilayer structure of the sandwich stack and successfully measure the thickness of the C-cluster-PVP sandwiches. The stacks can be diced by either mechanical diamond saw or laser, without significant effect on the clusters. Finally, it was demonstrated that small supported Au clusters platelets could be released from the multilayer stacks by dissolving the PVP layer in isopropanol. Using the same instrument setup, the production size-selected Au colloidal clusters by directly dissolving the PVP-cluster multilayer sample in isopropanol was also demonstrated. From the HAADF STEM analysis, it can be seen that the size-selected Au colloidal clusters generally conserve their original size and shape, with a relatively narrow size distribution. This new approach to the manufacture of size-selected colloidal Au clusters shows distinct advantage in the high size resolution and the tenability of the cluster size (and potentially composition

and shape). This has the potential to contribute significantly to the design of new colloidal catalyst systems. Also, it will help to optimize the catalysis performance with the more accurate configuration of the nanoclusters, where the size and atomic structure can be controlled by the cluster beam source. The multilayer deposition method that has been developed shows a promising future in the large scale supported catalyst production, adaptable with the next generation high flux cluster beam source (MACS). The produced multilayer stacks can be regarded as a new storage form of the supported catalysts with better protection for the clusters than the normal powder form. The next step will be improving the morphology of the PVP layer to achieve 100% single-layer supported clusters and have the whole multilayer deposition process automated to increase the deposition speed and efficiency.

Reference:

1. Baletto, F. & Ferrando, R. Structural properties of nanoclusters: Energetic, thermodynamic, and kinetic effects. *Rev. Mod. Phys.* **77**, 371–423 (2005).
2. Ferrando, R., Jellinek, J. & Johnston, R. L. Nanoalloys: From theory to applications of alloy clusters and nanoparticles. *Chemical Reviews* **108**, 845–910 (2008).
3. Schmid, G., Baumle, M., Geerkens, M., Heim, I., Osemann, C. & Sawitowski, T. Current and future applications of nanoclusters. *Chem. Soc. Rev.* **28**, 179–185 (1999).
4. Toshima, N. & Yonezawa, T. Bimetallic nanoparticles—novel materials for chemical and physical applications. *New J. Chem.* **22**, 1179–1201 (1998).
5. Templeton, A. C., Wuelfing, W. P. & Murray, R. W. Monolayer-protected cluster molecules. *Acc. Chem. Res.* **33**, 27–36 (2000).
6. Judai, K., Abbet, S., Wörz, A. S., Heiz, U. & Henry, C. R. Low-Temperature Cluster Catalysis. *J. Am. Chem. Soc.* **126**, 2732–2737 (2004).
7. Burch, R. Gold catalysts for pure hydrogen production in the water-gas shift reaction: activity, structure and reaction mechanism. *Phys. Chem. Chem. Phys.* **8**, 5483–500 (2006).
8. Klein, D. L., Roth, R., Lim, A. K. L., Alivisatos, A. P. & McEuen, P. L. A single-electron transistor made from a cadmium selenide nanocrystal. *Nature* **389**, 699–701 (1997).
9. Chi, L., Hartig, M., Drechsler, T., Schwaack, Th., Seidel, C., Fuchs, H. & Schmid, G. Single-electron tunneling in Au₅₅ cluster monolayers. *Appl. Phys. A Mater. Sci. Process.* **190**, 187–190 (1998).
10. Buchenau, H., Knuth, E. L., Northby, J., Toennies, J. P. & Winkler, C. Mass

- spectra and time-of-flight distributions of helium cluster beams. *J. Chem. Phys.* **92**, 6875 (1990).
11. Pratontep, S., Carroll, S. J., Xirouchaki, C., Streun, M. & Palmer, R. E. Size-selected cluster beam source based on radio frequency magnetron plasma sputtering and gas condensation. *Rev. Sci. Instrum.* **76**, 045103 (2005).
 12. Duval, P. B., Burns, C. J., Clark, D. L., Morris, D. E., Scott, B. L., Thompson, J. D., Werkema, E. L., Jia, L. & Andersen, R. A. Synthesis and Structural Characterization of the First Uranium Cluster Containing an Isopolyoxometalate Core. *Angewandte Chemie (International ed. in English)* **13**, 3357–3361 (2001).
 13. Maity, P., Xie, S., Yamauchi, M. & Tsukuda, T. Stabilized gold clusters: from isolation toward controlled synthesis. *Nanoscale* **4**, 4027 (2012).
 14. Ghosh, A. & Pradeep, T. Synthesis of Atomically Precise Silver Clusters by Using the Miscibility Principle. *Eur. J. Inorg. Chem.* n/a–n/a (2014). doi:10.1002/ejic.201402587
 15. Huard, D. J. E., Kane, K. M. & Tezcan, F. A. Re-engineering protein interfaces yields copper-inducible ferritin cage assembly. *Nat. Chem. Biol.* **9**, 169–76 (2013).
 16. Thakkar, K. N., Mhatre, S. S. & Parikh, R. Y. Biological synthesis of metallic nanoparticles. *Nanomedicine Nanotechnology, Biol. Med.* **6**, 257–262 (2010).
 17. Song, J. Y. & Kim, B. S. Rapid biological synthesis of silver nanoparticles using plant leaf extracts. *Bioprocess Biosyst Eng* **32**, 79–84 (2009).
 18. Wegner, K., Piseri, P., Tafreshi, H. V. & Milani, P. Cluster beam deposition: a tool for nanoscale science and technology. *J. Phys. D. Appl. Phys.* **39**, R439–R459 (2006).

19. Palmer, R. E., Cao, L. & Yin, F. Note: Proof of principle of a new type of cluster beam source with potential for scale-up. *Rev. Sci. Instrum.* **87**, 046103 (2016).
20. Ellis, P., Brown, C. M., Bishop, P. T., Yin, J., Cooke, K., Terry, W. D., Liu, J., Yin, F. & Palmer, R. E. The cluster beam route to model catalysts and beyond. *Faraday Discuss.* **188**, 39-56 (2016).
21. von Issendorff, B. & Palmer, R. E. A new high transmission infinite range mass selector for cluster and nanoparticle beams. *Rev. Sci. Instrum.* **70**, 4497 (1999).
22. Pratontep, S., Preece, P., Xirouchaki, C., Palmer, R. E., Sanz-Navarro, C. F., Kenny, S. D. & Smith, R. Scaling relations for implantation of size-selected Au, Ag, and Si clusters into graphite. *Phys. Rev. Lett.* **90**, 055503 (2003).
23. Dahmen, U., Erni, R., Radmilovic, V., Kisielowski, C., Rossell, M. & Denes, P. Background, status and future of the Transmission Electron Aberration-corrected Microscope project. *Phil. Trans. A* **367**, 3795–3808 (2009).
24. Pennycook, S. J., Lupini, A. R., Varela, M., Borisevich, A. Y., Peng, Y., Oxley, M. P., van Benthem, K. & Chisholm, M. F. Scanning Transmission Electron Microscopy for Nanostructure Characterization. *Scanning Microsc. Nanotechnol.* 152–191 (2007). doi:10.1007/978-0-387-39620-0_6
25. Kisielowski, C., Freitag, B., Bischoff, M., van Lin, H., Lazar, S., Kinppels, G., Tiemeijer, P., van der Stam, M., von Harrach, S., Stekelenburg, M., Haider, M., Uhlemann, S., Muller, H., Hartel, P., Kabius, B., Miller, D., Petrov, I., Olson, E. A., Donchev, T., Kenik, E. A., Lupini, A. R., Bentley, j., ennycook, S. J., Anderson, I. M., Minor, A. M., Schmid, A. K., Duden, T., Radmilovic, V., Ramasse, Q. M., Watanable, M., Erni, R., Stach, E. A., Denes, P. & Dahmen, U. Detection of single atoms and buried defects in three dimensions by

- aberration-corrected electron microscope with 0.5-Å information limit. *Microsc. Microanal. Off. J. Microsc. Soc. Am. Microbeam Anal. Soc. Microsc. Soc. Canada* **14**, 469–477 (2008).
26. van Benthem, K., Lupini, A. R., Oxley, M. P., indlay, S. D., llen, L. J. & Pennycook, S. J. Three-dimensional ADF imaging of individual atoms by through-focal series scanning transmission electron microscopy. *Ultramicroscopy* **106**, 1062–1068 (2006).
27. Habibpour, V., Song, M. Y., Wang, Z. W., Cookson, J., Brown, C. M., Bishop, P. T. & Palmer, R. E. Novel powder-supported size-selected clusters for heterogeneous catalysis under realistic reaction conditions. *J. Phys. Chem. C* **116**, 26295–26299 (2012).
28. Schmid, G. & Chi, L. F. Metal clusters and colloids. *Adv. Mater.* **10**, 515–526 (1998).
29. Schmid, G., West, H., Malm, J., Bovin, J. & Grenthe, C. Catalytic Properties of Layered Gold- Palladium Colloids. *Inorg. Chem.* **2**, 1099–1103 (1996).
30. Lewis, L. N. Chemical catalysis by colloids and clusters. *Chem. Rev. (Washington, DC, United States)* **93**, 2693–2730 (1993).
31. Schon, G. A Fascinating New Field in Colloid Science: Small Ligand Stabilized Metall Clusters and Possible Applications in Microelectronics. *Colloid Polym. Sci.* **273**, 101–117 (1995).
32. Narayanan, R. & El-Sayed, M. A. Catalysis with transition metal nanoparticles in colloidal solution: Nanoparticle shape dependence and stability. *J. Phys. Chem. B* **109**, 12663–12676 (2005).
33. Bradley, J. S., Hill, E., Leonowicz, M. E. & Witzke, H. Clusters, colloids and catalysis. *J. Mol. Catal.* **41**, 59–74 (1987).

34. Li, Y., Boone, E. & El-Sayed, M. A. Size effects of PVP-Pd nanoparticles on the catalytic Suzuki reactions in aqueous solution. *Langmuir* **18**, 4921–4925 (2002).
35. Narayanan, R. & El-Sayed, M. A. Effect of colloidal catalysis on the nanoparticle size distribution: Dendrimer-Pd vs PVP-Pd nanoparticles catalyzing the Suzuki coupling reaction. *J. Phys. Chem. B* **108**, 8572–8580 (2004).
36. HARUTA, M. Gold catalysts prepared by coprecipitation for low-temperature oxidation of hydrogen and of carbon monoxide. *J. Catal.* **115**, 301–309 (1989).
37. Haruta, M., Kobayashi, T., Sano, H. & Yamada, N. Novel gold catalysts for the oxidation of carbon monoxide at a temperature far below 0.DEG.C. *Chem. Lett.* 405–408 (1987). doi:10.1246/cl.1987.405
38. Nakagawa, Y., Takada, K., Tamura, M. & Tomishige, K. Total hydrogenation of furfural and 5-hydroxymethylfurfural over supported Pd-Ir alloy catalyst. *ACS Catal.* **4**, 2718–2726 (2014).
39. Jin, R. Atomically precise metal nanoclusters: stable sizes and optical properties. *Nanoscale* **7**, 1549–65 (2015).
40. Xu, Q., Kumar, S., Jin, S., Qian, H., Zhu, M. & Jin, R. Chiral 38-gold-atom nanoclusters: synthesis and chiroptical properties. *Small* **10**, 1008–14 (2014).
41. Das, A., Liu, C., Zeng, C., Li, G, Li, T. Rosi, N. L. & Jin, R. Cyclopentanethiolato-protected Au₃₆(SC₅H₉)₂₄ nanocluster: Crystal structure and implications for the steric and electronic effects of ligand. *J. Phys. Chem. A* **118**, 8264–8269 (2014).
42. Li, G., Zeng, C. & Jin, R. Thermally Robust Au 99 (SPh) 42 Nanoclusters for Chemoselective Hydrogenation of Nitrobenzaldehyde Derivatives in Water. **99**,

- (2014).
43. Das, A., Li, T., Nobusada, K., Zeng, C., Rosi, N. L. & Jin, R. Crystal structure and electronic properties of a thiolate-protected Au₂₄ nanocluster. *Nanoscale* **6**, 6458–62 (2014).
 44. Levi-Kalishman, Y., Jadzinsky, P. D., Kalishman, N., Tsunoyama, H., Tsukuda, T., Bushnell, D. A. & Kornberg, R. D. Synthesis and characterization of Au₁₀₂(p-MBA)₄₄ nanoparticles. *J. Am. Chem. Soc.* **133**, 2976–82 (2011).

CHAPTER 8

CONCLUSION

In this thesis, we have presented research on the size and atomic structure investigation of the nanoclusters, including phosphite protected monometallic clusters, thiol protected bimetallic clusters, TiO₂ supported ultra-small monometallic cluster and biological metallic clusters by using aberration corrected HAADF-STEM.

The research on the atomic structure of the phosphite ligand protected Au₅₅ Schmid clusters has been presented in chapter 3. The atom counting method with size selected clusters as mass balance was utilized to successfully “fractionate” the relative broad size distributed sample and make the structure study focus on the “true Au₅₅” clusters. We found that nearly half of these “true Au₅₅ clusters” HAADF STEM images matched the simulation STEM images of a hybrid structure.

When we studied the bimetallic thiol protected AuAg alloy clusters in chapter 4, the situation became more complicated. The atom counting that was performed in chapter 3 cannot be directly used because of the unknown composition of every single cluster. Therefore, the analysis on the 2D projection area of the alloy clusters was performed with a combination with normal atom counting method to determine both the size and composition of the AuAg alloy cluster. With these results, we investigated the atomic

structure of the AuAg alloy cluster with the size range of 312 ± 55 as a function of AuAg composition. The silver rich clusters tend to have an icosahedral structure while the gold rich clusters prefer the fcc structure.

The HAADF intensity based atom counting method is not limited to normal physical or chemically produced clusters. It can also be applied to bio-produced clusters. The ferritin, as the major iron storage protein, stores the excess iron in the livings in was obtained by the atom counting method with HAADF STEM. The iron loading varies from few hundred iron atoms to around 5000 iron atoms. Different morphology of the ferritin iron core was observed as a function of iron loading, suggesting the iron core growth process in the protein shell.

The incoherent nature of the HAADF-STEM provides the high ability on observing ultra-small clusters. In chapter 6, the HAADF-STEM was successfully employed to investigate small Au cluster supported on the TiO_2 . Two sets of Au/ TiO_2 catalysts with very similar size distribution base on the observation by conventional TEM have very different catalytic performance. By the aberration corrected HAADF-STEM, the ultra-small Au clusters with only few atoms can only be found in the high activity catalysts, explaining the reason of the better catalytic property.

With the development of the high flux matrix assembly cluster source (MACS), the current deposition system cannot handle the extremely increased high flux cluster

beam. A multilayer deposition method was developed to accommodate and process the large abundance of clusters by producing the stack of support layer-cluster-release layer sandwiches. The through focal HAADF-STEM analysis was successfully performing on the multilayer sample, confirmed the multilayer structures of the stack and the thickness of each layer. The multilayer stacks can be diced by either a diamond saw or laser to small pieces. The release layers of the diced multilayer pieces can be dissolved in the organic solution to release the single layer supported clusters. With the similar experimental setup, the size-selected colloidal clusters were produced by dissolving the multilayer cluster-PVP stacks. The colloidal cluster solution was drop cast onto the TEM grid and analyzed by the HAADF-STEM. The colloidal clusters were observed and their sizes were found to be conserved during the dissolving process, proving the success of production of size-selected colloidal clusters.

In general, the aberration corrected HAADF-STEM has been successfully employed on different nanoparticle systems. The objectives mentioned in chapter 1 were all achieved. The integrated HAADF intensity has been proved to be capable for determining size and composition of the nanoparticle with size-selected clusters as calibration references, which opens a new window to investigate the wide size range nanoparticles in a more precise way. The through focal analysis on the multilayer samples implies that the utilization of aberration corrected HAADF STEM can be extended from 2D to 3D, showing the potential of a new method of resolving the 3D nanostructure by electron microscopy.

Appendix I Extraction of integrated HAADF intensity of nanoparticle

In the incoherent HAADF mode, the integrated HAADF intensity of a certain area can directly reflect the total atomic number in this area. So in the HAADF-STEM image of a nanoparticle, the integrated HAADF intensity of the nanoparticle area is contributed from both nanoparticle and its support materials. In this thesis, the extraction of the integrated HAADF intensity of the nanoparticle is achieved by deleting the contribution of the support materials. The practical method is to draw a ring with the nanoparticle inside. Then measure the integrated HAADF intensity of the inner circle I_i and the outer shell I_o . As shown in the Figure S1, the I_i is the combination of the contributions of nanoparticle I_{np} and support material I_{si} , the I_o is only the contribution of the support material I_{so} . Assuming the support material is homogeneous, then we can get $I_{si}/I_{so}=S_i/S_o$, where S_i and S_o are the area of the inner circle and outer ring, respectively. So the integrated HAADF intensity of the nanoparticle can be calculated by

$$I_{np} = I_i - I_{si} = I_i - I_o \times \frac{S_i}{S_o}$$

So we only need to measure the area and integrated HAADF intensity of the inner circle and outer ring to get the integrated HAADF intensity of the nanoparticle. There are a few tips for this method: first, employ this method on the clusters with homogeneous background. This method is base on the assumption that the support material is homogeneous. So if the background is too complicated, it will significantly affect the accuracy of the result. Second, make sure the images are not affected by the contamination, as it can also break the homogeneity of the background. Third, if the nanoparticle has the ligand surround, make sure the inner circle is big enough to

cover the ligand. Then the ligand effect should also be deleted if the ligand type and number is known. Finally, if we want to compare different nanoparticles' integrated HAADF intensity, make sure the STEM parameters that can affect the HAADF intensity are all the same, such as pixel size, pixel dwell time, probe current, HAADF detection angle range etc.

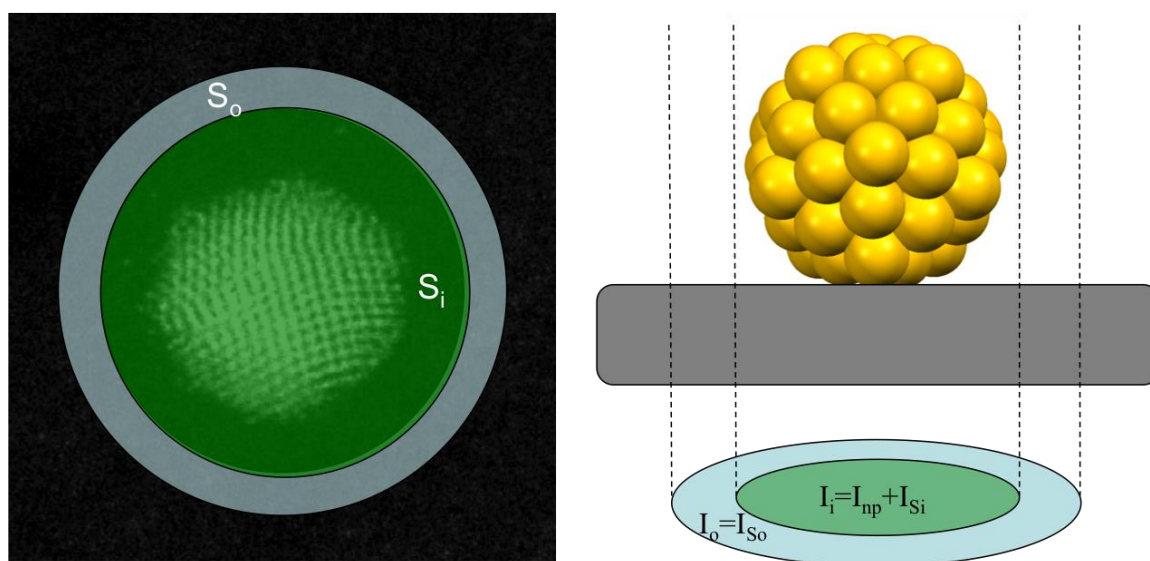
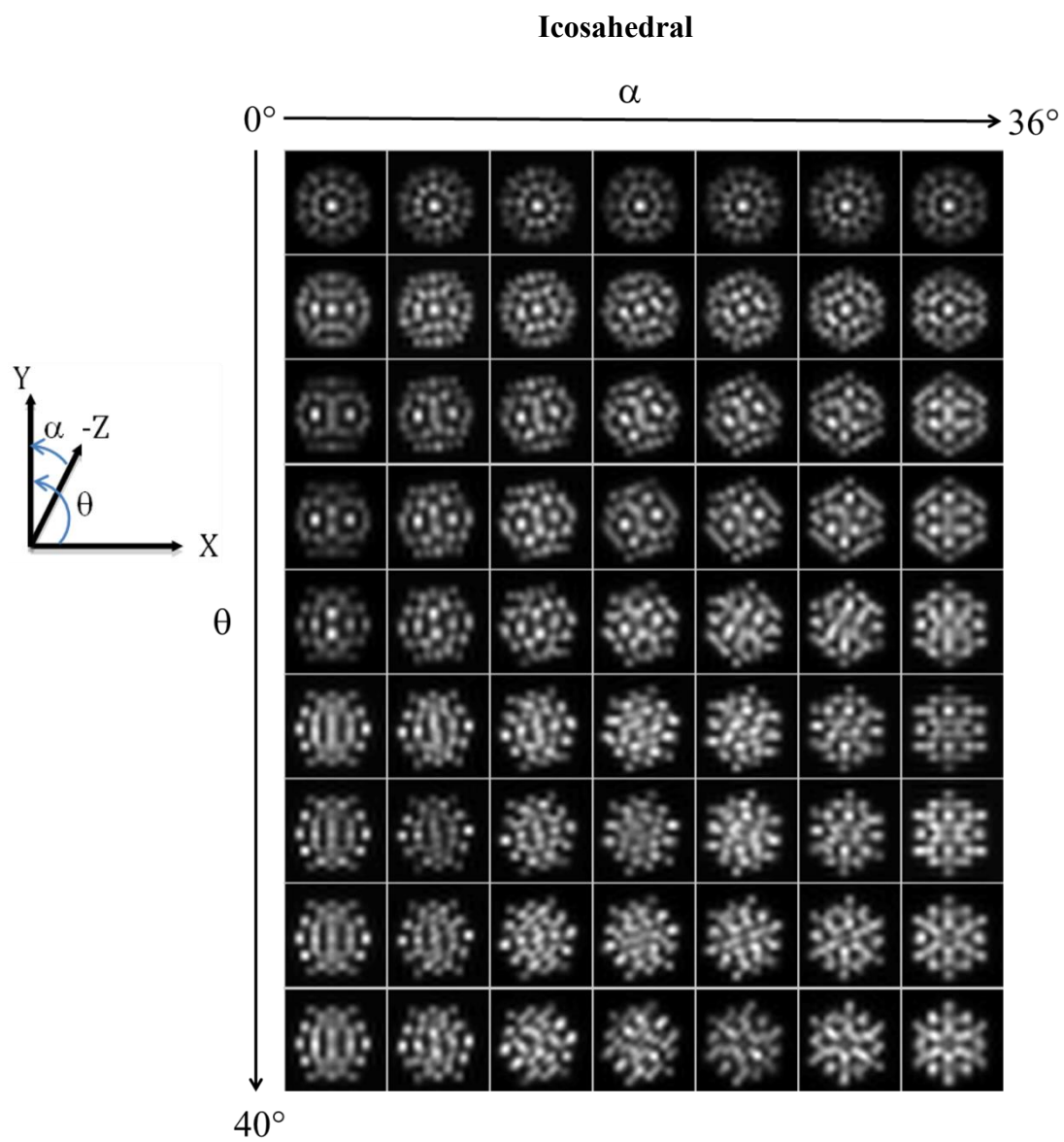
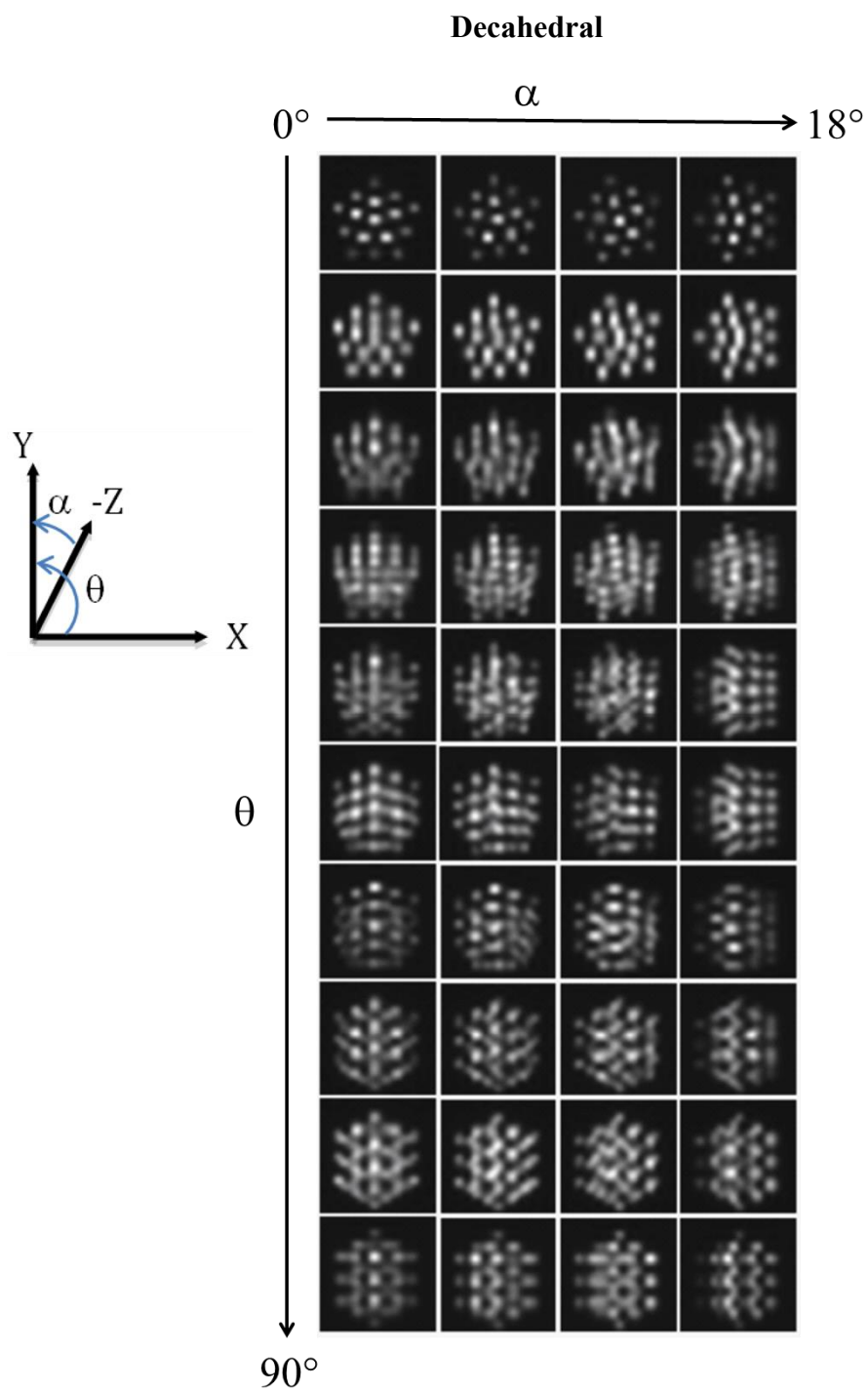
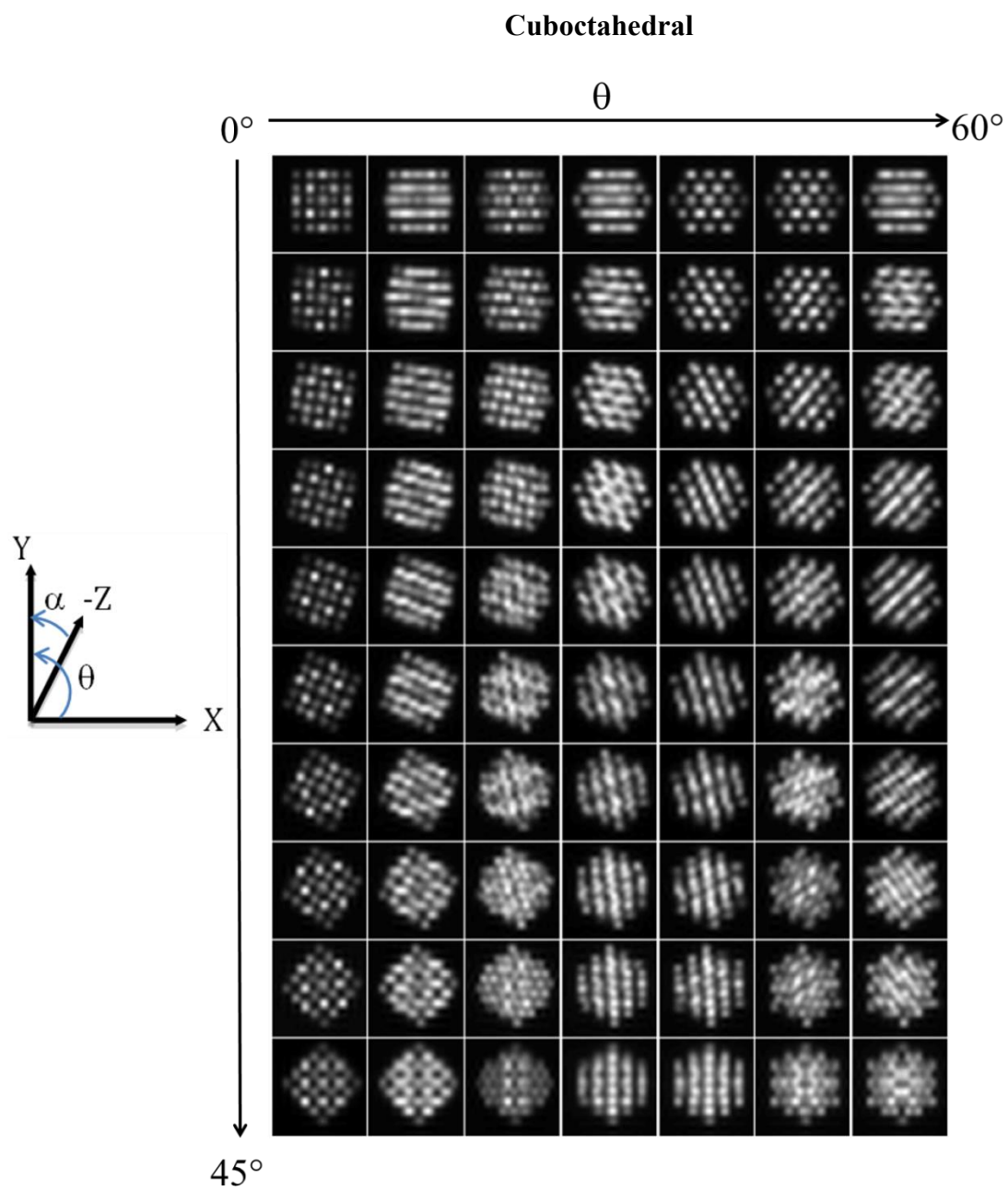


Figure S1. The schematic of the extraction of the integrated HAADF intensity of nanoparticle.

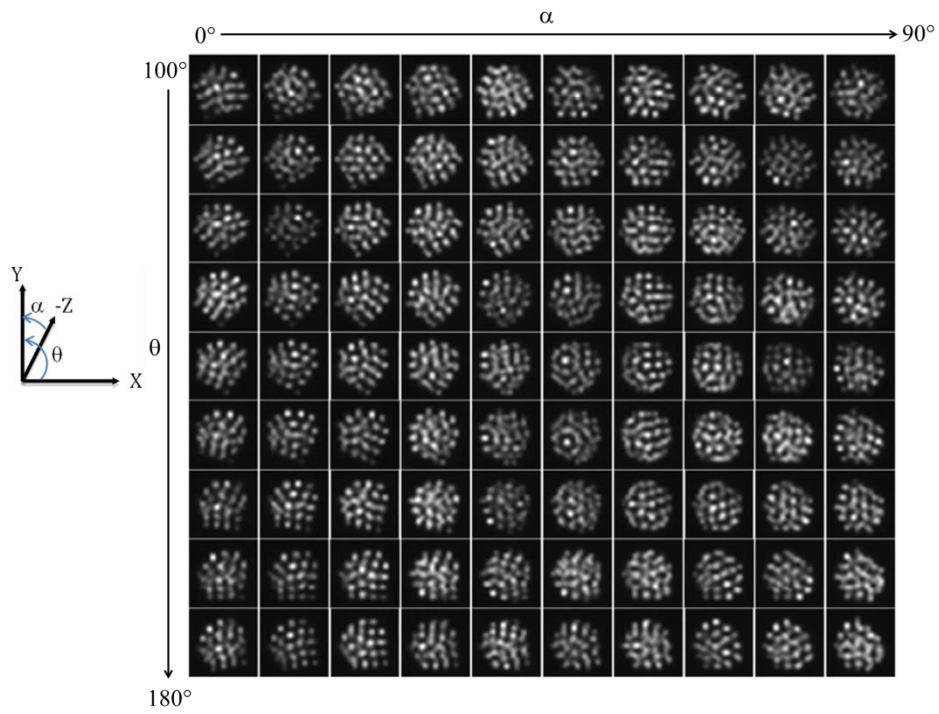
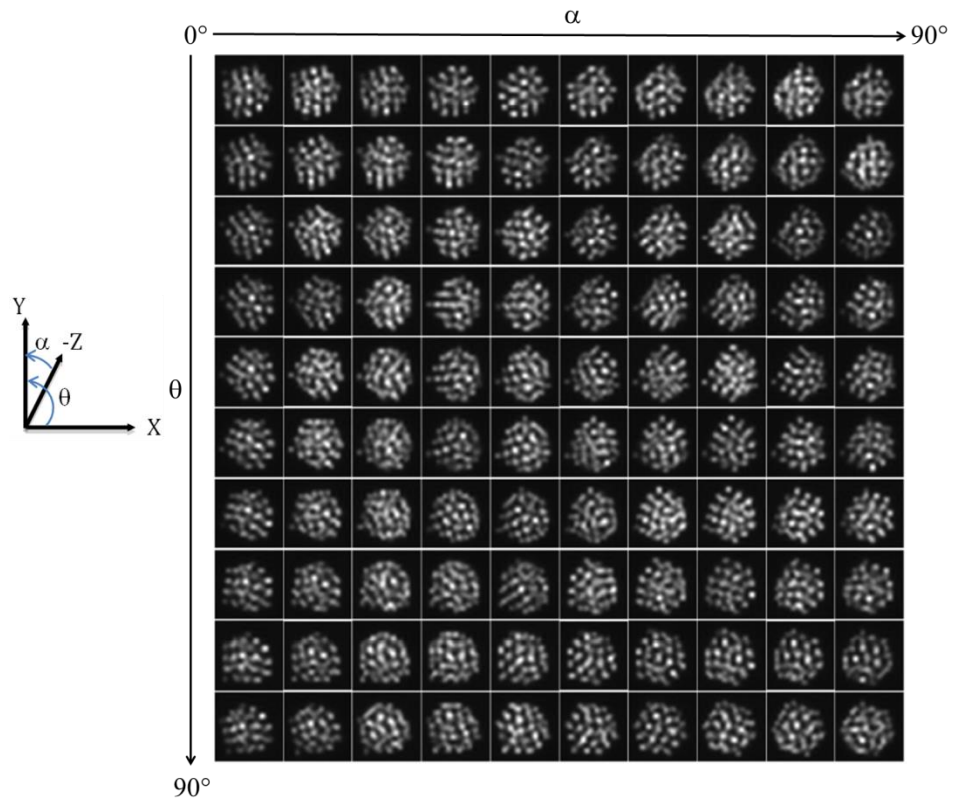
Appendix II Simulation Atlas of Au55 clusters

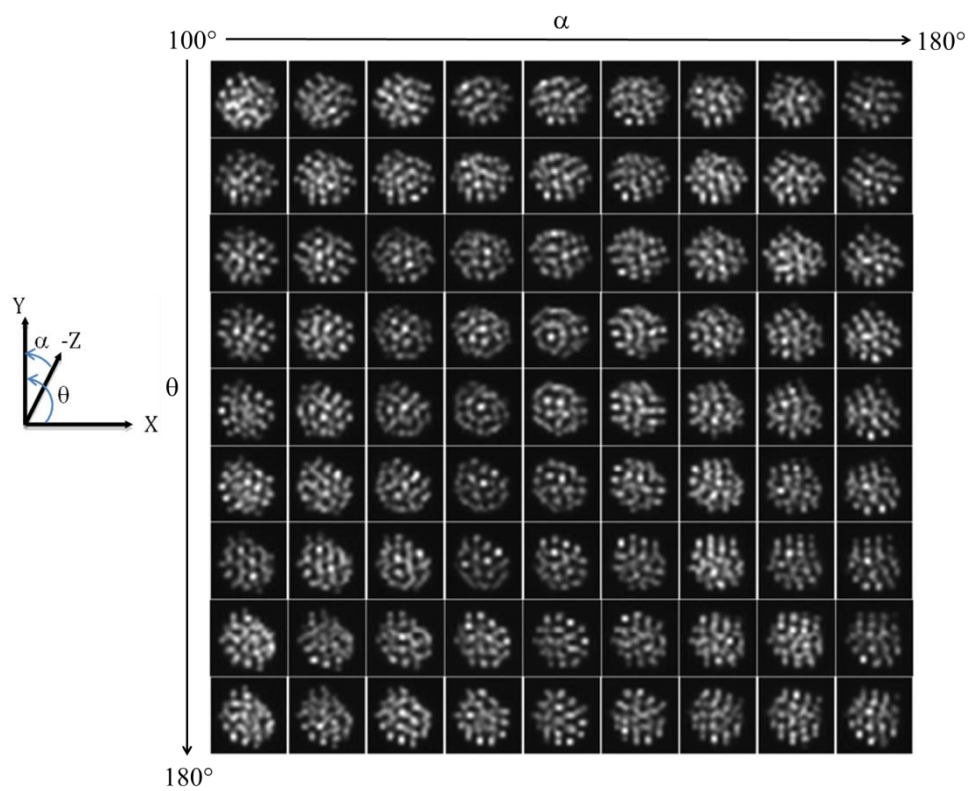
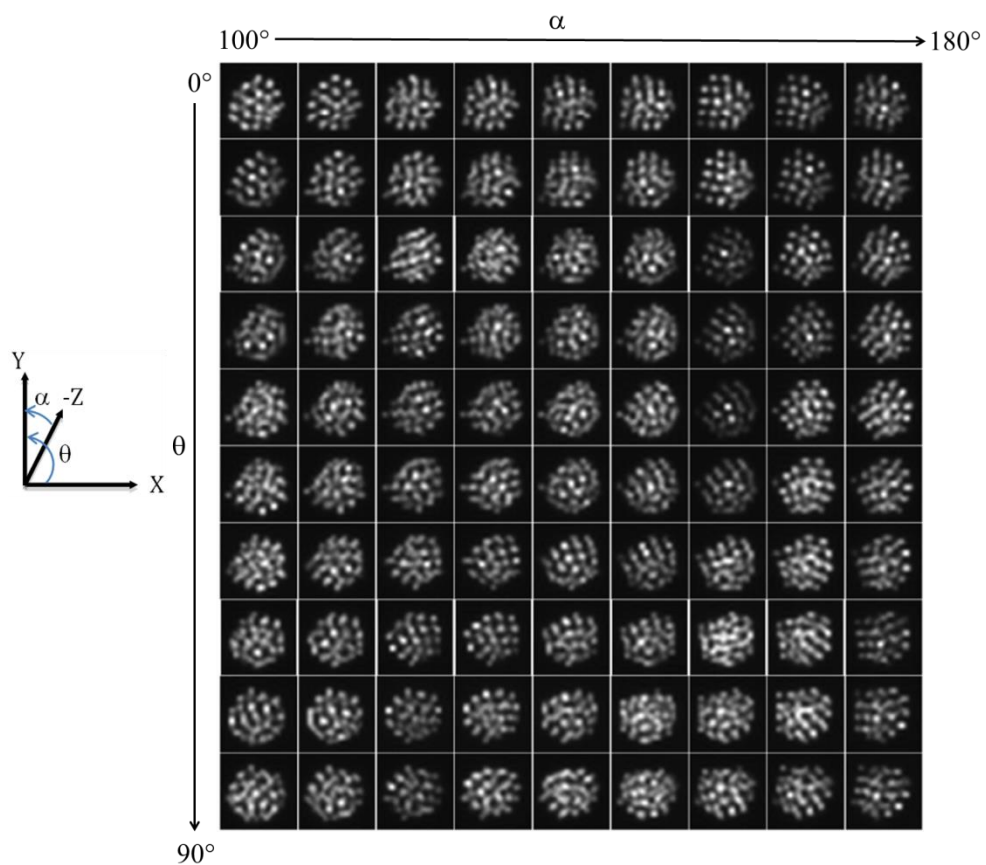






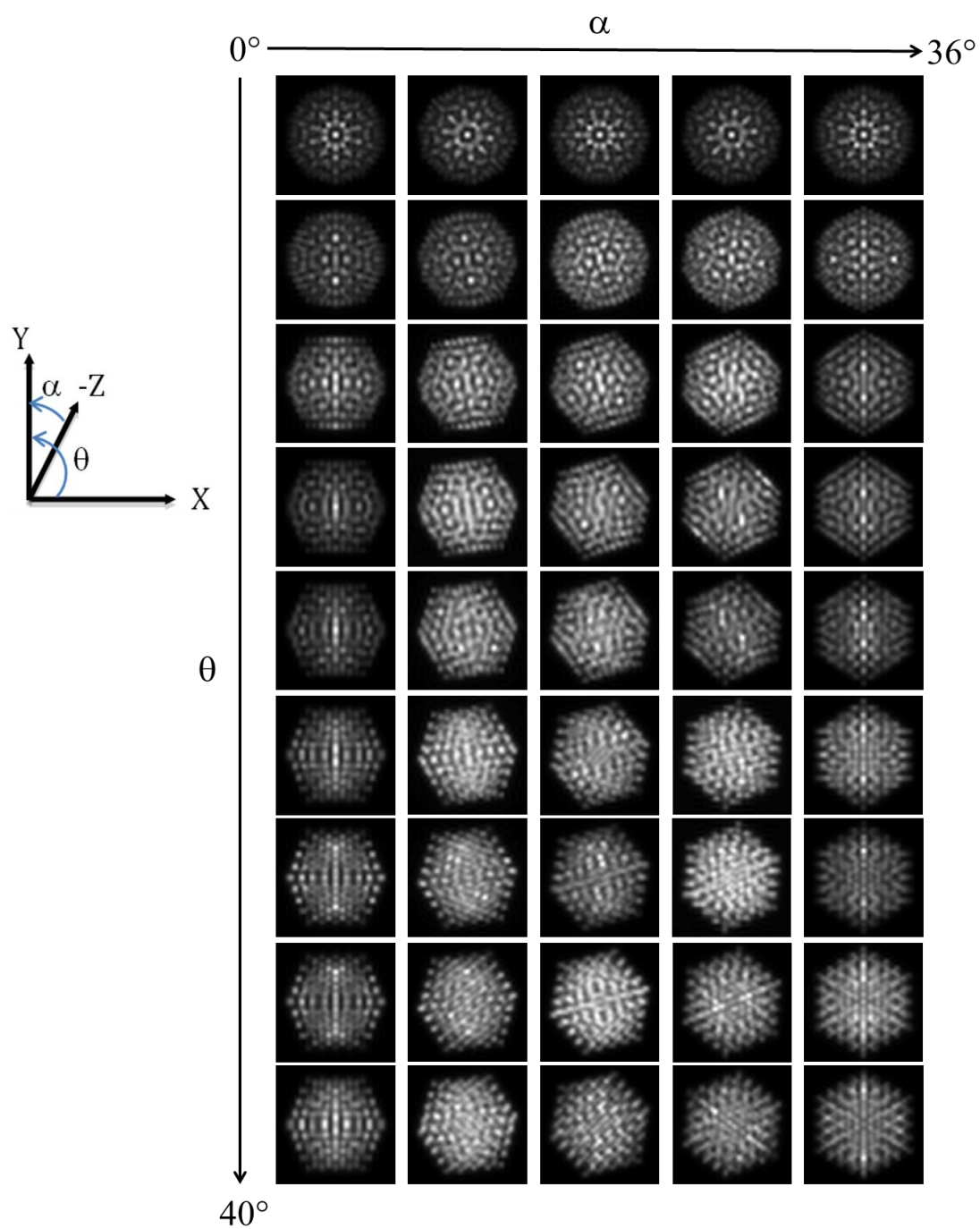
Hybrid structure

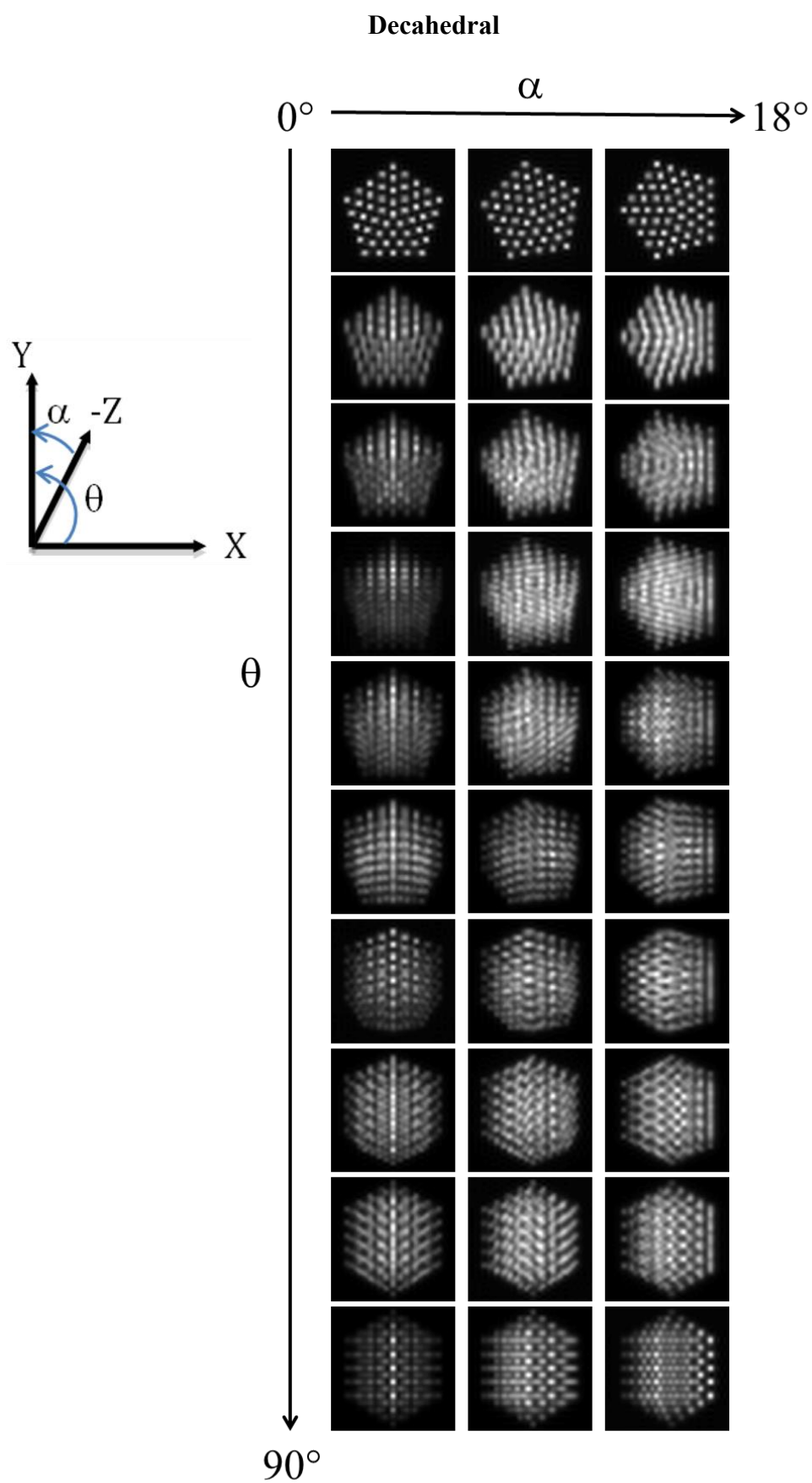




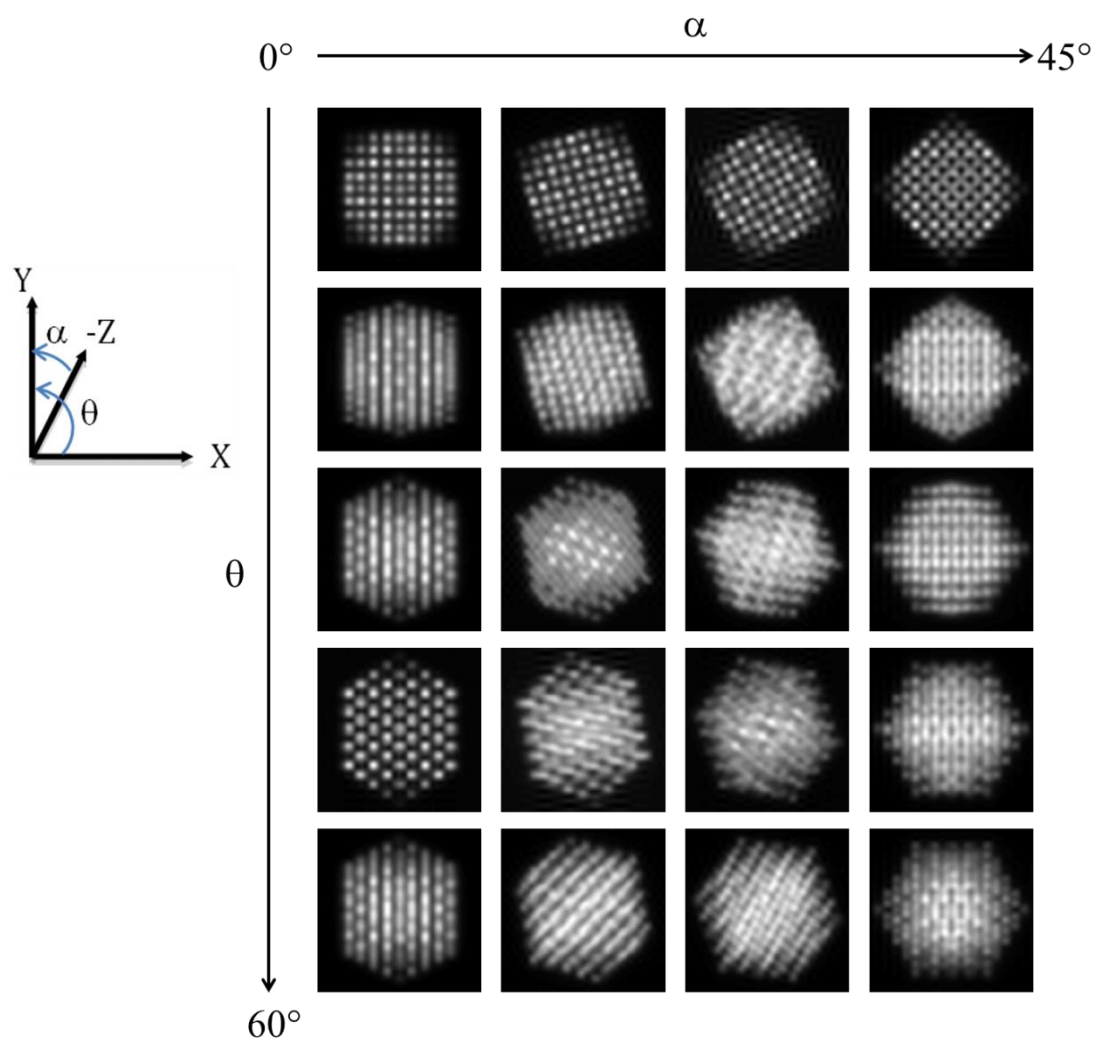
Appendix III Simulation Atlas of Au₃₀₉ clusters

Icosahedral





Cuboctahedral



Appendix IV Validity test of geometric analysis

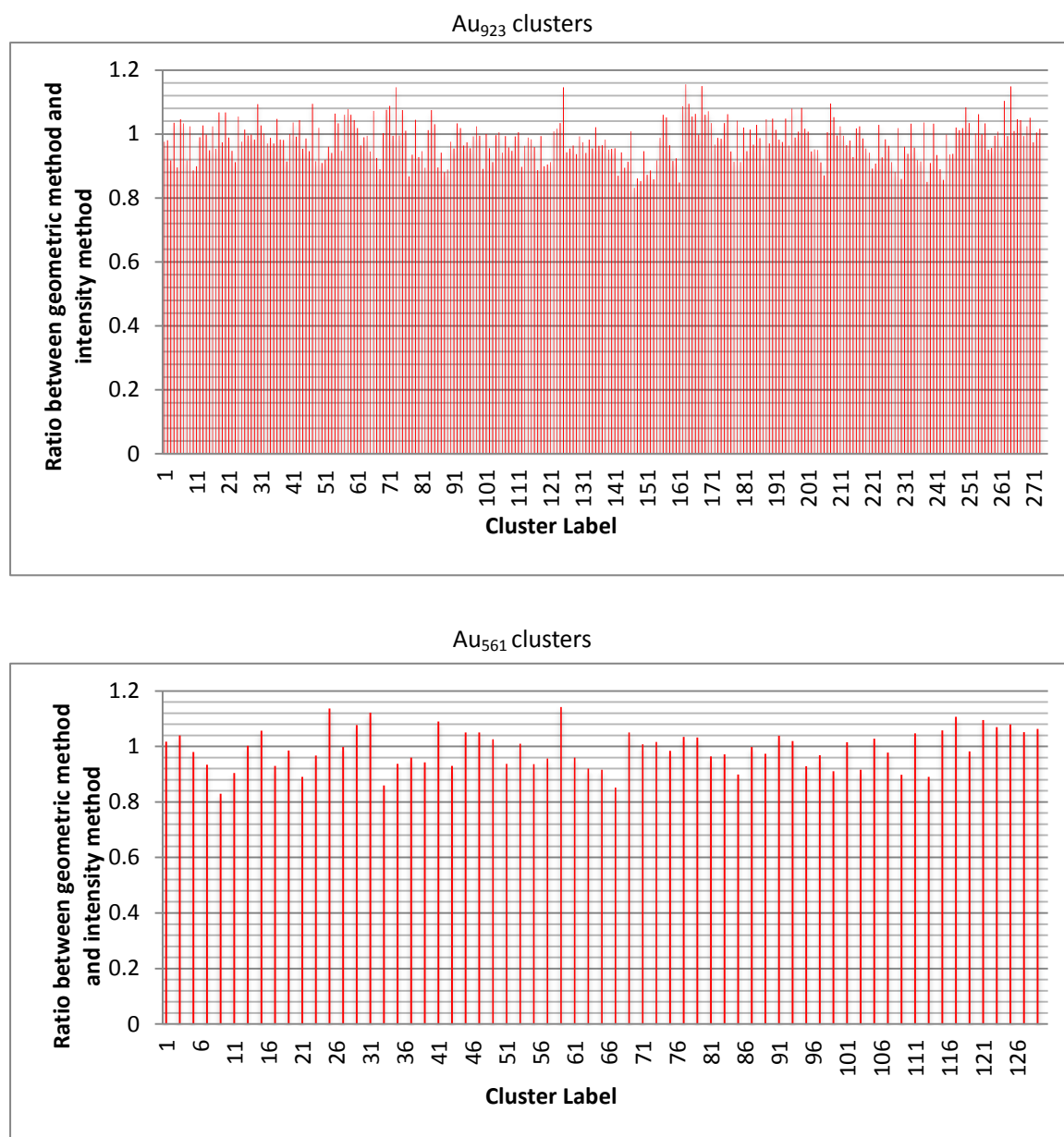


Figure S1. These graphs are a test of the geometric method we employ to obtain the nuclearity of the binary Au-Ag clusters. They compare the atom counting (HAADF-STEM intensity) method for size-selected Au₉₂₃ and Au₅₆₁ clusters with the geometric (diameter measurement) method. The value “1” on the Y axis means the nuclearity of the cluster obtained from its projected area is the same from the HAADF intensity. Each bar is one cluster.

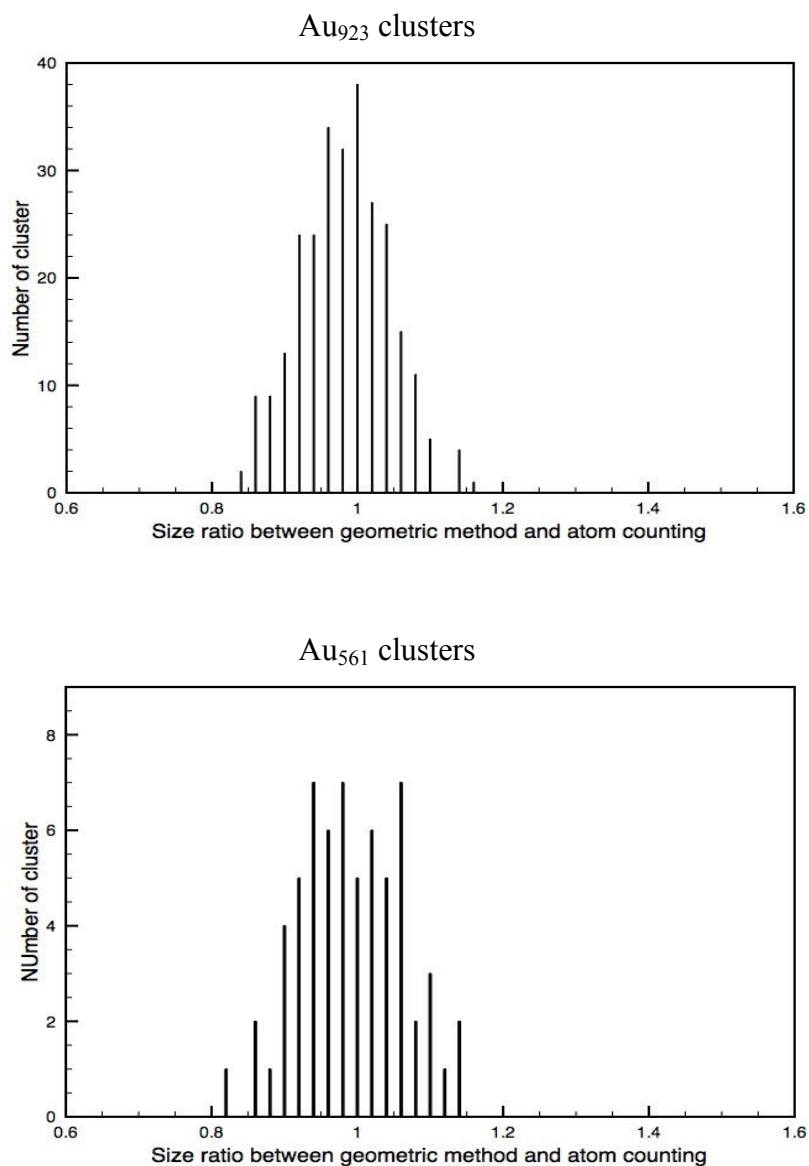


Figure S2. These two graphs show the distribution of the size ratio between the geometric and atom counting methods. The peak for Au₉₂₃ clusters is at 0.984 ± 0.060 and for Au₅₆₁ is at 0.986 ± 0.080 . Their cosine similarities are 0.9976 and 0.9980.